

Structural and Geochemical Analyses of fragment-rich pseudotachylite bodies and the Vredefort Granophyre of the Vredefort Impact Structure, South Africa

Thesis submitted to the Department of Earth Sciences, Free University of Berlin, Germany, in partial fulfilment of the requirements for the degree of Doctor rerum Naturum.

Department of geoscience (FB Geowissenschaften) at the Freie Universität Berlin supported by the Museum für Naturkunde, Humboldt-Universität

Daniel Lieger

Berlin 2011

**Structural and Geochemical Analyses of fragment-rich pseudotachylite bodies
and the Vredefort Granophyre of the Vredefort Impact Structure, South
Africa**

Daniel Lieger

1. Gutachter: Prof. Dr. Harry Becker

2. Gutachter: Prof. Dr. Ulrich Riller

Disputation am: 16.05.2011

ZUSAMMENFASSUNG

Meteoriteneinschläge (Impakte) werden heute als eine der wichtigsten Prozesse in der planetaren Geologie angesehen. Obwohl detaillierte strukturelle, petrografische und geochemische Studien von terrestrischen Impaktstrukturen existieren, sind deren Daten und Zusammenhänge kaum verstanden. Unsicherheiten existieren vor allem in der geometrischen und kinematischen Bedeutung von Dislokationszonen, der zeitlichen und mechanischen Bedeutung zwischen kontinuierlicher und diskontinuierlicher Deformation während der Zentralbergbildung sowie in der Entstehung und Platznahme der pseudotachylitischen Schmelze von großen fragmentreichen Körpern.

Die vorliegende Arbeit untersucht die Entstehung des Zentralberges und der fragmentreichen pseudotachylitischen Zonen der komplexen, 2.023 ± 4 Ga alten Vredefort Impaktstruktur in Südafrika. Der zentrale Bereich der Vredefort Impaktstruktur, der sogenannten Vredefort Dome, repräsentiert den erodierten Rest der angehobenen Gesteinspakete des Zentralberges. Der Vredefort Dome umfasst einen 40 Kilometer breiten archaischen Kern (Vredefort Core) bestehend aus migmatischen Gneisen mit einer Tonalit-Trondhjemit-Granodiorit-Vergesellschaftung sowie granitoide Plutone und Gesteine des Grünsteingürtels. Dieser innere Bereich des Vredefort Domes ist umgeben von dem 15-20 Kilometer breiten „Collar“, der aus steil gestellten bis überkippten, 3.07 bis 2.1 Ga alten Metasedimentgesteinen sowie intrudierten Alkaligraniten und Dioriten besteht. Das Vorkommen der Pseudotachylite ist die Gemeinsamkeit aller Gesteine des gesamten Vredefort Domes. Die Pseudotachylite kommen als unregelmäßig verlaufende, Millimeter bis Zentimeter breite Gänge sowie Dezimeter bis einige zehner Meter mächtige Körper mit meist scharfem Kontakt zum Nebengestein vor. Die Präsenz von stoßwellenmetamorphen Mineralen in einigen kleinen Gängen zeigt, dass diese Gänge das Produkt von Wechselwirkung der Stoßwelle mit dem Zielgestein sind. Zusätzlich entsteht bei der Wechselwirkung Reibungswärme, die ebenfalls verantwortlich für lokal gebildete Schmelzen ist. Reibungsschmelzen in Impaktstrukturen können auch ohne Einwirkung der Stoßwelle entstehen, indem Kraterrandschollen an übersteilten Kraterrändern an listischen Störungen abgleiten und Pseudotachylite bilden. Jedoch können weder stoßwelleninduzierte Schmelzen noch

Reibungsschmelzen die Vorkommen von Meter mächtigen Pseudotachyliten in den Impaktstrukturen erklären.

Die umfangreiche strukturelle Analyse dieser Arbeit von dem prä-impakt Mineralgefüge und fragmentreichen Pseudotachyliten des Vredefort Domes hat gezeigt, dass die Gefüge und Pseudotachylite radial und konzentrisch hinsichtlich des Kraterzentrums angeordnet sind. Dabei ergab die Gefügeanalyse eine nordwest-südost streichende Spiegelebene. Die Gefügesymmetrie ist konsistent mit einer vertikalen Dehnung und Anhebung des inneren Kernbereichs sowie einer auswärts gerichteten Rotation und Dilatation des äußeren Kernbereichs, was durch numerische Modellierungen von Impaktereignissen berechnet wurde. Die symmetrische Anordnung, Geometrie und Brekzienintensität von pseudotachylitischen Körper stimmen mit der Verformung überein, die ebenfalls die numerischen Modelle wiedergaben.

Mit Hilfe petrografischer und geochemischer Analysen sollte der Impaktschmelzsee als Quelle für die großen fragmentreichen Pseudotachylite bestätigt werden. Der Vergleich von geochemischen Daten der fragmentreichen Pseudotachylite mit denen der unmittelbaren Nebengesteinstypen zeigte, dass diese signifikant voneinander abweichen und dass die Assimilation des Nebengesteins die Schmelzzusammensetzung der pseudotachylitischen Schmelze modifizierte. Die chemischen Trends der kompositionellen Abweichung von Meter breiten fragmentreichen Pseudotachyliten vom direkten Nebengestein sind konsistent mit der Präsenz einer allochthonen granitoiden Schmelze, deren Zusammensetzung dem Vredefort Granophyr ähnelt. Der Vredefort Granophyr gilt als das Produkt der Differentiation des originalen Impaktschmelzsees. Die Untersuchung des Schmelztransportes anhand Zentimeter zu Meter breiten pseudotachylitischen Körpern ergab einen gerichteten Schmelztransport von großen in kleine pseudotachylitische Körper und Apophysen. Mit Hilfe der Mineralogie von Sulfiden und Silikaten wurde die Temperatur dieser Schmelze zwischen 1200-1700 °C bestimmt. Die Analysen der strukturellen und geochemischen Daten zeigten, dass in der Spätphase der Kraterbildung eine allochthone Schmelze aus dem überhitzten Impaktschmelzsee in Extensionsbrüche im Kraterboden intrudiert sein muss, um fragmentreiche Pseudotachylite zu bilden. Es ist wahrscheinlich, dass während des Kollapses des Zentralberges und der auswärts gerichteten Gesteinsbewegung die Schmelzbewegung dem Druckgradienten folgte und in fragment-reiche Dilatationszonen intrudierte.

Zusätzlich zur geochemischen Analyse der pseudotachylitischen Körper wurden geochemische Daten vom Vredefort Granophyr ermittelt, um den Einfluss der Impaktschmelze auf fragmentreichen Pseudotachylite zu bestimmen. Strukturell ähneln sich die Vorkommen der fragmentreichen Pseudotachylite und Vredefort Granophyre. Die Vredefort Granophyre sind ebenfalls radial und konzentrisch hinsichtlich des Kraterzentrums angeordnet. Jedoch durchschlagen sie, im Gegensatz zu den fragmentreichen Pseudotachyliten, den Kontakt zwischen dem Archaischen „Core“ und dem proterozoischen „Collar“. Geochemische Untersuchungen von Vredefort Granophyrgängen ergab eine chemische Heterogenität zwischen Gängen im Vredefort „Core“ und denen, die im „Core“ und „Collar“ verlaufen sowie innerhalb einzelner Gänge. Innerhalb der Gänge wurden zusätzlich neben den chemischen auch textuelle Unterschiede sowie unterschiedliche Fragmentverteilungen festgestellt, die sich in zwei Zonen trennen lassen. Diese beiden Zonen innerhalb der Vredefort Granophyre geben dabei zwei Intrusionsphasen an. Die strukturelle Betrachtung dieser Gänge deutet darauf hin, dass die Vredefort Granophyr-Impaktschmelze in ein Bruchsystem intrudierte, welches erst während der isostatischen Ausgleichsbewegung der darunterliegenden Kruste zehntausende Jahre später angelegt wurde.

ABSTRACT

Despite the fact that large meteorite impacts belong to one of the most processes in planetary geology, detailed structural, petrographic and geochemical studies of terrestrial impact structures, let alone of large complex ones, are little understood. Major uncertainties centre around the geometric and kinematic significance of prominent dislocations, the temporal and mechanical relationships between continuous and discontinuous deformation during formation of the central uplift as well as the formation and emplacement of pseudotachylitic melt in large breccia bodies.

This study investigated the formation of the central uplift structure and pseudotachylitic breccia zones of the large, complex 2023 ± 4 Ma old Vredefort Impact Structure. The central portion of the impact structure, the so-called Vredefort Dome, is the eroded relic of structurally uplifted rocks, generally referred to as the central uplift. The Vredefort Dome consists of a core, ca. 40 km in diameter, of a predominantly polydeformed Archean migmatitic gneisses, with subsidiary tonalite-trondhjemite-granodiorite assemblage, syn-tectonic granitoids and remnants of greenstone units. The core is surrounded by a 15-20 km wide ‘collar’ of subvertical to overturned, 3.07 and 2.1 Ga supracrustal strata that were deposited unconformably on the Archean crystalline basement rocks. The Vredefort dome is well known for its prominent pseudotachylite zones. The geometry of these zones ranges from mm- to cm-wide veins, dm- to m-scale dike-like bodies to tens of metres wide, irregular but overall planar zones. The presence of shock-metamorphic minerals in some very thin bodies indicates that these bodies were formed as a result of shock heating, whereby shear heating by friction may well have contributed to localized melting. However, neither in situ shock-induced nor frictional melting can explain the local occurrence of hundreds of meter wide pseudotachylite bodies.

Comprehensive structural analysis of pre-impact mineral fabrics and properties of fragment-rich pseudotachylite in the Vredefort Dome have shown that these fabrics and pseudotachylite zones have commonly radial or concentric trends. The high spatial coverage of the data revealed that fabric strike is symmetric about a NW-SE striking vertical mirror plane passing through the Dome centre. The fabric symmetry is consistent with vertical stretching and uplift of the inner core and outward rotation and dilation in the outer core zone as is predicted for rocks at the current erosion level by numerical modelling of the impact event. More specifically, the well-

developed centro-symmetric patterns of distribution, geometry and brecciation intensity of pseudotachylite bodies correspond geometrically to the variation in total strain predicted by numerical modelling.

Comprehensive petrographical and geochemical analyses of matrices in pseudotachylitic veins and dikes and their respective wall rocks from the Vredefort Dome have shown that locally the chemical compositions of matrices deviate significantly from their immediate wall rocks and that assimilation of wall rock substantially modified the pseudotachylite matrix compositions. Chemical trends in the compositional deviation of metre-wide pseudotachylite dikes from their respective wall rocks would be consistent with the presence of a primary melt component having a broadly granitoid composition akin to the composition of the Vredefort Granophyre, possibly a product of differentiation of the original impact melt sheet. Within veins, melt transport can be geochemically and petrographically traced for distances of centimetres to metres, with the direction of melt transport from larger pseudotachylite veins toward smaller ones and into apophyses. Sulphide and silicate mineralogy indicates that the initial temperature of pseudotachylitic melt must have been at least 1200-1700 °C. Collectively, these points suggest that the melt is allochthonous and was emplaced into tensional fracture systems in the crater floor at an advanced stage of cratering, i.e. during collapse of the central uplift. Melt may be drained from the overlying impact melt sheet or from sites within the crater floor and transported into fragment-rich dilation zones.

In order to determine the influence of impact melt on the pseudotachylite melt, it is necessary to know the chemical composition of the Vredefort Granophyre. Therefore, the melt of the Vredefort Granophyre was analyzed. Whole-rock chemical and thin section analyses of profiles across two dikes have shown moderate but general chemical heterogeneity between core and core/collar dikes as well as within one core/collar dike. Thereby, the analyzed core/collar dikes contain fragment-rich and fragment-poor areas with compositional differences. Two chemically and texturally different areas in the Granophyre have shown that two emplacement melt pulses were involved. Structural consideration of the Vredefort Granophyre dikes points to dike formation by crater floor fracturing, possibly driven by late-stage isostatic readjustment of crust underlying the impact structure. The Granophyre melt were possibly formed by injection of melt from the overlying impact melt sheet into target rocks. In contrast to the pseudotachylitic melt,

fractures (Vredefort Granophyre) were filled by two impact melt emplacement pulses from a differentiated impact melt pool some thousands of years after impact.

ACKNOWLEDGEMENTS

I would like to extend my thanks to my supervisors, Ulrich Riller and Uwe Reimold, who invited me to come to South Africa and who provided the funding for the project. They were always keen to help me whenever I needed access to material and data for my thesis, and provided excellent support and input both in and out of the field.

I thank Roger Gibson for access to properties and excellent support in the field. He was a superb discussion partner.

Kirstin Born, Lutz Hecht and Uwe Reimold introduced me to new analytical techniques and conducted analyses on my behalf.

Dieter Stöffler und Lutz Hecht discussed and contributed towards my project whenever there was need.

I thank land owners in the Vredefort area for access to their properties and the staff of the World Heritage Office for their support and Claudia Crasselt for assistance in the field.

Last, but not least, my most sincere appreciation goes to Andreas Jahn, Andreas Petau, Kay Hofmann, Siyamend Al Barazi and Tanja Mohr, who stayed patiently at my side during the most difficult stages of this project.

TABLE OF CONTENT

CHAPTER 1: INTRODUCTION	18
1.1 Geology	18
1.1.1. Geology of Kaapvaal Craton	18
1.1.2. Geology of the Vredefort Impact Structure	24
1.1.3. The collar strata	28
1.1.4. The Archean Basement Complex	29
1.1.5. Metamorphism in the Vredefort Dome	30
1.2. Origin of pseudotachylite bodies	31
1.2.1. Types of impact-induced pseudotachylites	31
1.2.2. E-Type Pseudotachylite formation	35
1.2.3. S-Type Pseudotachylites on interfaces orientated vertical and oblique to the wave front	36
1.2.4. S-Type Pseudotachylites in interfaces orientated parallel to the wave front	40
1.3. Decompression melting	43
 CHAPTER 2: THIS STUDY	 44
 CHAPTER 3: GENERATION OF FRAGMENT-RICH PSEUDOTACHYLITE BODIES DURING CENTRAL UPLIFT FORMATION IN THE VREDEFORT IMPACT STRUCTURE, SOUTH AFRICA	 49
Abstract	49
1. Introduction	50
2. Geological background	53
3. Pre-impact planar mineral fabrics of the Vredefort Dome	55
4. Brecciation intensity and geometry of pseudotachylite bodies	56
5. Kinematics of deformation during formation of pseudotachylite zones	59
6. Shape fabrics of fragments	63

7. Geometric relationship between pseudotachylite properties and cratering strain	64
8. Emplacement of pseudotachylitic melt	67
9. Possible origin of pseudotachylitic melt	68
10. Conclusions	70
Acknowledgements	71

CHAPTER 4: PETROGRAPHIC AND GEOCHEMICAL EVIDENCE FOR AN ALLOCHTHONOUS ORIGIN FOR PSEUDOTACHYLITE MELTS WITH A POSSIBLE INFLUENCE OF THE IMPACT MELT SHEET IN THE VREDEFORT DOME, SOUTH AFRICA

72

Abstract	72
1. Introduction	73
2. Geological Setting	76
3. Previous geochemical work	77
4. Analytical methods	78
5. Results	87
5.1. Field characteristics and petrography of pseudotachylite	87
5.2. Whole-Rock Analysis	91
5.3. SEM Analysis	94
5.4. Electron Microprobe Analysis	100
6. Interpretation of geochemical data	106
7. Conclusions	112
Acknowledgements	113

CHAPTER 5: EMPLACEMENT HISTORY OF GRANOPHYRE DIKES IN THE VREDEFORT IMPACT STRUCTURE, SOUTH AFRICA, INFERRED FROM GEOCHEMICAL EVIDENCE

114

Abstract	114
1. Introduction	115
2. Geological Setting	117

3. Previous work on the Vredefort Granophyre	118
4. Analytical Methods	120
5. Results	120
5.1. Field characteristics and petrography of Vredefort Granophyre dikes	120
5.2. XRF Analyses of Vredefort Granophyre	123
6. Discussion	135
7. Conclusions	138
Acknowledgements	139
 CHAPTER 6: SUMMARY, SYNTHESIS AND OUTLOOK	 140
6.1. Summary	140
6.1.1. Summary of structural data of pseudotachylites	140
6.1.2. Summary of geochemical data of pseudotachylites	141
6.1.3. Summary of geochemical data of Vredefort Granophyre	144
6.2. Synthesis	145
6.3. Outlook	149
 REFERENCES	 152
 APPENDIX I: ORIGIN OF LARGE-VOLUME PSEUDOTACHYLITE IN TERRESTRIAL IMPACT STRUCTURES	 173
APPENDIX II: FIELD DATA	188
APPENDIX III	210
Eidesstattliche Erklärung	211

TABLE OF CONTENT

CHAPTER 1

Figure 1.1: Kaapvaal craton with the Vredefort Dome (field work area) and greenstone belts, e.g., Barberton Greenstone Belt. **18**

Figure 1.2: Distribution of granite-greenstone terranes in the Kaapvaal craton. Also indicated is the Witwatersrand Basin (from De Wit et al., 1992). **19**

Figure 1.3: Lithological map of the Barberton Greenstone Belt (from De Ronde and De Wit, 1994). **20**

Figure 1.4: Sketch showing the tectonic accretion of granite-greenstone terranes along a crescent-shaped volcanic arc in the northern and western parts of the Kaapvaal craton (modified from Poujol et al., 2003). Light grey colour represent the >3.1 Ga Kaapvaal shield. Dark grey colour depicts Archean basement complexes. Black colour represents greenstone belts (Pietersburg, Barberton, Murchison). Limits of the erosional remnant of the Witwatersrand and Pongola basins are indicated. **21**

Figure 1.5: Stratigraphic sequence of the different rock layers and types that were formed on the Kaapvaal craton between about 3.0 and 2.1 Ga ago (after Fletcher and Reimold, 1989). **23**

Figure 1.6: Simplified geological map showing the location of the Vredefort Dome, composed of Archean basement rocks enveloped by supracrustal collar rocks, in the central portion of the Vredefort impact structure. Note concentric antiforms and synforms around the Vredefort Dome. Rectangle indicates the field area of this study. **25**

Figure 1.7: Schematic map of the Vredefort Dome showing the distribution of lithologies and the known occurrences of coesite and stishovite (from Gibson and Reimold, 2001). Thick dashed line indicates the limit of the pre-impact amphibolite-facies metamorphic assemblages. Note, well exposed north and northeast sectors of the Dome, which is largely obscured in the south and southeast by Phanerozoic sedimentary strata of the Karoo Supergroup. **27**

Figure 1.8a-f: Stages of impact crater formation and their characteristics after French, 1998. For explanation see text. **34**

Figure 1.9: Formation of E-Type pseudotachylites on listric faults. Mega rock blocks slide on listric faults and apparently form clast-laden pseudotachylitic dikes (after Scott und Benn, 2002). **35**

Figure 1.10a and b: Pressure profile of the shock-loading simulation during the passage of the shock front through dunite (left) and quartzite (right) after a) 2.5 and b) after 3.5 μ sec. Note, the shock velocity in dunite is higher than in the quartzite caused by their density and, thus, the shock front in dunite is ahead of the shock front in quartzite and the interface is orientated perpendicular to the incoming shock front. The shock wave is split into a leading (left side) and a trailing shock front (right side) (after Heider und Kenkmann, 2003). **38**

Figure 1.11a and b: Temperature distribution of the shock loading experiment after 3.0 μ sec in material with 0.1 mm gap (Fig. 1.11a) and 0.03 mm gap (Fig. 1.11b) after the passage of the shock wave through two different lithologies orientated perpendicular to wave front. Stronger temperature increase occurs for a gap size of 0.1 mm than in smaller gap. (after Heider and Kenkmann, 2003). **38**

Figure 1.12a and b: Relative displacements of different rock types after the passage of the shock front orientated vertically (Fig. 1.12a) and oblique (Fig. 1.12b) to the wave front. An interface which is oriented vertically to the

wave front shows a lower displacement and wider interface (Fig. 1.12a), than an interface which is oriented oblique to the wave front (Fig. 1.12b) caused by the decoupling of particle velocity and tensile forces. (after Kenkmann et al., 2000). **39**

Figure 1.13: Propagation of a longitudinal wave in spring experiment (Tipler, 1994). **40**

Figure 1.14a and b: Reflection of a pressure pulse that encounters an interface between high- and low-velocity material (Fig. 1.14a) and the inverse case (Fig. 1.14b). In Fig. 1.14a part of the wave is reflected back into the high-velocity material as a tensile wave, while the rest of the wave continues into the low-velocity material. Fig. 1.14b Reflection of a pressure pulse that encounters an interface between low- and high-velocity material. In this case all the pulses are compressional. No tensile stress results between both materials (Melosh, 1989). **42**

CHAPTER 3

Figure 3.1: Stages of impact crater formation based on hydrocode modeling by Ivanov and Deutsch (1999) showing the geometric evolution of originally horizontal stratigraphic marker layers (solid lines) and isotherms (stippled lines) for an impact structure the size of Vredefort. T denotes time in seconds after impact. (a) Undisturbed configuration of model lithosphere prior to impact. (b) Maximum growth of the transient cavity. (c) Formation of the central uplift of material following gravitationally-induced collapse of the transient cavity. (d) Final configuration of marker layers and isotherms below a flat impact melt sheet. Bold stippled line indicates approximate level of erosion of the Vredefort impact structure. **51**

Figure 3.2: Simplified geological map showing the location of the Vredefort Dome, composed of Archean basement rocks enveloped by supracrustal collar rocks, in the central portion of the Vredefort impact structure. Note concentric antiforms and synforms around the Vredefort Dome. Rectangle indicates enlarged areas in Figures 3.3, 3.4 and 3.7. **54**

Figure 3.3: Simplified geological map of the Vredefort Dome showing trajectories of inclined planar mineral shape fabrics (migmatitic layering) that formed prior to meteorite impact. The mineral fabric symbols shown are average orientations from a total of 745 stations. The boundary between the inner core and the outer core zone (stippled line) is defined by the change in mineral fabric strike from NW-SE in the inner core to concentric in the outer core zone. Note the symmetry of the boundary and the fabric strike with respect to the trace of a NW-striking mirror plane passing through the centre of the Vredefort Dome. Lower-hemisphere equal-area projections show poles to planar pre-impact fabrics of the respective sectors in the map. Numbers in projections are respectively number of measurements (n), maximum density of measurements in % and the orientation of the maximum in terms of dip direction and dip. Locations a and b refer respectively to the Salvamento and the Esperanza quarries. **56**

Figure 3.4: Map of the Vredefort Dome showing the distribution of brecciation intensity and trend of fragment-rich pseudotachylite bodies at a total of 531 stations. Note radial and concentric trends of bodies concentrated at radially inward distances of about 1 to 4 km and 7 to 9 km from the core-collar boundary as well as paucity of pseudotachylite occurrences in the inner core zone. **58**

Figure 3.5: Diagrams showing pseudotachylite properties with respect to radially inward distance from the core-collar boundary. (a) Brecciation intensity versus radially inward distance. (b) Number of pseudotachylite exposures versus radially inward distance. Brecciation intensity and number of pseudotachylite exposures are enhanced at distances of 1 to 4 km and 7 to 9 km from the core-collar boundary. **59**

Figure 3.6: Photos of pseudotachylite veins and dikes indicating the dilational strain field during melt emplacement. Arrows indicate component vectors of maximum dilation. (a) and (b) Examples of pseudotachylite veins permitting

determination of directions of vein openings based on the pre-impact geometrical fit of opposite margins. (c) Pseudotachylite veins displaying en-echelon geometry. (d) and (e) Example of pseudotachylite veins showing pull-apart geometry. Note apparent sense of displacement of pre-impact pegmatite dike indicated by half arrows. (f) and (g) Pseudotachylite apophyses formed at higher-order fracture zones. **60**

Figure 3.7: Map of the Vredefort Dome showing the distribution and magnitude of component vectors of maximum dilation inferred from the geometry of pseudotachylitic veins and dikes. Note enhanced concentric and radial stretching of rock in the outer core zone. By contrast, the inner core is characterized by minor magnitudes of concentric stretching in its periphery. **62**

Figure 3.8: Shape fabrics of pseudotachylitic breccia fragments. Arrows point to incipient separation of angular fragments from pseudotachylite zone margins, areas of enhanced fracture density and fragmentation of acute fragment tips. (a) and (b) Photos showing two brecciation intensity 5 pseudotachylite bodies from Salvamento and Esperanza quarries (locations a and b, respectively, in Figure 3.3). (c) and (d) Digitized images of (a) and (b), respectively, used for shape fabric analysis. Grey lines indicate traces of pre-impact planar mineral fabrics in target rock fragments. Note progressive rotation of fragments with increasing distance from breccia body margin in (d). (e) and (f) Diagrams showing sectional ellipticity of fragments (value of 1 represents the unit circle) versus distance of fragments to margins of pseudotachylite zones. Note the decrease in sectional fragment ellipticity with increasing distance from margins. Bold lines approximate the overall variation in fragment ellipticity. **64**

Figure 3.9: Radial profile of the Vredefort Dome depicting the variation in accumulated strain, indicated by distorted rectangles, due to cratering based on hydrocode modelling by Ivanov (2005). Bold lines in the core near present erosion level indicate directions of total stretching. Note vertical stretching in the inner core and subhorizontal stretching directions in the outer core zone. Radial widths of the inner core and the outer core zone are defined for the present erosion level. **65**

CHAPTER 4

Figure 4.1: Geological setting of the Vredefort region. (a) Simplified geological map of the Witwatersrand Basin. Rectangle denotes area in (b). (b) Geological map of the Vredefort Dome showing sample sites of this study (Lieger et al., 2009). **75**

Figure 4.2: Outcrop and thin section images of pseudotachylite and wall rock from the SunWa, Salvamento and Kudu locations. (a) Photo showing the drill site of the SunWa 6 sample, a pseudotachylite vein cutting granitoid wall rock. (b) Thin section image of SunWa 6 sample. Note apophysis of the pseudotachylite vein. (c) Photo showing a pseudotachylite vein cutting a pegmatite dike within granitoid wall rock at SunWa 13. Arrows illustrate displacement of vein margins indicating that the vein formed from an extension fracture. (d) Thin section image of a sample from SunWa 13. The pseudotachylite matrix shows distinct domains, evident by the variation in matrix colour, that are parallel to the vein margin. Surface area of wall rock fragments is higher in bright than in dark domains. (e) Photo showing the sample site in a fragment-rich pseudotachylite dike at Salvamento. (f) Thin section image of the sample taken from Salvamento shown in (e). The matrix is replete with wall rock fragments and resembles bright matrix domains of the SunWa 13 vein displayed in (d). (g) Photo showing the sample site at Kudu. Pseudotachylite (Pt) is seen as a dike bordering on granitoid and amphibolite wall rock, and as a vein emanating from the dike and transecting both wall rock types. Pseudotachylite is demarcated by stippled line (length of pen is 15 cm). (h) Hand specimen from Kudu showing pseudotachylite vein cutting granite and amphibolite wall rock. Areas A - D denote the locations of thin sections used for electron microprobe analyses. **89**

Figure 4.3: Thin section photomicrographs showing pseudotachylite matrices of selected samples. Except (g), all photomicrographs are taken under cross-polarized light. q: quartz, bt: biotite, fsp: feldspar, mc: mica, op: opaque

mineral, A: domain A, B: domain B. (a) Pseudotachylite matrix from Salvamento displaying microcrystalline matrix with intersertal plagioclase enveloping minute quartz fragments. (b) Flow-banded pseudotachylite matrix from Salvamento enveloping quartz fragments showing resorbed margins. Note straight subgrain boundaries displaying 120° dihedral angles in large polycrystalline quartz fragment. (c) Pseudotachylite matrix from sample SunWa 13 showing intersertal biotite, feldspar and muscovite. (d) Pseudotachylite matrix from sample SunWa 13 displaying texturally and mineralogically different domains A and B. For explanation of domains see text. (e) Pseudotachylite matrix from sample SunWa 13 showing the locations of domain A at the margin and domain B in the centre of the vein. Note resorbed margins of fragments. (f) Flow-banded matrix enveloping polycrystalline quartz fragment characterized by resorbed margins and straight subgrain boundaries from sample SunWa 13. (g) Thin section micrograph of matrix from sample SunWa 9 (plane-polarized light). Aphanitic matrix is found at vein margin, whereas a microcrystalline matrix is associated with quartz fragments. Plagioclase fragment at the vein margin is broken off from the immediate wall rock. However, quartz fragments within microcrystalline matrix seem to be exotic. Grey line denotes profile, along which 155 spots were analysed with the electron microprobe (see Figure 4.9). (h) Same field of view as (g) but taken under cross-polarized light. **90**

Figure 4.4: Diagrams showing selected major and trace element contents of pseudotachylite matrices and their respective wall rocks obtained by XRF analyses. Published XRF data are from Schwarzman et al. (1983) – 1, Bisschoff (1972), Bisschoff (1973) – 2, Reimold (1991) – 3, Wilshire (1971) – 4, McIver et al. (1981) – 5, and Tankard et al. (1982) - 6. Also shown is the average chemical composition of Vredefort Granophyre with standard deviation (ellipse) compiled from Hall and Molengraff (1925), Willemse (1937), Wilshire (1971), Reimold et al. (1990a), Koeberl et al. (1996) and Therriault et al. (1997). (a) Diagram showing the distribution of ferromagnesian oxides versus SiO₂. There are conspicuous trends (grey arrows) in the compositional deviation of pseudotachylite matrices from their respective wall rocks towards a granitoid composition that is close to that of the average Vredefort Granophyre. Note also that the Vredefort Granophyre composition is intermediate between that of all wall rock types and respective pseudotachylite matrices. The strong deviation in matrix composition of samples KUDUA1 and KUDUA2 towards mafic compositions is due to contamination of melt by amphibolite (see Figures 4.2h, 10). (b) Diagram showing the distribution of MgO versus CaO. (c) Diagram showing the distribution of Zr versus V. Note the strong excursion of Zr in matrix with respect to wall rock in one West Rand quartzite pseudotachylite pair. **93**

Figure 4.5: Thin section and back-scattered electron (BSE) images of pseudotachylite matrix of sample SunWa 13. Alkali feldspar – kf, amphibole – amph, apatite – ap, biotite – bt, chalcopyrite – cp, chlorite – chl, Ti-augite – Ti-aug, other clinopyroxene – cpx, magnetite – mt, muscovite – mc, plagioclase – plg, pyrrhotite – pt, quartz – q, domain A – A, domain B – B. (a) Thin section image showing matrix domains A and B, the boundaries of which are delineated by dashed lines, as well as the locations of the BSE images of areas 1 to 6 displayed in (c) to (h). (b) BSE image showing a close-up of domain A bordering on domain B. Note textural differences between both domains. Rectangles 1 and 2 denote respectively areas 1 and 2 indicated in (a). (c) – (h) BSE images showing respectively close-ups of areas 1 to 6 indicated in (a). Area 2 (d) hosts quartz, plagioclase, Ti-augite and alkali feldspar fragments. Areas 3 to 5 (e - g) illustrate domains B that hosts fewer and smaller quartz and plagioclase fragments than domains A. **95**

Figure 4.6: BSE images showing selected matrix portions of pseudotachylite body at Salvamento. For abbreviations see caption to Figure 4.5. (a) Overview of selected matrix portion. Note absence of any domainal compositional zoning. (b) Close-up of area enclosed by rectangle in (a). Note magnetite in the vicinity of plagioclase. **96**

Figure 4.7: Scanning electron microprobe spectral diagrams of elements and element mapping images of samples from SunWa and Salvamento (Fig. 4.1b). (a) Spectral diagram of elements of domain A from SunWa. (b) Spectral diagram of elements of domain B from SunWa. (c) Spectral diagram of elements from Salvamento. Note similarity

of spectrum to that of SunWa domain A displayed in (a). (d) Element mapping images of Si, Fe, Cu and S in domain B from SunWa. S, Cu and Fe are locally enriched (white circles). **97**

Figure 4.8: BSE and spectral element images of pseudotachylite matrix of a vein and an apophysis from sample SunWa 6 at SunWa (Fig. 4.2a). For abbreviations see caption to Figure 4.5. (a) Schematic representation of thin section image (see Figure 4.2b) showing pseudotachylite vein, apophysis, ferromagnesian ribbon and granitoid wall rock containing large ferromagnesian mineral. Rectangles 1 to 5 indicate areas of BSE images depicted respectively in (b) to (f). (b) - (f) BSE images showing the mineralogical composition respectively of areas 1 to 5 depicted in (a). Plagioclase displays symplectitic intergrowth with alkali feldspar in (c). Idiomorphic magnetite is found close to the wall rock and next to feldspar and quartz fragments in (d). In areas 4 and 5, (e) and (f) respectively, the matrix is rich in amphibole and contains the ferromagnesian ribbon. (g) Spectral element image of ferromagnesian mineral. (h) Spectral element image of ferromagnesian ribbon. Note the similarity in chemical signature between the ferromagnesian mineral and the ribbon. **99**

Figure 4.9: Thin section, BSE image and electron microprobe analyses of sample SunWa 9. (a) Thin section image showing domainal character of the matrix. Note bright haloes around large wall rock fragments. White rectangle displays area depicted in (b). (b) BSE image showing domains A and B and line along which a total of 155 spot analyses with a beam width of 20µm were conducted. (c) and (d) Diagrams showing chemical compositions of wall rock and pseudotachylite matrix domains analysed by XRF and electron microprobe. (e) Diagram showing FeO content with position along line depicted in (b). **101**

Figure 4.10: Electron microprobe spot analyses of 14 transects across a pseudotachylite vein hosted by amphibolite and granitoid wall rock at Kudu (Figs. 4.1b, 4.2h). (a) – (d) Thin section photomicrographs of vein segments showing the locations of the transects (Tr 1 to Tr 14). The positions of vein segments correspond respectively to areas A – D displayed in Figure 4.2h. Chemical compositions were averaged over defined stretches of each transect. The stretches are: wall rock to the left of vein - A, matrix at left vein margin - B, matrix in vein centre - C, matrix at right vein margin - D and wall rock to the right of vein - E. (e) Diagram showing the variation in SiO₂ for individual stretches of transects. (f) Diagram showing the variation in FeO for individual stretches of transects. (g) Diagram showing the variation in MgO for individual stretches of transects. (h) Diagram showing the variation in CaO for individual stretches of transects. **105**

Figure 4.11: Thin section and BSE images displaying respectively pseudotachylite vein and corroded zircon (X) at Kudu (Fig. 4.1b). (a) Thin section photomicrograph showing location of zircons in wall rock at vein margin depicted in (b). (b) BSE image of fractured, zoned and corroded zircons. **110**

CHAPTER 5

Figure 5.1: Geological setting of the Vredefort Dome. (a) Simplified geological map of the Witwatersrand Basin. Rectangle denotes area in (b). (b) Geological map of the Vredefort Dome showing samples sites of the geochemical study and the position of the nine known radial and concentric Granophyre dikes. **116**

Figure 5.2: Outcrop images of Vredefort Granophyre dike in granitoid host rock. (a) Photo showing the zoning of the dike and locations of photos b – d. (b) and (c) Photos showing the fragment-rich zone containing elongate, up to 10 cm long, mostly angular fragments aligned parallel to dike margins. The planar shape fabric of fragments points to laminar flow during melt emplacement. Note evidence for melt mingling at top left in (b). (d) Photo showing convolute melt flow pattern in the fragment-poor marginal zone of Granophyre dike indicated by variable orientation of long axes of wall rock fragments. **121**

Figure 5.3: Thin section micrographs showing Granophyre matrices of selected samples. All micrographs are taken under crossed polarized light. (a-b) Spherulitic feldspar and pyroxene matrix from fragment-rich zone at site 188. (c-d) Granular feldspar and pyroxene matrix from fragment-poor zone at site 188. Note feldspar myrmekite in upper left corner of (c). (e) Spherulitic granophyre matrix in a zone with mm-wide rounded felsic fragments which comprise most quartz. (f) Granular feldspar and pyroxene matrix from fragment-poor zone at site 355. Note, plg = plagioclase, px = pyroxene, op = opaque mineral, opx = orthopyroxene, q = quartz, kf = kalifeldspar, plg = plagioclase. **122**

Figure 5.4: Diagrams showing selected major and trace element contents of Granophyre matrices with regard to the location in the core of the Vredefort Dome and fragment population obtained by XRF analyses. Published XRF data are from Reimold et al., 1990 – 1 and Therriault et al., 1997 – 2; - 2a (contact to epidiorite wall rock; sample numbers VAT 113 and VAT 156 in Table 5-1). (a) Diagram showing the distribution of CaO versus SiO₂. (b) Diagram showing the distribution of CaO versus Fe₂O₃. (c) Diagram showing the distribution of Cr versus Fe₂O₃. (d) Diagram showing the distribution of Zr versus MgO. Fragment-poor zones of Granophyre dikes show higher values of CaO, MgO, Fe₂O₃, most Cr and lower values of SiO₂ and Zr in contrast to fragment-rich zones. Chemical composition varies also within a given dike. **125**

Figure 5.5: Diagrams showing selected major and trace element contents of Granophyre matrices and the target rocks obtained by XRF analyses and calculated mixing of the main component. Published XRF Granophyre data are from Therriault et al. (1997) – 1. Target rock data are from Bisschoff, (1972), Bisschoff, (1973) – 2, Wilshire, (1971) – 3, McIver et al. (1981) – 4, Tankard et al. (1982) – 5, Reimold, (1991) – 6 and Koeberl et al. (1996) – 7. (a) Diagram showing the distribution of CaO versus SiO₂. (b) Diagram showing the distribution of MgO versus Fe₂O₃. (c) Diagram showing the distribution of Zr versus Cr. (d) Diagram showing the distribution of Sr versus Rb. Granophyre composition is intermediate between that of all wall rock types, notably basalt of the Ventersdorp Supergroup and granitoid wall rock. This requires a significant involvement of a mafic component in the formation of Granophyre dikes, particularly in those that are located away from epidiorite and shale of the core-collar boundary. **135**

CHAPTER 6

Figure 6.1: Model of the pseudotachylite formation in the cratering processes. Stage 1 represents phase 1 with the excavation and the beginning of central uplift of the target rocks short after the impact. Thereby, shock-induced microfractures figured as small reddish and greyish veins (1) are formed in the ground in the contact/compression stage. Stage 2 begins with the collapse of the central uplift and shows the centripetal and upward motion of rock during gravitational collapse of the transient cavity followed by gravitational outward spreading of uplifted rock. Thereby, tensional fracture zones opened in an overall dilational strain field and formed low pressure zones (2) and apophysis (3), into which melt was drawn. Melt may have been drained from the overlying impact melt sheet into low pressure sites including apophyses. However, small shock-induced veins served as weakness zone into which impact melt could have been emplaced in still-molten shock networks (4). Stages 3 and 4 comprise the early and the later modification stage, whereby in stage 3 pseudotachylite veins were displaced by gravitational downward movement of the target rock indicated by younger reddish veins (5). In the later modification stage large cooled pseudotachylite bodies were displaced or contain small reddish veins (6). **147**

Figure 6.2: Model of injection of impact melt from the overlying melt sheet into low pressure sites in the Vredefort dome. Large pink to purple arrow indicates the variable magnitudes of assimilation. Note, fragmentation of target rock and melt generation to form pseudotachylitic breccia bodies are processes that are separated in time and space during cratering. Brittle deformation caused by localization of bending strains accounts for in situ brecciation of target rock and generation of low pressure sites. The link of different pseudotachylite zones to each other is unclear (yellow to brown arrow). **149**

APPENDIX I

Figure A.1: Simplified geological maps of (A) the Sudbury Basin and (B) the Vredefort impact structure. SRBB and POD in (A) denote South Range Breccia Belt and Podolsky Dike, respectively. **175**

Figure A.2: A: Pseudotachylite body from Sudbury containing globular mafic fragments (m) and cusped felsic fragments (f) indicating a significant contrast in mechanical competency between both fragment types within matrix (x). B: Highly stretched and partially melted felsic fragment (f) entrained in convoluted matrix (x) containing globular mafic fragments (m) close to the SIC (Sudbury). C: Pseudotachylite dike in granitoid rock located ca. 3 km west of the SIC shows geometric fit of its margins (Sudbury). D: Jigsaw geometry of pseudotachylite dikes and fragments in granitoid rock (Vredefort). E: En-echelon geometry of overstepping pseudotachylite veins (Vredefort). F: Elliptical host rock fragment enveloped by overstepping pseudotachylite vein (Vredefort). G: Schematic diagram displaying stages of elliptical fragment formation by overstepping en-echelon fractures propagating toward each other. **177**

Figure A.3: Diagram depicting the variation in Fe_2O_3 with SiO_2 for pairs of pseudotachylite matrix and immediate host rock samples from the Vredefort impact structure. Note overall dissimilar composition of matrix and host rock, regardless of target rock type. **179**

Figure A.4: Geometry of pseudotachylite dikes and impact-induced target rock distortion at Vredefort. A: Diagram showing angular departures from radial directions (α) of pseudotachylite dikes with distance to the crater center. B: Diagram showing angular departures from radial directions (α) of maximal dilation directions of pseudotachylite dikes with distance to the crater center. C: Diagram showing the width of concentric pseudotachylite dikes (D) with respect to distance from the crater center. D: Diagram showing the width of radial pseudotachylite dikes (D) with respect to distance from the crater center. Zones of low and high dilation in (C) and (D) are delineated by δ_{\min} and δ_{\max} , respectively. E: Radial profile of the Vredefort Dome depicting the variation in impact-induced target rock distortion after Ivanov (2005). Bold lines near present erosion level indicate directions of total stretching. Note uniform vertical stretching and limited differential target rock rotation (ΔR_{\min}) in the inner part and subhorizontal stretching and significant differential rotation (ΔR_{\max}) in the outer part of the Dome. **181**

CHAPTER 1: INTRODUCTION

1.1. Geology

1.1.1. Geology of Kaapvaal Craton

The 3.5 Ga old Kaapvaal craton is made up of the oldest known Archean rocks of southern Africa. De Wit et al. (1992) document early thin-skin thrusting in oceanic and arc settings (from 3.6 – 3.4 Ga), followed by amalgamation of the displaced oceanic and arc terranes (from 3.3 to 3.2 Ga), along with extensive granitoid magmatism, which collectively generated the early Kaapvaal cratonic nucleus by 3.1 Ga (Fig. 1.1).

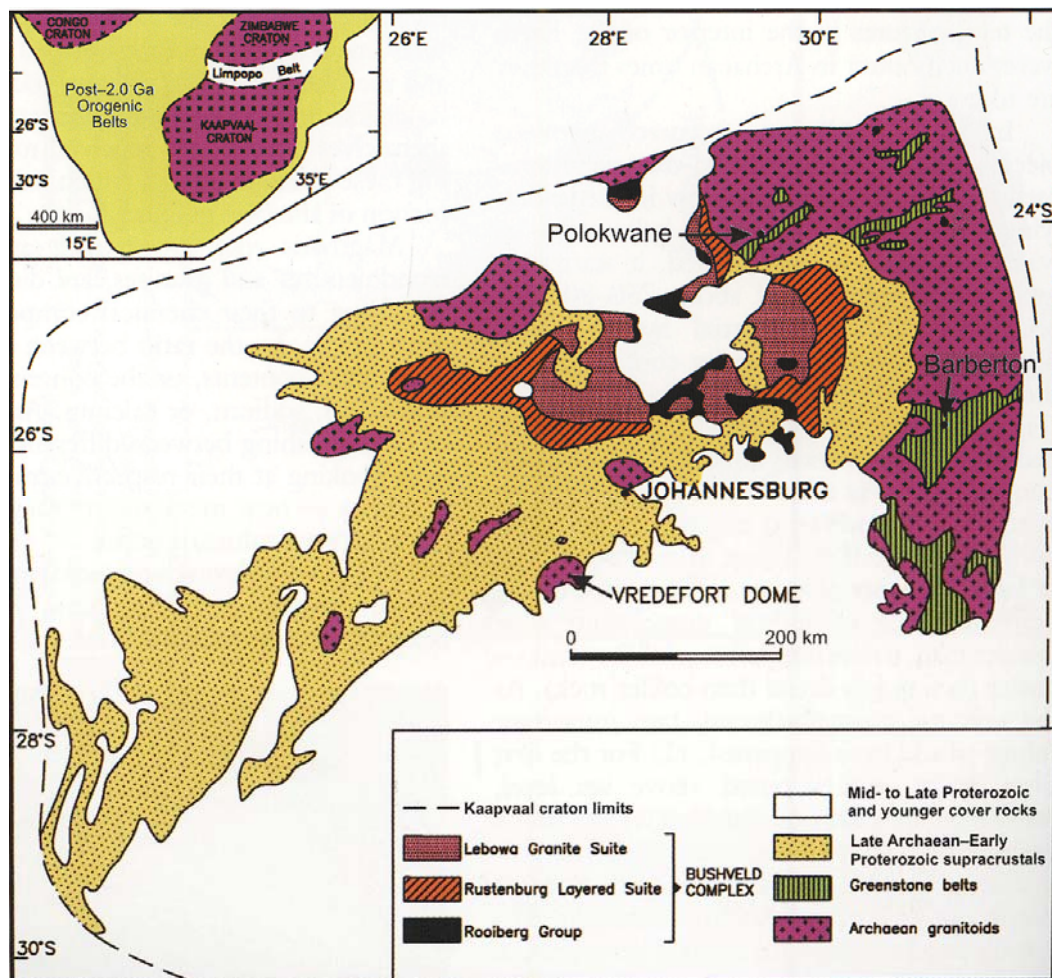


Figure 1.1: Kaapvaal craton with the Vredefort Dome (field work area) and greenstone belts, e.g., Barberton Greenstone Belt (Reimold and Gibson, 2005a).

The Kaapvaal craton of southern Africa (Fig. 1.2) is one of the most extensive, largely pristine Archean crustal fragments on Earth, which was divided into a number of subdomains separated by tectonic boundaries, interpreted as thrust and strike slip zones (De Wit et al., 1992).

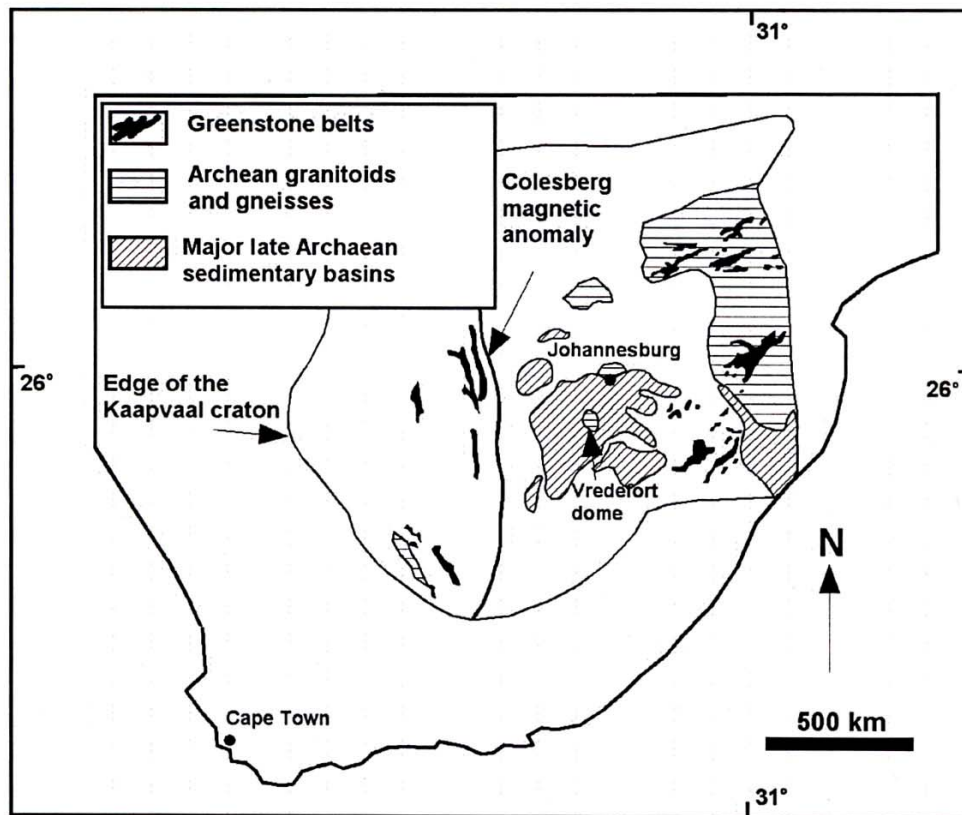


Figure 1.2: Distribution of granite-greenstone terranes in the Kaapvaal craton. Also indicated is the Witwatersrand Basin (from De Wit et al., 1992).

The oldest and best-studied subdomains are defined by the Barberton Greenstone Belt and adjacent granite-greenstones in the eastern region of the craton (Fig. 1.1, 1.3). The Barberton Greenstone Belt is characterized by an initial phase of mafic and ultramafic volcanism, followed by intrusion of a tonalite-trondhjemite-granodiorite suite (TTG) and related extrusion of dacite, rhyodacite and rhyolite (Lowe, 1999). The geochemistry of the Barberton Greenstone Belt rocks suggests that plate tectonics operated during the evolution of these crustal fragments (Lowe 1999).

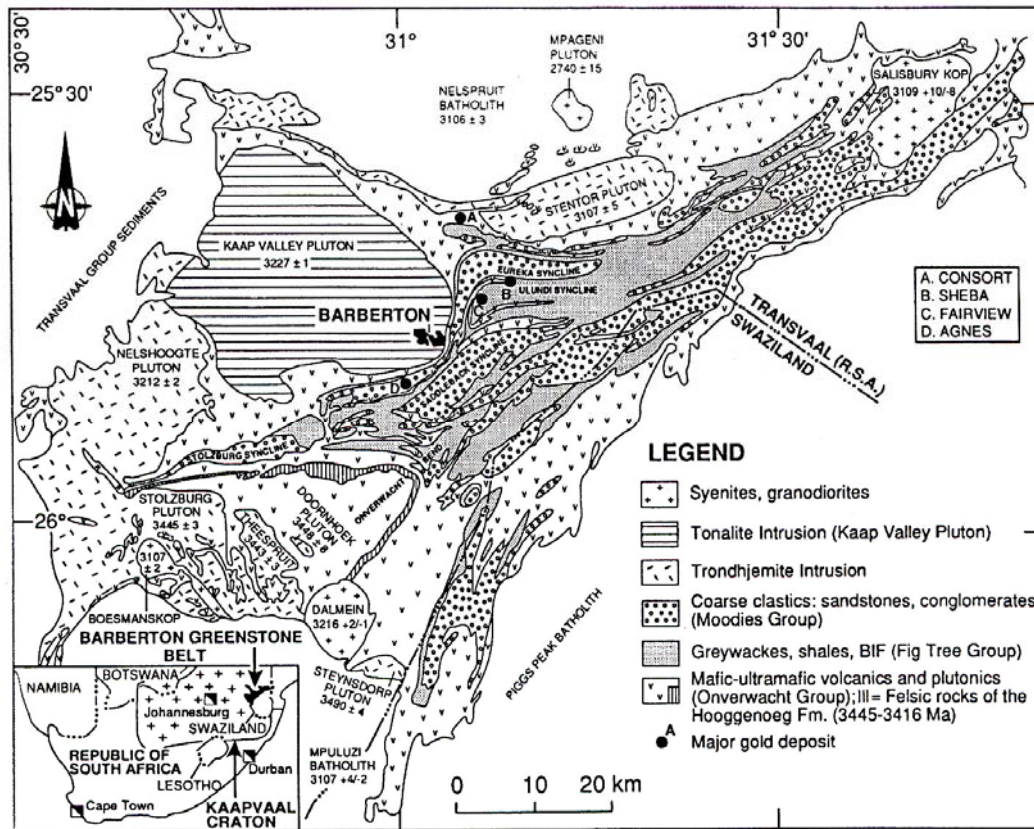


Figure 1.3: Lithological map of the Barberton Greenstone Belt (from De Ronde and De Wit, 1994).

Several authors have pointed out important structural evidence of horizontal shortening, tectonic stacking and duplication of the greenstone sequences (Heubeck and Lowe, 1994; Lowe 1999). In addition, the deformation in the Barberton Greenstone Belt produced structures which are similar with well-documented fold and thrust belts are commonly linked to continental growth and plate interaction in Phanerozoic times (Lowe (1994). In the Barberton region, crustal fragments amalgamated between 3.6 and 3.2 Ga (De Wit et al., 1992). The stabilisation of these fragments occurred after 3.1 Ga and formed a solid continental Kaapvaal Shield, which only occurred as a result of significant partial melting of the TTG rocks and formation of granodiorite-monzogranite-granite suite (De Wit et al., 1992; De Wit 1998; Moser et al., 2001). In contrast, 3.3 – 3.1 Ga rocks are located in the vicinity of Johannesburg and the Vredefort Dome and 2.9 – 2.7 Ga old rocks are found near Polokwane (Fig. 1.1). This variation may indicate that the initial

continental nucleus of the craton was formed from the rocks in the Barberton region and that, over a few hundred million years, younger rocks were added along the margins of this first continental nucleus (Reimold and Gibson, 2005a). Poujol et al., (2003) suggested that the Kaapvaal Shield included the basement complex in the central parts of the craton by 3.1 Ga, and that this shield served as a base for deposition of a sequence of late Archean to Paleoproterozoic intracratonic basins. Crustal fragments in the northern and western sectors of the craton were accreted along a major 3.1 Ga crescent-shaped, juvenile arc (Poujol et al., 2003; Fig. 1.4).

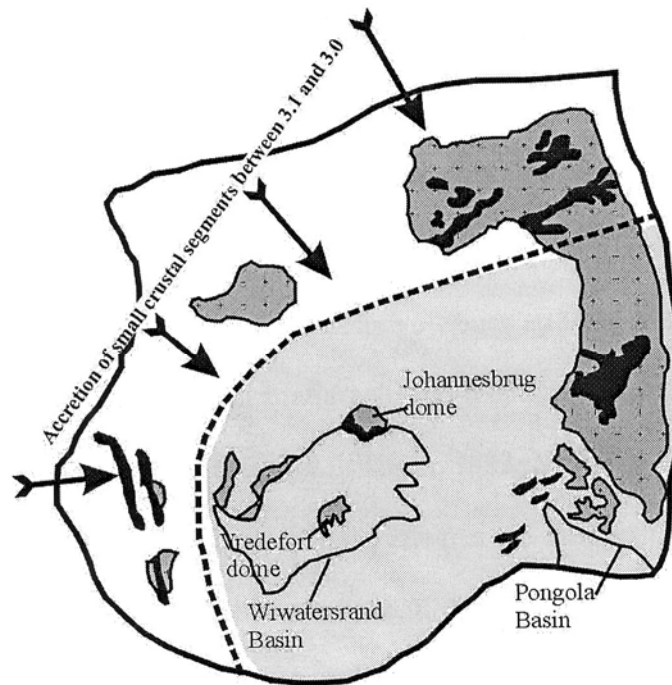


Figure 1.4: Sketch showing the tectonic accretion of granite-greenstone terranes along a crescent-shaped volcanic arc in the northern and western parts of the Kaapvaal craton (modified from Poujol et al., 2003). Light grey colour represent the >3.1 Ga Kaapvaal shield. Dark grey colour depicts Archean basement complexes. Black colour represents greenstone belts (Pietersburg, Barberton, Murchison). Limits of the erosional remnant of the Witwatersrand and Pongola basins are indicated.

The Kaapvaal craton accreted further composite terranes between 3.0 and 2.7 Ga along the western and northern margins of the initial nucleus (Eriksson et al., 2005). The 3.1 – 2.7 Ga Witwatersrand Basin formed during this period of craton evolution. As an example of these accretionary processes, the Murchison Greenstone Belt (northeastern margin of the Kaapvaal craton; Fig. 1.4), encompassing 3.09 Ga mafic volcanic and granitic rocks, formed a composite

terrane, analogous to, but younger than that around the Barberton belt to the south, in the Kaapvaal craton (Poujol and Robb, 1999).

Between 3.1 and 2.9 Ga the late Archean Witwatersrand basin was influenced by significant regional extension of the central parts of the craton (Armstrong et al., 1991). Within this time span, the Dominion Group was emplaced and peaked with the development of the bimodal Dominion Group volcanism at 3.074 ± 0.009 Ga (Armstrong et al., 1991). Geochemical data and stratigraphic correlations seem to be consistent with a continental rift environment (Bickle and Erikson, 1982; McCarthy et al., 1990). Regional correlations and age data suggest that the continental rift developed close to a continental margin facing open oceanic conditions to the north and west (Robb et al., 1991). Thereby, large erupted volumes of basaltic and granitic magma and local sediments were deposited into the rift valleys. In the Vredefort Dome the Dominion Group is represented by a locally up to 500 m thick layer of lavas in the northwestern part of the Dome (Reimold and Gibson, 2005a).

After the formation of volcanic rocks of the Dominion Group epicontinental sediments of the West Rand Group were deposited. This Group formed approximate 95 Ma after the Dominion Group and represents the lowest unit of the Witwatersrand Supergroup (Robb et al., 1991). McCarthy et al. (1990) suggested that the deposition of these sediments began as a response to thermal cooling and subsidence of the Dominion volcanics and development of a fluvio-deltaic foreland basin. West Rand Group is characterized by an up to 5 km thick pile of shales, quartzites, cherts and iron-rich sediments and diamictite (Fig. 1.5). These rocks testify to changes within the basins over long periods of time. The change of shale and quartzite deposition reflects movement of the ancient shoreline back and forth over millions of years which was caused by either changes in global sea level or a variation of the surface caused by geological forces, or to different rates of sediments influx into the basin (Reimold and Gibson, 2005a).

The upper unit of the Witwatersrand Supergroup, known as Cental Rand Group, is characterized by an up to several kilometres thick piles of coarse quartzites and conglomerates with grains of gold (Fig. 1.5). The sedimentary features in the quartzites and conglomerates indicate that the sediments were deposited along the shoreline of the Witwatersrand Sea, and in rivers flowing from nearby mountains to the northwest and west of the shore (Reimold and Gibson, 2005a).

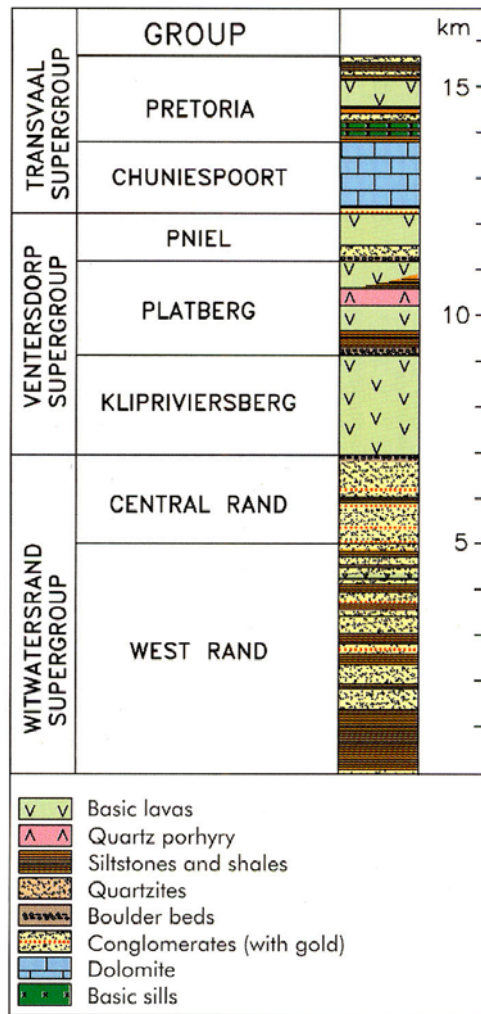


Figure 1.5: Stratigraphic sequence of the different rock layers and types that were formed on the Kaapvaal craton between about 3.0 and 2.1 Ga ago (after Fletcher and Reimold, 1989).

A period of extension affected the Kaapvaal Shield after the deposition of Witwatersrand Supergroup. This period is characterized by a high-grade metamorphic event and formation of thick volcano-sedimentary succession of the 2.7 Ga old Ventersdorp Supergroup (Schmitz and Bowring, 2003). Geochemical and isotopic signatures suggest tholeiitic Ventersdorp Supergroup lavas, which indicate interaction between a precursor mafic magma and the Kaapvaal mantle keel (Nelson et al., 1992). About 2 km of Ventersdorp basaltic lava covered an area of more than 100.000 km², followed by deposition of up to 2 km of rift sediments and subsidiary felsic volcanic rocks (Nelson et al., 1992).

After the extensional period, much of the Kaapvaal continent was covered by the Transvaal Sea and quartzite, known as the 2.650 Ga old Black Reef Formation. The deposition of Black Reef Formation sediments was followed by deposition of dolomite and subsidiary banded iron formation of the Transvaal Supergroup (Fig. 1.5). The dolomite is characterized by stromatolites, which is mainly found in the central parts of the craton and indicates a shallow sea between 2.6 and 2.43 Ga (Walraven and Martini, 1995). After the deposition of the chemical sediments a sequence of 3 km thick pelite-sandstone of the Pretoria Group of the Transvaal Supergroup was deposited between 2.35 and 2.1 Ga (Walraven and Martini, 1995).

At 2.06 Ga, the central parts of the Kaapvaal continent were influenced by voluminous intrusions of ultramafic and mafic magmas of the Rustenburg Layered Suite, emplacement of the Lebowa Granite Suite and extrusion of felsic volcanic rocks of the Rooiberg Group of the Bushveld Complex. The Bushveld event was followed by a massive meteorite impact, which formed the 2.02 Ga Vredefort Impact Structure (e.g., Kamo et al., 1996; Gibson and Reimold, 2001).

1.1.2. Geology of the Vredefort Impact Structure

The Vredefort impact structure (Fig. 1.6) has been dated at 2023 ± 4 Ma (Kamo et al., 1996) and is, thus, the oldest known impact structure and, with an estimated diameter of up to 250 km, likely also the largest one known on Earth (Henkel and Reimold, 1998; Grieve and Theriault, 2000; Turtle et al., 2005). The impact structure has been eroded to a depth of about 7 to 10 km (Gibson et al., 1998; Henkel and Reimold, 1998) and, thus, offers an unprecedented view of the structure of target rocks underlying a large, complex terrestrial impact structure. The central portion of the impact structure, the so-called Vredefort Dome (Fig. 1.6), is the eroded relic of structurally uplifted rocks, generally referred to as the central uplift (Melosh, 1989). The Vredefort Dome consists of a core, about 40 km in diameter, of a 3.1-3.2 Ga tonalite-trondhjemite-granodiorite and greenstone assemblage (Lana et al., 2004). The core is surrounded by a 15-20 km wide 'collar' of subvertical to overturned, 3.07 and 2.1 Ga supracrustal strata (Armstrong et al., 1991) which were deposited unconformably on the Archean crystalline basement rocks.

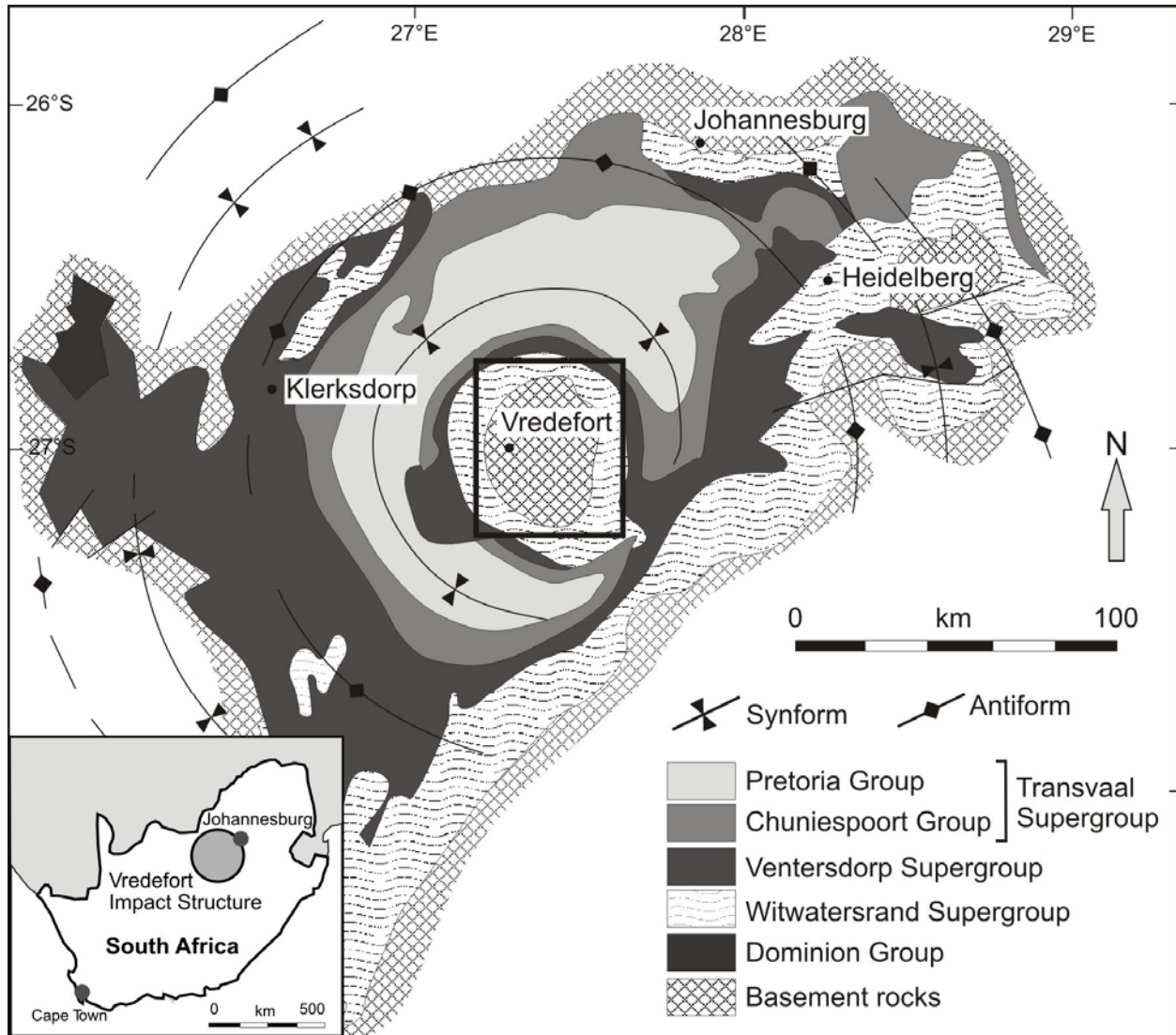


Figure 1.6: Simplified geological map showing the location of the Vredefort Dome, composed of Archean basement rocks enveloped by supracrustal collar rocks, in the central portion of the Vredefort impact structure. Note concentric antiforms and synforms around the Vredefort Dome. Rectangle indicates the field area of this study.

In addition, the crystalline basement comprises metasedimentary and metavolcanic granulite xenoliths (e.g. Stepto 1979; Hart et al., 1990a; Lana et al., 2004). The southeastern sector of the core consists predominantly of greenschist- to amphibolites facies mafic and ultramafic schists of komatiitic basalt composition and metasediments (Minnitt et al., 1994). The Dome is well exposed in the northern and northeastern sectors, but it is largely obscured in the south and southeast by Phanerozoic sedimentary strata and dolerite sills (Fig. 1.7).

Since the earliest studies of the Vredefort area, the Vredefort Dome was subject of scientific controversy. It was recognized that its origin involved catastrophic forces (e.g., Shand, 1916; Hall and Molengraaff, 1925), caused either by impact or endogenic (tectonic or cryptoexplosion) processes. Shand (1916), Hall and Molengraaff (1925) and Nel (1927) documented large volumes of melt rock (pseudotachylite) and the general observation of strong rock deformation. Based on this recognition and the circularity of the Dome, Boon and Albritton (1936) suggested first that this structure might be formed by meteorite impact. Dietz (1947) advocated the presence of shatter cones as a diagnostic criterion for meteorite impact, which was confirmed by Hargraves (1961) for the Vredefort Dome. Further impact criteria such as microdeformation features in quartz from the Vredefort rocks (Carter, 1968), occurrences of pseudotachylites (Wilshire, 1971; Schwarzman et al., 1983), and Martini's (1978) identification of coesite and stishovite in pseudotachylite pointed to an impact origin for the Vredefort structure (Fig. 1.7). However, other geoscientists favoured tectonic processes (Du Toit, 1954; Coward et al., 1995), diapirism (Brock and Pretorius, 1964; Ramberg, 1967), or tectonism plus cryptoexplosion for the Dome formation (Nicolaysen and Ferguson, 1990). The acceptance of the impact origin for the Dome was underpinned through the confirmation by Leroux et al. (1994) that the basal planar microdeformation features in quartz from the Vredefort Dome are a shock deformation effect. Kamo et al. (1996) identified shocked zircon in the Vredefort melt rocks. In addition, the Dome exposes voluminous pseudotachylite bodies (Reimold and Colliston, 1994) and dikes of an unusual clast-laden melt rock, known as the Vredefort Granophyre (Reimold et al., 1990; Koeberl et al., 1996), which has been confirmed as impact melt rock due to the presence of a meteoritic component (Fig. 1.7). A 2.02 Ga age for the Vredefort Granophyre and pseudotachylites (Spray et al., 1995; Kamo et al., 1996) has now been widely accepted as the age for the Vredefort impact event.

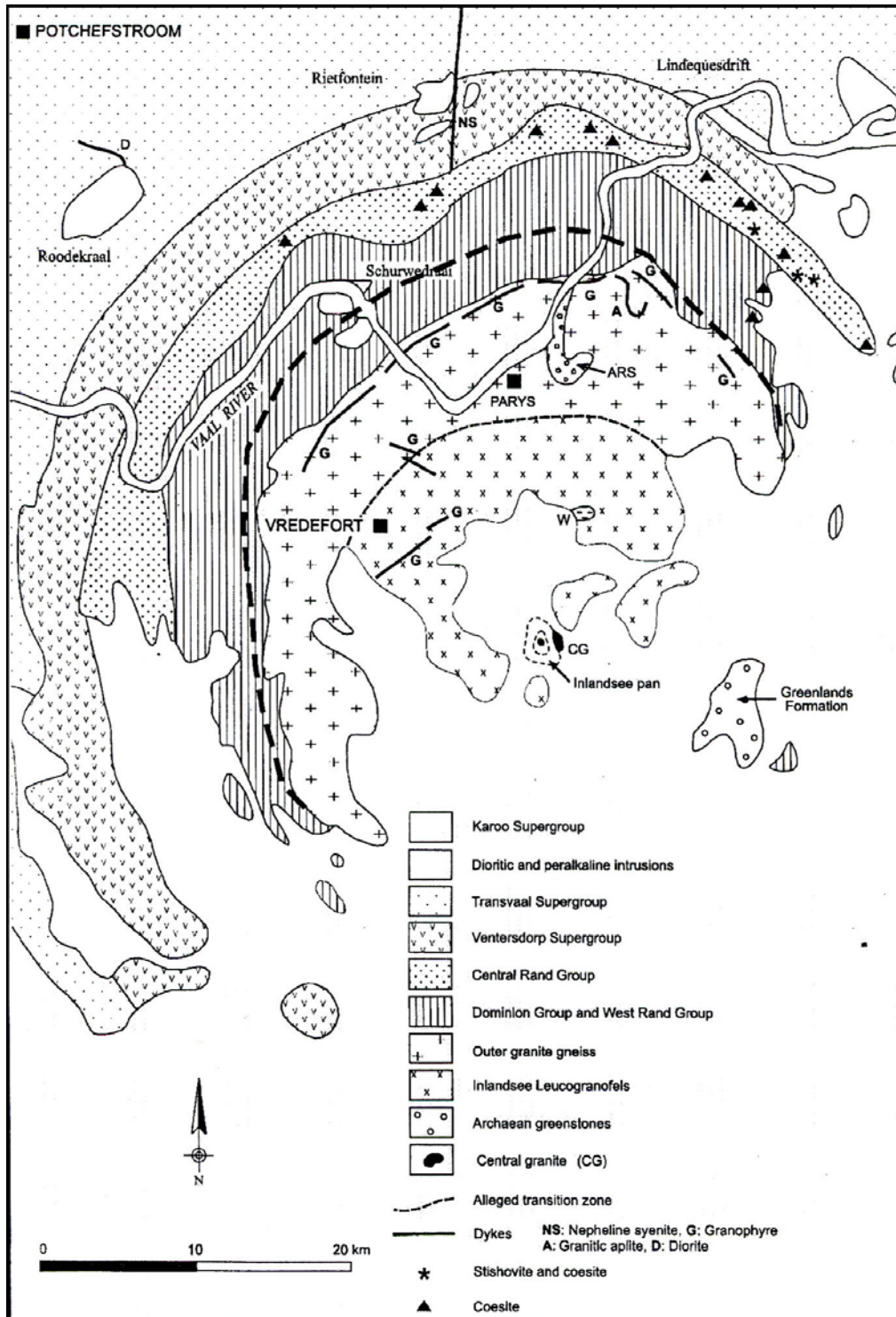


Figure 1.7: Schematic map of the Vredefort Dome showing the distribution of lithologies and the known occurrences of coesite and stishovite (from Gibson and Reimold, 2001). Thick dashed line indicates the limit of the pre-impact amphibolite-facies metamorphic assemblages. Note, well exposed north and northeast sectors of the Dome, which is largely obscured in the south and southeast by Phanerozoic sedimentary strata of the Karoo Supergroup.

1.1.3. The collar strata

The collar rocks of the Vredefort Dome are made up of lavas of the Dominion Group which are covered, successively, by quartzite, conglomerate, siltstone and shale of the Witwatersrand Supergroup, lavas of the Ventersdorp Supergroup and dolomite, quartzite and shale of the Transvaal Supergroup (Figs. 1.6, 1.7), which range in age from 3.07 to 2.1 Ga (Armstrong et al., 1991). These rocks are intruded by a series of post-Transvaal alkali granites and diorites known as the Roodekraal, Schurwedraai, Baviaanskrantz, Rietfontein and Lindequesdrift bodies (Fig. 1.7). All of these intrusions were affected by impact-related deformation. Recent U-Pb dating suggests that at least some of these intrusions could be related to the emplacement of the 2.06 Ga Bushveld Igneous Complex (Moser, 1997).

Recent investigation of the collar structure (Wieland et al., 2005; Jahn and Riller, 2009) indicates that the supracrustal sequence displays both symmetric and asymmetric folds and fault-bounded blocks that display offsets consistent with significant tangential compression. Jahn and Riller (2009) have suggested that radial and concentric faults accomplished centripetal rock flow followed by radial spreading of uplifted and gravitationally unstable rocks in the crater centre. Moreover, these authors suggested that concentric faults formed likely as normal faults during transient crater rim collapse, steepened and were transformed to reverse faults during central rock uplift and finally, were overturned during gravitational collapse of the central uplift. Radial faults, by contrast, formed at a later stage of convergent rock flow towards the crater centre (Jahn and Riller, 2009).

Pre-impact regional metamorphism in the collar rocks decreases from mid-amphibolite facies in the Dominion Group to greenschist facies in the upper Witwatersrand Supergroup (Fig. 1.7) (Gibson and Wallmach, 1995). The gradient in post-impact thermal overprint on rocks of the Vredefort Dome ranges from $\geq 1000^{\circ}\text{C}$ in the Dome centre to about 300°C in the collar rocks located at a distance of about 25 km from the centre (Gibson et al., 1998; Gibson, 2002). These metamorphic grades are significantly higher than the metamorphic conditions estimated for the same stratigraphic horizons exposed along the outer margin of the Witwatersrand basin. The lack of syn-metamorphic fabrics in the collar rocks indicates that the metamorphic assemblages resulted from contact metamorphism, whereby the heat source is localized in the central part of

the Dome or the alkali granite intrusions (Molengraaff, 1903; Bisschoff, 1982). More recently, detailed metamorphic studies have established that the collar rocks and the sedimentary strata in the goldfield record a similar peak metamorphic geothermal gradient of $\sim 40^{\circ}\text{C}/\text{km}$ (Phillips and Law, 1994; Gibson and Wallmach, 1995). These results led Gibson and Wallmach (1995) to suggest that the variation in metamorphic grade across the basin reflects a greater depth of burial of strata in the collar rocks relative to those of the goldfields and outer parts of the Witwatersrand basin, during regional metamorphism. The anticlockwise P-T path and ^{40}Ar - ^{39}Ar dating by Gibson et al. (2000) show that the crustal thickening is associated with the intrusion of the Bushveld Complex.

1.1.4. The Archean Basement Complex

The increase in metamorphic grade from greenschist-facies in the outer collar to granulite-facies in the central parts of the Dome leads several authors to suggest that progressively deeper levels of the Archean crust are exposed towards the centre of the Dome. Based on geochemical data and on modelling of diapiric structures, the so-called “crust-on-edge-model” was proposed, in which the rocks in the basement complex ascended diapirically into the supracrustal rocks, exposing a vertical section of the crust in the Kaapvaal craton (Slawson, 1976).

Detailed lithological mapping of the Vredefort Dome by Stepto (1979, 1990) suggested that the Archean basement gneiss core comprises two concentrically arranged units, the Outer Granite Gneiss (OGG) and the Inlandsee Leucogranofels (ILG). The ~ 10 km wide OGG may further be subdivided into areas with poorly foliated, relatively massive granite or small zone of strongly foliated metagranite close to the collar-basement contact as well as strongly foliated trondhjemites and tonalities closer to the centre, which have a gradational contact zone. In contrast, the ILG comprises an about ~ 20 - 24 km wide core of migmatitic quartz-feldspar leucogneisses with abundant charnokite, mafic and ironstone xenoliths metamorphosed up to granulite facies.

The contact between the OGG and ILG is described as gradational over a distance of several kilometres (Stephens, 1979, 1990; Hart et al., 1981). Hart et al. (1990a) suggest that this contact is as a ~100 m wide, relatively well-defined, brittle-ductile shear zone that truncated the syn-metamorphic fabrics and intense folds in the ILG. Both terranes are separated by a structural discontinuity, which they named the “Vredefort Discontinuity”.

Based on major and trace elements variation along geochemical traverses across the core of the Dome, Hart et al. (1981, 1990a) suggested that the OGG had a fractionated character with decreasing content of large ion lithophile elements (LILE) and total rare earth elements (REE) towards the ILG. According to them, the most fractionated upper layers (close to the collar-basement contact) show depletion in U relative to K and Th, and a strong negative Eu anomaly in their REE patterns. The ILG rocks were reported to display a more fractionated REE pattern, with a slightly positive Eu anomaly and very low U and Th contents relative to those in the OGG rocks. These geochemical results show the compositional differences of OGG and ILG terranes which propose that the OGG and ILG units represented upper and lower crust, respectively, and to suggest that the Dome exposed a crustal profile of 25 km (Hart et al. (1981). Moreover, the occurrence of harzburgite in the core centre represented uplifted Archean upper mantle (Tredoux et al. 1999) which supported the hypothesis that the core of the Dome indicate a full profile through the early Archean crust of the Kaapvaal craton (Hart et al., 1990b).

1.1.5. Metamorphism in the Vredefort Dome

Pre-impact metamorphism of the Vredefort core rocks has been constrained mainly from metamorphic assemblages obtained from mafic granulites and pelitic migmatites in the central parts of the Archean basement gneiss. The composition of these rocks indicated to Stevens et al. (1997) that the temperature of peak metamorphism was above 850°C. Mineral reaction textures, e.g., inclusions of quartz and spinel in garnet, lead Stevens et al. (1997) to infer an anticlockwise P-T path for the metamorphic event, which implies that the heating during this event occurred during tectonic and/or magmatic thickening of the overlying crust (Stevens et al., 1997).

The pre-impact metamorphic assemblages are crosscut by pseudotachylitic bodies and contain evidence of shock metamorphic effects. Shock metamorphic features such as planar deformation features in quartz as well as shock-induced twinning and planar fractures in pyroxene and hornblende are observed in concentric zones around the central parts of the Dome (Gibson et al., 2002). Grieve et al. (1990) suggested that there is a considerable increase of shock pressures toward the centre of the Dome. But, detailed analysis of the impact-related metamorphic features show that most of the shock features in the central parts of the core of the Dome have been overprinted by a post-impact metamorphic event (Gibson et al. 2002).

1.2. Origin of pseudotachylite bodies

1.2.1. Types of impact-induced pseudotachylites

Pseudotachylites are vitreous or microcrystalline dikes which show regular, irregular, or tube-like shapes. These pseudotachylites are millimetres to some centimetres wide or up to hundreds of metres wide bodies which contain centimetres to several metre-size wall rock fragments. The bodies show sharp contacts with the wall rock. They apparently originate from extremely high strain rates and consequently, high temperatures which lead locally to the melting and brecciation of the target rock. As a result of a fast temperature decrease after deformation the melt solidifies to a vitreous or microcrystalline matrix, whereby this matrix may contain angular to rounded wall rock fragments or minerals.

The generation of pseudotachylites is a very controversially discussed subject in the impact community. They form apparently either by the interaction of the shock wave with the target rock (S-Type) or by friction on listric fault surfaces during gravitational sliding of giant crater rim blocks (E-Type) (Spray, 1987; Spray et al., 2004). The generation of both pseudotachylite types within the impact structure is caused by the crater mechanics and the three stages of the crater formation (Fig. 1.8) (Melosh, 1989; French, 1998).

In the first stage, the so-called compression stage, the projectile is arrested at a depth, which corresponds to about twice the projectile diameter (Fig. 1.8a), before its kinetic energy is transferred to the target rocks as shock waves that are generated at the interface between projectile and target (e.g. Melosh, 1989). Shock waves from the compressed projectile are

spreading from the interface toward the rear of the projectile. Subsequently shock waves will be reflected at the rear of the projectile as a tensional wave or rarefaction (French, 1998). This leads to unloading of the projectile and transformation into melt and vapor (Fig. 1.8b). The shock waves transmitted into the target rocks lose rapidly energy as they travel away from the impact point (French, 1998). Heating, deformation and acceleration of target rocks as well as the expanding shock front with increasing radial distance are responsible for the reducing of the energy density (French, 1998). At the impact point, peak shock-wave pressures exceed 100 GPa or more which lead to total melting and vaporization of the projectile and large volumes of target rocks (French, 1998). With a distance of several kilometres from the impact point, distinctive shock-deformation effects in unmelted target rocks are produced at 10 – 50 GPa. At even greater distance from the impact point, the peak shock-wave pressure eventually drop to about 1 – 2 GPa (Kieffer and Simonds, 1980). At this point, near the eventual crater rim, the shock waves become regular elastic waves or seismic waves, which may cause fracturing, brecciation and faulting. The duration of the contact/compression stage is no more than a few seconds and caused by the behavior of the shock wave that was reflected back into the projectile from the projectile/target interface (Melsosh, 1989). The emitted shock wave is in interaction with the target rock and is associated with shock-induced pseudotachylite generation (S-Type). This early stage of the crater formation is linked with structural modification and phase transformation in the area of the impact.

In contrast to the contact/compression stage, the excavation and post-impact modification stages (Fig. 1.8e) are responsible for the morphology of the crater. The excavation stage (Fig. 1.8c, d) is characterized by ejection of material and collapse of the central uplift. At the end of the contact/compression stage, the projectile is surrounded by a roughly hemispherical envelope of shock waves that expand rapidly through the target rock (French, 1998). Thereby, the projectile has penetrated into the target from a point which is located within the centre of this hemisphere within the target rock below the original ground face. Within this hemispherical envelope, the shock waves that travel upward and intersect the original ground surface are reflected downward as rarefaction waves. French (1998) documented that in a near-surface region where the stresses in the tensional release wave exceed the mechanical strength of the target rocks, the release wave is accompanied by fracturing and shattering of the target rock. This reflection process also

converts some of the initial shock-wave energy to kinetic energy, and the rock is accelerated outward, much of it travelling at high velocities (French, 1998). These processes lead to ejection of the target material of the upper levels upwards and outward from the impact point and downward and outward material flow within target rocks. This shows a symmetric excavation flow around the centre of the developing structure. These material movements produce a bowl-shaped depression, the transient cavity, in the target rocks (e.g. Grieve and Cintala, 1981; Melosh, 1989).

The excavation stage ends when the transient crater has grown to its maximum size, and the subsequently, modification stage begins immediately. The transient crater is immediately modified by gravity (Fig. 1.8e, f). Thereby, the transient crater is mostly modified by sliding of oversteepened crater rim blocks. This process may form E-Type pseudotachylites. The formation of the final crater and consequently, the E-Type pseudotachylites are generated therefore after the formation of the S-Type pseudotachylite which apparently originates from the shock wave few seconds after the collision of the projectile with the Earth's crust.

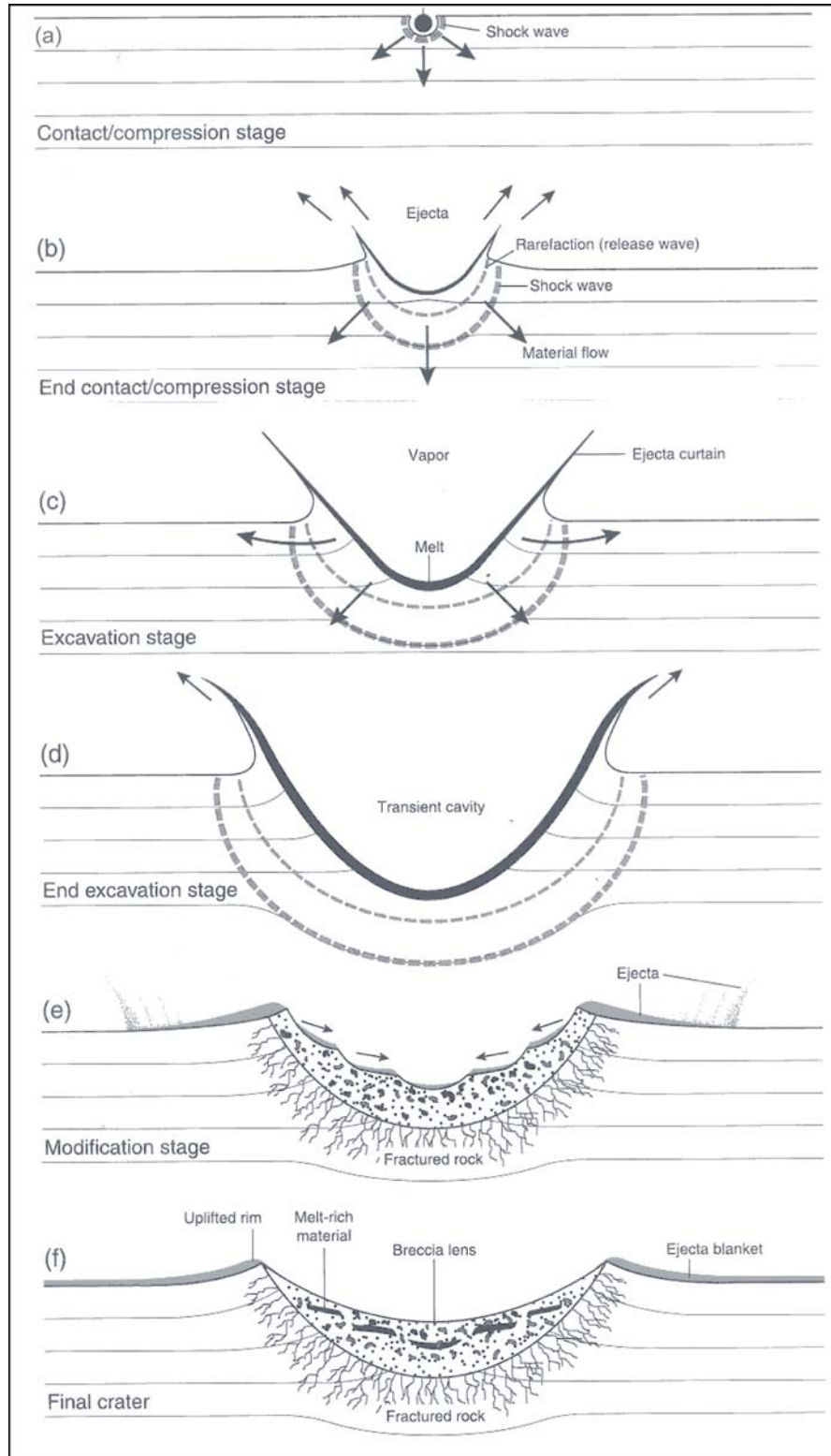


Figure 1.8a-f: Stages of impact crater formation and their characteristics after French, 1998. For explanation see text.

1.2.2. E-Type Pseudotachylite formation

The process of gravitational sliding of mega blocks on listric faults may induce friction melts (Fig. 1.9), which are known as E-Type pseudotachylite.

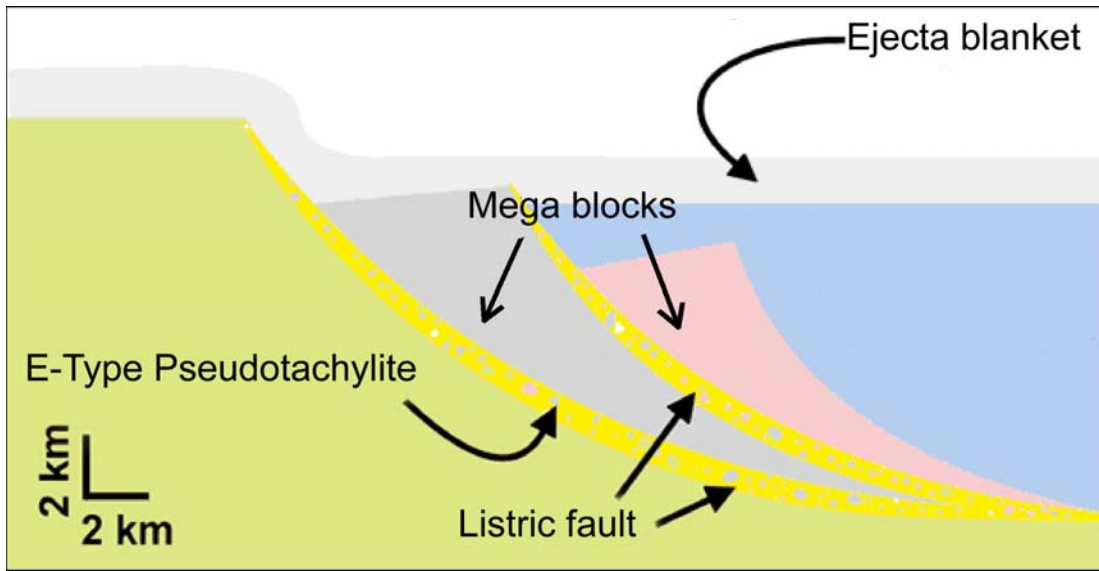


Figure 1.9: Formation of E-Type pseudotachylites on listric faults. Mega rock blocks slide on listric faults and apparently form clast-laden pseudotachylitic dikes (after Scott und Benn, 2002).

During gravitational sliding wall rock fragments are formed in listric fault zones in which they may rotate (Fig. 1.9). Thereby, monomict or polymict wall rock breccias will form with angular to rounded fragment shapes. High-pressure mineral phases within or in the vicinity of the originating pseudotachylites are not observed (Spray et al., 2004), because the pressure plays a subordinated role, in contrast to the formation of S-Type pseudotachylite. The hypothesis of the formation of E-Type pseudotachylites suggests that these pseudotachylites take place in the longer continuing post-impact modification stage (Fig. 1.8e, f) and form larger melt bodies. Hence, E-Type pseudotachylites are more voluminous than S-Type pseudotachylites, which are only few millimetres in width (Kenkmann et al., 2000; Spray et al., 2004). Moreover, sliding wall rock blocks may not be controlled necessarily by lithological boundaries, however, they should be limited at sides by radial faults which indicate displacements at the surface. In addition, frictional melt production is a self-limiting process. Unless friction-induced melts are removed

from fault surfaces during slip, the first melt produced on a given fault surface will decrease its friction coefficient to zero, thus inhibiting further melt production on this fault surface (Melosh, 2005). Although it is conceivable that frictional melting can be induced by ultra-high slip rates, the presence of discrete kilometre-scale shear faults and corresponding magnitudes of differential target rock displacement remain to be ascertained.

In addition, S-Type pseudotachylite surfaces in the modification stage may serve as detachment for the E-Type pseudotachylites so that S-Type pseudotachylites may overprint the E-Type pseudotachylites. Due to high temperature, which develops during E-Type pseudotachylite formation, high-pressure indicators of the S-Type pseudotachylites are rarely observed (Spray et al., 2004). Shock-induced pseudotachylites may serve as an origin for E-Type pseudotachylites.

1.2.3. S-Type Pseudotachylites on interfaces orientated vertical and obliquely to the wave front

S-Type pseudotachylites form in the compression stage during passage of the shock wave by the target rock and may induce 2 millimetres thin pseudotachylites (Kenkmann et al., 2000; Spray et al., 2004). The strong compression of the target rock by the shock wave (primary wave) is responsible for high pressures and temperatures. Therefore, high-pressure minerals are found primarily within S-Type pseudotachylites (Spray et al., 2004). The precise mechanisms which lead to the formation of S-Type pseudotachylites are still not well understood. Kenkmann et al., (2000) and Heider and Kenkmann (2003) show that mechanical interaction between target rock and shock wave plays an important role in the understanding of the formation of these pseudotachylites. S-Type pseudotachylites are formed by local increase of the shock temperature and pressure due to shock wave reverberation and interference; the collapse of open fractures; or by shock wave-induced micro-shear, which induces plastic work and friction (Kenkmann et al., 2000). Different shock-loading experiments show that heterogeneities of the target rock, e.g. lithological boundaries, grain boundaries or crystal defects, are responsible for these mechanical interactions and therefore for the formation of S-Type pseudotachylites (Kenkmann et al., 2000). For the melt generation, an increase in pressure and temperature is required during passage of the shock wave through heterogeneous target rock.

The simulation by Heider and Kenkmann (2003) shows that shock wave propagation through two rock types with different density orientated perpendicular to the incoming shock front (Fig. 1.10). The shock velocity in the rock type with higher density is higher than in the rock type with lower density and, thus, the shock front in the denser part is ahead of the shock front of the part with lower density (Fig. 1.10). The shock wave velocity depends on the density of the materials. If the interface is oriented perpendicular to the shock wave front, a decoupling with respect to the particle velocity and stress appears possible. The shock wave is split into a leading and a trailing shock front because of lithological density variations. This may cause shearing and tensile forces in the zone of the shock front offset (Gibson and Spray, 1998). Generally, a lithological interface which is oriented oblique to the wave front generates lower melt volumes than interfaces oriented vertically to the wave front (Kenkmann et al., 2000). This is possibly caused by an accelerated material transport vertical to the wave front (horizontal velocity) from denser in the less dense medium shortly after the passage of the shock wave (Heider and Kenkmann, 2003). Thereby, the impact of this accelerated material causes an additional shock wave that interacts with the original incoming shock wave in the material with lower density (Heider and Kenkmann, 2003). The interference of the amplitudes and the impedance difference of the materials are responsible for a pressure and temperature increase (Heider and Kenkmann, 2003). However, the acceleration process depends on the available space the material finds before closing the gap between the two lithologies (Fig. 1.11a and b). The temperature increases with increasing gap size.

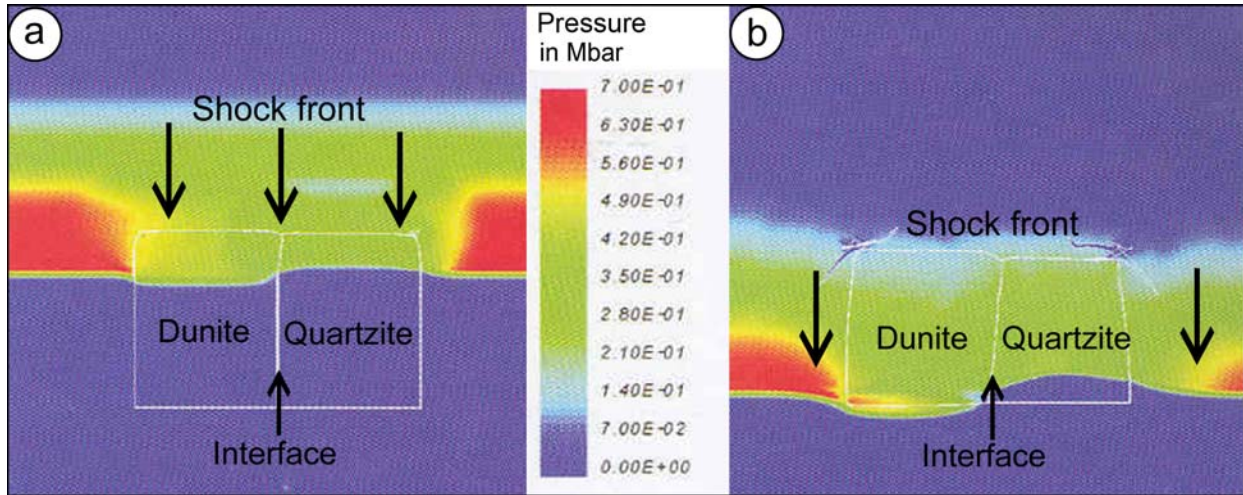


Figure 1.10a and b: Pressure profile of the shock-loading simulation during the passage of the shock front through dunite (left) and quartzite (right) after a) 2.5 and b) after 3.5 μsec . Note, the shock velocity in dunite is higher than in the quartzite caused by their density and, thus, the shock front in dunite is ahead of the shock front in quartzite and the interface is orientated perpendicular to the incoming shock front. The shock wave is split into a leading (left side) and a trailing shock front (right side) (after Heider und Kenkmann, 2003).

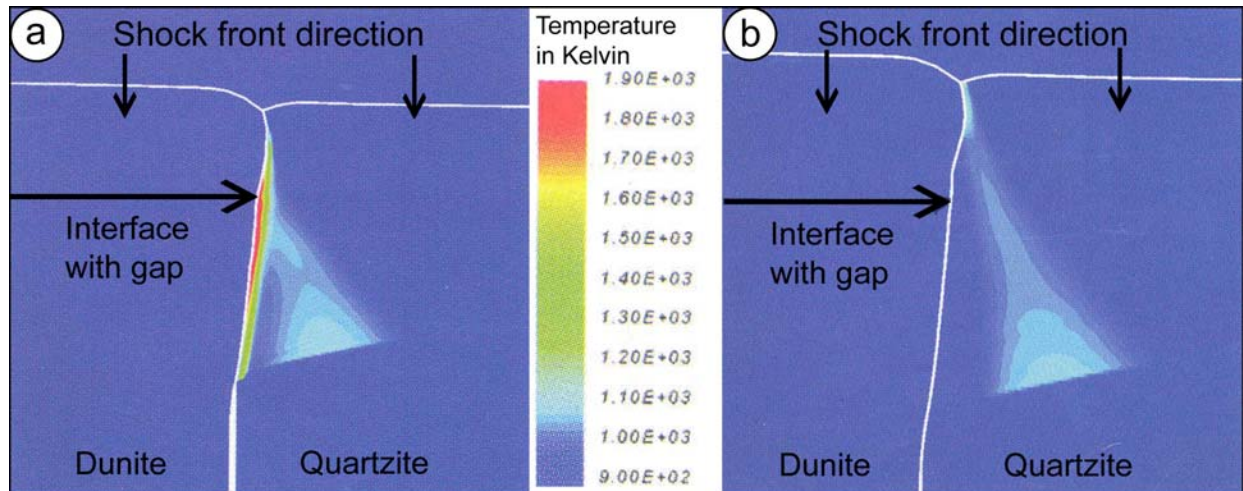


Figure 1.11a and b: Temperature distribution of the shock loading experiment after 3.0 μsec in material with 0.1 mm gap (Fig. 1.11a) and 0.03 mm gap (Fig. 1.11b) after the passage of the shock wave through two different lithologies orientated perpendicular to wave front. Stronger temperature increase occurs for a gap size of 0.1 mm than in smaller gap. (after Heider and Kenkmann, 2003).

Besides the temperature and pressure increase by shock-induced material transport (second shock wave) between two different lithologies with respect to their density, shearing may produce S-Type pseudotachylite (Fig. 1.12a and b). To induce frictional melting in target rocks, an effective

localization of stress and strain is required, which is caused by target rock heterogeneities. The compressibility of different target rock types is different during shock compression. Relative displacements after the passage of the shock front are consequences of this process and different shock-induced particle velocities of the target rock types. The relative motion of rocks with respect to each other caused by the leading shock wave (rock type with higher density) and trailing shock wave (rock type with lower density) induces shearing at the interface. The conversion of friction to heat may induce a rapid temperature increase at the interface, which may eventually cause frictional melting. In this case, the combination of shock loading and friction heating may form pseudotachylitic melt.

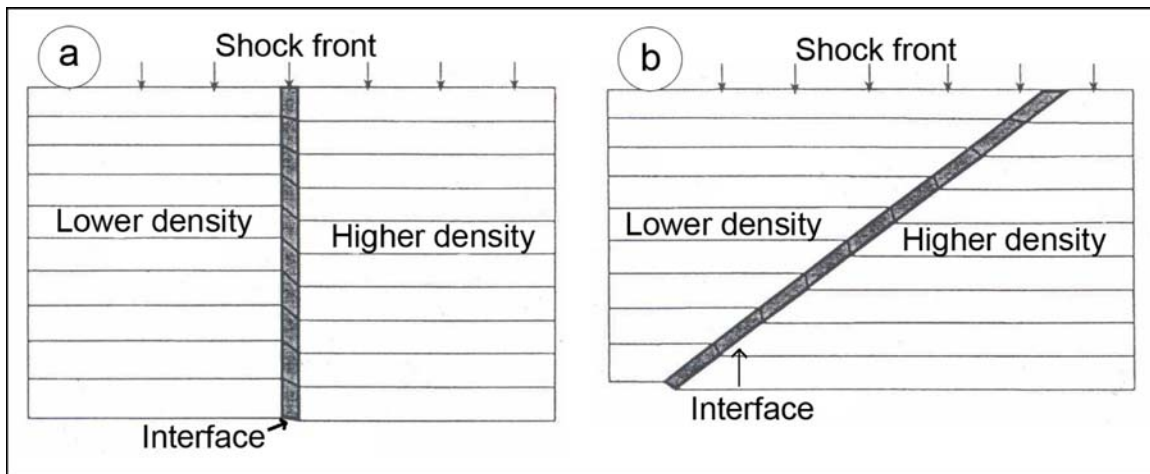


Figure 1.12a and b: Relative displacements of different rock types after the passage of the shock front orientated vertically (Fig. 1.12a) and oblique (Fig. 1.12b) to the wave front. An interface which is oriented vertically to the wave front shows a lower displacement and wider interface (Fig. 1.12a), than an interface which is oriented oblique to the wave front (Fig. 1.12b) caused by the decoupling of particle velocity and tensile forces. (after Kenkmann et al., 2000).

The amount of displacements may depend on the shock wave magnitude, the impedance contrast (defined as the product of the density of the shocked material times the shock velocity), and the orientation of the interface (Fig. 1.12a and b). The impedance contrast leads to shock wave refraction and reflection. An interface which is oriented vertical to the propagation of the wave front shows a lower displacement and wider interface (Fig. 1.12a), than an interface which is oriented obliquely to the wave front (Fig. 1.12a) caused by the decoupling of particle velocity and tensile forces (Kenkmann et al., 2000). An oblique interface represents an intermediate state

between full decoupling (vertical interface) and full coupling (parallel interface). Thus, the interface between the leading and trailing shock front is smaller in comparison to the vertical interface (Fig. 1.12a and b). In addition, the decoupling at oblique interfaces is lower than in vertical interfaces, which creates a smaller gap between the lithologies and consequently lower melt volume (Fig. 1.12a and b). The effect of the orientation of the interface with respect to the shock front on the formation of frictional melts appears important for the heat input by frictional sliding. Melt veins formed at oblique interface resemble most strongly natural S-Type pseudotachylites.

1.2.4. S-Type Pseudotachylites in interfaces orientated parallel to the wave front

The impact induces shock waves which spread out radially from the impact centre through the target rock. These shock waves belong to the group of the longitudinal waves, which are deflected parallel to the propagation speed (Fig. 1.13). The interaction of impact-generated stress waves with interfaces is an important part of cratering. Longitudinal waves spread out in mediums with volume elasticity, such as in solid, liquid and gaseous materials. Thereby, an elastic restoring force has to take effect which is directed against the change in volume (Tipler, 1994).

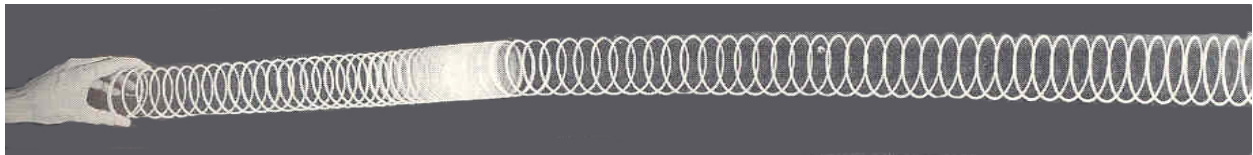


Figure 1.13: Propagation of a longitudinal wave in spring experiment (Tipler, 1994).

Figure 1.14a shows the interaction of a compressional rectangular pulse (wave front parallel to interface) at an interface between high- and low-velocity materials caused by their density, whereby the pulse travels from a high-velocity material into a low-velocity material. This pulse of the longitudinal wave with the longitudinal wave speed (C_L) and longitudinal stresses (σ_L) creates at the interface to the low-velocity material a third compressional pulse from high to low-velocity material that travels into the elastic material to the right of the interface (Fig. 1.14a). A tensional pulse is still reflected into the high-velocity material at the left. The energy of the

original pulse is now divided between the transmitted compressional pulse ($-\sigma_L$) and the reflected tensional pulse (σ_L). By the appearance of the stress difference between both materials caused by different velocities and a tensional pulse, exists a tensile stress at the interface which may facilitate the melt generation (Fig. 1.14a). In Figure 1.14b the compressional rectangular pulse travels across an interface from a low-velocity material into a high-velocity material. As before, there is a transmitted wave and a reflected wave, but in this case all the pulses are compressional. In both cases the whole pressure of the shock wave is the sum of the pressures of both single waves. In comparison to the first case, elongation component in the second case plays a minor part for the tensile stress caused by lack of tensional pulse (Fig. 1.14b). But, the tensional pulse may be important for larger melt generation at interfaces oriented in parallel with wave front (Kenkmann et al., 2000).

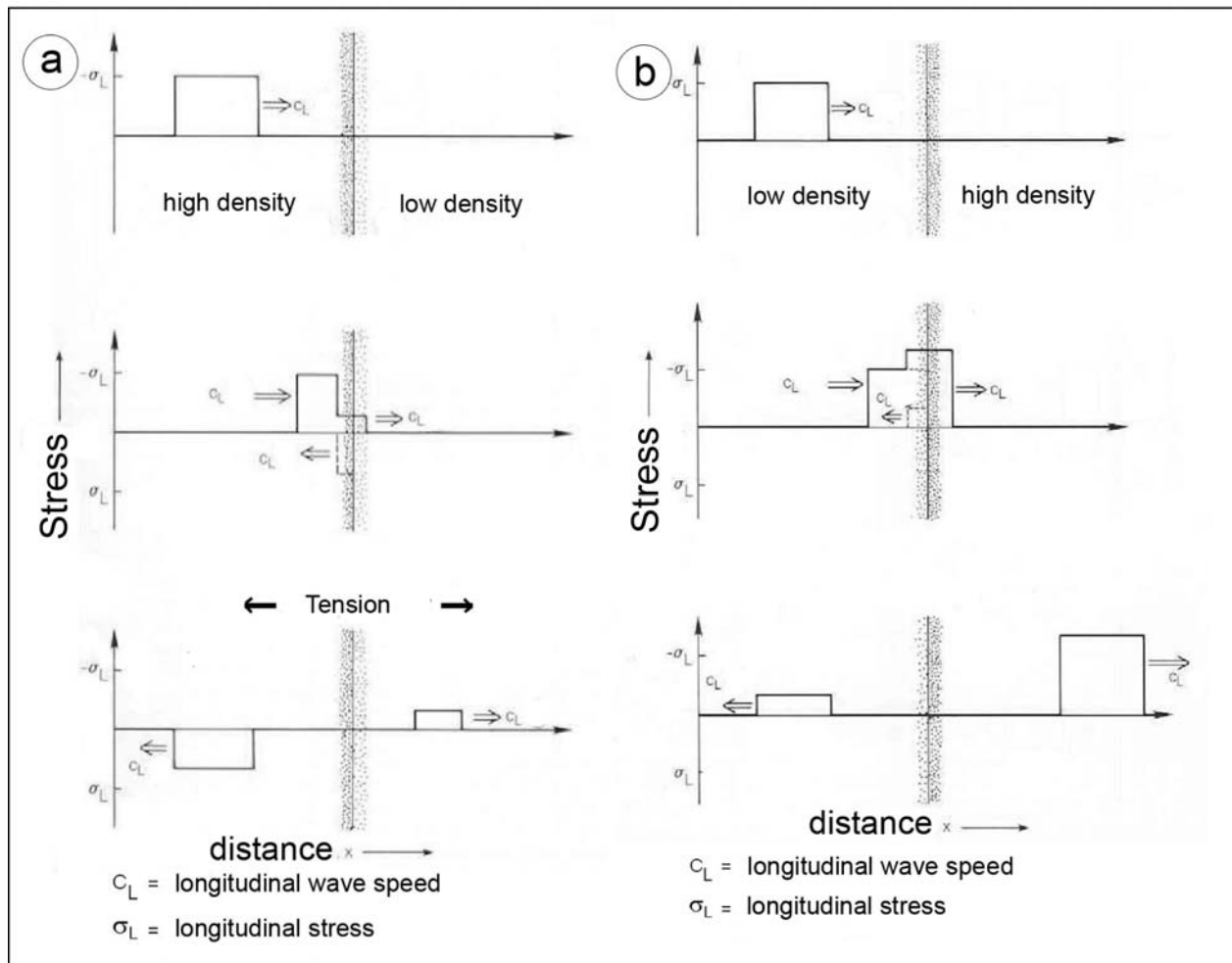


Figure 1.14a and b: Reflection of a pressure pulse that encounters an interface between high- and low-velocity material (Fig. 1.14a) and the inverse case (Fig. 1.14b). In Fig. 1.14a part of the wave is reflected back into the high-velocity material as a tensile wave, while the rest of the wave continues into the low-velocity material. In Fig. 1.14b reflection of a pressure pulse that encounters an interface between low- and high-velocity materials. In this case all the pulses are compressional. No tensile stress results between both materials (Melosh, 1989).

1.3. Decompression melting

The formation of decompression melt related to impact structures is still unclear. The existence of such melts is advocated by some geophysicists. It has been suggested that such endogenous melts are caused by thinned lithosphere or hot rising mantle plumes. The energy released is largely derived from gravitational energy and is outside the conventional calculations of impact modelling, where energy is derived solely from the kinetic energy of the impacting projectile. Some researcher suggested that there is a direct link between impacts and volcanism (Jones et al., 2002), e.g., the Bushveld Complex and the Deccan Traps (Hamilton, 1970; Seyfert et al., 1979; Negi et al., 1993), but evidence for impact was erased by subsequent large-scale igneous activity. Melosh (2000) contends that there is no firm evidence that impacts can induce volcanic activity in the impact crater region, and he presents arguments, based on the amount of energy available, against the proposal that an impact could trigger volcanism at a distance. In addition, he correlated the terrestrial crater size and the total volume of impact melt and points out that the volume of melt generated is based on calculations, as experiments are not able to access this high-energy regime (Melosh, 1989).

Ivanov and Melosh (2003) performed numerical simulations of the excavation and modification of a large impact crater (projectile size of 20 km; velocity of the projectile of 15 km s^{-1}) that include the effects of decompression melting and the thermal gradients in the target (gradually decreases to $\sim 1 \text{ K km}^{-1}$ for depth below $\sim 90 - 200 \text{ km}$). They used a “hot” model with 30 K km^{-1} and a “cold” model with 13 K km^{-1} both near the surface. The results of these models show a maximum transient-crater depth of $\sim 55 \text{ km}$ what suppose that the mantle material is hot enough to just melt as it reaches the surface. This means, if the maximum stratigraphic uplift is approximately one-tenth of the final crater diameter (e.g. Melosh and Ivanov, 1999), so must be the final crater-rim diameter 500 km for the hot case and 1200 km for the cold case. But such large impact basins are unknown on Earth. In addition, the final position of the transient crater level is at a depth of $\sim 5\text{-}10 \text{ km}$. This depth implies a pressure release of 10%-20% of the initial value, which is not enough to reach the solidus at the final pressure (Ivanov and Melosh, 2003). All these characteristics show that the impact of a 20 km diameter asteroid may create partially molten mantle material, but without any significant input from decompression melt.

CHAPTER 2: THIS STUDY

This project presents results of a multidisciplinary study involving comprehensive structural analysis of pre-impact mineral fabrics, properties of fragment-rich pseudotachylite and Vredefort Granophyre dikes as well as geochemical analysis of matrices in pseudotachylites and their respective wall rocks as well as Vredefort Granophyre dikes of the Vredefort Dome. The investigation was directed at the examination of the nature and origin of the melt rocks, specifically the correlation of structural and geochemical data and source of melt generation suggest that melt may have been drained from the overlying impact melt sheet and transported into fragment-rich dilation zones to form pseudotachylite zones and the Vredefort Granophyre dikes, both processes occurring at different times.

The tectonic evolution of the Archean basement complex with regards to impact cratering processes was investigated by means of structural data e.g. trajectories of inclined planar mineral shape fabrics (migmatitic layering), geometry and arrangement of pseudotachylite bodies, distribution and magnitude of component vectors of maximum dilation as well as the shape fabrics of fragments in pseudotachylite bodies. This field-based structural work was undertaken during the first two years of the project comprising a total of 6 month of fieldwork. Rocks of the Archean basement complex were partly mapped by Lana et al. (2003, 2004), but mapping of the fabrics as part of this thesis was conducted in order to better constrain the extent of the core affected by outward rotation during central uplift formation. Moreover, this structural analysis was focused on the distribution and arrangement of pseudotachylite bodies and vectors of maximum dilation in the Vredefort dome in order to find out the possible relationship between the cratering flow field and formation of fragment-rich pseudotachylite bodies, the kinematics of deformation associated with the emplacement of the pseudotachylites on the outcrop scale.

The hypothesis of this thesis is that pseudotachylitic melt is allochthonous and was emplaced at an advanced stage of cratering into tensional fracture zones within the crater floor and was not formed by (1) frictional heating, (2) shock loading or (3) decompression melting. Pseudotachylites were evaluated by means of geochemical data obtained by polarization microscope, X-ray fluorescence spectrometry (XRF), SEM and electron microprobe analysis of 62 samples of pseudotachylite matrices and respective wall rocks. This geochemical work was

undertaken during the second year of the project comprising a total of 10 month of laboratory work and two month of fieldwork. Trends in the compositional deviation of pseudotachylite matrices from their respective wall rocks suggest that the primary melt had a broadly granitoid composition, i.e., close to the average composition of Vredefort Granophyre dikes, which are derivatives of the original, now-eroded, impact melt sheet.

The hypothesis that pseudotachylitic melt in fragment-rich dilation zones may have been drained from pools from the overlying impact melt and that the Granophyre melt was formed by injection of two-stage melt emplacement from the overlying impact melt sheet into target rocks, possibly driven by late stage isostatic readjustment of crust underlying the impact structure was evaluated by means of geochemical and structural analyses of Vredefort Granophyre dikes. This shows that the melt of pseudotachylite bodies and Vredefort Granophyre dikes drained from the same source, the overlaying impact melt pool, and the generation of both bodies are the same but at different stages of impact cratering.

The ensuing chapters present results of this study as four papers (three in the Vredefort Impact Structure, one in the Sudbury Impact Structure (Appendix I)) that have already been published (Chapter 3; Appendix) or submitted (Chapter 4, 5). All Chapters and the Appendix are reproduced in the format accepted by the journals and contain their relevant abstracts, introductions and conclusions. The formatting (internal subdivisions of text, references) and the language styles are those of the journals, all manuscripts use British spelling. Chapter 6 summarizes all results and provides a synthesis as well as an outlook about possible works and approach to solutions.

The reproduction of four published or submitted papers in the thesis obviously leads to considerable duplication in the introductions and locality maps.

All papers are multi-authored. The bulk of the data collection and interpretation was done by the author and the thesis project supervisor U. Riller. U. Riller and R.L. Gibson are co-authors on all papers. W.U. Reimold assisted in the interpretation of geochemical data. The thesis project was funded by DFG projects awarded to U. Riller and W.U. Reimold.

Chapter 3 provides the results of a systematic analysis of the geometry of pre-impact mineral fabrics and structural properties of fragment-rich pseudotachylite zones of the Vredefort Dome (all data generated by Daniel Lieger). Therefore, the orientation of migmatitic and gneissic

layering, defined by granitic leucosomes, trondhjemitic-tonalitic melanosomes and the shape-preferred orientation of feldspar, quartz and mafic clots was recorded at 745 stations. To facilitate inspection of this comprehensive data set, trajectories delineating the overall strike of inclined planar mineral fabrics were drawn and fabric orientation is plotted in lower-hemisphere equal-area projections for 13 sectors of the crystalline core. In addition, this chapter provides the results of detailed mapping of a self created brecciation intensity scale and trend of fragment-rich pseudotachylite bodies at a total of 531 stations (data generated by Daniel Lieger). These geometry of pseudotachylite bodies in 531 stations originate of an about 1000 measurements of width, length, strike and dip of pseudotachylite as well as the horizontal component vector of the maximum dilation direction. Thereby, an about 200 measurements of the maximum dilation direction provide the results of a geological map of distribution and magnitude of component vectors of maximum dilation inferred from the geometry of pseudotachylitic veins and dikes (all data generated by Daniel Lieger). In addition, the pseudotachylitic body trend, brecciation intensity and component vectors of dilation are compared with a hydrocode model by Ivanov (2005). Based on hydrocode modelling, vertical stretching and uplift of the inner core and outward rotation and dilation in the outer core zone was examined (interpreted by Daniel Lieger and discussed with Ulrich Riller).

The variation in fragment shape with distance from pseudotachylite zone margins was quantified using the image analysis software Q-Win (Leica). For this purpose, an about 400 fragment outlines of the two fragment-rich pseudotachylite zones were digitized from photos and analyze in terms of sectional ellipticity, i.e., departure from circularity.

Chapter 4 addresses the geochemical and petrographic analysis of the matrices in pseudotachylitic veins and dikes and of their respective wall rocks of the Vredefort dome (all new data generated by Daniel Lieger). Pseudotachylite matrix and respective wall rocks were examined petrographically using an Olympus stereomicroscope and a LEITZ DM RXP polarization microscope at the Museum of History, Berlin. A total of 62 thin sections from samples of many locations and covering a wide range of wall rock types and associated pseudotachylite matrices were inspected. Major and trace elements of eleven pseudotachylite matrix-wall rock sample pairs and ten additional samples of pseudotachylite matrices were analyzed using X-ray fluorescence spectrometry (XRF) at the University of the Witwatersrand,

Johannesburg (data produced by Roger Gibson). The XRF and SEM analyses show that the chemical compositions of matrices in pseudotachylite veins and dikes deviate in part significantly from those of their immediate wall rock. In addition, the chemical analyses indicate that compositions of pseudotachylite matrices were modified by assimilation of wall rock components (data generated by Daniel Lieger).

SEM analysis was carried out at the Museum für Naturkunde on a JEOL JSM-6300 instrument equipped with a tungsten cathode, operated at 8-30 kV and using an energy-dispersive X-ray spectrometer (EDX). Pseudotachylite matrix analyses were conducted in EDX mode. Backscattered electron (BSE) imagery was used to investigate the microtexture and mineralogy of pseudotachylite matrices. Except for a reduced working distance (11 mm), the settings for generating BSE images were the same as mentioned above. The data were processed using the AXS software Quantax 400 by Bruker Company. SEM analysis provides results of pseudotachylite matrices which show local assimilation of wall rock as well as a case of melt transport from a larger pseudotachylite into a smaller one (all data generated by Daniel Lieger).

Four samples from the Kudu quarry and one sample from the SunWa location were investigated with a Jeol JXA-8800 electron microprobe at 15 kV and 15 nA, also at the Museum für Naturkunde Berlin (investigated by Daniel Lieger). Energy-dispersive (EDX) and wavelength-dispersive spectrometry (WDX) were used to determine the mineralogy of wall rock and adjacent pseudotachylite matrices. The chemical composition of matrix and wall rock of Kudu was measured along 14 transects across the vein, each of which comprises between 100 and 200 spot analyses, using a defocused electron beam of 35 μm diameter. Electron microprobe analysis of Kudu location shows the melt transport from the larger pseudotachylite body into a smaller one in the documented case. SunWa location provides results of the chemical composition of the matrix originated by measurements at 155 spot analyses with a defocused electron beam. The electron microprobe analyses of this thin section of SunWa show the chemical variation of pseudotachylite matrix is caused by assimilation as well as large chemical differences of pseudotachylite matrix and their immediate wall rock (all data and interpretation by Daniel Lieger, discussed with Uwe Reimold, Roger Gibson and Ulrich Riller).

Chapter 5 focuses on the geochemistry of the Vredefort Granophyre of the dome. Granophyre matrices were examined petrographically using an Olympus stereomicroscope and a LEITZ DM

RXP polarization microscope at the Museum of History. For this purpose, thin sections of two samples from Granophyre locations associated with and without macroscopic clasts in these matrices were inspected (data, samples and thin section by Daniel Lieger). Major and trace elements of eight Granophyre matrices were analysed using wavelength dispersive X-ray fluorescence spectroscopy (WDXRF) at the Witwatersrand University, Johannesburg (data produced by Roger Gibson). Whole-rock chemical and thin section analyses of profiles across two dikes, together with previous data of samples from all dikes, provide data of the chemical heterogeneity between core and core/collar dikes as well as within one core/collar dike (all new data generated by Daniel Lieger, interpreted by Daniel Lieger and discussed with Ulrich Riller).

Chapter 6 provide a summary of chapter 2-5 as well as an outlook about possible works and approach to solutions for the formation of pseudotachylitic melt and their origin. Furthermore, this chapter presents a synthesis of the formation of the pseudotachylitic melt in the central uplift with help by a model (model and interpretation by Daniel Lieger).

Appendix I focuses on structural data of the Sudbury Impact Structure with the comparison to the data of the Vredefort Impact Structure. All structural data of the Vredefort Impact Structure are from Daniel Lieger. Data of the Sudbury Impact Structure paper are by Ulrich Riller and Daniel Lieger. The interpretation of these data is from Ulrich Riller and discussed with Daniel Lieger.

Appendix II shows all structural data of this thesis from Daniel Lieger.

Appendix III shows fragment orientation and distribution in back-scattered electron image of the matrix of the apophysis in SunWa (6). All data generated by by Daniel Lieger.

CHAPTER 3:

GENERATION OF FRAGMENT-RICH PSEUDOTACHYLITE BODIES DURING CENTRAL UPLIFT FORMATION IN THE VREDEFORT IMPACT STRUCTURE, SOUTH AFRICA

Daniel Lieger¹, Ulrich Riller² and Roger L. Gibson³

¹ Museum für Naturkunde, Humboldt-Universität zu Berlin, Invalidenstraße 43, 10115 Berlin, Germany

² McMaster University, School of Geography and Earth Sciences, 1280 Main Street West, Hamilton, Ontario, Canada, L8S 4K1

³ Impact Cratering Research Group, School of Geosciences, University of the Witwatersrand, Private Bag 3, P.O. Wits 2050, Johannesburg, South Africa

Published in Earth and Planetary Science Letters 279 (2009) 53 – 64.

<http://dx.doi.org/10.1016/j.epsl.2008.12.031>

Abstract

Target rocks underlying the central portions of large terrestrial impact structures are characterized by the pervasive presence of fragment-rich pseudotachylite bodies. Debates regarding the formation of these bodies include the origin of pseudotachylitic melts, i.e., friction- versus shock-induced melting, melt mobility, causes of target rock fragmentation, and timing of fragmentation and melt emplacement with respect to stages of cratering. Comprehensive structural analysis of pre-impact mineral fabrics and properties of fragment-rich pseudotachylite in the Vredefort Dome suggests that melt is allochthonous and was emplaced at an advanced stage of cratering into tensional fracture zones within the crater floor. Both concentration of bending strains imparted on target rocks during central uplift formation and thermal stresses induced by the emplacement of allochthonous melt led to fragmentation of target rock. Tensional fracture zones opened in an overall dilational strain field towards the end of cratering, likely during collapse of the central uplift, and formed low pressure zones, into which melt was forcefully drawn. Melt may have been drained from the overlying impact melt sheet or from sites within the crater floor and transported into fragment-rich dilation zones.

Our field-based analysis failed to identify the presence of bona fide shear faults that could potentially have generated in situ frictional melts and fragments. Rather, target rock fragmentation and melt generation that resulted in fragment-rich pseudotachylite bodies are processes separated in space and time during cratering.

1. Introduction

Formation of complex impact structures is one of the least well-understood processes in planetary geology, and detailed structural studies of terrestrial impact structures, notably large complex ones, are rare. Numerical models of complex crater formation (Fig. 3.1) impressively demonstrate that cratering is accomplished by target rock displacements on the order of tens of kilometres during the phases of both transient crater formation and subsequent crater modification (Ivanov and Deutsch, 1999; Pierazzo and Melosh, 1999; Wünnemann and Ivanov, 2003; Collins et al., 2004; Gisler et al., 2004; Wünnemann et al., 2005; Ivanov, 2005). Looking at natural prototypes, however, uncertainty exists regarding the mode of target rock deformation during central uplift formation, i.e., the centripetal and upward motion of rock during gravitational collapse of the transient cavity followed by gravitational outward spreading of uplifted rock (Fig. 3.1). More specifically, there is considerable debate regarding (1) the geometric and kinematic significance of prominent structural dislocations, (2) the temporal and mechanical relationships between continuous and discontinuous deformation at various scales and (3) the mechanical role of impact-induced melt systems, specifically fragment-rich pseudotachylite, during these processes.

Large terrestrial impact structures, notably the Sudbury (Canada) and the Vredefort (South Africa) structures, are characterized by the pervasive presence of fragment-rich pseudotachylite zones in the crater floor (e.g., Dressler, 1984; Killick and Reimold, 1990; Reimold and Colliston, 1994; Gibson and Reimold, 2001; Dressler and Reimold, 2004; Reimold and Gibson, 2005). The zones generally form complex networks of dark and flinty rocks (Shand, 1916) enveloping angular as well as rounded wall rock fragments and are millimetres to hundreds of meters wide (e.g., Rousell et al., 2003). It is still uncertain at which stage or stages during the cratering

process and by which processes fragment-rich pseudotachylite zones form (Melosh, 2005; Riller, 2005).

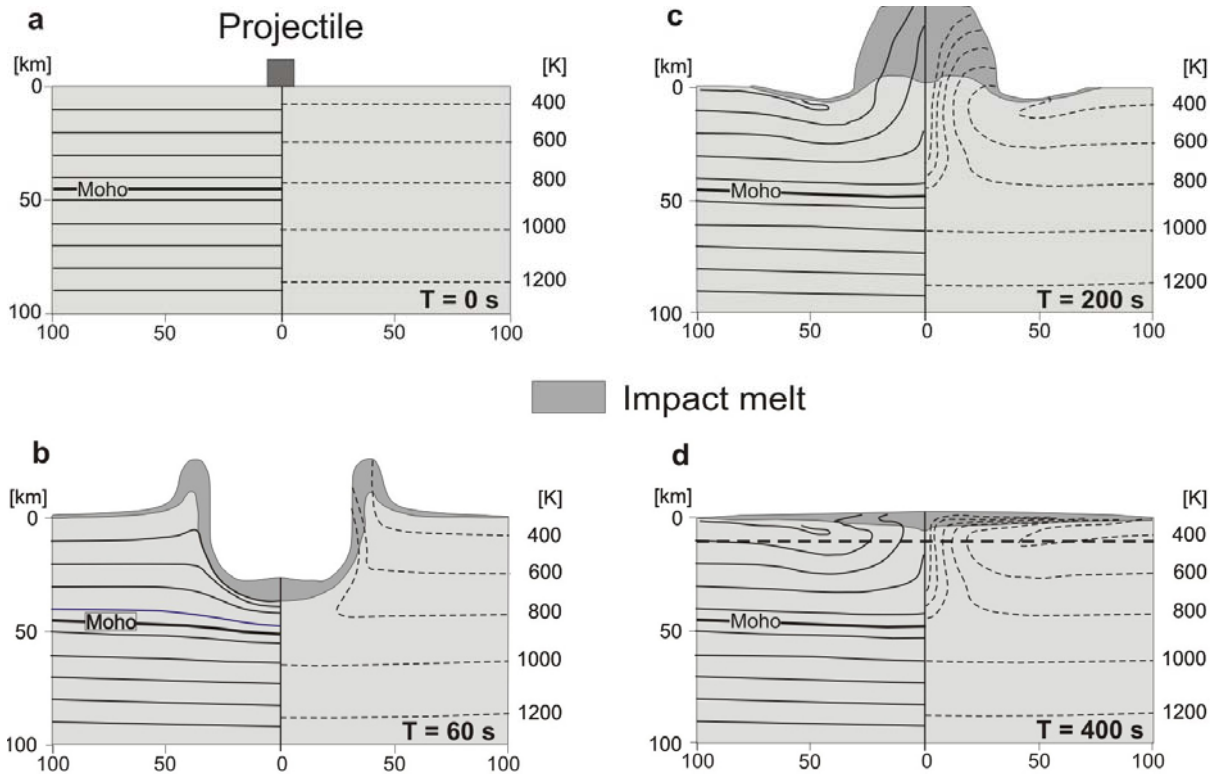


Figure 3.1: Stages of impact crater formation based on hydrocode modeling by Ivanov and Deutsch (1999) showing the geometric evolution of originally horizontal stratigraphic marker layers (solid lines) and isotherms (stippled lines) for an impact structure the size of Vredefort. T denotes time in seconds after impact. (a) Undisturbed configuration of model lithosphere prior to impact. (b) Maximum growth of the transient cavity. (c) Formation of the central uplift of material following gravitationally-induced collapse of the transient cavity. (d) Final configuration of marker layers and isotherms below a flat impact melt sheet. Bold stippled line indicates approximate level of erosion of the Vredefort impact structure.

Spray (1998) suggested that impact-induced pseudotachylite is generated by shock wave-rock interaction and frictional sliding. Shock-induced pseudotachylite may be generated by shock compression and release (Reimold, 1995; Spray, 1995). Compositional and structural heterogeneity of target rock and its mechanical interaction with the shock wave front can lead to the generation of temperature and pressure peaks and localized melting in target rock (Kenkmann et al., 2000; Heider and Kenkmann, 2003). Typically, melt volumes generated by this process do not form melt veins exceeding a few millimeters in width (Kenkmann et al., 2000; Spray et al., 2004). Shock compression experiments show also that melt can be produced by differential

sliding of mechanically competent rocks (Fiske et al., 1995; Kenkmann et al., 2000; Heider and Kenkmann, 2003). However, the rather small melt volume produced as shock-induced pseudotachylite is at variance with the presence of up to hundreds-of-meters-wide, fragment-rich pseudotachylite bodies observed at Sudbury and Vredefort and, thus, does not seem to account for the bulk of pseudotachylite in large terrestrial impact structures (Melosh, 2005).

In order to explain the rather large volumes of fragment-rich pseudotachylite, frictional melting and target rock fragmentation along so-called “superfaults” (Spray, 1997), formed during catastrophic collapse of crater walls and/or central uplifts, have been invoked (Spray, 1992; 1995; Spray et al., 2004). Although it is conceivable that frictional melting can be induced by ultra-high slip rates, the presence of discrete kilometre-scale shear faults and corresponding magnitudes of differential target rock displacement remain to be ascertained at Sudbury and Vredefort. Moreover, frictional melt production is a self-limiting process. Unless friction-induced melts are removed from fault surfaces during slip, the first melt produced on a given fault surface will decrease its friction coefficient to zero, thus inhibiting further melt production on this fault surface. Based on this concept, Melosh (2005) proposed that frictional melts are transported during slip into low-pressure zones, e.g., tensional cracks at the lateral tips of bona fide shear faults. This process is akin to deformation-assisted mobility of endogenic melts (e.g., Petford et al., 2000) and requires accumulation of pseudotachylite in dilation zones kinematically linked to shear faults.

At Vredefort the origin of pseudotachylite has been ascribed to both shock melting (Schwarzman et al., 1983; Reimold and Gibson, 2005) and frictional melting on small-scale shear faults (Spray, 2000; Lana et al. 2003b). Similar uncertainty exists regarding the spatial distribution of fragment-rich pseudotachylite, concentrated in broad zones (Reimold and Colliston, 1994) but also chaotic on the outcrop scale (Dressler and Reimold, 2004). This hampers interpretations regarding the emplacement mode of pseudotachylitic melt. Therefore, we conducted a systematic analysis of the distribution and geometry of fragment-rich pseudotachylite zones, fragment shapes and pre-impact mineral fabrics from the central Vredefort impact structure (Fig. 3.2). Our field-based study aims at providing quantitative ground truth data that is aimed at understanding better the kinematics of central uplift formation and emplacement of pseudotachylitic melts. In particular, we seek to elucidate to what extent the emplacement of these melts is controlled by the strain

field imparted on target rocks during central uplift formation, in an attempt to better constrain the respective cratering stage at which these fragment-rich melt bodies formed. It should be noted that we use in this study the term pseudotachylite without implying any specific origin of its melt (for more details see Stöffler and Grieve, 2007).

2. Geological background

The Vredefort impact structure (Fig. 3.2) has been dated at 2023 ± 4 Ma (Kamo et al., 1996) and is, thus, the oldest known impact structure and, with an estimated diameter of up to 250 km, likely also the largest one known on Earth (Henkel and Reimold, 1998; Grieve and Theriault, 2000; Turtle et al., 2005). The impact structure has been eroded to a depth of about 7 to 10 km (Gibson et al., 1998; Henkel and Reimold, 1998) and, thus, offers an unprecedented view of the structure of target rocks underlying a large, complex terrestrial impact structure. The central portion of the impact structure, the so-called Vredefort Dome (Fig. 3.2), is the eroded relic of structurally uplifted rocks, generally referred to as the central uplift (Melosh, 1989). The Vredefort Dome consists of a core, ca. 40 km in diameter, of a 3.1-3.2 Ga tonalite-trondhjemite-granodiorite and greenstone assemblage (Lana et al., 2004). The core is surrounded by a 15-20 km wide ‘collar’ of subvertical to overturned, 3.07 and 2.1 Ga supracrustal strata (Armstrong et al., 1991) that were deposited unconformably on the Archean crystalline basement rocks.

The core of the Vredefort Dome consists of a central zone of granulite-facies metamorphic rock that is enveloped by migmatite and gneiss metamorphosed to upper amphibolite-facies and intruded by synmetamorphic granitoid bodies (Fig. 3.3, Lana et al., 2004). The collar rocks are made up of lavas of the Dominion Group which are covered, successively, by quartzite, conglomerate, siltstone and shale of the Witwatersrand Supergroup, lavas of the Ventersdorp Supergroup and dolomite, quartzite and shale of the Transvaal Supergroup (Fig. 3.2). Pre-impact regional metamorphism in the collar rocks decreases from mid-amphibolite facies in the Dominion Group to greenschist facies in the upper Witwatersrand Supergroup (Gibson and Wallmach, 1995). The gradient in post-impact thermal overprint on rocks of the Vredefort Dome ranges from $\geq 1000^{\circ}\text{C}$ in the Dome centre to about 300°C in the collar rocks located at a distance of about 25 km from the centre (Gibson et al., 1998; Gibson, 2002).

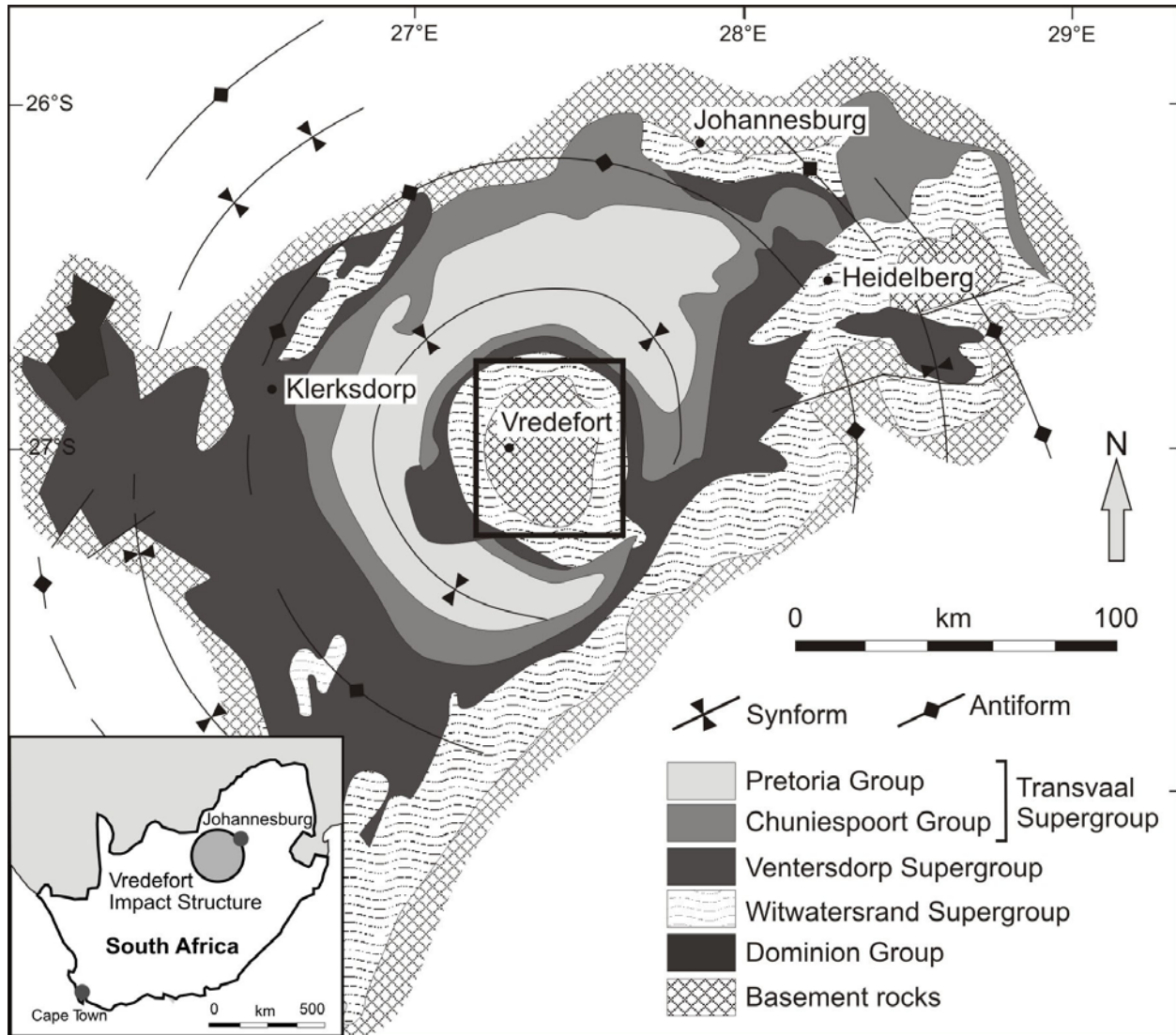


Figure 3.2: Simplified geological map showing the location of the Vredefort Dome, composed of Archean basement rocks enveloped by supracrustal collar rocks, in the central portion of the Vredefort impact structure. Note concentric antiforms and synforms around the Vredefort Dome. Rectangle indicates enlarged areas in Figures 3.3, 3.4 and 3.7.

Beyond the collar rocks, strata of the Transvaal Supergroup are thrown into a series of circumferential, open antiforms and synforms up to a distance of about 120 km from the Dome centre (Fig. 3.2; McCarthy et al., 1990; Theriault et al., 1997). This fold pattern is typical for centro-symmetric strain fields expected to be generated by meteorite impact into layered targets (Kenkmann et al., 2005; Grieve et al., 2008). Much of the southeastern portion of the impact structure is covered by Phanerozoic sedimentary rocks and dolerite of the Karoo Supergroup

(Minnitt et al., 1994; Lana et al., 2003a) and, thus, does not lend itself to an analysis of impact processes.

3. Pre-impact planar mineral fabrics of the Vredefort Dome

Pre-impact metamorphic mineral shape fabrics in the crystalline core of the Dome show a distinct pattern, which has been attributed to central uplift formation (Lana et al., 2003b). In the central portion of the core, planar mineral shape fabrics, notably migmatitic layering, strike NW-SE (see Lana et al., 2003a, b for a detailed account of ductile strain fabrics). At a distance of about 3 to 6 km from the collar, migmatitic layering is subvertical and broadly concentric with respect to the centre of the impact structure. Assuming a uniform orientation of this layering (S2 fabrics of Lana et al., 2003b) prior to impact, its concentric strike near the core-collar boundary has been explained by outward rotation of crystalline core rocks during impact-induced rock uplift (Lana et al., 2003b).

Adhering to the hypothesis that planar metamorphic mineral shape fabrics were oriented uniformly prior to impact and regarding these fabrics as markers to constrain the cratering flow field (Lana et al., 2003b, 2004), their orientation was mapped systematically in the exposed portion of the crystalline core (Fig. 3.3). More specifically, mapping of the fabrics was conducted in order to better constrain the extent of the core affected by outward rotation during central uplift formation. Therefore, the orientation of migmatitic and gneissic layering, defined by granitic leucosomes, trondhjemitic-tonalitic melanosomes and the shape-preferred orientation of feldspar, quartz and mafic clots was recorded at 745 stations. To facilitate inspection of this comprehensive data set, trajectories delineating the overall strike of inclined planar mineral fabrics were drawn and fabric orientation is plotted in lower-hemisphere equal-area projections for 13 sectors of the crystalline core (Fig. 3.3, Appendix II).

Overall, fabric trajectories agree with the fabric pattern mapped by Lana et al. (2003b, 2004), i.e., sub-vertical, NW-SE striking fabrics prevail in the core centre (diagram of sector 13 in Fig. 3.3) and a circumferential fabric strike is found near the core-collar boundary (Fig. 3.3). The high spatial coverage of our data revealed that fabric strike is symmetric about a NW-SE striking vertical mirror plane passing through the Dome centre (Fig. 3.3). Moreover, our fabric data

allowed us to constrain more precisely the areal extent of the outer core zone affected by outward rotation. The outer margin of this zone is defined by the core-collar-boundary, whereas the inner margin is largely defined by the departure of fabric strike from NW-SE to circumferential (stippled line in Fig. 3.3). The outer core zone is generally 10 - 15 km wide but apparently narrows significantly where the mirror plane intersects the core-collar boundary (Fig. 3.3). Interestingly, the zone is crudely symmetric with respect to the NW-SE striking mirror plane.

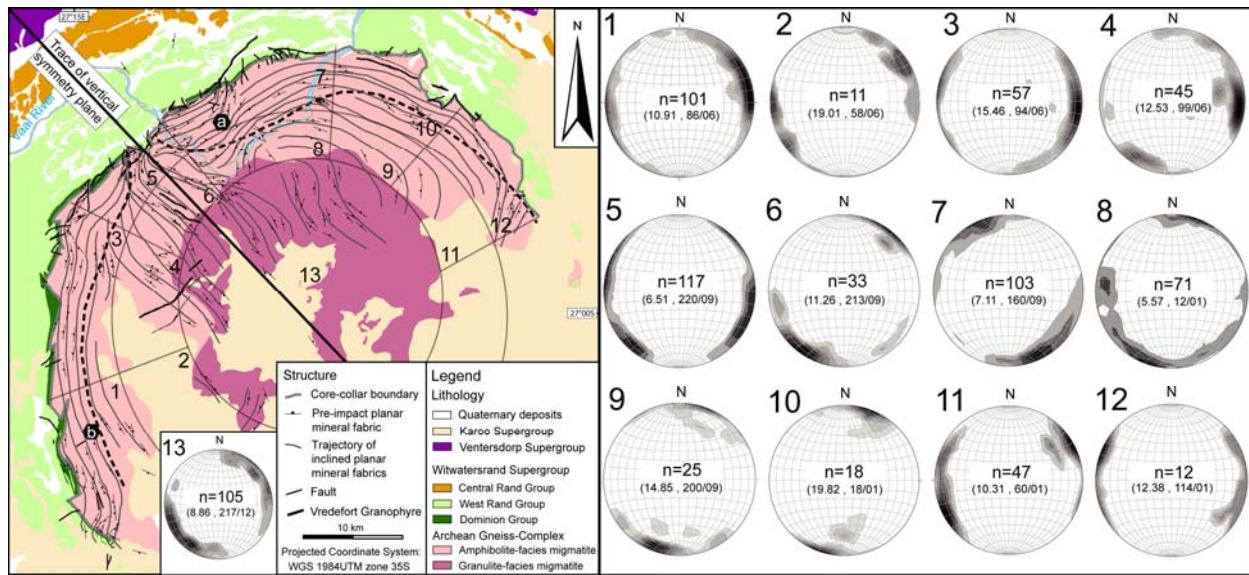


Figure 3.3: Simplified geological map of the Vredefort Dome showing trajectories of inclined planar mineral shape fabrics (migmatitic layering) that formed prior to meteorite impact. The mineral fabric symbols shown are average orientations from a total of 745 stations. The boundary between the inner core and the outer core zone (stippled line) is defined by the change in mineral fabric strike from NW-SE in the inner core to concentric in the outer core zone. Note the symmetry of the boundary and the fabric strike with respect to the trace of a NW-striking mirror plane passing through the centre of the Vredefort Dome. Lower-hemisphere equal-area projections show poles to planar pre-impact fabrics of the respective sectors in the map. Numbers in projections are respectively number of measurements (n), maximum density of measurements in % and the orientation of the maximum in terms of dip direction and dip. Locations a and b refer respectively to the Salvamento and the Esperanza quarries.

4. Brecciation intensity and geometry of pseudotachylite bodies

It is well known that the size of fragment-rich pseudotachylite zones in the Vredefort Dome ranges from mm- to cm-wide veins, dm- to m-scale dikes, to tens of meters wide, irregular or pocket-like bodies (Gibson and Reimold, 2001; Dressler and Reimold, 2004; Reimold and Gibson, 2005). As part of our systematic structural analysis of the Vredefort Dome, we

quantitatively assessed the orientation of pseudotachylite zones, the strain field under which the melts were emplaced and the intensity of fragmentation associated with the formation of the fragment-rich zones. The latter is denoted herein as brecciation intensity and will be described next along with the orientation of pseudotachylite zones.

Brecciation intensity was visually estimated and calibrated with defined breccia properties on the outcrop scale adopting the calibration by Lieger (2005). The calibration is based on visual appraisal of fragment-rich pseudotachylite body exposures in terms of the size range, content, shape and polymict versus monomict character of fragments (Table 3-1). Brecciation intensities were assigned values between “1”, denoting the lowest intensity, and “5”, indicating the highest intensity. This allowed us to quantitatively record for each pseudotachylite exposure the brecciation intensity and to relate it to the orientation of the respective pseudotachylite body (Fig. 3.4). Moreover, the distribution of brecciation intensity and number of pseudotachylite occurrences can be conveniently assessed with respect to radially inward distance from the core-collar boundary (Fig. 3.5; Appendix II).

Brecciation intensity	Intensity 1	Intensity 2	Intensity 3	Intensity 4	Intensity 5
Width of pseudotachylite zone	< 5 cm	5 cm – 1 m	1 m – 5 m	5 m – 10 m	> 10 m
Fragment diameter	< 1 cm	1 cm – 2 cm	< 0.5 m	< 1 m	> 1 m
Amount of fragments	< 5 %	10 - 50 %	50 – 70 %	70 – 80 %	> 80 %
Fragment shape	rounded	mostly rounded	rounded and angular	rounded and angular	rounded and angular
Fragment assemblage	monomict	monomict	monomict	occasionally polymict	occasionally polymict

Table 3-1: Macroscopic characteristics used for estimating brecciation intensity.

Large pseudotachylite bodies correspond to high brecciation intensity and are found chiefly in the outer core zone and sporadically in the collar rocks (Figs. 3.4, 3.5). By contrast, the inner core

hosts pseudotachylite zones with rather low brecciation intensity, whereby the majority of stations are effectively devoid of pseudotachylite occurrences (Figs. 3.4, 3.5). A marked decrease in brecciation intensity and occurrence of pseudotachylite exposure toward the Dome centre occurs at a radial distance between 9 and 15 km from the core-collar boundary (Fig. 3.5). In the outer core zone, maximal concentration of pseudotachylite zones occurs at radially inward distances of about 1 to 4 km and 7 to 9 km from the core-collar boundary (Fig. 3.5).

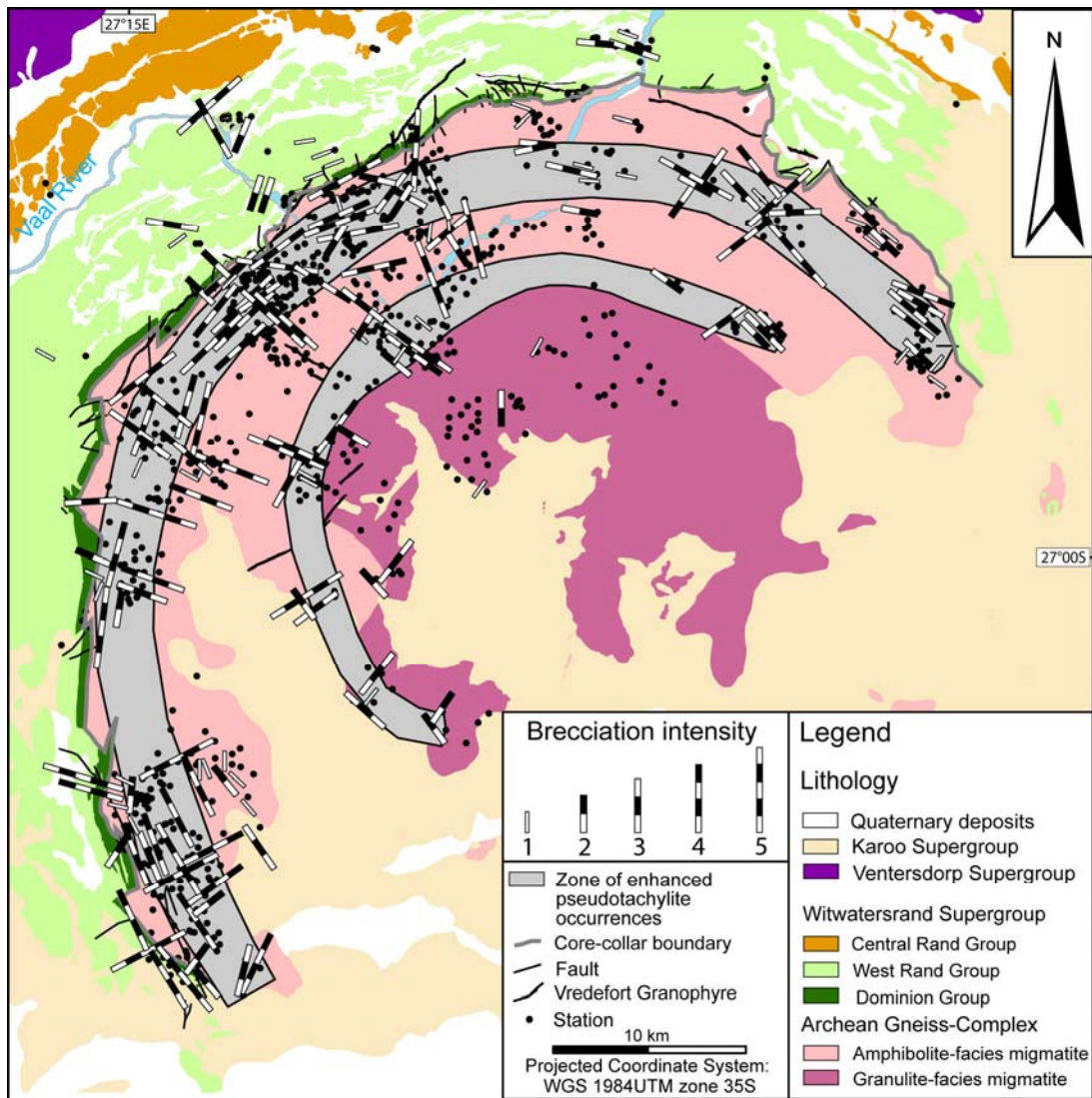


Figure 3.4: Map of the Vredefort Dome showing the distribution of brecciation intensity and trend of fragment-rich pseudotachylite bodies at a total of 531 stations. Note radial and concentric trends of bodies concentrated at radially inward distances of about 1 to 4 km and 7 to 9 km from the core-collar boundary as well as paucity of pseudotachylite occurrences in the inner core zone.

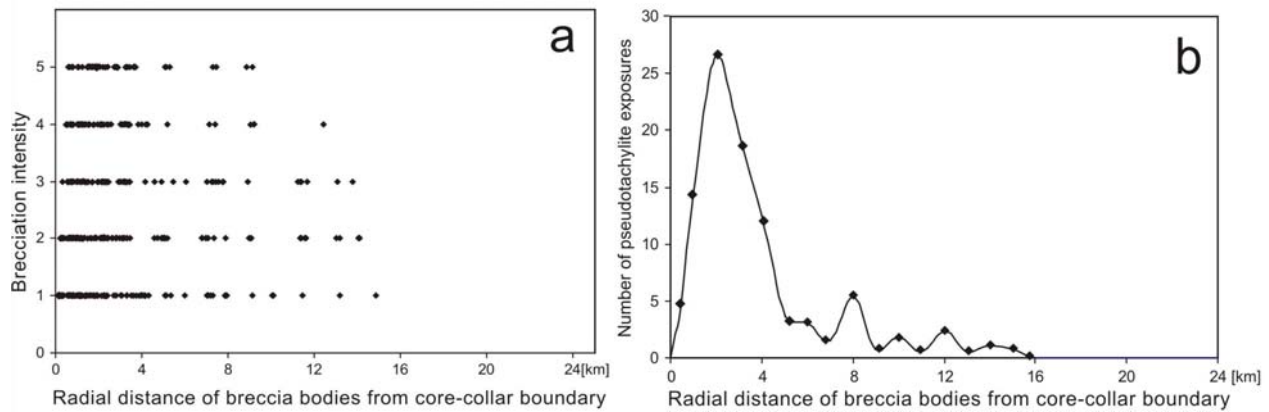


Figure 3.5: Diagrams showing pseudotachylite properties with respect to radially inward distance from the core-collar boundary. (a) Brecciation intensity versus radially inward distance. (b) Number of pseudotachylite exposures versus radially inward distance. Brecciation intensity and number of pseudotachylite exposures are enhanced at distances of 1 to 4 km and 7 to 9 km from the core-collar boundary.

The overall concentric disposition of the zones may be due to enhanced fragmentation in zones of mechanical weakness, such as sedimentary layering in the collar rocks and pre-impact planar mineral fabrics in the outer core zone (cf. Figs. 3.3 and 3.4). However, a significant number of pseudotachylite zones also trend radially, i.e., transverse to the mineral fabric, in the outer core zone (Fig. 3.4). Finally, it is important to note that only a small number of pseudotachylite zones deviates from the radial or concentric trends. This underscores the highly centro-symmetric pattern of pseudotachylite zone orientation in the Vredefort Dome.

5. Kinematics of deformation during formation of pseudotachylite zones

In order to elucidate the possible relationship between the cratering flow field and formation of fragment-rich pseudotachylite bodies, the kinematics of deformation associated with the emplacement of the pseudotachylites on the outcrop scale is discussed next. Dilation in the brittle realm is indicated by the geometry of pseudotachylite zone margins generally allowing one to reconstruct the exact fit of opposite margins prior to dilation (Fig. 3.6a, b). En-echelon pseudotachylitic vein geometry (Fig. 3.6c) underscores their formation as tension gashes, well known from brittle deformation regimes (e.g., Pollard and Segall, 1987). Strike separations indicated by pre-impact structures such as displaced pegmatite dikes (Fig. 3.6d, e) are generally

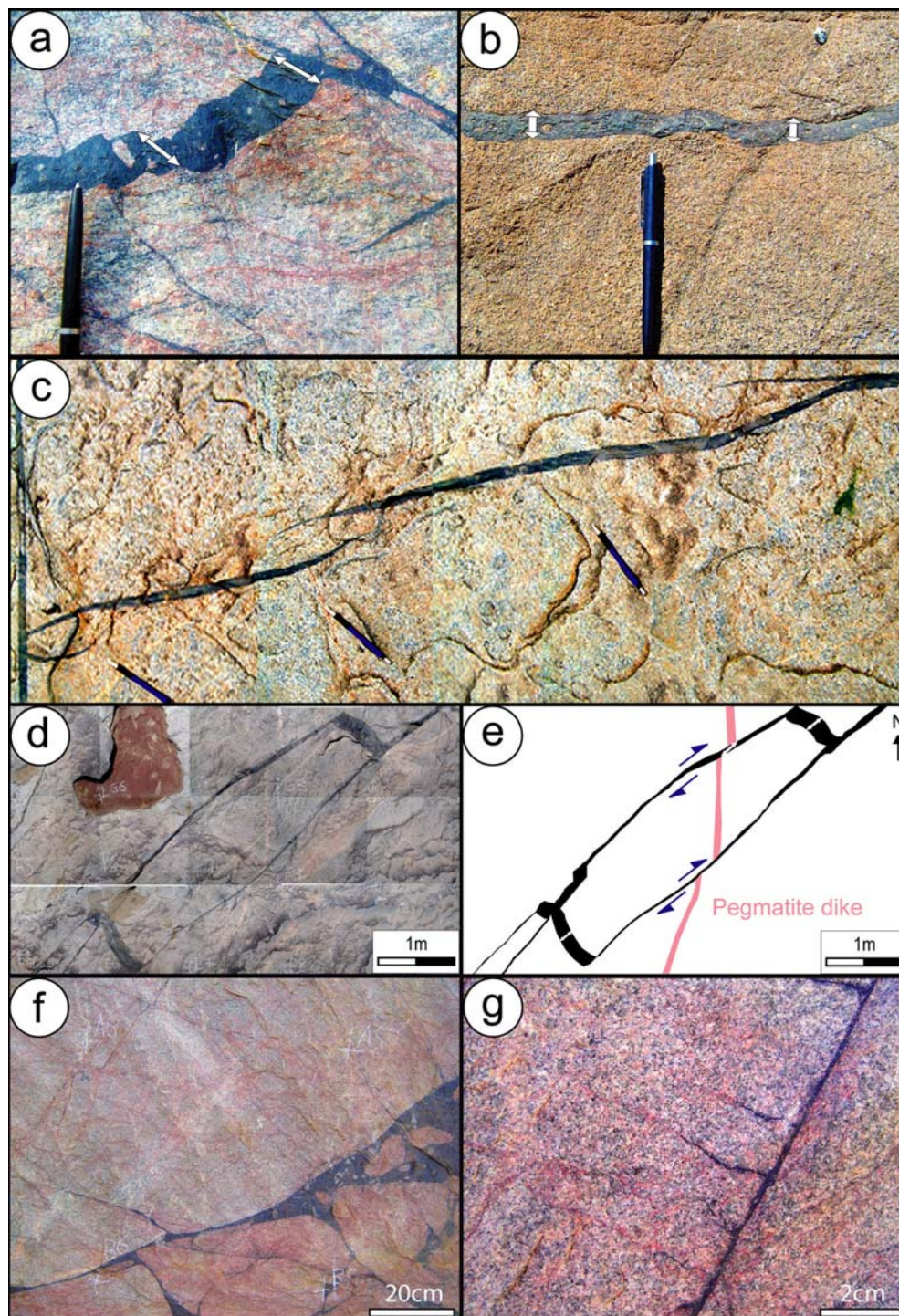


Figure 3.6: Photos of pseudotachylite veins and dikes indicating the dilational strain field during melt emplacement. Arrows indicate component vectors of maximum dilation. (a) and (b) Examples of pseudotachylite veins permitting determination of directions of vein openings based on the pre-impact geometrical fit of opposite margins. (c) Pseudotachylite veins displaying en-echelon geometry. (d) and (e) Example of pseudotachylite veins showing pull-apart geometry. Note apparent sense of displacement of pre-impact pegmatite dike indicated by half arrows. (f) and (g) Pseudotachylite apophyses formed at higher-order fracture zones.

less than a few centimetres and are caused by oblique opening of fractures. Consequently, pseudotachylite zones formed as tension gashes or hybrid shear faults, i.e., faults characterized by wall-orthogonal and wall-parallel displacement. Dilation and preservation of primary asperities of fracture margins exclude in-situ generation of pseudotachylitic melt by frictional sliding on fracture margins.

The pre-impact fit of marker points, such as asperities of, and pegmatite dikes truncated at, opposite margins of pseudotachylite veins and dikes (Fig. 3.6a, b, d, e) permits determination of the horizontal component vector of the maximum dilation direction at a given outcrop surface. Although more variable in orientation, pseudotachylite bodies of lower brecciation intensity were better suited than large bodies for this analysis. Measurement of the horizontal component vectors in the outer core of the Vredefort Dome indicates either radial or concentric stretching of material (Fig. 3.7; Appendix II), regardless of pseudotachylite body orientation. Dilation magnitudes are maximal in the outer core zone close to the core-collar boundary, whereas the inner core is dominated by small dilation magnitudes and concentric stretching of material. The horizontal component vectors of dilation display a remarkably centro-symmetric pattern with respect to the Vredefort Dome. They also support the notion by Dressler (1984) that pseudotachylite zones are effectively fragment- and melt-filled fractures formed by dilation, i.e., overall volume increase of target rock.

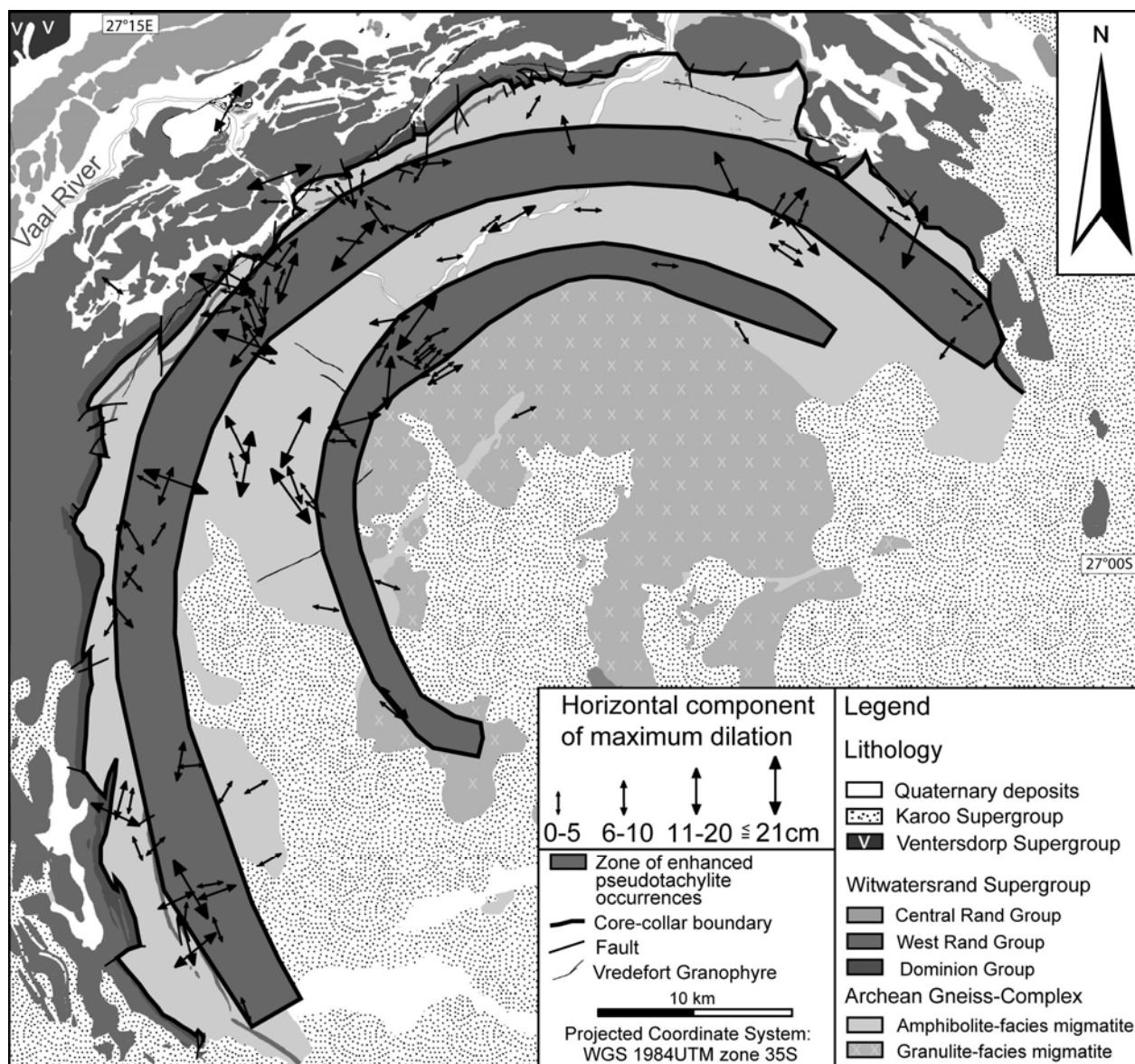


Figure 3.7: Map of the Vredefort Dome showing the distribution and magnitude of component vectors of maximum dilation inferred from the geometry of pseudotachylitic veins and dikes. Note enhanced concentric and radial stretching of rock in the outer core zone. By contrast, the inner core is characterized by minor magnitudes of concentric stretching in its periphery.

6. Shape fabrics of fragments

Knowledge of the processes that led to fragmentation of target rocks under an overall dilational strain regime is critical to understand the generation of fragment-rich pseudotachylite bodies. We address this issue by quantifying fragment properties, notably shape and rotation, at two prominent pseudotachylitic bodies (Fig. 3.8).

The pseudotachylite bodies are bounded by well-defined, curvi-planar boundaries. Numerous pseudotachylite dikes emanate from the main bodies and, in turn, veins and veinlets emanate from the dikes into the host rock. Networks of thin pseudotachylite dikes are also preferentially found at, and linked with, larger pseudotachylite bodies at other locations. Fragments in these bodies are almost exclusively derived from the immediate host rock, generally display jigsaw geometry, vary greatly in size and are angular to well-rounded (Fig. 3.8a, b). Generally, fragments are more angular and elliptical near zone margins and more rounded and circular in the interior of pseudotachylite zones. The traces of pre-impact mineral fabrics on outcrop surfaces suggest that the fragments underwent limited but progressive rotation towards the centre of the pseudotachylite bodies (Fig. 3.8d).

The variation in fragment shape with distance from pseudotachylite zone margins was quantified using the image analysis software Q-Win (Leica). For this purpose, the fragment outlines of the two fragment-rich pseudotachylite zones were digitized from photos and analysed in terms of sectional ellipticity, i.e., departure from circularity. Despite the strong heterogeneity in fragment shape, there is an overall decrease in fragment ellipticity with distance from the zone boundaries (Fig. 3.8e, f).

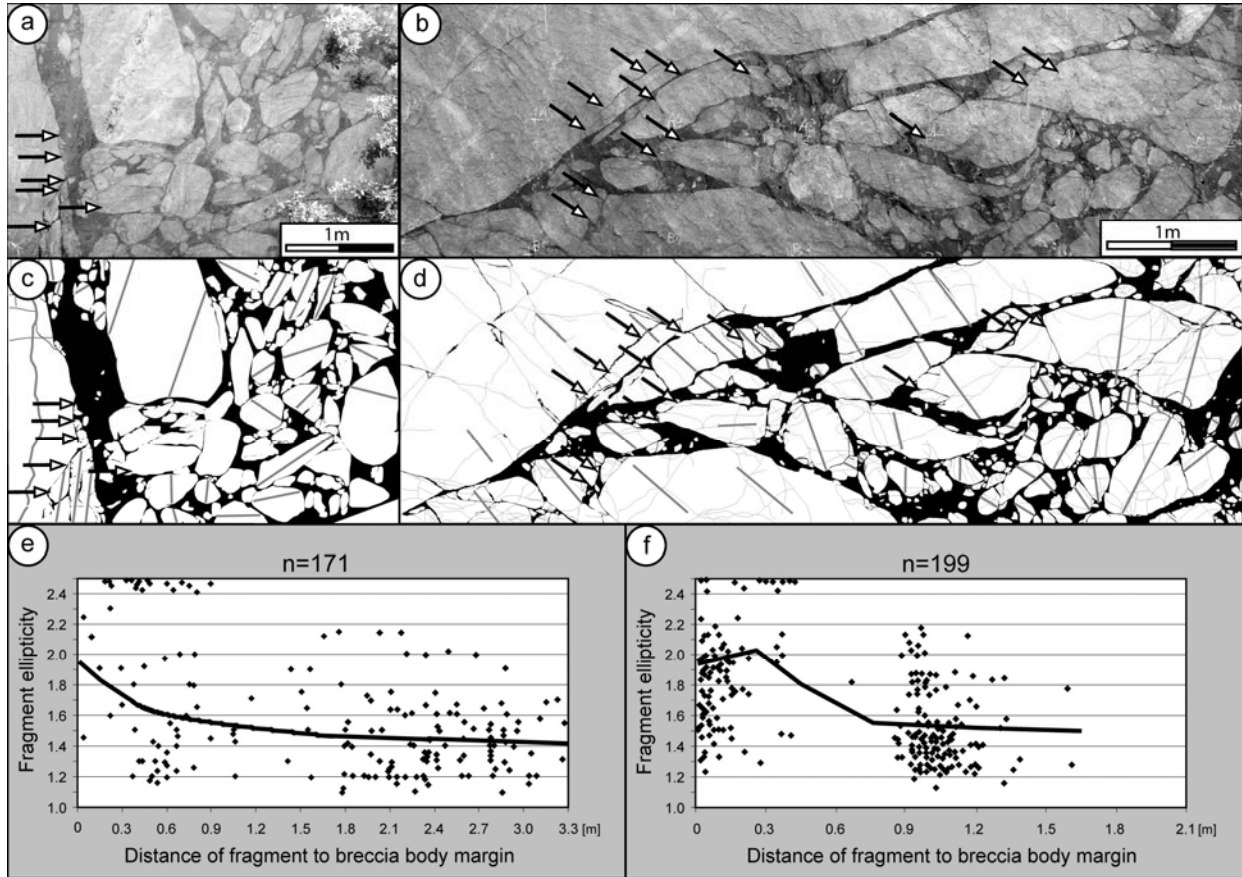


Figure 3.8: Shape fabrics of pseudotachylitic breccia fragments. Arrows point to incipient separation of angular fragments from pseudotachylite zone margins, areas of enhanced fracture density and fragmentation of acute fragment tips. (a) and (b) Photos showing two brecciation intensity 5 pseudotachylite bodies from Salvamento and Esperanza quarries (locations a and b, respectively, in Figure 3.3). (c) and (d) Digitized images of (a) and (b), respectively, used for shape fabric analysis. Grey lines indicate traces of pre-impact planar mineral fabrics in target rock fragments. Note progressive rotation of fragments with increasing distance from breccia body margin in (d). (e) and (f) Diagrams showing sectional ellipticity of fragments (value of 1 represents the unit circle) versus distance of fragments to margins of pseudotachylite zones. Note the decrease in sectional fragment ellipticity with increasing distance from margins. Bold lines approximate the overall variation in fragment ellipticity.

7. Geometric relationship between pseudotachylite properties and cratering strain

Collectively, the well-developed centro-symmetric patterns of pseudotachylitic body trend, brecciation intensity and component vectors of dilation call for a comparison with other evidence for impact-induced rock distortion at Vredefort. Based on hydrocode modelling, Ivanov (2005) predicted the variation in total strain accumulated at the end of cratering in a profile through the centre of the Vredefort impact structure (Fig. 3.9).

At the present erosion level, the hydrocode model shows a central zone, about 25 km in diameter, that underwent vertical stretching, i.e., constrictional strains, and uplift of rock from mid-crustal levels without undergoing rotation (Fig. 3.9). This zone of rock uplift corresponds crudely to the inner core, i.e., sector 13 (Fig. 3.3) that is defined by sub-vertical NW-SE striking mineral fabrics (see also Lana et al., 2003b). The outer core zone, up to 15 km wide at the current erosion level, agrees well with the zone in the model that underwent outward rotation and components of radial stretching, both increasing in magnitude toward the core-collar boundary (Fig. 3.9).

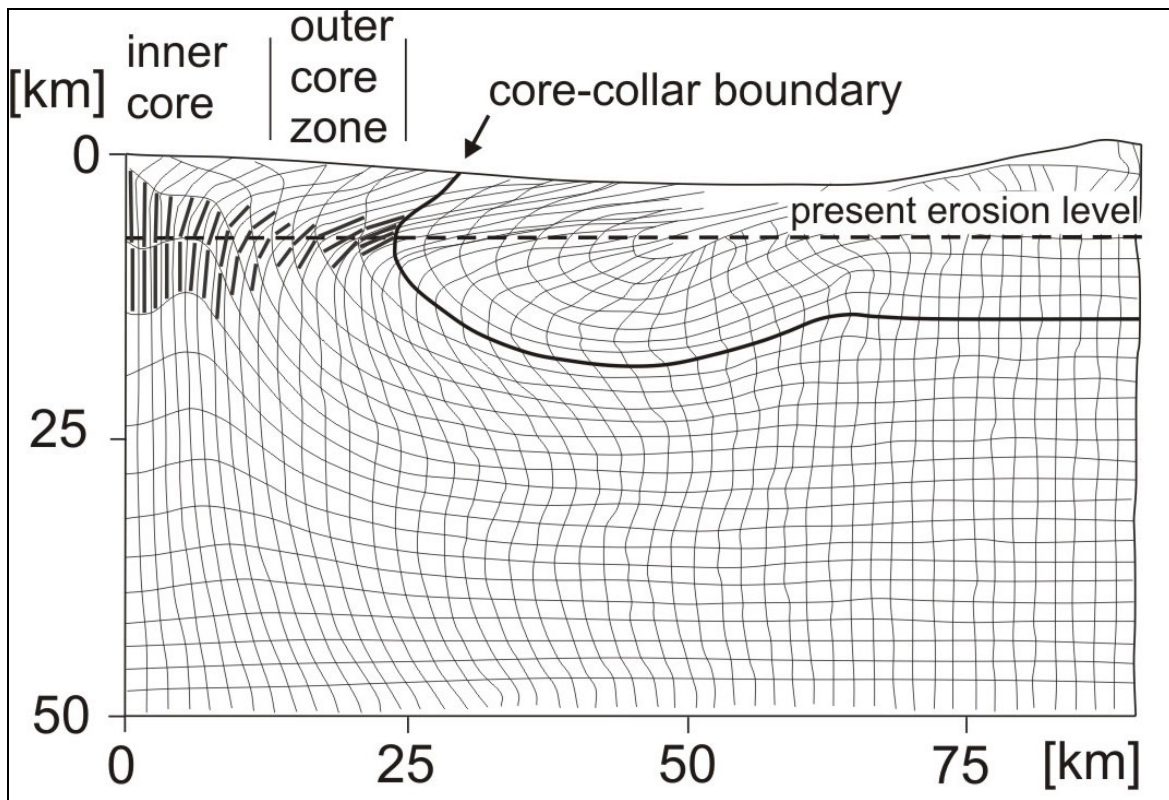


Figure 3.9: Radial profile of the Vredefort Dome depicting the variation in accumulated strain, indicated by distorted rectangles, due to cratering based on hydrocode modelling by Ivanov (2005). Bold lines in the core near present erosion level indicate directions of total stretching. Note vertical stretching in the inner core and subhorizontal stretching directions in the outer core zone. Radial widths of the inner core and the outer core zone are defined for the present erosion level.

The apparent narrowing of the outer core zone, as defined by the pre-impact shape fabrics, toward the symmetry plane (Fig. 3.3) can be explained by the effective lack of geometric reorientation of sub-vertical, NW-SE striking fabrics, by outward rotation in this area. Thus, the

very presence of a fabric pattern symmetric about a NW-SE striking mirror plane underpins the hypothesis that mineral fabrics in the inner core were sub-vertical and oriented NW-SE prior to impact (Lana et al., 2003b). The mirror symmetry of the fabric pattern can be accounted for by central uplift formation and agrees remarkably well with rock distortion predicted by numerical modelling.

The inner core of the Dome, which appears to be devoid of pseudotachylite at the erosion level (Fig. 3.4), matches the area that underwent vertical stretching in the model (Fig. 3.9). The concentration of pseudotachylite zones at distances of 7 to 9 km and 1 to 4 km from the core-collar boundary corresponds, respectively, to the transition from vertical stretching to outward rotation and to maximum radial stretching of material close to the boundary. Interestingly, the zone of maximum radial stretching in the numerical model coincides spatially with the concentric trends of pseudotachylite zones (Fig. 3.4). Orthogonality between local stretching directions and trends of pseudotachylitic bodies points to a causal relationship between the two.

Particles in the outer core zone diverge from each other during outward rotation and associated outward radial rock displacement (Ivanov, 2005). Thus, a component of concentric stretching is expected to be evident in the outer core zone. Considering the orthogonality between stretching directions and trends of pseudotachylitic bodies mentioned beforehand, concentric stretching is indeed indicated by radial pseudotachylite zones in the outer core (Fig. 3.4). This suggests that the formation of pseudotachylite zones is kinematically linked to total strain accumulated during central uplift formation, i.e., the zones form as tensile fractures trending orthogonal to maximum principal stretching directions.

Evidence for vertical stretching of material is not readily apparent on horizontal outcrop surfaces. It is, therefore, not surprising that recorded component vectors of dilation in the inner core of the Vredefort Dome are rather small in magnitude and concentric in geometry (Fig. 3.7). The apparent orthogonality between stretching directions and the orientation of pseudotachylite zones predicts the latter to be developed as horizontal sheets in the inner core. Divergent, sub-horizontal particle flow increases in the outer core zone, at the erosion level, toward the core-collar boundary (Ivanov, 2005). Therefore, component vectors of maximum dilation are significantly larger and disposed radially and concentrically in the outer core zone (Fig. 3.7). The pattern of

these vectors corroborates the close kinematic relationship between formation of fragment-rich pseudotachylite bodies and the development of the central uplift.

8. Emplacement of pseudotachylitic melt

The geometry of breccia body margins (Fig. 3.6) and jigsaw pattern of fragments (Fig. 3.8a - d) point to fragmentation of target rock in the brittle realm. However, the variation in angularity, sectional ellipticity and progressive rotation of fragments can be accounted for best by the thermal and mechanical effects of melt on fragments. Melt in the interior of breccia bodies would have remained hotter for a longer time than at the margins. Thus, the capacity to thermally corrode fragments, i.e., decrease the ellipticity of fragments, is expected to be higher in the interior of breccia bodies. Further evidence for thermal corrosion is seen by the somewhat increased fracture density and incipient fragmentation at acute tips of elongate fragments (Fig. 3.8b, d). Similarly, the temperature difference between melt and host rock likely induced thermal stresses in the host rocks that evidently led to separation of highly angular fragments from breccia zone margins (arrows in Fig. 3.8a - d). Such incipient fragmentation is particularly evident in the outer core zone, as the temperature difference between melt and target rocks is higher there than in the inner core, where deeper and, thus, hotter rocks were uplifted during transient crater collapse (Figs. 3.1c, d, 3.9; Gibson, 2002; Ivanov, 2005).

Progressive rotation of fragments towards the centre of pseudotachylite bodies is typical for rigid bodies embedded in a mobile viscous matrix, such as melt. Although we do not consider all fragments to result from thermal corrosion, their shape fabric characteristics are similar to fragments of intrusion breccias known from endogenic melt systems (Clarke et al., 1998). The pre-impact configuration of fragments in the pseudotachylite zones and the overall paucity of exotic fragments indicate that the vast majority of fragments in the largest zones were not transported distances larger than tens of meters, if at all. However, this may not apply for the pseudotachylitic matrix, i.e., former melt. Collectively, (1) overall dilation during fracturing, (2) incipient fragmentation, (3) jigsaw geometry of fragments, (4) en-echelon vein geometry, (5) evidence for thermal corrosion of fragments and (6) apparent lack of bona fide shear faults point to an allochthonous origin of the melt.

The close geometric relationship between pseudotachylite properties and total strain predicted from numerical modelling suggests that pseudotachylitic melt was emplaced during uplift of the inner core and outward rotation of the outer core zone. This points to melt emplacement during the final stages of cratering, more specifically, during collapse of the central uplift (Fig. 3.1c). Ample evidence for tensile fracturing during melt emplacement can be explained by discontinuous deformation accomplishing differential rotation along with radial and concentric stretching of outer core rocks as a consequence of large-scale bending of rocks.

Brittle deformation caused by localization of bending strains accounts for in situ brecciation of target rock in concentric and radial tensile fracture zones. Opening of the fracture zones created likely low-pressure voids, into which melt was drawn forcefully. This process explains the presence of pseudotachylite in minute tensile fracture systems of highly irregular geometry commonly found in the vicinity of larger breccia bodies. This requires melt transport from larger pseudotachylite bodies into smaller ones and is corroborated by the presence of pseudotachylite apophyses formed at higher-order fracture zones (Fig. 3.6f, g).

9. Possible origin of pseudotachylitic melt

The structural evidence for pseudotachylite matrix representing allochthonous melt raises the question about the location of its primary origin. Pseudotachylitic melt may have been drained from melt pools formed locally by shock amplification or stress relief within target rocks (Martini, 1991; Gibson et al., 2002; Gibson and Reimold, 2005; Reimold and Gibson, 2006), the pools of which remain to be identified. Alternatively, most of the pseudotachylitic matrix may represent melt from the overlying impact melt sheet that was driven into tensile fracture zones by pressure gradients and gravity during the final stages of cratering (Stöffler, 1977; Pohl et al., 1977; Stöffler et al., 1979). This is consistent with the modelled distribution of impact melt in the crater floor (Ivanov, 2005).

Elucidating the origin of pseudotachylite has also been attempted by geochemical studies. At Sudbury, such studies indicate that the composition of the pseudotachylite matrix cannot be accounted for by melting of the immediate host rock or its fragments alone (Speers, 1957; Dressler, 1984; Rousell et al., 2003; Lafrance et al., 2008). Although geochemical similarity

between matrix and immediate host rock has been reported for Vredefort (Schwarzman et al., 1983; Reimold, 1991; Killick, 1994; Reimold and Gibson, 2006), some systematic differences between the two have been noted. Specifically, the matrix of pseudotachylite bodies within granitic host rock is depleted in SiO_2 and enriched in Ca and Fe with respect to the host rock. By contrast, SiO_2 in the pseudotachylite matrix of bodies within mafic host rock is enriched, whereas Ca and Fe is depleted (Schwarzman et al., 1983; Reimold et al., 1985a, b; Reimold, 1991).

Collectively, geochemical data are in conflict with an in situ melt origin due to selective melting of hydrous ferromagnesian minerals of the host rock by frictional heating (Reimold, 1991; Spray, 1992) or shock melting (Dressler and Reimold, 2004). However, the data are consistent with an allochthonous origin of melt, especially when injection of impact melt into uplifted target rocks is invoked. In this scenario, assimilation of host rock by superheated impact melt may well have rendered the chemical composition of pseudotachylite matrix at the margins of pseudotachylite bodies toward that of the immediate host rock (Reimold and Gibson, 2006). Small differences in melt composition with regard to the host rock may also be due to mobilisation of pools of shock melt sourced in rocks of slightly different bulk compositions. Thus, geochemical data are inconclusive with regard to differentiating between shock melt generated and relocated within target rock and emplacement of impact melt into target rock. This may be resolved by analysing the pseudotachylite matrix for a geochemical signature from the projectile.

Traces of a meteoritic component at Vredefort were identified in the so-called Granophyre Dikes (Fig. 3.3) indicating an impact melt origin of the Dikes (Koeberl et al., 1996). A meteoritic component has not been reported from the pseudotachylitic matrix. This may be due to an origin of the matrix as shock melt formed within target rock or strong dispersion of projectile material in impact melt during cratering, which prevented the accumulation of detectable quantities of such material in pseudotachylitic melt.

Granophyre Dikes are unstrained but transect the interfaces of overturned strata in the collar of the Vredefort Dome (Fig. 3.3). Consequently, the Dikes were emplaced after the stage of crater modification (Fig. 3.1d) and are, therefore, younger than pseudotachylite bodies (Bisschoff, 1988, 1996). The Granophyre Dikes share many petrographic characteristics, notably the concentration of target rock fragments in dike centres, with the so-called Offset Dikes at Sudbury (Grant and Bite, 1984) and, thus, may have formed by the same emplacement mechanism as

Offset Dikes. Correlation of melt temperature estimates of Offset Dikes with modelled cooling rates of the impact melt sheet at Sudbury suggests that Offset Dikes were emplaced up to ten thousand years after impact (Hecht et al., 2008). Chemical differentiation of the impact melt sheets at Sudbury and Vredefort prior to dike emplacement led to accumulation of siderophile elements at the base of the sheets, from which Granophyre and Offset Dikes were derived. Melt sheet differentiation accounts also for the remarkable chemical homogeneity of the Granophyre Dikes (French et al., 1989; French and Nielsen, 1990; Therriault et al., 1997). Accordingly, chemical differentiation can account for the sporadic presence of a meteoritic component in Granophyre Dikes but their apparent absence in the pseudotachylite matrix at Vredefort. We consider injection of superheated impact-melt into target rock as a viable hypothesis for the origin of large volumes of pseudotachylitic melt.

10. Conclusions

A systematic analysis of the geometry of pre-impact mineral fabrics and structural properties of fragment-rich pseudotachylite zones was conducted in the Vredefort Dome to elucidate the formation of these zones as observed in large terrestrial impact structures. Pre-impact planar mineral fabrics display mirror symmetry with respect to a NW-trending plane passing through the Dome centre. The fabric symmetry is consistent with vertical stretching and uplift of the inner core and outward rotation and dilation in the outer core zone as is predicted for rocks at the current erosion level by numerical modelling of the impact event. More specifically, the well-developed centro-symmetric patterns of distribution, geometry and brecciation intensity of pseudotachylite bodies correspond geometrically to the variation in total strain predicted by numerical modelling. Collectively, these characteristics agree with an allochthonous origin of the melt that was emplaced into tensional fracture systems in the crater floor at an advanced stage of cratering, i.e., during collapse of the central uplift.

Analysis of fragment shapes in breccia bodies suggests that fragmentation occurred as a consequence of localization of strains that accomplished bending of the outer core zone and by thermal stresses induced on target rocks by allochthonous melt. Fracture zones that opened served as low pressure zones, into which melt was likely drawn forcefully during cratering.

Pseudotachylitic melt in fragment-rich dilation zones may have been drained from pools within nearby target rocks or from the overlying impact melt sheet. Our analysis failed to identify the presence of bona fide shear faults on any scale that could potentially have generated in situ frictional melts and fragments. Rather, fragmentation of target rock and melt generation to form pseudotachylitic breccia bodies are processes that are separated in time and space during cratering.

Acknowledgements

This work was funded by the German Science Foundation (grant Ri 916 / 8-1). We thank the staff of the World Heritage Office at Vredefort for logistical support. The manuscript benefitted from discussions with Barry Clarke, Richard Grieve, Uwe Reimold and Dieter Stöffler. Reviews by Jay Melosh, Fred Hörz and one anonymous reviewer for the journal are greatly appreciated.

CHAPTER 4:
PETROGRAPHIC AND GEOCHEMICAL EVIDENCE FOR AN ALLOCHTHONOUS ORIGIN
FOR PSEUDOTACHYLITE MELTS WITH A POSSIBLE INFLUENCE OF THE IMPACT
MELT SHEET IN THE VREDEFORT DOME, SOUTH AFRICA

Daniel Lieger¹, Ulrich Riller² and Roger L. Gibson³

¹ Museum für Naturkunde, Humboldt-Universität zu Berlin, Invalidenstraße 43, 10115 Berlin, Germany

² McMaster University, School of Geography and Earth Sciences, 1280 Main Street West, Hamilton, Ontario, Canada, L8S 4K1

³ Impact Cratering Research Group, School of Geosciences, University of the Witwatersrand, Private Bag 3, P.O. Wits 2050, Johannesburg, South Africa

Accepted in *Geochimica et Cosmochimica Acta* (GCA7223)

<http://dx.doi.org/10.1016/j.gca.2011.05.017>

Abstract

Hypotheses proposed to explain the origin of pseudotachylite bodies formed during impact cratering include either: (1) frictional heating, (2) shock loading, (3) decompression or (4) drainage of impact melt into target rocks. In order to differentiate these processes, we conducted detailed geochemical and petrographic analysis of the matrices in pseudotachylitic veins and dikes and of their respective wall rocks. Our analyses indicate that locally the chemical compositions of matrices deviate significantly from their immediate wall rocks and that assimilation of wall rock substantially modified the pseudotachylite matrix compositions. Variable magnitudes of assimilation can be explained by the surface area of wall rock (fragments) in contact with melt, as well as the initial temperature and cooling rate of the pseudotachylitic melt. Chemical trends observed can be explained either by admixture of an exotic melt component with respective wall rock or by mixing of melts derived from local lithologies. In our view, trends in the compositional deviation of centimetre to metre-wide pseudotachylite dikes from their respective wall rocks are consistent with presence of a primary

melt component having a felsic composition akin to the average Granophyre composition or, possibly, a product of differentiation of an original massive impact melt body. Within veins, melt transport can be geochemically and petrographically traced for distances of centimetres to metres, with the direction of melt transport from larger pseudotachylite veins toward smaller ones and into apophyses. Sulphide and silicate mineralogy indicates that the initial temperature of pseudotachylitic melt must have been at least 1200-1700 °C. Collectively, these characteristics point to an allochthonous origin of pseudotachylitic melt. This allows for the possibility that impact melt from a superheated melt pool contributes to larger occurrences of pseudotachylite. We advocate that pseudotachylite dike formation by injection of melt from the overlying impact melt sheet into target rocks during or after central uplift formation of the Vredefort impact structure is a viable possibility.

Key words: Vredefort impact structure, XRF, SEM, electron microprobe, pseudotachylite, melt transport, assimilation.

1. Introduction

Extreme pressures and temperatures, and violent rock movements during impact crater formation all have the potential to generate melt of pseudotachylite bodies. Target rocks of, e.g., the Vredefort, Sudbury, Araguinha and Slate islands impact structures are characterized by pervasive presence of fragment-rich pseudotachylite bodies (Reimold, 1991; Dressler and Sharpton, 1997; Spray et al., 2004; Machado et al., 2009). These bodies form geometrically complex systems of veins, dikes and pods that in the case of Sudbury can be hundreds of meters wide. In Sudbury, the term ‘Sudbury Breccia’ has been used to describe a variety of breccia types that may have different origins (e.g. Dressler, 1984; Müller-Mohr, 1992). These melt breccias are generally characterized by rounded wall rock fragments set in a dark, aphanitic to microcrystalline matrix (Shand, 1916; Rousell et al., 2003; Dressler and Reimold, 2004). The term “pseudotachylite” was coined first by Shand (1916) who described the widespread occurrences of this lithology in the Vredefort Dome of South Africa.

The origin of pseudotachylite bodies and, more specifically, of their matrices, which are generally believed to have formed from a melt, is a matter of scientific controversy. Nowhere is this controversy more obvious than in the two largest exhumed impact structures in the world – Vredefort and Sudbury. Mechanisms referred to account for the formation of pseudotachylite melt include shock loading (Bisschoff, 1962; Martini, 1978, 1991; Schwarzman et al., 1983; Gibson et al., 2002; Dressler and Reimold, 2004; Gibson and Reimold, 2005), frictional heating on fault surfaces (Dence et al., 1977; Lambert 1981; Reimold, 1991; Spray and Thomson, 1995; Spray, 2000; Melosh, 2005), a combination between the two (Kenkmann et al., 2000; Dressler et al., 2001; Langenhorst et al., 2002), and injection of impact melt into crater floor fractures (Stöffler, 1977; Pohl et al., 1977; Lieger et al., 2009; Riller et al., 2010). The recent IUGS recommended definition of impact pseudotachylite as “Dyke-like breccias formed by frictional melting in the basement of impact craters” (Fettes and Desmons, 2007, p. 162; see also Stöffler and Grieve, 2007) and associated genetic implications remain controversial (e.g., Reimold et al., 2008).

Differentiating individual hypotheses on geochemical grounds is complicated by the fact that, except for injection of impact melt, these hypotheses have called for an origin of pseudotachylite melt locally within target rock. This is essentially based on compositional similarity between pseudotachylite matrix and adjacent wall rock, unless melt relocation within target rock is invoked (Dressler and Reimold, 2004; Gibson and Reimold, 2005; Melosh, 2005). Indeed, many geochemical studies report that compositions of pseudotachylite matrix and adjacent wall rock are largely similar, although distinct differences between the two have been noted as well (e.g., Speers, 1957; Dressler, 1984; Reimold, 1991; Rousell et al., 2003). Compositional similarity between matrix and wall rock as seen in whole-rock analyses may, however, be of limited significance if the matrix contains a high content of fine wall rock fragments. More refined analytical methods are required to unravel the origin of matrices.

Here we present results of combined X-ray fluorescence spectrometric (XRF), electron microprobe (EMP), and scanning electron microprobe (SEM) analyses of pairs of pseudotachylite matrices from both centimetre to decimetre thick veins and several-metre-wide pseudotachylite bodies and their respective wall rocks from the Vredefort Dome (Fig. 4.1). Thereby, we seek to elucidate to what extent the chemical variation in matrix composition could have been influenced

by wall rock assimilation and melt transport. We discuss the possibility that an allochthonous melt component was involved in the formation of pseudotachylite bodies.

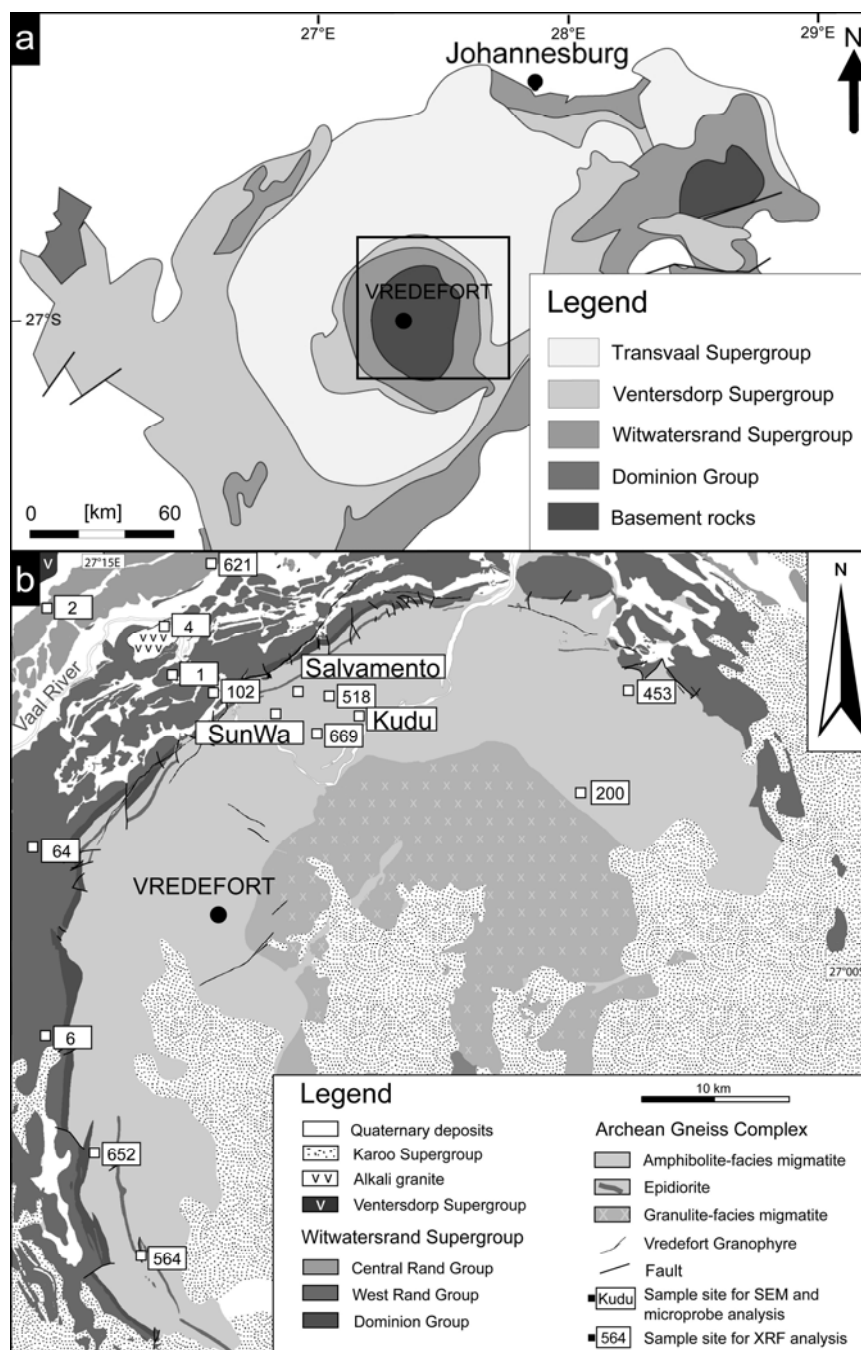


Figure 4.1: Geological setting of the Vredefort region. (a) Simplified geological map of the Witwatersrand Basin. Rectangle denotes area in (b). (b) Geological map of the Vredefort Dome showing sample sites of this study (Lieber et al., 2009).

2. Geological Setting

The 2023 ± 4 Ma Vredefort impact structure (Kamo et al., 1996), originally encompassing the region occupied to date by the Witwatersrand Basin (Fig. 4.1a), is the oldest known impact structure on Earth and, with an estimated diameter of up to 250 km, also the largest (Henkel and Reimold, 1998; Grieve and Therriault, 2000; Turtle et al., 2005). The impact structure has been eroded to a depth between 7 and 10 km (Gibson et al., 1998) and, thus, offers an unprecedented view of target rock configuration below a large terrestrial impact structure. The central portion of the impact structure, the so-called Vredefort Dome (Fig. 4.1b), is the eroded relic of structurally uplifted rocks, generally referred to as the central uplift (Melosh, 1989). The Vredefort Dome consists of a core, ca. 40 km in diameter, of a 3.1-3.2 Ga tonalite-trondhjemite-granodiorite and greenstone assemblage (Lana et al., 2004). The core is surrounded by a 15-20 km wide ‘collar’ of subvertical to overturned, 3.07 to 2.1 Ga supracrustal strata (Armstrong et al., 1991) that were deposited unconformably on the Archean crystalline basement rocks.

The core of the Vredefort Dome consists of migmatitic gneisses intruded by synmetamorphic granitoid bodies that range from granulite-facies grade in the centre of the core to upper amphibolite-facies grade towards the collar (Lana et al., 2004). The collar rocks are made up of lavas of the Dominion Group which are covered, successively, by quartzite, conglomerate, siltstone and shale of the Witwatersrand Supergroup, lavas of the Ventersdorp Supergroup, and dolomite, quartzite and shale of the Transvaal Supergroup (Fig. 4.1b). Pre-impact regional metamorphism in the collar rocks decreases from mid-amphibolite facies in the Dominion Group to greenschist facies in the upper Witwatersrand Supergroup (Gibson and Wallmach, 1995). Post-impact temperatures on rocks of the Vredefort Dome range from ≥ 1000 °C in the centre of the Vredefort Dome to about 300 °C in the collar rocks at a distance of about 25 km from the centre (Gibson et al., 1998; Gibson, 2002; Ivanov, 2005).

3. Previous geochemical work

Some geochemical studies report pseudotachylite matrices to be similar in chemical composition to that of their immediate wall rock, in particular where pseudotachylite is hosted by granitoid rocks (Schwarzman et al., 1983; Killick, 1994; Reimold and Gibson, 2006). For example, Dressler and Reimold (2004) analysed a millimetre-wide vein and found that the glassy matrix mirrors the stoichiometric composition of its immediate wall rock minerals, notably biotite, quartz and feldspar. The compositional variation, accompanied by abrupt colour changes of pseudotachylite matrix, at the contact between two different host rocks, was attributed to *in situ* wall rock melting by shock loading (Dressler and Reimold, 2004).

However, systematic compositional differences have also been reported between the matrices and immediate wall rocks of pseudotachylites (Reimold, 1991). For example, the matrices of pseudotachylite bodies within felsic Archean granitoid wall rock of the Vredefort Dome are depleted in SiO₂ but enriched in Fe₂O₃, MgO, Al₂O₃, Na₂O, CaO and K₂O (Schwarzman et al., 1983; Reimold et al., 1985a,b; Reimold, 1991; Reimold and Gibson, 2006). By contrast, the matrix of pseudotachylite within mafic wall rock is enriched in SiO₂ but depleted in MgO and CaO (Reimold, 1991; Reimold and Gibson, 2006). The same systematic compositional differences between matrix and granitoid as well as mafic wall rock compositions has been documented for pseudotachylite matrix-wall rock pairs from the Sudbury impact structure, Canada (Speers, 1957; Rousell et al., 2003; Al Barazi et al., 2009; Riller et al., 2010).

Adhering to an *in situ* origin of pseudotachylite melt nonetheless, a number of processes have been invoked to account for the observed compositional differences between matrix and immediate wall rock. For example, wall rock may have melted selectively, caused either by dissimilar fracturing behaviour of different mineral phases (Schwarzman et al., 1983) or by preferred melting of hydrous ferromagnesian minerals (Reimold, 1991) akin to the process promoted for the formation of tectonic friction melt suggested for tectonic pseudotachylite formation (Spray, 1992) and for breccia occurrences in the Sudbury Impact Structure (Reimold, 1991; Spray, 1992). Other causes invoked include local wall rock heterogeneity (Killick et al., 1988), faulting, fault zone metasomatism and mineral comminution prior to melting (Spray, 1992), assimilation of fragments and crystals into pseudotachylitic melt (Maddock, 1986), as well

as sub-solidus and post-quenching alteration. In summary, geochemical analyses of pseudotachylite matrices have been interpreted mostly in terms of *in situ* wall rock melting without contribution of an exotic melt component.

In addition, Reimold (1991) considered the para-autochthonous to allochthonous origin of some melt occurrences in the Dome as a possible cause of compositional differences; for instance, many xenoliths of amphibolite in a large, granite-hosted pseudotachylite occurrence at Otavi (northeast of the Vredefort Dome), can be explained by transport of melt and entrained clasts over a distance of at least 50 m. In contrast, Lieger et al. (2009) recently suggested that admixture of an exotic (i.e., not immediate wall rock) melt component could have been an essential part of the formation of pseudotachylite at Vredefort. In fact, in our view major element concentrations in the pseudotachylite matrix point to mixing of local parent rock material with an exotic melt. This process is further investigated in this study.

4. Analytical methods

Pseudotachylite matrix and respective wall rocks were examined petrographically using an Olympus stereomicroscope and a LEITZ DM RXP polarization microscope. A total of 62 thin sections from samples of many locations (Fig. 4.1b) and covering a wide range of wall rock types (Table 4-1) and associated pseudotachylite matrices were inspected. Major and trace elements of eleven pseudotachylite matrix-wall rock sample pairs and ten additional samples of pseudotachylite matrices were analysed using X-ray fluorescence spectrometry (XRF) at the University of the Witwatersrand, Johannesburg (geographic coordinates of samples are provided in the Table 4-2). For whole rock analyses, samples of between 0.2 and 1 kg mass were used. Accuracies for the analysed major elements are: SiO₂ [0.5]; Al₂O₃ [0.1]; Fe₂O₃ [0.05], MgO [0.05], CaO [0.05], Na₂O [0.05] and K₂O [0.05]; TiO₂ [0.01], MnO [0.01] and P₂O₅ [0.01] (all in wt.%), and for trace elements: Ba [30]; Cu [25]; Zn [25]; Rb [5], Sr [5], Y [5], Zr [5], Nb [5], Co [5], Ni [5], V [5] and Cr [5] (all in ppm). In Tables 4-2 and 4-3, as well as in Fig. 4.1, detail about sampling locations and sample character (size of occurrence of pseudotachylite, host rock type, clast populations) is provided, and in Table 4-1 the XRF results are presented. In addition,

selected analyses of pseudotachylites covering a range of wall rock types, from the literature, are compiled in Table 4-1 for comparison.

SEM analysis was carried out at the Museum für Naturkunde on a JEOL JSM-6300 instrument equipped with a tungsten cathode, operated at 8-30 kV and using an energy-dispersive X-ray spectrometer (EDX). Pseudotachylite matrix analyses were conducted in EDX mode at count times of 1000 s, beam operating conditions of 15 kV and 1 nA, and a working distance of 39 mm. Backscattered electron (BSE) imagery was used to investigate the microtexture and mineralogy of pseudotachylite matrices. Except for a reduced working distance (11 mm), the settings for generating BSE images were the same as mentioned above. The data were processed using the AXS software Quantax 400 by Bruker Company.

Four samples from the Kudu quarry and one sample from the SunWa location (Fig. 4.1b) were investigated with a Jeol JXA-8500F electron microprobe at 15 kV and 15 nA, also at the Museum für Naturkunde Berlin. Analyses were calibrated using Smithsonian and Astimex international mineral standards. The calibrated elements and respective average detection limits [in ppm] are: Si [230], Na [79], Fe [205], K [31], Ti [124], Al [158], Mg [66], Ca [38], Mn [97], P [125] and S [75]. Counting times were 30 s on peak and 15 s on background, with a beam diameter of 35 μm . Energy-dispersive (EDX) and wavelength-dispersive spectrometry (WDX) were used to determine the mineralogy of wall rock and adjacent pseudotachylite matrices.

Table 4-1: Whole rock analyses of pseudotachylite matrices (Pt) and their wall rocks (WR). Also shown are analyses by Bisschoff (1972, 1973); McIver et al., (1981); Reimold, (1991); Schwarzman et al., (1983); Tankard et al., (1982) and Wilshire, (1971).

Lithology	Granitoid	Granitoid	Granitoid	Granitoid	Granitoid	Granitoid	Granitoid	Granitoid	Granitoid	Granitoid	Granitoid	Granitoid	Granitoid
WR/Pt pair	WR	Pt	WR	Pt	WR	Pt	Pt	Pt	WR	Pt	Pt	WR	Pt
Sample number	669A3	669A2	200C2	200C1	453A2	453A1	652A1	652A2	KuduA3	KuduA2	KuduA1	518A2	518A1
Major elements in [%]													
SiO ₂	72.10	72.95	73.25	71.56	73.12	65.73	73.62	73.74	72.99	51.41	52.07	67.13	55.64
TiO ₂	0.32	0.21	0.02	0.25	0.24	0.52	0.25	0.23	0.16	2.20	1.92	0.51	1.89
Al ₂ O ₃	13.89	14.08	15.55	14.98	14.47	15.26	13.06	14.33	13.97	9.90	11.52	14.46	14.46
Fe ₂ O ₃	2.33	1.81	0.30	2.18	1.40	5.05	1.82	1.81	1.49	13.98	12.94	5.77	11.25
MnO	0.02	0.03	0.01	0.02	0.03	0.08	0.02	0.02	0.02	0.19	0.20	0.07	0.14
MgO	0.34	0.38	0.01	0.35	0.24	2.09	0.07	0.08	0.28	6.24	6.44	1.18	2.98
CaO	1.16	1.41	1.13	1.51	1.07	2.55	0.45	0.71	1.35	7.74	8.06	2.21	4.55
Na ₂ O	2.52	4.68	5.02	5.03	5.25	4.10	3.03	4.15	8.23	4.64	4.41	5.03	5.94
K ₂ O	5.69	4.16	5.15	3.96	3.28	3.17	5.01	4.62	0.80	0.46	2.02	1.95	1.74
P ₂ O ₅	0.09	0.08	0.01	0.07	0.08	0.29	0.11	0.06	0.02	0.44	0.42	0.24	0.47
LoI.	0.75	0.67	0.39	0.56	0.96	0.81	0.95	0.86	0.99	1.23	0.88	1.88	0.68
Total	99.21	100.46	100.83	100.47	100.14	99.65	98.39	100.61	100.30	98.43	100.88	100.43	99.74
Trace elements in [ppm]													
Rb	155	119	101	90	113	197			23	11	41	61	32
Sr	280	275	390	366	240	260			664	253	476	627	653
Y	12	19	5	12	15	38			4	15	15	29	21
Zr	314	168	100	232	184	187			185	94	128	306	224
Nb	6	7	<3	4	6	12			<3	21	20	9	18
Co	<6	6	<6	6	<6	18			7	49	45	10	32
Ni	11	12	10	12	9	26			11	87	88	42	37
Cu	13	14	<6	8	<6	77			24	313	301	47	126
Zn	38	40	6	34	35	113			23	130	118	90	129
TiO ₂ [%]	0.30	0.22	0.01	0.25	0.24	0.54			0.16	2.06	1.81	0.54	1.87
V	25	16	<12	22	18	76			<12	286	257	47	225
Cr	144	142	138	149	104	165			186	182	192	1626	107
Ba	1492	902	1189	981	616	495			675	174	584	1205	881

Table 4-1 continued.

Quartzite/Conglomerate	Quartzite/Conglomerate	Quartzite	Quartzite	Quartzite	Quartzite	Quartzite	Quartzite	Quartzite	Quartzite	Quartzite	Quartzite
WR	Pt	WR	Pt	Pt	Pt	Pt	WR	Pt	Pt	WR	Pt
6A4	6A1	621A3	621A2	621A1	2A2	2B2	64A3	64A2	64A1	102A2	102A1
96.92	94.94	91.55	80.46	81.45	81.19	79.78	94.81	91.59	89.96	95.85	93.73
0.03	0.21	0.08	0.38	0.38	0.32	0.45	0.12	0.16	0.18	0.19	0.21
1.06	2.58	4.96	11.12	11.24	10.39	12.06	2.40	3.78	4.21	1.98	4.40
0.38	1.46	1.34	1.53	1.33	2.57	1.23	0.55	1.56	1.80	2.78	0.79
0.00	0.01	0.00	0.01	0.01	0.01	0.01	0.01	0.01	0.05	0.01	0.01
0.05	0.01	0.01	0.24	0.25	0.27	0.17	0.00	0.05	0.79	0.01	0.12
0.04	0.00	0.00	0.00	0.03	0.00	0.00	0.08	0.00	0.35	0.00	0.00
0.02	0.00	0.03	0.10	0.12	0.08	0.73	0.02	0.06	0.00	0.02	0.02
0.28	0.24	1.21	3.16	3.01	2.48	2.80	0.64	0.88	0.98	0.50	1.04
0.01	0.01	0.02	0.02	0.03	0.01	0.02	0.01	0.03	0.06	0.01	0.02
1.72	1.11	1.11	2.46	3.02	2.51	2.09	0.39	1.02	0.71	0.02	0.72
100.51	100.56	100.30	99.48	100.87	99.83	99.34	99.03	99.14	99.09	101.37	101.06
7		40	107	108	87		20		31	17	30
9		28	30	31	41		15		32	14	25
5		6	20	22	15		7		19	15	14
35		47	300	305	138		70		661	568	206
<3		<3	3	4	3		<3		5	4	3
<6		<6	7	7	8		<6		24	6	<6
13		18	20	18	23		12		104	36	25
9		13	30	34	30		11		84	29	23
<6		6	14	15	12		<6		53	7	19
0.02		0.09	0.40	0.40	0.35		0.14		0.20	0.22	0.24
<12		21	50	52	48		24		19	30	21
309		342	468	478	382		559		1069	2282	422
88		330	751	724	696		200		243	137	221

Table 4-1 continued.

Quartzite	Quartzite	Quartzite	Alkali Granite	Alkali Granite	Epidiorite	Epidiorite	Granitoid	Diorite	Diorite
Pt	Pt	Pt	WR	Pt	WR	Pt	Pt	WR	Pt
1A1	1A2	1A3	4A2	4A1	564A2	564A1	Schwarzman et al. 1983	Bischoff 1972	Schwarzman et al. 1983
73.56	73.47	72.64	70.01	67.32	51.18	54.12	65.00	54.80	58.70
0.53	0.56	0.57	0.25	0.29	0.30	0.35	0.73	1.60	0.98
12.86	13.12	14.24	14.89	15.35	14.65	13.78	17.50	15.70	13.80
3.72	3.74	3.57	2.65	6.30	7.55	7.28	8.60	8.50	8.16
0.04	0.04	0.03	0.07	0.08	0.12	0.13	0.05	0.16	0.11
1.41	1.38	1.29	0.20	0.72	9.28	8.59	1.20	2.70	4.20
0.75	0.65	0.08	0.69	0.60	13.41	12.00	4.00	5.80	4.10
1.86	1.85	0.00	7.82	7.86	1.37	2.08	5.20	5.70	6.70
2.32	2.43	2.47	2.94	2.51	0.08	0.55	1.30	1.50	1.40
0.01	0.01	0.01	0.06	0.08	0.02	0.04			
1.45	1.34	4.96	0.61	0.33	1.08	0.79			
98.51	98.59	99.86	100.19	101.44	99.04	99.71	99.00	98.00	99.60
76	76		56	79	7	26			
164	167		225	272	99	112			
19	21		12	17	13	15			
336	345		297	381	38	53			
7	8		18	31	3	4			
26	23		6	9	40	35			
115	118		7	33	217	175			
79	82		6	12	63	75			
66	67		55	58	58	62			
0.58	0.60		0.22	0.32	0.28	0.30			
72	78		12	31	137	120			
656	546		137	171	985	854			
609	612		772	819	61	179			

Table 4-1 continued.

Gabbro	Gabbro	Gabbro	Gabbro	Norite	Norite	Alkali Granite	Alkali Granite
WR	Pt	Pt	Pt	WR	Pt	WR	Pt
Reimold 1991	Reimold 1991	Schwarzman et al. 1983	Schwarzman et al. 1983	Reimold 1991	Reimold 1991	Bischoff 1973	Schwarzman et al. 1983
50.70	54.50	57.60	59.30	51.80	56.70	73.57	65.60
1.80	1.40	0.36	0.33	0.40	0.40	0.15	0.36
13.50	13.30	11.30	12.10	15.70	15.10	13.58	15.60
14.30	12.00	8.12	8.13	8.60	7.90	8.40	8.14
0.20	0.20	0.16	0.14	0.10	0.10	0.05	0.10
6.00	6.10	11.60	9.40	9.30	7.30	0.13	0.59
9.30	7.70	7.80	6.60	12.70	10.10	0.49	1.00
2.20	2.60	1.60	1.70	1.40		5.85	8.90
1.00	1.50	0.53	0.56	0.10	0.60	3.98	1.70
0.30	0.30			0.10	0.10		
				1.10	0.90		
101.10	100.00	100.40	98.10	101.30	99.30	99.57	100.10
69	73			3	24.5		
46	43			43	37		
124	119			247	189		
338	331			138	85		
270	286			111	148		

Table 4-1 continued.

Alkali Granite	Epidiorite	Epidiorite	Epidiorite	mafic rock	mafic rock	mafic rock
Pt	Pt	Pt	Pt	WR	WR	WR
Schwarzman et al. 1983	Wilshire 1971	Schwarzman et al. 1983	Schwarzman et al. 1983	Mclver et al. 1981	Mclver et al. 1981	Tankard et al. 1982
66.10	52.80	52.50	52.40	43.56	49.02	54.92
0.33	0.43	0.44	0.45	1.00	1.04	1.22
15.80	14.50	15.50	15.40	8.56	8.44	14.72
8.15	8.30	8.80	8.90	1.27	1.06	12.70
0.10	0.15	0.15	0.15	0.21	0.18	0.19
0.62	8.50	8.10	8.10	17.58	14.42	4.93
0.87	12.10	12.50	12.50	8.50	7.91	6.88
8.20	1.70	2.20	2.20	0.04	0.83	3.51
2.60	0.14	0.19	0.18	0.21	0.18	0.68
					0.21	0.27
100.30	98.60	100.60	100.30	99.28	99.72	100.02
					1	12
				33	90	311
				16	15	22
				84	88	174
				5	4	4
				1241	804	
				98	88	
				103	56	
				200	196	
				1982	1867	
				67	129	

Table 4-2: Latitude-longitude coordinates of our locations (projected coordinate system: WGS 1984 UTM zone 35S).

Sample number	Latitude	Longitude
Salvamento	7025728S	539856E
SunWa	7024323S	538561E
669A3/669A2	7024782S	540549E
200C2/200C1	7021056S	554467E
453A2/453A1	7025761S	555679E
652A1/652A2	7001566S	529253E
KuduA3/KuduA2/KuduA1	7024638S	543059E
518A2/518A1	7025073S	541214E
6A4/6A1	7007108S	525760E
621A3/621A2/621A1	7039155S	545097E
2A2/2B2	7027088S	525010E
64A3/64A2/64A1	7019625S	526939E
102A2/102A1	7027453S	538096E
1A1/1A2/1A3	7028451S	534564E
4A2/4A1	7029744S	533538E
564A2/564A1	6996833S	531784E

Table 4-3: Some macroscopic characteristics of wall rocks.

Lithology	Granitoid	Granitoid	Granitoid	Granitoid	Granitoid	Quartzite/ Conglomerate
Sample number	669A3	200C2	518A2	453A2	KuduA3	6A4
Wall rock	Granodioritic quartz-feldspar-biotite-hornblende gneiss with dioritic and amphibolitic xenoliths	Granodioritic quartz-feldspar-biotite-hornblende gneiss	Granodioritic quartz-feldspar-biotite-hornblende gneiss with dioritic and amphibolitic xenoliths	Granodioritic quartz-feldspar-biotite-hornblende gneiss and quartz veins	Granodioritic quartz-feldspar-biotite-hornblende gneiss and 50 cm wide amphibolite dike	Coarse grained Quartzite with crome muscovite
Width of pseudotachylite dike in metre	10 - 12	1 - 2	11	1 - 2	1 - 2	0.1

Lithology	Alkali Granite	Quartzite	Quartzite	Quartzite	Epidiorite
Sample number	4A2	621A3	64A3	102A2	564A2
Wall rock	Alkali granite and quartz alkali syenite	Red-brown fine grained argillaceous quartzite	Fine grained quartzite with chrome muscovite	Fine grained quartzite with chrome muscovite	15 meters wide dike within the granitic rocks
Width of pseudotachylite dike in metre	5	0.1	0.5	0.25	1

5. Results

5.1. Field characteristics and petrography of pseudotachylite

To characterize the compositional relationship between pseudotachylite matrix and wall rock, respective sample pairs were chosen from a large variety of wall rock types, including felsic and mafic igneous as well as metasedimentary rocks, covering many of the lithologies occurring over much of the exposed portion of the Vredefort Dome (Fig. 4.1b). Detailed petrographic and geochemical analyses were conducted on matrices of veins and their wall rocks from the SunWa and Kudu locations and of samples from metre-scale bodies from Salvamento quarry (Fig. 4.1b). At SunWa, pseudotachylite veins and dikes are up to 40 centimetres wide, cut across granitoid gneiss, migmatite, amphibolite and pegmatite, and were locally emplaced into extension fractures (Fig. 4.2a, c). This is apparent by the geometry of their margins and displaced Archean pegmatite dikes (Fig. 4.2c, see also Lieger et al., 2009; Riller et al., 2010). Some pseudotachylite veins at this location show domainal zoning seen by the variation in matrix colour and variable content of rounded mafic and felsic wall rock fragments (Fig. 4.2c, d).

Pseudotachylite dikes at Salvamento are up to 7 metres wide, subvertical, and contain wall rock fragments that are millimetres to metres in diameter (Fig. 4.2e, f). Smaller dikes and apophyses emanating from master dikes are a common characteristic at Salvamento (Fig. 4.2e). Fragments are rounded or angular and are predominantly derived from immediate granitoid wall rock (Fig. 4.2e, f). The sampled pseudotachylite dike at Kudu is between 20 and 40 cm wide and occurs along the contact of granitoid and amphibolite wall rock (Fig. 4.2g). Offshoots of this dike cut both wall rock types (Fig. 4.2g, h).

The margins of pseudotachylite veins are characterized by a microcrystalline matrix, locally displaying an intersertal texture defined by biotite, muscovite and feldspar (Fig. 4.3a - d). The matrix of the central portion of pseudotachylite veins can be aphanitic (Fig. 4.3e). Besides quartz, the matrix is generally composed of alkali feldspar, plagioclase, pyroxene, amphibole, Ti-augite, biotite, muscovite and opaque minerals. The latter are observed mostly in the vicinity of feldspar and quartz fragments (Fig. 4.3d). In places, biotite and muscovite are replaced by chlorite and sericite.

Flow banding of the pseudotachylite matrix is evident by mingling of differently coloured matrix phases and by the shape-preferred alignment of matrix minerals and fragments (Fig. 4.3b, f). The size of fragments, consisting mostly of quartz and feldspar, varies greatly. Quartz fragments are generally well-rounded and display resorbed margins (Fig. 4.3b, f, g). Moreover, quartz grains show straight grain boundaries; subgrain boundaries display 120° dihedral angles (Fig. 4.3b, f, h). These microstructural characteristics point to static recrystallisation of quartz. Feldspar fragments are mostly angular and considerably smaller than quartz in the same area.

Some centimetre-wide pseudotachylite veins in granitoid wall rock commonly show two texturally and mineralogically distinct domains, i.e., domain A and domain B (Fig. 4.3d, e, g, h). Domains A are located either at vein margins or in the centre of veins where they are associated with abundant quartz and feldspar fragments (Fig. 4.3d, e). Matrices of domains A are generally coarser-grained and more felsic than those of domains B and consist mainly of biotite, muscovite, feldspar, quartz, and millimetre-wide, cubic-shaped opaque mineral grains (Fig. 4.3d, e). Domains B are mostly mafic, indicated by more pyroxene and amphibole in the matrix, and contain comparatively fewer wall rock fragments set in an aphanitic matrix containing sub-millimetre-size opaque minerals. A few samples, however, show an inverse zoning with regard to felsic domains A and more mafic domains B, whereby domains B are found at the vein margin (Fig. 4.3g, h). Petrographic study of pseudotachylite veins indicates that the matrix consists of two phases that differ significantly in terms of fragment content and mineralogical composition. These domains are separated by a sharp contact and do not show any evidence for intrusive relationships (Fig. 4.3d, e and Fig. 4.9b).

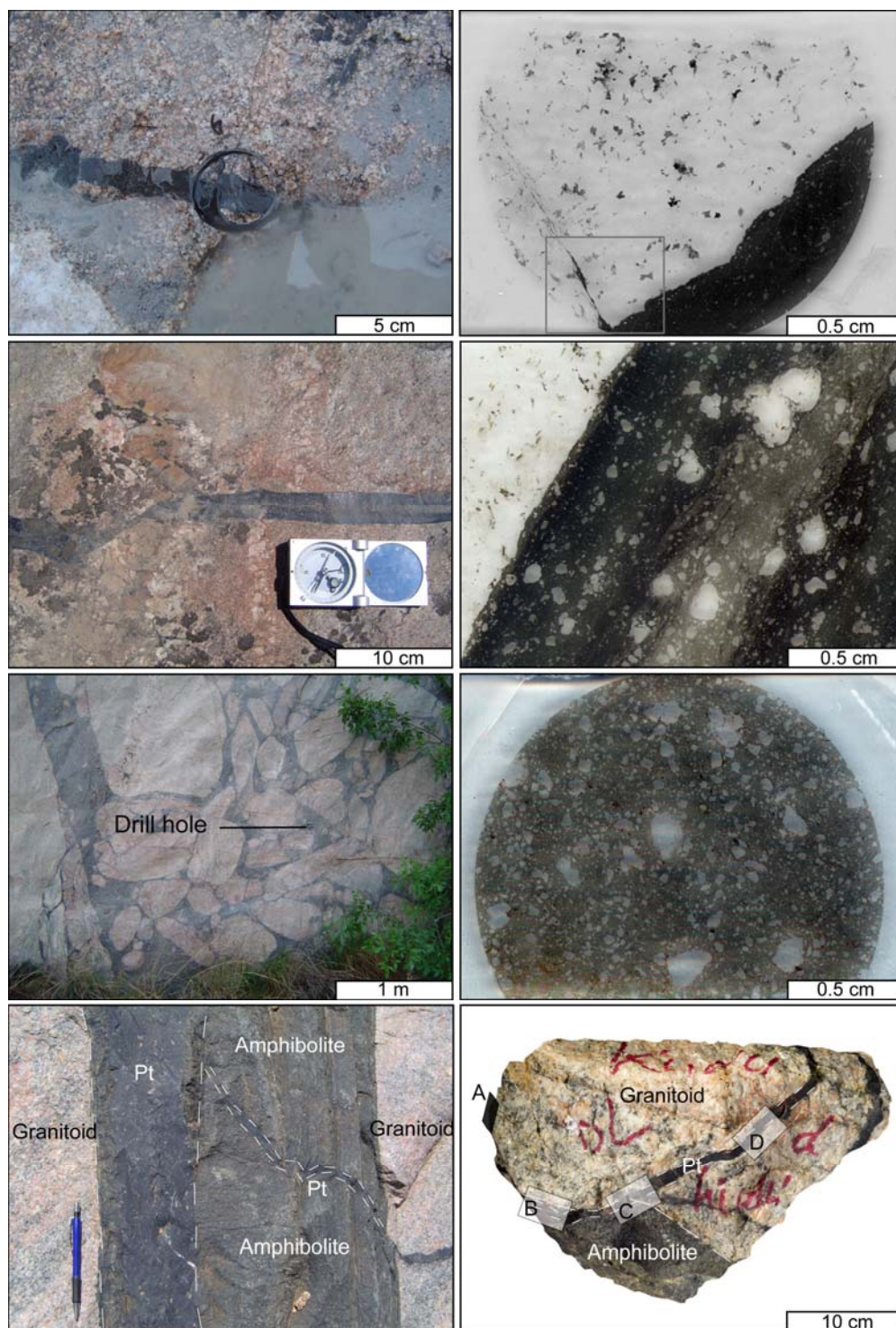


Figure 4.2: Outcrop and thin section images of pseudotachylite and wall rock from the SunWa, Salvamento and Kudu locations.

(a) Photo showing the drill site of the SunWa 6 sample, a pseudotachylite vein cutting granitoid wall rock. (b) Thin section image of SunWa 6 sample. Note apophysis of the pseudotachylite vein.

(c) Photo showing a pseudotachylite vein cutting a pegmatite dike within granitoid wall rock at SunWa 13. Arrows illustrate displacement of vein margins indicating that the vein formed from an extension fracture. (d) Thin section image of a sample from SunWa 13.

The pseudotachylite matrix shows distinct domains, evident by the variation in matrix colour, that are parallel to the vein margin. Surface area of wall rock fragments is higher in bright than in dark domains. (e) Photo showing the sample site in a fragment-rich pseudotachylite dike at Salvamento. (f) Thin section image of the sample

taken from Salvamento shown in (e). The matrix is replete with wall rock fragments and resembles bright matrix domains of the SunWa 13 vein displayed in (d). (g) Photo showing the sample site at Kudu. Pseudotachylite (Pt) is seen as a dike bordering on granitoid and amphibolite wall rock, and as a vein emanating from the dike and transecting both wall rock types. Pseudotachylite is demarcated by stippled line (length of pen is 15 cm). (h) Hand specimen from Kudu showing pseudotachylite vein cutting granite and amphibolite wall rock. Areas A - D denote the locations of thin sections used for electron microprobe analyses.

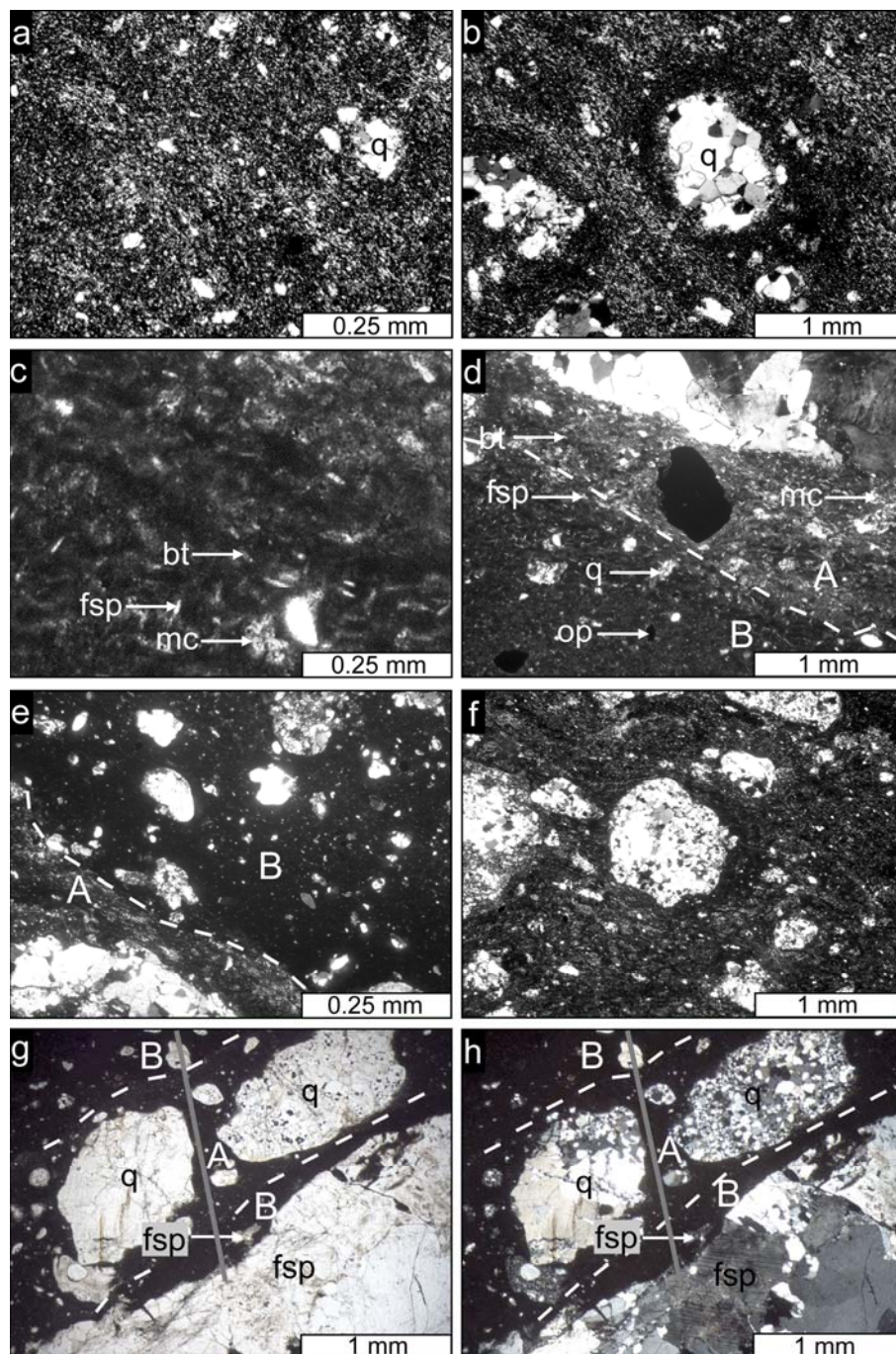


Figure 4.3: Thin section photomicrographs showing pseudotachylite matrices of selected samples. Except (g), all photomicrographs are taken under cross-polarized light. q: quartz, bt: biotite, fsp: feldspar, mc: mica, op: opaque mineral, A: domain A, B: domain B. (a) Pseudotachylite matrix from Salvamento displaying microcrystalline matrix with interstitial plagioclase enveloping minute quartz fragments. (b) Flow-banded pseudotachylite matrix from Salvamento enveloping quartz fragments showing resorbed margins. Note straight subgrain boundaries displaying 120° dihedral angles in large polycrystalline quartz fragment. (c) Pseudotachylite matrix from sample SunWa 13 showing interstitial biotite, feldspar and muscovite. (d) Pseudotachylite matrix from sample SunWa 13 displaying texturally and mineralogically different domains A and B. For explanation of domains see text. (e) Pseudotachylite matrix from sample SunWa 13 showing the locations of domain A at the margin and domain B in the centre of the vein. Note resorbed margins of fragments. (f) Flow-banded matrix enveloping polycrystalline quartz fragment characterized by resorbed margins and straight subgrain boundaries from

sample SunWa 13. (g) Thin section micrograph of matrix from sample SunWa 9 (plane-polarized light). Aphanitic matrix is found at vein margin, whereas a microcrystalline matrix is associated with quartz fragments. Plagioclase fragment at the vein margin is broken off from the immediate wall rock. However, quartz fragments within microcrystalline matrix seem to be exotic. Grey line denotes profile, along which 155 spots were analysed with the electron microprobe (see Figure 4.9). (h) Same field of view as (g) but taken under cross-polarized light.

5.2. Whole-Rock Analysis

A total of 32 samples, i.e., 11 pseudotachylite matrix - wall rock pairs and 10 individual matrix samples, from a variety of wall rock types were analysed for whole-rock chemical composition (Fig. 4.1, Table 4-1). In addition, we compiled major and trace element contents of published chemical data of pseudotachylite matrix and wall rock, as well as chemical compositions of the Vredefort Granophyre (Fig. 4.4, Table 4-1). As observed by other workers (Schwarzman et al., 1983; Reimold et al., 1985a, b; Reimold, 1991; Reimold and Gibson, 2006), MgO, CaO, Fe₂O₃, V, Zr and Cr are frequently depleted, whereas SiO₂, K₂O, Rb, Sr and Ba are correspondingly enriched, in pseudotachylite matrix hosted in mafic wall rock. A first-order general observation is that the SiO₂ content in pseudotachylite matrices may be up to 7 wt.% higher, and CaO, MgO, MnO, TiO₂ and Fe₂O₃ contents up to about 3 wt.% lower, in matrices than in respective mafic wall rock (Fig. 4.4a, b).

In felsic wall rock, notably granitoid rocks of the core but also quartzite and coarse-grained quartz conglomerate of the West Rand and Central Rand Groups of the collar, pseudotachylites are enriched in MgO, CaO, Fe₂O₃, Rb, Sr, and Cr, but depleted in SiO₂, V and Zr with sometimes considerable differences (Fig. 4.4). Note that in Table 4-1 and Figure 4.4 there are some cases where more pseudotachylite analyses are presented than analyses of corresponding wall rock. This was done to be sure that the chemical composition of pseudotachylite matrices is not controlled by fragments. In some cases, chemical compositions of wall rock types without corresponding pseudotachylite values are presented, whereby these data serve to introduce the chemical variability of various wall rock types.

In the matrices of felsic pseudotachylite, SiO₂ contents can be 5-11 wt.% lower, but K₂O, CaO, MgO and Fe₂O₃ contents 1-5 wt.% higher, than in the corresponding felsic wall rock. Some pseudotachylite matrices in quartzite of the West and Central Rand Groups and in granitoid wall rock of the Kudu location show the strongest depletion in SiO₂, up to 20 wt.%, of all rock types (Fig. 4.4a). Thereby, Kudu quarry is characterized by the occurrence of granitoid and amphibolite wall rocks in the immediate vicinity of the analysed pseudotachylite. Pseudotachylite in quartzitic collar rocks is characterized by significantly increased alumina values which suggest that in these cases a metapelite component occurring close to the host quartzite may be involved (Table 4-1

and 3). Granitoid wall rocks are similar in Fe_2O_3 content to corresponding pseudotachylite matrices, whereas alkali granite is somewhat lower in Fe_2O_3 than related pseudotachylite matrix (Table 4-1).

Geochemical analyses of the contents of pseudotachylitic veins and dikes and their respective wall rocks from the Vredefort Dome indicate more or less compositional difference between pseudotachylite matrix and immediate wall rock. Major elements of pseudotachylite matrices generally plot in our diagram closer to the average Vredefort Granophyre composition than the major elements of the corresponding wall rocks (Fig. 4.4a). In fact, there are conspicuous trends in the compositional deviation of pseudotachylite matrices from their respective wall rocks towards a granitoid composition. The chemical composition of relatively wider pseudotachylite veins in quartzite (sample 64A3) and in granitoid wall rock, in such cases where no mafic host strata are involved (as at Kudu), deviate hardly from the compositions of the immediate wall rock (Table 4-1, 4-3). However, small pseudotachylite veins in granitoid wall rock (e.g. at SunWa) and in quartzite (e.g. 621A3) may show different chemical compositions. Sometimes they have texturally and, as demonstrated for some granitoid occurrences, compositionally different domains (Table 4-1; Fig. 4.4a).

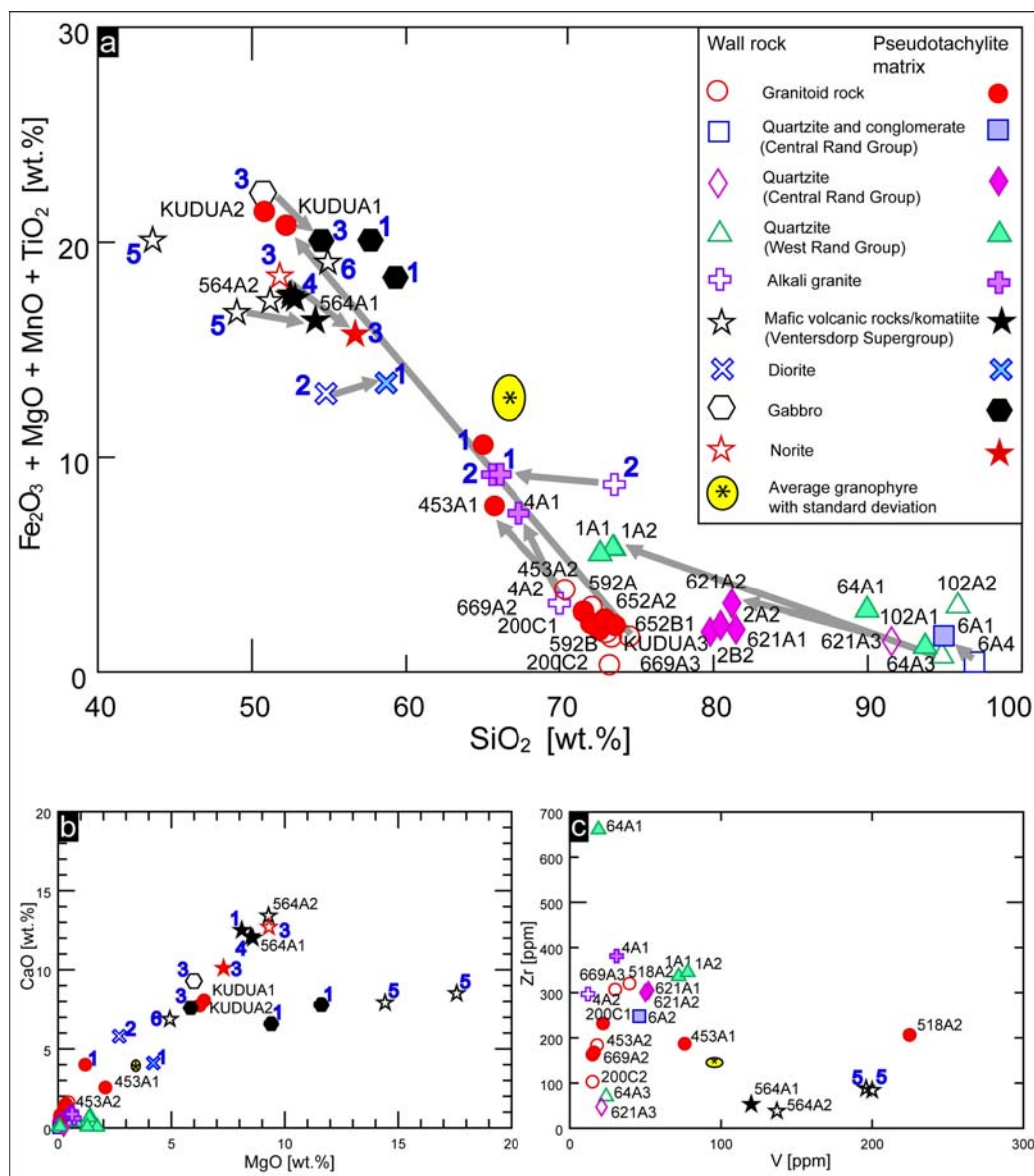


Figure 4.4: Diagrams showing selected major and trace element contents of pseudotachylite matrices and their respective wall rocks obtained by XRF analyses. Published XRF data are from Schwarzman et al. (1983) – 1, Bisschoff (1972), Bisschoff (1973) – 2, Reimold (1991) – 3, Wilshire (1971) – 4, McIver et al. (1981) – 5, and Tankard et al. (1982) – 6. Also shown is the average chemical composition of Vredefort Granophyre with standard deviation (ellipse) compiled from Hall and Molengraff (1925), Willemse (1937), Wilshire (1971), Reimold et al. (1990a), Koeberl et al. (1996) and Therriault et al. (1997). (a) Diagram showing the distribution of ferromagnesian oxides versus SiO_2 . There are conspicuous trends (grey arrows) in the compositional deviation of pseudotachylite matrices from their respective wall rocks towards a granitoid composition that is close to that of the average Vredefort Granophyre. Note also that the Vredefort Granophyre composition is intermediate between that of all wall rock types and respective pseudotachylite matrices. The strong deviation in matrix composition of samples KUDUA1 and KUDUA2 towards mafic compositions is due to contamination of melt by amphibolite (see Figures 4.2h, 10). (b) Diagram showing the distribution of MgO versus CaO . (c) Diagram showing the distribution of Zr versus V . Note the strong excursion of Zr in matrix with respect to wall rock in one West Rand quartzite pseudotachylite

5.3. SEM Analysis

SEM analysis of pseudotachylite matrices was conducted to find out whether matrix minerals are the same as those identified in wall rock or wall-rock clasts. This may aid in identifying the cause(s) of the compositional similarity between pseudotachylite matrix and wall rocks noted in some studies (see references above) and possible melt transport suggested by the major and trace element analysis. In order to examine these processes for different pseudotachylite matrix volumes occurring in the same wall rock type, matrix-wall rock pairs of a 3 to 5 cm wide vein from SunWa (Fig. 4.1b, 4.2c, d) and samples from an up to 7 metres thick pseudotachylite dike from Salvamento (Fig. 4.1b, 4.2e, f) were analysed.

In order to characterize the compositional zoning evident in the pseudotachylite matrix of the vein from SunWa, six areas (areas 1 – 6; Fig. 4.5a) exhibiting domains A and B were analysed. The pseudotachylite matrix in areas 1 and 6 represents domain A and contains fragments of quartz, plagioclase, alkali feldspar as well as biotite, muscovite, amphibole, Ti-augite and magnetite minerals embedded in a plagioclase-dominated matrix (Fig. 4.5c, h). The granitoid wall rock is made up of the identical mineral assemblage to the fragment population and pseudotachylite matrix minerals. Area 2 represents the transition between domains A and B and consists of plagioclase, quartz and alkali feldspar fragments as well as amphibole, Ti-augite and magnetite minerals (Fig. 4.5b, d). It is noteworthy that in area 2 quartz and feldspar fragments as well as biotite, muscovite and magnetite are less abundant, and the matrix is finer-grained than in area 1 (Fig. 4.5b).

The pseudotachylite matrix in domain B is represented by areas 3 to 5. The matrix of this domain is finer-grained than that of domain A and contains sulphides (Fig. 4.5e, f, g). An increase in clinopyroxene and amphibole in the pseudotachylite matrix away from granitoid wall rock (Fig. 4.5e, g) shows that mineralogical input from wall rock is of minor importance in domain B. A decrease in abundance of quartz and feldspar fragments in domain B is accompanied by a decrease in magnetite abundance in this domain with respect to domain A (Fig. 4.5c - h).

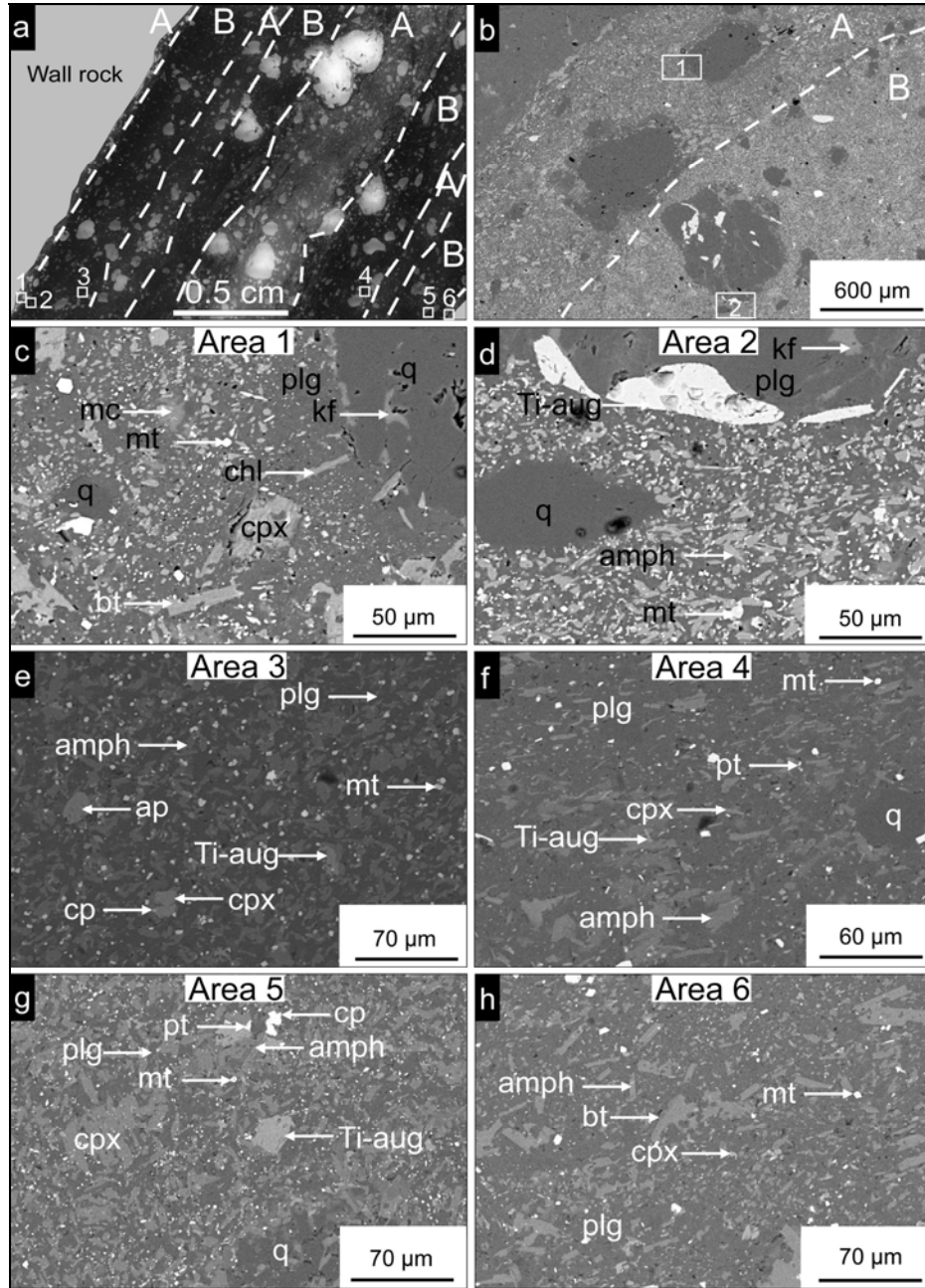


Figure 4.5: Thin section and back-scattered electron (BSE) images of pseudotachylite matrix of sample SunWa 13. Alkali feldspar – kf, amphibole – amph, apatite – ap, biotite – bt, chalcopyrite – cp, chlorite – chl, Ti-augite – Ti-aug, other clinopyroxene – cpx, magnetite – mt, muscovite – mc, plagioclase – plg, pyrrhotite – pt, quartz – q, domain A – A, domain B – B. (a) Thin section image showing matrix domains A and B, the boundaries of which are delineated by dashed lines, as well as the locations of the BSE images of areas 1 to 6 displayed in (c) to (h). (b) BSE image showing a close-up of domain A bordering on domain B. Note textural differences between both domains. Rectangles 1 and 2 denote respectively areas 1 and 2 indicated in (a). (c) – (h) BSE images showing respectively close-ups of areas 1 to 6 indicated in (a). Area 2 (d) hosts quartz, plagioclase, Ti-augite and alkali feldspar fragments. Areas 3 to 5 (e - g) illustrate domains B that hosts fewer and smaller quartz and plagioclase fragments than domains A.

The matrix in samples from the centre of the large, fragment-rich pseudotachylite body at Salvamento (Fig. 4.2e, f) is devoid of flow-banding, schlieren structures, or any domainal textural, mineralogical or chemical zoning (Fig. 4.6a). The chemical composition of the wall rock is identical to that of the granitoid wall rock of sample SunWa 13. The pseudotachylite matrix at Salvamento consists of plagioclase, amphibole, Ti-augite and other clinopyroxene some biotite, chlorite and magnetite and contains fragments made up of quartz and some alkali feldspar and plagioclase (Fig. 4.6b). Magnetite is preferentially associated with quartz and feldspar fragments (Fig. 4.6b).

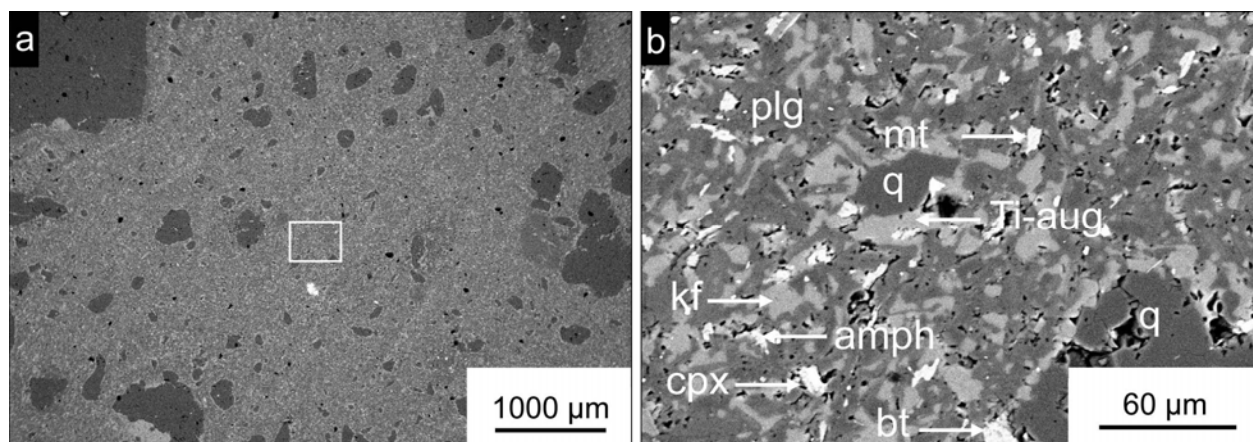


Figure 4.6: BSE images showing selected matrix portions of pseudotachylite body at Salvamento. For abbreviations see caption to Figure 4.5. (a) Overview of selected matrix portion. Note absence of any domainal compositional zoning. (b) Close-up of area enclosed by rectangle in (a). Note magnetite in the vicinity of plagioclase.

Domains A and B (Fig. 4.2d, e, g, h) are, in EDS analysis, characterized by strong element peaks of Si, Al, Mg, Na and weak peaks for K, Ca, Ti and Fe in EDX spectra, whereby Ca, Mg and Fe are relatively more abundant in domain B than in domain A (Fig. 4.7a, b). Element mapping of domain B shows that most opaque minerals contain Cu, S and Fe (Fig. 4.7d); these have been identified as chalcopyrite and pyrite. In terms of abundance of wall rock fragments and mineralogical composition, the matrix in the Salvamento sample is akin to that in domain A from the vein at SunWa. Moreover, the matrix at Salvamento shows the same element abundances (Fig. 4.7c) as domain A in the vein from SunWa (Fig. 4.7a). In the vicinity of their respective granitic wall rocks, the chemical compositions mapped for both matrices closely approximate

those of the respective wall rocks. This suggests that compositions of both matrices were influenced by assimilation of wall rock. In particular, assimilation seems to be more effective in large-volume pseudotachylite bodies, such as at Salvamento, that are devoid of any compositional zoning but rich in wall rock fragments. Domain B matrices, by contrast, are devoid of felsic wall rock fragments and, thus, are more mafic in character and, constitute, likely, less contaminated (i.e., containing less assimilated material) matrix material.

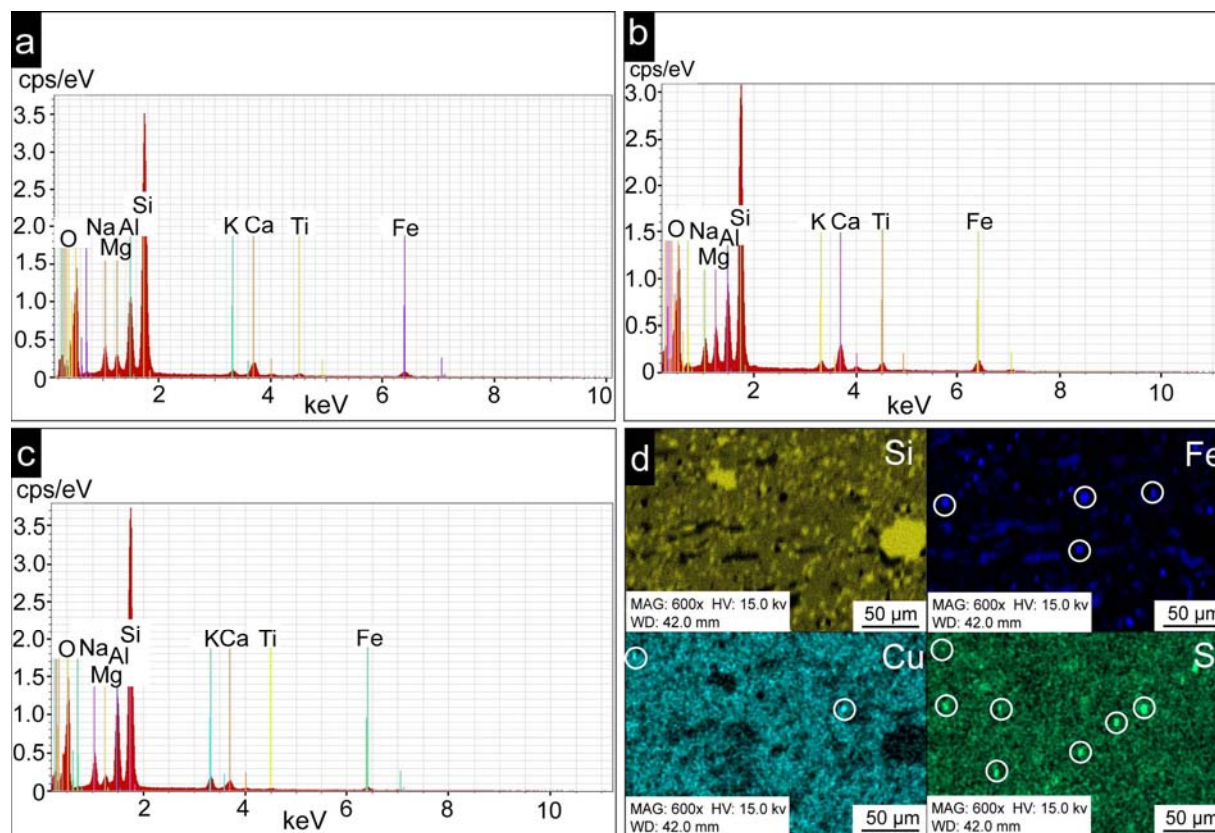


Figure 4.7: Scanning electron microprobe spectral diagrams of elements and element mapping images of samples from SunWa and Salvamento (Fig. 4.1b). (a) Spectral diagram of elements of domain A from SunWa. (b) Spectral diagram of elements of domain B from SunWa. (c) Spectral diagram of elements from Salvamento. Note similarity of spectrum to that of SunWa domain A displayed in (a). (d) Element mapping images of Si, Fe, Cu and S in domain B from SunWa. S, Cu and Fe are locally enriched (white circles).

To examine the possible variation in matrix composition at the sub-millimetre scale, five areas in a 1 mm wide apophysis of a 2-3 cm wide pseudotachylite vein in sample SunWa 6 (Fig. 4.1b; 4.2a, b) were analysed. Area 1 is located in the host vein and areas 2 to 5 are within the apophysis

(Fig. 4.8a). The matrix of the host vein consists chiefly of plagioclase, quartz, amphibole, Ti-augite, other pyroxenes and magnetite, as well as quartz and plagioclase fragments (Fig. 4.8b). The pseudotachylite matrix in the apophysis contains mostly quartz and feldspar fragments within a matrix of amphibole, pyroxene (excluding Ti-augite), plagioclase and magnetite (Fig. 4.8c -f). A conspicuous gradation in overall matrix composition is evident by the increase in abundance of mafic minerals, notably amphibole, from areas 2 and 3 (Fig. 4.8c, d) toward areas 4 and 5 (Fig. 4.8e, f). Idiomorphic magnetite is found close to the wall rock and next to feldspar and quartz fragments (Fig. 4.8b - e). The wall rock of the apophysis is made up of, e.g., plagioclase with alkali feldspar displaying symplectitic intergrowth, and biotite, and contains a large ferromagnesian mineral grain, possibly amphibole, close to the margin of the apophysis (Fig. 4.8a).

A mineralogical peculiarity of the apophysis is the presence of a ferromagnesian ribbon (Fig. 4.8a) that is identical in composition to the large ferromagnesian mineral in the wall rock (Fig. 4.8g, h). The ribbon emanates from the wall rock close to area 4, where it is physically connected to the large ferromagnesian mineral (Fig. 4.8a) and continues all the way through the apophysis to area 5 (Fig. 4.8f). This indicates local entrainment of wall rock material into the pseudotachylite matrix of the apophysis, whereby transport of material occurred from the host vein into the apophysis. In summary, the SEM analyses indicate local assimilation of wall rock. In addition, a case of melt transport from a larger pseudotachylite into a smaller one has been demonstrated (Fig. 4.8; Appendix III).

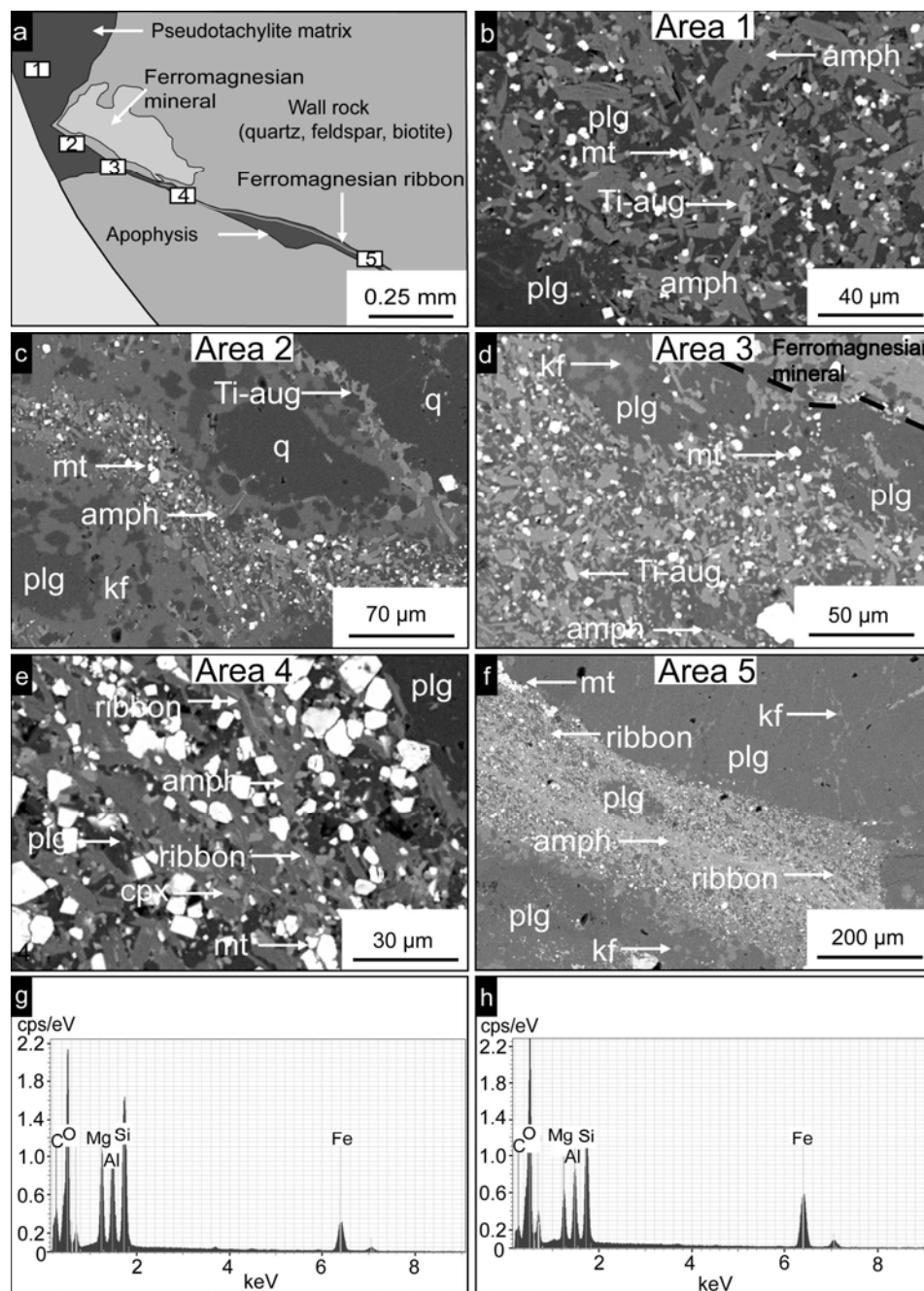


Figure 4.8: BSE and spectral element images of pseudotachylite matrix of a vein and an apophysis from sample SunWa 6 at SunWa (Fig. 4.2a). For abbreviations see caption to Figure 4.5. (a) Schematic representation of thin section image (see Figure 4.2b) showing pseudotachylite vein, apophysis, ferromagnesian ribbon and granitoid wall rock containing large ferromagnesian mineral. Rectangles 1 to 5 indicate areas of BSE images depicted respectively in (b) to (f). (b) - (f) BSE images showing the mineralogical composition respectively of areas 1 to 5 depicted in (a). Plagioclase displays symplectitic intergrowth with alkali feldspar in (c). Idiomorphic magnetite is found close to the wall rock and next to feldspar and quartz fragments in (d). In areas 4 and 5, (e) and (f) respectively, the matrix is rich in amphibole and contains the ferromagnesian ribbon. (g) Spectral element image of ferromagnesian mineral. (h) Spectral element image of ferromagnesian ribbon. Note the similarity in chemical signature between the ferromagnesian mineral and the ribbon.

5.4. Electron Microprobe Analyses

Quantitative chemical analysis of the matrix of a pseudotachylite vein hosted by granitoid wall rock at SunWa (Fig. 4.1b) was performed using EMP (Table 4-4). Thereby, this technique gives a greater spatial control to avoid clasts, but some grain size in the matrix still exceeded the beam size. Like other samples from this location (Fig. 4.5), the matrix of the SunWa 9 sample shows the same domainal characteristics and flow banding (Fig. 4.9a). Domains A are felsic, relatively coarser-grained crystalline, and contain more and larger wall rock fragments than domains B, which contain biotite, muscovite, feldspar, quartz, pyroxene, amphibole, Ti-augite, sulphides and some idiomorphic magnetite (Fig. 4.9b). The chemical composition of the matrix was measured at 155 spots with a defocused electron beam (35 μm beam diameter) along a line crossing domains A and B, whereby the measured profile is located close to the vein margin (Fig. 4.9b). Compositional averages of each domain and the wall rock, including their XRF compositions, demonstrate large differences between the compositions of the domains and the wall rock (Fig. 4.9c - e).

Specifically, domain A is characterized by a large number of felsic fragments, and it has considerably more SiO_2 (62 wt.%) but significantly less MgO (1.5 wt.%), CaO (2.9 wt.%) and FeO (3.7 wt.%) than domain B with e.g. 52 wt.% SiO_2 and 7 wt.% CaO (Fig. 4.9c, d). However, close to the vein margin, domain B has significantly less MgO (4.8 wt.%) and FeO (8.55 wt.%) than toward the vein centre where MgO and FeO are enriched by about 1.5 wt.% (Fig. 4.9c - e, Table 4-4). With respect to its wall rock, domain A is, however, more mafic, evident by its lower SiO_2 content and somewhat higher content in MgO, CaO and FeO (Fig. 4.9c - e). The electron microprobe data show that domain A is closer in chemical composition to wall rock than to domain B.

Table 4-4: Average data of electron microprobe analyses of SiO_2 , FeO, MgO and CaO contents of samples from SunWa 9. Data in wt.% with standard deviation (σ) and number of spot analyses (n). For definition of areas see text.

Oxides	Wall rock (n=9)	σ	Domain A (n=95)	σ	Domain B (n=29)	σ	Domain B close to	σ
SiO_2	84.40	4.74	62.59	3.30	51.75	3.14	52.31	3.42
FeO	1.36	1.44	3.71	1.77	10.03	3.46	8.55	2.31
MgO	0.83	0.77	1.56	0.94	6.04	1.61	4.80	2.02
CaO	1.93	1.54	2.92	1.45	6.97	1.71	7.14	1.88

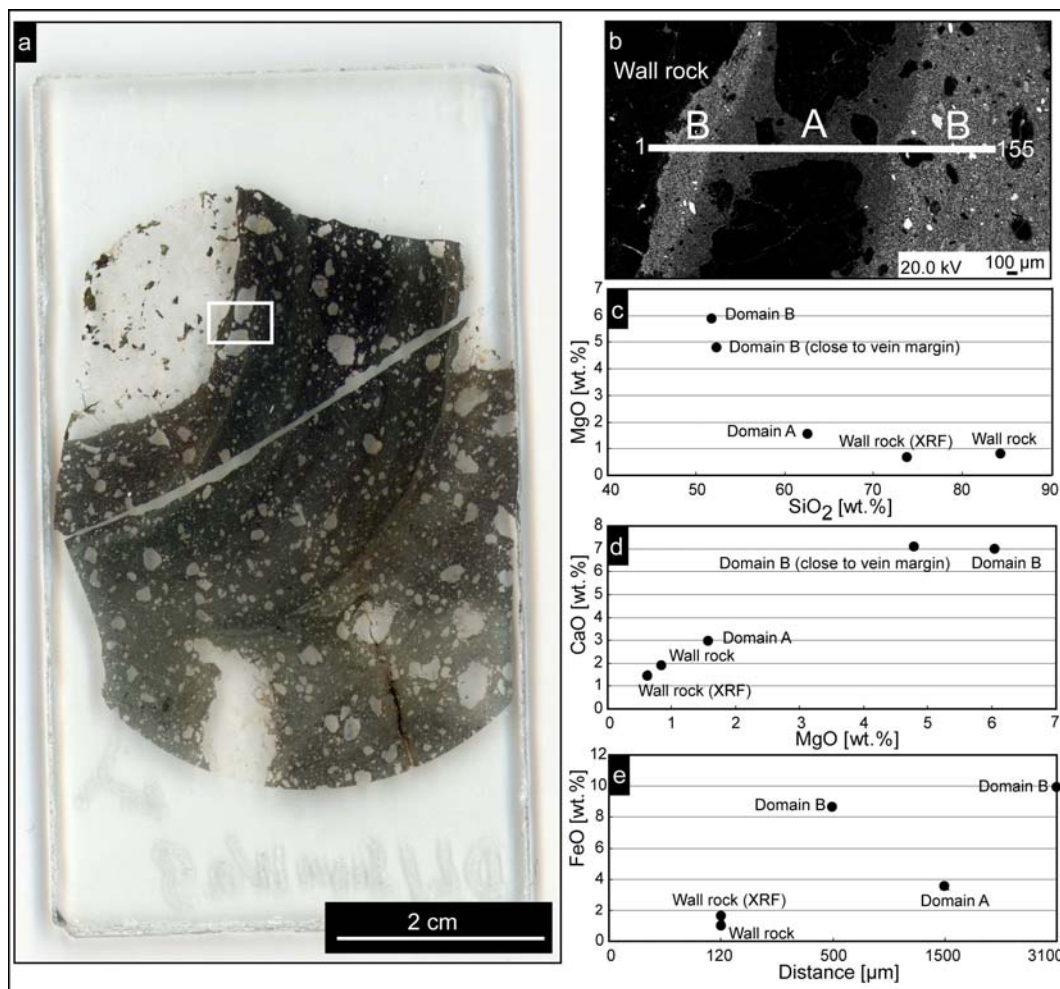


Figure 4.9: Thin section, BSE image and electron microprobe analyses of sample SunWa 9. (a) Thin section image showing domainal character of the matrix. Note bright haloes around large wall rock fragments. White rectangle displays area depicted in (b). (b) BSE image showing domains A and B and line along which a total of 155 spot analyses with a beam width of 20 μm were conducted. (c) and (d) Diagrams showing chemical compositions of wall rock and pseudotachylite matrix domains analysed by XRF and electron microprobe. (e) Diagram showing FeO content with position along line depicted in (b).

In order to examine the compositional variation of pseudotachylite matrix bordering on two wall rock types, i.e., granitoid and amphibolite, the matrix composition of a vein from the Kudu location (Fig. 4.1b) was examined in small samples from four sites (sites A-D; Fig. 4.2h, 4.10). The vein is poor in wall rock fragments and transects granitoid wall rock at sites A and D (Fig. 4.10a, d) and is hosted by amphibolite on one side and granitoid on the other at sites B and C (Fig. 4.10b, c). The chemical composition of matrix and wall rock was measured along 14 transects across the vein, each of which comprises between 100 and 200 spot analyses, using a

defocused electron beam of 35 μm diameter. Spot analyses were averaged over individual intervals of each transect, i.e., typically averages for two wall rock stretches, two marginal vein stretches and one central vein stretch (Fig. 4.10e - h, Table 4-5) are compared.

In general, the matrix in this vein is somewhat more mafic than matrices of other veins within granitoid wall rock (Fig. 4.4). Electron microprobe data show that the chemical composition of the pseudotachylite matrix is rather uniform but significantly different from the respective wall rock type (Fig. 4.10, Table 4-5). Locally, the contents of oxides in the matrix deviate from those in the wall rock by up to 40 wt.%. With respect to site A, almost all matrices in sites B, C and D are slightly lower in SiO_2 and MgO , but enriched in CaO and FeO (Fig. 4.10e - h, Table 4-5). Matrix compositions in sites B, C and D are similar to each other, despite the fact that respective wall rock types are dissimilar, i.e., partly amphibolite in sites B and C, but entirely granitoid at site D (Fig. 4.10a - d). The matrix in site D is more mafic than at site A, despite the same granitoid wall rock on both sites.

In summary, the mafic character of the pseudotachylite matrix increases from sites A to D. This can be explained by input from the mafic wall rock component at sites B and C. The fact that the matrix at Kudu is significantly more mafic than its granitoid wall rock and pseudotachylite matrices elsewhere (Fig. 4.4a) may be due to progressive incorporation of mafic material on the decimetre- or larger scale as the vein transects amphibolite wall rock (Fig. 4.2g). Electron microprobe analysis points to melt transport from the larger pseudotachylite body into a smaller one in the documented case. This is indicated by the fact that the pseudotachylite matrix at site A, which is located about 1 m from the amphibolite in granitoid wall rock on both sides of the vein, is more mafic than all other pseudotachylite matrices in the granitoid wall rock. These characteristics point to melt transport of approximately 1 m from larger into smaller bodies. Moreover, this analysis indicates a mixing of melt derived from several local lithologies, but this could mean that mixing of an exotic melt component with local wall rock is possible, too.

Table 4-5: Average SiO_2 , FeO , MgO and CaO contents (data in wt.%) obtained by microprobe spot analyses along transects across a pseudotachylite vein from the Kudu location with standard deviation (σ) and number of spot analyses (n). For definition of analysed areas see text and Figure 4.10.

Transect 1										n=117
Average wt.[%]	Area A	σ	Area B	σ	Area C	σ	Area D	σ	Area E	σ
SiO ₂	39.83	3.28	52.64	2.09	53.36	2.70	51.14	1.92	37.48	1.12
FeO	21.09	2.17	10.72	1.75	11.54	2.12	11.24	2.06	19.41	0.90
MgO	10.80	1.51	7.21	1.27	7.74	2.63	8.65	1.54	12.09	0.37
CaO	0.75	0.55	7.35	1.80	7.81	2.28	8.24	1.63	0.67	0.57
Transect 2										n=120
Average wt.[%]										
SiO ₂	66.18	0.93	51.25	1.05	55.44	4.23	52.10	1.66	95.89	0.14
FeO	0.17	0.04	11.92	1.16	12.25	2.14	11.11	1.87	0.04	0.04
MgO	0.28	0.28	7.81	1.20	7.81	1.63	7.56	1.38	0.01	0.003
CaO	1.00	0.6	8.06	1.34	8.54	1.78	7.95	1.53	0.02	0.009
Transect 3										n=153
Average wt.[%]										
SiO ₂	35.05	2.00	52.13	1.79	52.09	2.28	52.84	2.22	66.84	1.03
FeO	24.70	2.13	11.01	1.88	11.49	2.42	11.63	3.03	0.42	0.29
MgO	13.40	0.28	7.67	1.78	7.52	2.16	7.61	1.69	0.18	0.17
CaO	0.67	0.36	8.63	1.80	8.38	2.05	7.13	1.41	0.62	0.22
Transect 4										n=172
Average wt.[%]										
SiO ₂	49.38	0.47	51.40	2.02	50.34	3.67	51.54	3.14	64.64	2.01
FeO	14.14	0.37	10.95	1.64	12.31	2.98	12.09	2.42	0.27	0.12
MgO	13.92	1.25	7.09	1.17	7.44	1.54	7.58	2.07	0.06	0.07
CaO	11.07	0.05	8.81	1.55	8.62	2.18	7.67	2.48	0.46	0.04
Transect 5										n=167
Average wt.[%]										
SiO ₂	65.44	1.17	50.61	2.41	50.18	2.99	50.04	1.97	53.09	1.05
FeO	3.92	2.35	12.28	3.56	12.54	2.84	12.50	2.89	11.72	0.95
MgO	3.42	2.39	7.79	2.20	7.62	2.00	7.48	1.09	14.90	1.12
CaO	3.31	1.84	8.47	2.54	8.64	2.34	8.12	2.33	11.64	0.70
Transect 6										n=115
Average wt.[%]										
SiO ₂	64.96	1.06	52.27	2.13	51.50	3.76	51.62	2.50	41.54	4.50
FeO	0.73	0.41	10.79	3.36	11.58	3.12	10.83	2.37	1.16	0.80
MgO	0.41	0.31	7.22	2.62	7.45	2.02	7.65	1.66	0.76	0.71
CaO	2.14	0.55	7.80	2.47	8.31	2.37	8.03	2.13	21.24	3.83
Transect 7										n=41
Average wt.[%]										
SiO ₂	67.63	0.32	50.83	3.47	49.47	3.07	48.12	2.80	63.25	3.10
FeO	1.14	0.97	11.04	2.81	12.27	3.56	13.01	2.69	2.42	2.09
MgO	0.71	0.67	6.90	1.25	7.83	1.37	8.25	0.95	2.34	1.70
CaO	2.74	2.00	10.47	2.24	9.54	2.66	10.13	2.34	3.74	1.93

Table 4-5 continued.

Transect 8										n=34
Average wt.[%]	Area A	σ	Area B	σ	Area C	σ	Area D	σ	Area E	σ
SiO ₂	65.59	1.45	49.26	2.00	49.40	3.35	49.51	3.18	54.45	1.26
FeO	0.82	0.54	12.45	2.35	12.47	3.01	12.70	3.01	7.27	1.54
MgO	0.42	0.31	6.44	0.89	7.66	1.44	7.48	1.15	9.80	0.20
CaO	1.92	1.29	9.73	1.98	9.34	2.26	9.16	2.42	9.94	1.74
Transect 9										n=99
Average wt.[%]										
SiO ₂	92.27	3.15	50.97	2.80	50.92	3.26	51.08	3.54	66.09	1.56
FeO	0.06	0.06	12.07	2.48	12.33	3.01	12.27	3.74	1.58	1.46
MgO	0.01	0.0004	7.53	1.71	7.59	2.57	7.19	3.41	4.21	2.45
CaO	0.05	0.05	7.61	1.49	8.05	2.23	7.77	2.65	1.89	1.09
Transect 10										n=104
Average wt.[%]										
SiO ₂	65.32	3.31	51.10	3.56	51.11	2.80	50.87	2.27	43.74	9.16
FeO	0.12	0.03	10.91	4.22	11.95	2.75	11.92	2.68	17.73	7.14
MgO	2.26	1.84	7.48	3.14	7.46	2.19	7.32	1.74	5.27	3.94
CaO	1.09	0.70	8.73	3.91	8.28	2.65	8.63	2.44	1.66	0.58
Transect 11										n=90
Average wt.[%]										
SiO ₂	78.93	8.80	51.75	1.99	51.35	2.61	51.29	3.67	93.46	1.86
FeO	2.26	2.15	12.27	2.27	12.32	2.79	11.39	4.02	0.33	0.3
MgO	0.02	0.017	6.79	1.57	7.54	1.98	7.47	2.62	1.26	1.16
CaO	0.61	0.54	7.73	1.75	7.90	1.99	7.52	2.09	0.13	0.13
Transect 12										n=162
Average wt.[%]										
SiO ₂	92.29	3.61	51.57	3.28	51.29	2.78	51.35	1.84	64.91	1.69
FeO	0.06	0.05	11.19	6.99	12.02	3.43	11.52	1.42	0.71	0.61
MgO	0.01	0.007	7.53	2.29	7.45	1.84	7.62	1.69	1.39	1.06
CaO	0.07	0.07	8.87	2.66	8.14	2.35	8.69	1.96	2.18	1.67
Transect 13										n=179
Average wt.[%]										
SiO ₂	62.65	0.17	50.20	2.06	51.16	2.98	51.46	1.73	61.27	1.84
FeO	0.07	0.02	12.46	2.38	12.11	2.91	12.02	2.47	2.08	2.03
MgO	0.01	0.0005	7.78	1.50	7.61	1.90	7.09	1.43	1.11	0.60
CaO	3.54	0.22	8.02	2.08	7.79	2.69	8.15	2.33	3.80	0.40
Transect 14										n=125
Average wt.[%]										
SiO ₂	95.20	0.10	51.37	3.26	51.41	2.92	51.19	2.12	62.24	0.22
FeO	0.05	0.017	12.34	3.39	12.10	2.49	12.12	1.79	0.21	0.09
MgO	0.02	0.01	7.40	1.91	7.32	1.88	7.60	1.34	0.04	0.02
CaO	0.01	0.01	8.26	2.56	8.06	2.32	8.20	2.42	3.32	0.03

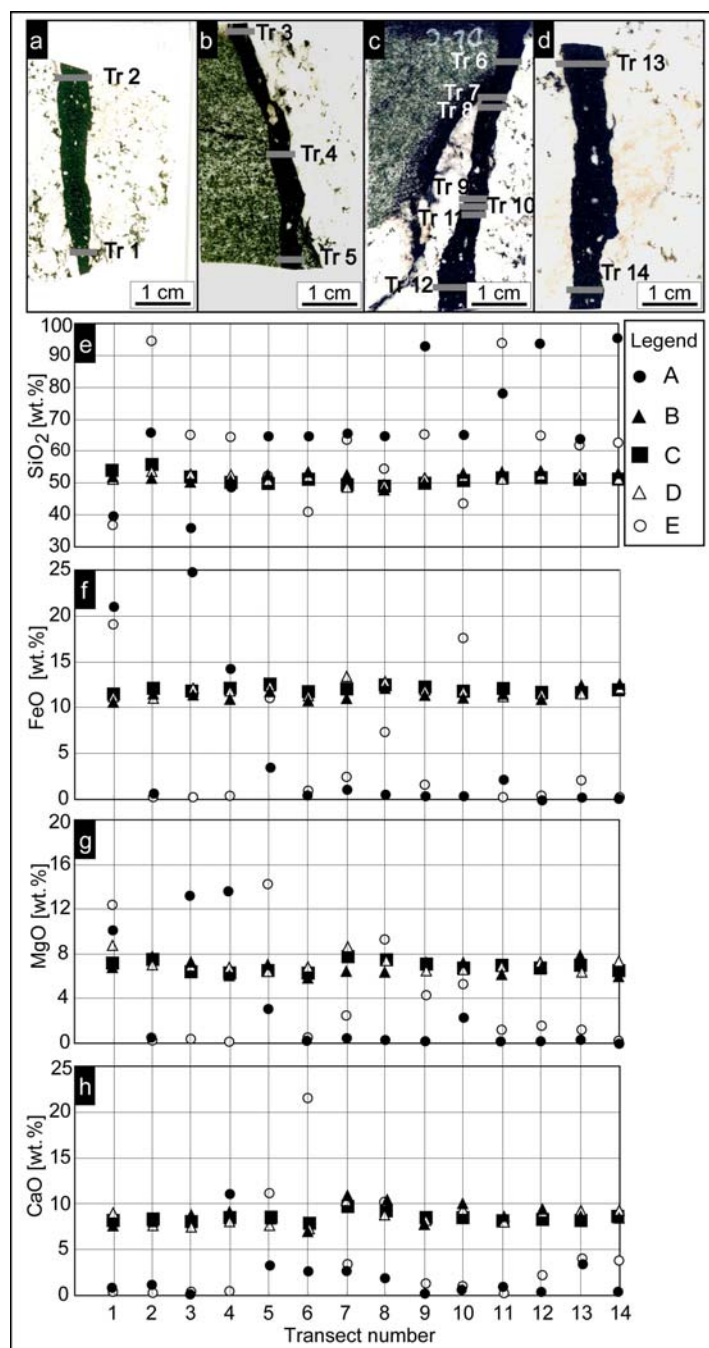


Figure 4.10: Electron microprobe spot analyses of 14 transects across a pseudotachylite vein hosted by amphibolite and granitoid wall rock at Kudu (Figs. 4.1b, 4.2h). (a) – (d) Thin section photomicrographs of vein segments showing the locations of the transects (Tr 1 to Tr 14). The positions of vein segments correspond respectively to areas A – D displayed in Figure 4.2h. Chemical compositions were averaged over defined stretches of each transect. The stretches are: wall rock to the left of vein - A, matrix at left vein margin - B, matrix in vein centre - C, matrix at right vein margin - D and wall rock to the right of vein - E. (e) Diagram showing the variation in SiO₂ for individual stretches of transects. (f) Diagram showing the variation in FeO for individual stretches of transects. (g) Diagram showing the variation in MgO for individual stretches of transects. (h) Diagram showing the variation in CaO for individual stretches of transects.

6. Interpretation of geochemical data

Whether pseudotachylite matrix is chemically similar, or even identical, to immediate wall rock is critical for the understanding of the origin of pseudotachylitic melts. At Vredefort, compositional similarity between matrix and granitoid wall rock has been documented for matrices in small (mm to cm) pseudotachylite veins (e.g., Reimold, 1991; Mohr-Westheide and Reimold, 2010), and this has been interpreted in terms of *in situ* shock or frictional melting of wall rock (e.g., review in Dressler and Reimold, 2004). However, some works on the geochemistry of pseudotachylite rock examined larger pseudotachylite bodies and concluded that their matrices are compositionally rather dissimilar from wall rock of variable lithology (e.g., Schwarzman et al., 1983). Reimold (1991) concluded from his analysis of Otavi quarry pseudotachylite and outcropping host rock types (granitoid rocks and amphibolite) that mixing of these components could generate a melt composition as observed for this pseudotachylite. We conclude that the extent to which pseudotachylite matrix is chemically akin to its wall rock may depend on scale, i.e., size of the pseudotachylite body, but also on the type(s) wall rock.

Our XRF and SEM analyses show that chemical compositions of matrices in pseudotachylite veins and dikes deviate in part significantly from those of their immediate wall rock. Moreover, our chemical analyses indicate that compositions of pseudotachylite matrices were modified by assimilation of wall rock components (Figs. 4.4, 4.5, 4.6), as noted also in other studies (e.g., Schwarzman et al., 1983; Killick and Reimold, 1990; Reimold, 1991; Coney, 2002; Dressler and Reimold, 2004). Based on the observed chemical trends (Fig. 4.4a), *in situ* bulk melting of a single lithology is excluded for the samples analysed here, and either an exotic melt component or mixing of melts from two (or more) local lithologies are possibilities to account for the compositional differences in many analysed pseudotachylite matrix-wall rock pairs (Fig. 4.4a, b). Trends in the compositional deviation of pseudotachylite matrices of large pseudotachylites from their respective wall rocks (Fig. 4.4a) suggest that if a primary melt (i.e., prior to assimilation) was present, it would have had a granitoid composition. The assumption that the primary melt had a granitoid composition is supported by the fact that pseudotachylitic matrices of large bodies within granitoid rocks show minimal deviation from their respective wall rocks, in contrast to matrices within pseudotachylite in other wall rock types (Fig. 4.4a). But, this minimal deviation

of pseudotachylite matrices from the granitoid wall rock could be caused by assimilation of wall rock fragments, too.

Smallest pseudotachylite bodies like in SunWa (in granitoid wall rock) or sample 621A (in quartzite) show sometimes strong deviation from their respective wall rock types in contrast to large pseudotachylite bodies from their respective wall rock. In these cases, it is possible that this small melt volume of small pseudotachylite bodies could indicate the results of local melting of immediate wall rock and small volume of assimilated wall rock or an allochthonous melt of unknown origin (Table 4-1). However, the melt volume of large pseudotachylite bodies could not be formed by in situ melt processes (e.g., shock melting - Kenkmann et al., 2000, or friction melting - Spray et al., 2004) and consequently, we suggest that the primary melt (i.e., prior to assimilation) had a granitoid composition.

In addition, Figure 4.4a suggests to us that the compositional trends of pseudotachylite matrices versus their wall rocks are directed toward the average composition of the Vredefort Granophyre. The Granophyre composition in this plot is intermediate with respect to all wall rock types and their pseudotachylite matrices. Whether this suggests that a Granophyre-like component is indeed present in large pseudotachylite melt rock occurrences must be, at present, viewed with caution. The raw data of pseudotachylite-host rock pairs, when compared against the specific chemical characteristics of Granophyre, do not allow significant admixture of such a component in most cases. But, it should be considered that the respective volume of assimilated wall rock and the chemical composition of a possibly intruded impact melt component are impossible to determine. Evidence for a primary melt component in pseudotachylite veins and dikes requires documentation of melt transport. Electron microprobe and SEM analyses indicate that transport of pseudotachylite melt in veins occurred over distances of at least centimetres to metres. This is generally consistent with the findings of Mohr-Westheide and Reimold (2010). As evident from the SunWa and Kudu locations, and also observed by Mohr-Westheide and Reimold (2010), direction of melt transport was from larger pseudotachylite bodies toward smaller ones and into apophyses. And the earlier work by Bisschoff (1962) and Reimold (1991) has shown that even transport distances of 50-100 m are, at least in the case of Otavi, indicated. The large-to-small vein polarity in melt transport calls into question large-scale melting by shock loading (e.g., Gibson and Reimold, 2005) and frictional heating (which was also questioned by Melosh, 2005,

on thermodynamic grounds), both apparently characterized by melt transport in the opposite direction, i.e., thin veins feeding larger melt dikes and ponds (Melosh, 2005; Gibson and Reimold, 2005). If the melt was shock-induced, then the volume of melt should increase towards the centre of the dome as shock pressures increase, but this is not observed. Moreover, if veins generated by frictional heating, then veins should be associated with slip surfaces, and slip should be commensurate with the melt volumes. However, frictional melt production is a self-limiting process and will decrease the friction coefficient of a shear fault to zero, thus inhibiting further melt production on this fault surface (Melosh, 2005). Alternatively, melt is drained from the impact melt sheet and transported into tensional fractures below the crater floor, i.e., from large dikes into veins (Stöffler, 1977; Lieger et al., 2009; Riller et al., 2010). This model does not require melt generation by frictional shearing. As the impact melt is initially superheated, the transported melt would be highly mobile and would have the capacity to assimilate considerable volume of wall rock before solidifying.

Compositional modification of matrices by assimilation of wall rock and wall rock fragments is petrographically evident in pseudotachylite veins by their domainal character. Where such veins are hosted by granitoid wall rock, wall rock assimilation is strongest in domains A, which are felsic and replete with felsic wall rock fragments. By contrast, domains B contain significantly less wall rock fragments, are more mafic than domains A and, thus, less affected by wall rock assimilation. Where pseudotachylite veins and dikes cut amphibolite wall rock, pseudotachylitic melt was more mafic than other pseudotachylites in the Vredefort core what is caused by the amphibolite wall rock (e.g., samples KUDUA1 and KUDUA2 in Figure 4.4a).

Some pseudotachylite matrices are characterized by domains of different mineralogical and chemical compositions (Figs. 4.2c, d, 4.3d, g, e, h, 4.5a, b, 4.9a), in contrast to matrices of larger pseudotachylite bodies, such as at Salvamento (Fig. 4.2f). SEM and electron microprobe analyses indicate that the matrix compositions of domains A in veins (Fig. 4.7a) resemble those of matrices in the centres of large pseudotachylite bodies (Fig. 4.7c), both approaching that of, mostly felsic, wall rock (Fig. 4.9c, d, e). Moreover, domains A next to vein margins are considerably thinner than in the central portions of veins and are replete with (felsic) wall rock fragments. Collectively, these observations can be explained by the magnitude of assimilation being controlled by the surface area of (felsic) wall rock fragments and cooling rate of the

pseudotachylitic melt. In particular, wall rock assimilation would be lower in veins that have straight margins and cooled quicker, than in thick pseudotachylite bodies where matrix enveloped abundant wall rock fragments. Melt in larger pseudotachylite bodies likely had a higher capacity to assimilate more wall rock fragments than veins, as melt in larger bodies remained hotter over longer time spans and injected into thinner veins before solidifying.

Besides the cooling rate, the capacity to assimilate wall rock will be determined by the temperature of melt and, thus, will be most efficient in superheated melts (Ivanov and Deutsch, 1999). Sulphide and silicate mineralogy may aid in estimating the temperature of this melt. Pyrrhotite and chalcopyrite are commonly found in the matrix of pseudotachylite veins (Fig. 4.5f, g and 4.7d). If formed from pyrite, which is present in wall rocks but not in the pseudotachylite matrix, the presence of pyrrhotite in the matrix would point to temperatures of the pseudotachylite melt above 1200 °C (Kullerud, 1967; Magloughlin, 2005). Pyrrhotite pseudomorphs after cubic pyrite have, however, not been observed in our samples. Furthermore, the margin of a zircon crystal in wall rock bordering on a pseudotachylite (Fig. 4.11a) was observed to be corroded (Fig. 4.11b). At ambient pressures, zircon decomposes to oxides at a temperature of about 1690°C (Finch and Hanchar, 2003). Thus, the initial temperature of pseudotachylitic melt could well have been as high as 1200 to 1700 °C. Generation of such hot melts is difficult to reconcile with mechanisms that are known from endogenous melt-forming processes, i.e., frictional heating and decompression. For tectonic pseudotachylites with volumetrically limited friction melt theoretical evaluations and petrographic evidence have indicated temperatures between 700 and perhaps up to 1400 °C (Spray, 1987; Magloughlin, 2005). Thus, our findings require a mechanism that is capable of producing large volumes of superheated silicate melt.

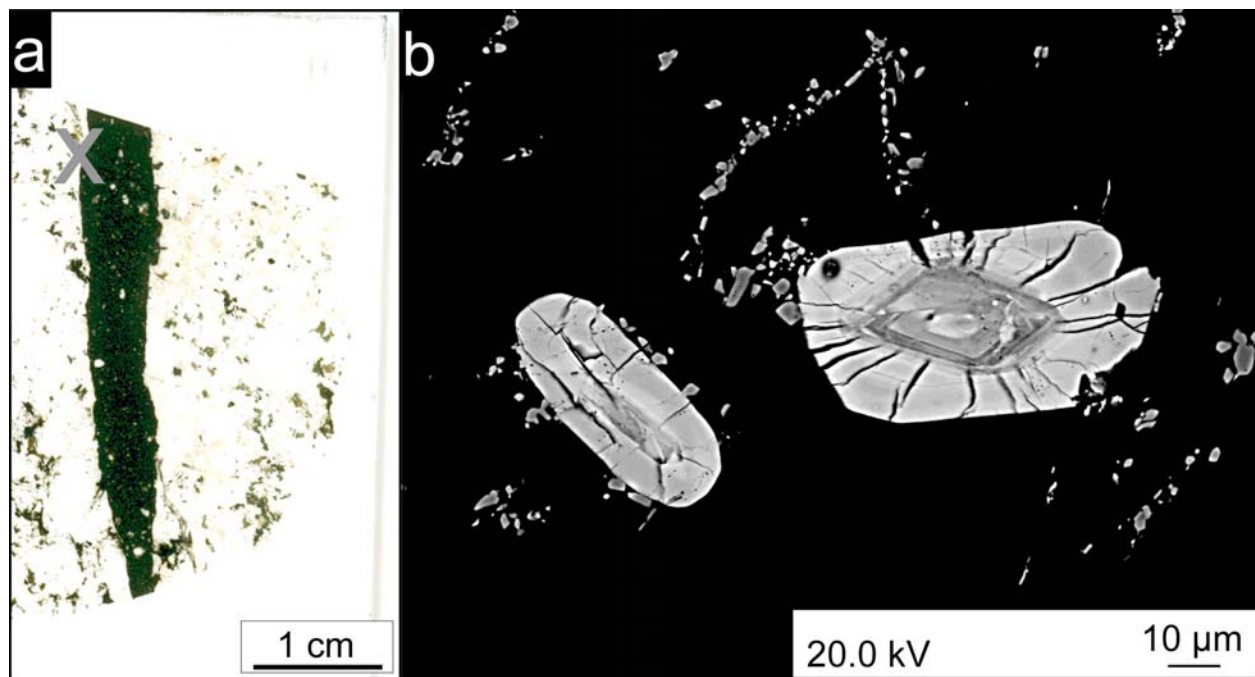


Figure 4.11: Thin section and BSE images displaying respectively pseudotachylite vein and corroded zircon (X) at Kudu (Fig. 4.1b). (a) Thin section photomicrograph showing location of zircons in wall rock at vein margin depicted in (b). (b) BSE image of fractured, zoned and corroded zircons.

Our geochemical data, in conjunction with structural information (Lieger et al., 2009) and the considerations delineated above, suggest that hypotheses for an origin of pseudotachylitic melt adhering to *in situ* melting processes by, e.g., frictional shearing, decompression or shock loading below the crater floor, are implausible for centimetre to metre wide pseudotachylite dikes examined in this study. Geochemical characteristics of pseudotachylitic melt and the sheer volumes of this melt observed at Vredefort and Sudbury are suggestive of injection of superheated melt from the overlying impact melt sheet into target rock during cratering. These characteristics include: (1) the overall compositional difference between pseudotachylite matrix and immediate wall rock, (2) chemical trends suggesting involvement of a primary melt component of likely granitoid (crustal) composition in large pseudotachylite bodies, (3) direction of transport of melt from decametre or wider pseudotachylite bodies towards millimetre scale bodies, (4) the superheated nature of pseudotachylitic melt, and (5) efficient assimilation of wall rock.

Structural evidence at Vredefort failed to identify the presence of bona fide shear faults that could potentially have generated large-scale in situ frictional melt (Reimold and Colliston, 1994; Lieger et al., 2009; Riller et al., 2010). Moreover, absence of significant wall-parallel displacement of pseudotachylite zone margins as well as evidence of flow textures and exotic clasts indicate that the melt was not generated *in situ*. Pseudotachylite occurrences have been related by Lieger et al. (2009) to dilation of target rocks during collapse of the central uplift. The horizontal component vectors of dilation display a remarkably centro-symmetric pattern with respect to the centre of Vredefort Dome (Lieger et al., 2009). In this study we suggested that impact melt was drawn into lower pressure tensional fracture zones. Based on numerical modelling and the structural study by Lieger et al. (2009), this pattern of dilational fractures has been attributed to the outward collapse of the central uplift. Injection of impact melt from the overlying melt sheet would account for the composition of the primary melt, which may well approximate the average composition of the Vredefort Granophyre, a proven derivative of the eroded impact melt sheet (Koeberl et al., 1996).

If a primary impact melt component was involved with pseudotachylite formation, some further considerations are required: The primary composition of the impact melt sheet depends on the heterogeneity of target rocks (e.g. Al Barazi et al., 2009) and will evolve, i.e., differentiate with time. This may be the reason why not all pseudotachylite matrix compositions can be explained by mixing of local host rock with a single exotic melt composition such as average Vredefort Granophyre (e.g., SunWa or Kudu). It is possible, furthermore, that large pseudotachylite bodies and some veins may have a different origin or that impact melt invaded into other pools of locally formed shock melt.

Dikes of the Vredefort Granophyre are unstrained, but transect the folded interfaces of overturned strata in the collar of the Vredefort Dome (Fig. 4.1), which is not observed with regard to pseudotachylite zones (Lieger et al., 2009). Moreover, pseudotachylite is found in faults of the collar rocks, whereas Granophyre dikes cut these faults (Fig. 4.1). Thus, Granophyre dikes were emplaced after the crater modification stage and are, therefore, younger than pseudotachylite bodies (Bisschoff, 1972; 1996). However, Reimold et al. (1990) cited a 1 cm wide pseudotachylite crosscutting a Granophyre dike.

Structural similarity of granophyre dikes, notably their radial and concentric geometry with respect to the crater centre, with Offset Dikes at Sudbury suggests that they were emplaced by the same mechanism. Correlation of melt temperature estimates of Offset Dikes with modelled cooling rates of the impact melt sheet at Sudbury suggests that Offset Dikes were emplaced up to ten thousand years after impact (Hecht et al., 2008). This remains to be ascertained for the Vredefort Granophyre dikes.

Our work bears significantly on the genesis of pseudotachylite bodies. According to the recommended IUGS glossary definition of impact-induced pseudotachylite, this rock type forms by frictional melting (Fettes and Desmons, 2007, p. 162). Geochemical evidence presented in this study and structural evidence (Lieber et al., 2009; Riller et al., 2010) suggest possible derivation of pseudotachylite melts from impact melt, and that fragmentation and melt generation of pseudotachylite bodies are processes that differed in time and space. Collectively, this casts doubt on the validity of the IUGS definition of impact pseudotachylite as friction-induced rocks (Stöffler and Grieve, 2007).

7. Conclusions

Geochemical and petrographic analysis of pseudotachylitic veins and dikes and their respective wall rocks from the Vredefort Dome indicate the following matrix characteristics: (1) overall compositional difference between pseudotachylite matrix and immediate wall rock, (2) evidence for involvement of a primary melt component of granitoid (crustal) composition or mixing of melt derived from several local lithologies, (3) transport of pseudotachylite melt from larger veins into smaller ones, (4) superheated nature of pseudotachylitic melt, and (5) efficient assimilation of wall rock. We interpret these findings as supporting an allochthonous origin of pseudotachylitic melt. In the context of the combined results of structural analysis and the exclusion of formation of large pseudotachylite melt by in situ melting processes, we advocate that massive pseudotachylite melt formed by injection of melt from the overlying impact melt sheet into target rocks.

Acknowledgements

This work was funded by the German Science Foundation (grants Ri 916/8-1 and Re 528/6-2). K. Born provided technical support. We thank landowners in the Vredefort area for access to their properties and the staff of the World Heritage Office for their support. Reviews for the Journal were provided by J.W. Horton, Jr. and A. Wittmann. Their effort in clarifying the content of the manuscript is greatly appreciated.

CHAPTER 5:

EMPLACEMENT HISTORY OF GRANOPHYRE DIKES IN THE VREDEFORT IMPACT STRUCTURE, SOUTH AFRICA, INFERRED FROM GEOCHEMICAL EVIDENCE

Daniel Lieger¹, Ulrich Riller² and Roger L. Gibson³

¹ Museum für Naturkunde, Humboldt-Universität zu Berlin, Invalidenstraße 43, 10115 Berlin, Germany

² McMaster University, School of Geography and Earth Sciences, 1280 Main Street West, Hamilton, Ontario, Canada, L8S 4K1

³ Impact Cratering Research Group, School of Geosciences, University of the Witwatersrand, Private Bag 3, P.O. Wits 2050, Johannesburg, South Africa

Abstract

The central Vredefort Impact Structure is characterized by impact melt rocks, known as the Vredefort Granophyre dikes. Whole-rock and petrographic analyses of two dikes were conducted and compared to published geochemical data to elucidate the mode and timing of dike formation. The dikes are characterised by compositional and textural heterogeneity between, and within, individual dikes. Specifically, central dike portions are felsic and rich in wall rock fragments, whereas marginal dike phases are mafic and fragment-poor. Collectively, this suggests that melt was derived from compositionally different parental melts and emplaced in at least two pulses. In addition, the chemical heterogeneity between fragment-rich and fragment-poor dike zones can be explained by variable assimilation of a mafic component, notably Ventersdorp basalt, at the base of the impact melt sheet, from which melt of the Granophyre dikes is derived. This scenario accounts for the mafic and fragment-poor character of melt emplaced first in the dikes and the more felsic and fragment-rich nature of melts of the following emplacement pulse, i.e., when the impact melt was less hot and thus unable to digest large quantities of (mafic) wall rock fragments. Granophyre dikes formed after cratering, whereby dike formation was possibly driven by late-stage isostatic readjustment of crust underlying the Vredefort impact structure. Differences in geometrical, textural, chemical and fragment characteristics between the Granophyre dikes and pseudotachylite bodies can be explained by the same process, i.e., impact melt drainage, but operating at different times after impact.

Key words: Vredefort impact structure, geochemistry, granophyres dikes, dike emplacement.

1. Introduction

Large complex impact structures are characterized by the presence of impact melt rocks such as the Sudbury Igneous Complex at Sudbury (Dressler, 1984) and the Granophyre dikes at Vredefort (Dietz, 1961; French et al., 1989; French and Nielsen, 1990). At the Vredefort Impact Structure (Fig. 4.1) the time and mode of emplacement of Granophyre dikes with respect to cratering stages are unclear. Proposed mechanisms of dike formation include the injection of mafic magma (Bisschoff, 1972; Nicolaysen, 1987) either during tectonism (Hart et al., 1987; Reimold et al., 1990) or during cratering into crater floor fractures (Dietz, 1961; French et al., 1989; French and Nielsen, 1990; Therriault et al., 1996; Reimold and Gibson, 2006). An impact melt origin of the Granophyre dikes is supported by a Re-Os isotope study indicating that dikes have considerably higher Os contents, significantly different Re-Os isotopic compositions than adjacent target rocks, and contain up to 0.2% of a chondritic component (Koeberl et al., 1996).

Almost all hypotheses on the emplacement of Granophyres dikes are based on geochemical and petrographic analyses of the matrix of, and host rock fragments in, the dikes. In particular, the impact melt hypothesis for the origin of the dikes was tested through analyses of possible mixtures of various target rock types (French and Nielsen, 1990; Reimold et al., 1990; Therriault et al., 1997). Based on the diversity of fragment types and mixing calculations (e.g., Stormer and Nicholls, 1978; Stöckelmann and Reimold, 1989; Reimold et al., 1990; Therriault et al., 1997), the Granophyre variants can be produced by multiple target rock proportions. However, there is uncertainty to what extent a mafic melt component, derived in particular from the bimodal Ventersdorp lava, contributed to the composition of the Granophyre melt (Reimold et al., 1990; Reimold and Gibson, 2006). Melt components of the Ventersdorp lava have not been taken into account as Granophyre dikes seem to be devoid of fragments from this lithology (Reimold et al., 1990). However, Therriault et al. (1997) and French and Nielsen (1990) obtained a plausible mixture of the Granophyre matrix by considering a mafic component of the lava in their analysis.

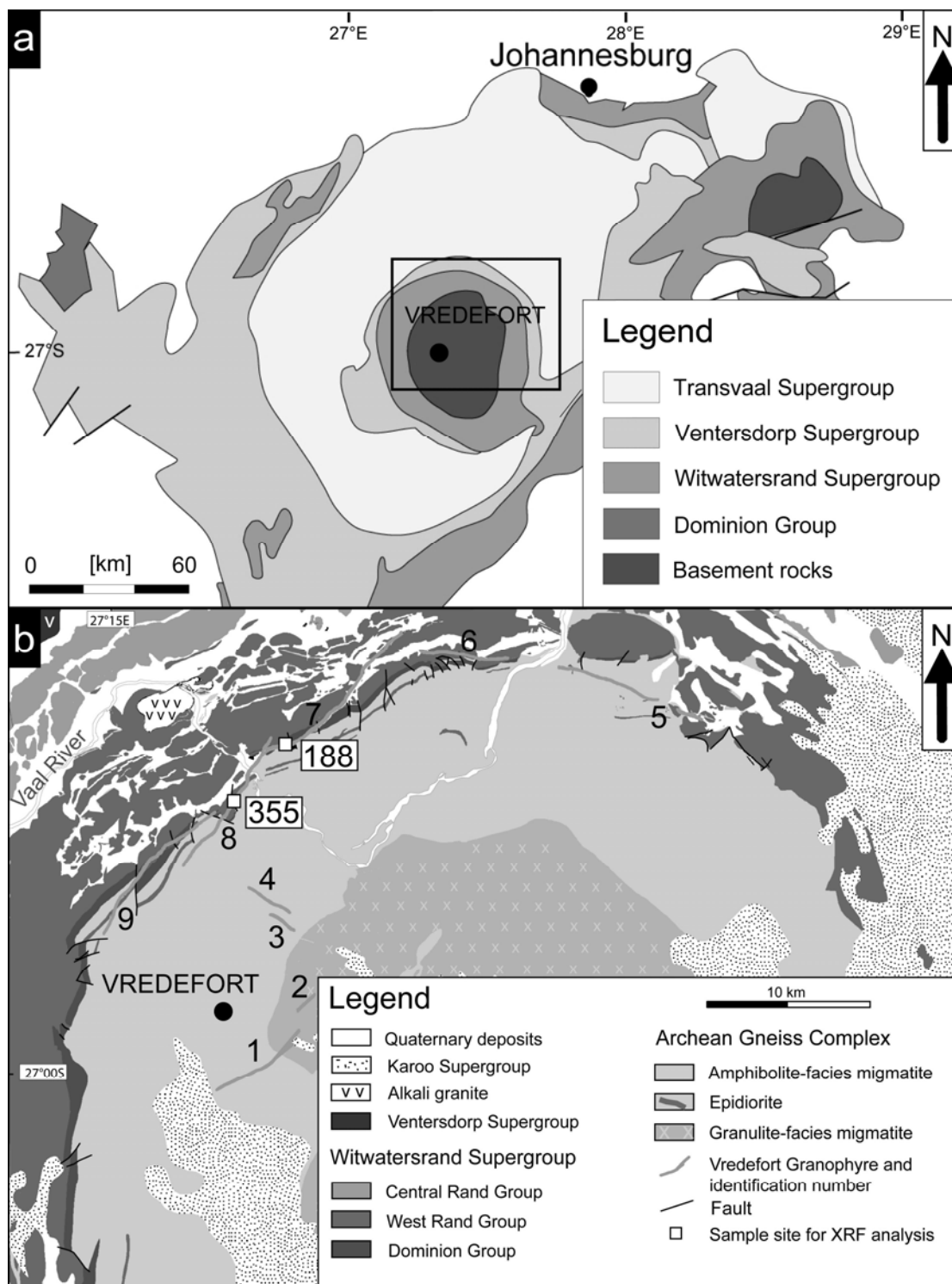


Figure 5.1: Geological setting of the Vredefort Dome. (a) Simplified geological map of the Witwatersrand Basin. Rectangle denotes area in (b). (b) Geological map of the Vredefort Dome showing sample sites of the geochemical study and the position of the nine known radial and concentric Granophyre dikes.

We present results of XRF and thin section analyses from two Granophyre dikes from the Vredefort Dome (Fig. 5.1). Our results are compared with published chemical data of Granophyre dikes from Reimold et al. (1990) and Therriault et al. (1997). Specifically, we focus on the chemical composition of Granophyre matrices of dikes in the granitoid and gneissic core of the Vredefort Dome and close to upturned metasedimentary strata. Granophyre dikes in the core differ chemically from those near metasedimentary strata (Therriault et al., 1996). This has been attributed to assimilation of mafic wall rock fragments (Reimold and Gibson, 2006). Thus, we seek to elucidate (1) to what extent the chemical variation in matrix composition was influenced by wall rock assimilation, (2) whether the chemical variation can be explained by differentiated impact melt and (3) whether emplacement of Granophyre melt occurred in separate intrusive pulses. With regard to the latter, we examined the chemical variation of the matrix from dike margins to dike centres.

2. Geological Setting

The 2023 ± 4 Ma Vredefort impact structure (Kamo et al., 1996), located in the Witwatersrand Basin (Fig. 5.1a), is the oldest known impact structure on Earth and, with an estimated diameter of up to 250 km, also the largest (Therriault et al., 1996; Henkel and Reimold, 1998; Grieve and Therriault, 2000; Turtle et al., 2005). The impact structure has been eroded to a depth of between 7 and 10 km (Gibson et al., 1998) and, thus, offers an unprecedented view of target rock configuration below a large, complex terrestrial impact structure. The central portion of the impact structure, the so-called Vredefort Dome (Fig. 5.1b), is the eroded relic of structurally uplifted rocks, generally referred to as the central uplift (Melosh, 1989). The Vredefort Dome consists of a core, ca. 40 km in diameter, of a 3.1-3.2 Ga tonalite-trondhjemite-granodiorite and greenstone assemblage (Lana et al., 2004). The core is surrounded by a 15-20 km wide ‘collar’ of subvertical to overturned 3.07 to 2.1 Ga supracrustal strata (Armstrong et al., 1991) that were deposited unconformably on the Archean crystalline basement rocks.

The core of the Vredefort Dome consists of migmatitic gneisses intruded by synmetamorphic granitoid bodies that range from granulite-facies grade in the centre to upper amphibolite-facies grade towards the collar (Lana et al., 2004). The collar rocks are made up of lavas of the

Dominion Group which were covered, successively, by quartzite, conglomerate, siltstone, shale and ironstone of the Witwatersrand Supergroup, bimodal lavas of the Ventersdorp Supergroup, and dolomite, quartzite and shale of the Transvaal Supergroup (Fig. 5.1b). Pre-impact regional metamorphism in the collar rocks decreases from mid-amphibolite facies in the Dominion Group to greenschist facies in the upper Witwatersrand Supergroup (Gibson and Wallmach, 1995). Post-impact temperatures in rocks of the Vredefort Dome range from ≥ 1000 °C in the centre to about 300 °C in the collar rocks located at a distance of about 25 km from the centre (Gibson et al., 1998; Gibson, 2002; Ivanov, 2005).

3. Previous work on the Vredefort Granophyre

The Vredefort Granophyre dikes are rich in host rock fragments set in a micropegmatitic and granophyric matrix of apparently homogeneous chemical composition (Reimold and Gibson, 2006). Nine 10 to 50 m wide dikes, with a total exposed length of 50 km, are known in the Vredefort Dome (Fig. 5.1) (Therriault, 1992; Therriault et al., 1996). Four of these dikes occur in the granitoid core of the Dome (Reimold and Gibson, 2006) and strike NE-SW and NW-SE. The other five Granophyre dikes straddle the core-collar boundary and, thus, intruded into granite-gneiss, quartzite, shale, ironstone and epidiorite, whereby epidiorite belongs to the Ventersdorp strata and intruded in all rock of the Vredefort Dome (Fig. 5.1). The orientation of the Vredefort Granophyre dikes corresponds to that of pseudotachylite bodies which are disposed radially and concentrically with respect to the centre of the dome (Reimold and Colliston, 1995; Lana et al., 2003; Lieger et al., 2009). Dikes within the core of the Dome are radial as well as shorter (< 4.5 km long) and thinner (< 20 m thick) than dikes at the core-collar boundary, which are up to 9 km long and 65 m wide (Reimold and Gibson, 2006). Therriault et al. (1996) noted that the latter ones are topographically elevated by 40-100 m relative to dikes in the core, and attributed differences in the textural character of the dikes to the vertical distance of exposed dikes to the eroded impact melt sheet.

Large fragments (2 - 80 cm in diameter) are less abundant than small fragments (< 2 cm in diameter), which make up 10 to 20 vol.% of the Granophyre dikes (Therriault et al., 1996). About 20-60 % of the fragments are up to several centimetres in diameter, whereby more than 20 % are

visible only in thin section. Collectively, fragments are derived predominantly from the immediate wall rock, notably from granitoid wall rocks (Therriault et al., 1996). Quartzite is the second-most abundant fragment type. Shale and epidiorite fragments (Reimold and Gibson, 2006) are found in dikes at the core-collar contact cutting respective lithologies. Therriault et al. (1996) noted also that an increase in matrix grain size towards dike centres correlates with a decrease in the content of large fragments. Dikes in the core of the Dome seem to have more large fragments than dikes at the core-collar boundary, and large fragments typically occur at one margin of a dike.

Two Granophyre types, one characterized by up to 5 cm large spherulites of orthopyroxene in a fine-grained groundmass of feldspar and quartz, and one consisting of granular orthopyroxene and feldspar, are known (Bisschoff, 1972; Reimold et al., 1990; Therriault, 1992). Dikes in the core of the dome are more spherulitic and show a higher modal abundance of biotite, clinopyroxene and opaque minerals than granular-textured dikes near the collar (Therriault et al., 1996). This textural zonation of dikes was explained in terms of crystallisation depth and melt flow (Therriault, 1992; Therriault et al. 1996). Moreover, Therriault et al. (1996) distinguished four microtextural types of Granophyre matrix. Despite the uniform mineral compositions, the Granophyre matrix displays significant variations in the abundance of major minerals, notably hypersthene, plagioclase, orthoclase, quartz, biotite, magnetite and ilmenite and traces of pyrite and chromite (Therriault et al. 1997). In addition to these, augite and pigeonite occur in granular textured Granophyre.

With regard to other igneous rock types, the chemical composition of Granophyre is unique. Based on the content of SiO₂ (67 wt.%), Fe₂O₃ (3 wt.%), MgO (4 wt.%) and CaO (3 wt.%), the Granophyre dikes were originally considered as a magma of dioritic composition that assimilated significant amounts of crust while stopping upwards (Willemse, 1937; Bisschoff, 1972). The average dike compositions are similar to each other, but differ in Sr, Ba and Cr (Therriault et al., 1996). Rare Earth Element (REE) patterns match those of granitoid rocks in the core of the Dome (Therriault et al., 1996).

4. Analytical Methods

Granophyre matrices were examined petrographically using an Olympus stereomicroscope and a LEITZ DM RXP polarization microscope. Ten thin sections of two samples from Granophyre locations associated with and without macroscopic fragments in the matrices were inspected. Major and trace elements of nine Granophyre matrices were analysed using wavelength dispersive X-ray fluorescence spectroscopy (WDXRF) in the School of Geosciences at the University of the Witwatersrand, Johannesburg. For chemical analysis of the matrix, millimetre-size wall rock fragments were removed from the matrix.

Samples with a mass of 0.2 to 1 kg were used for whole rock analyses. Accuracies (in wt.%) for the analysed major elements are: SiO₂ [0.5]; Al₂O₃ [0.1]; Fe₂O₃ [0.05], MgO [0.05], CaO [0.05], Na₂O [0.05], K₂O [0.05]; TiO₂ [0.01], MnO [0.01] and P₂O₅ [0.01]. The accuracy (in ppm) for trace elements is: Ba [30], Cu [25], Zn [25], Rb [5], Sr [5], Y [5], Zr [5], Nb [5], Co [5], Ni [5], V [5] and Cr [5]. The data were processed using the software *Igpet* and are plotted in Figure 5.4. Table 5-1 shows published XRF analyses of Granophyre dikes and different wall rock types as well as XRF analyses of Granophyre dikes from this study.

5. Results

5.1. Field characteristics and petrography of Vredefort Granophyre dikes

Samples for detailed microstructural, petrographic and geochemical analyses of dike matrices were chosen from sites 188 and 355 (Fig. 5.1b), and compared with published data of dike matrices (Reimold et al., 1990; Therriault et al., 1997). For the dike at site 188, the target rock is mostly quartzite, whereas at site 355 target rocks are quartzite, granitoid and epidiorite (Fig. 5.1). At these locations, the dikes differ in the amount, size and geometry of wall rock fragments as well as flow patterns indicated by the alignment of matrix minerals and small wall rock fragments (Fig. 5.2). Dike margins are generally poor in fragments, which consist of centimetre-wide rounded quartzite and granitoid fragments, and display a convolute melt flow pattern (Fig. 5.2d). By contrast, the central portions of dikes are rather fragment-rich (Fig. 5.2a). Here, fragments are elongate and angular, up to 30 cm in length and mostly aligned parallel to dike

margins (Fig. 5.2b, c). Shape fabrics defined by the fragments are planar (Fig. 5.2b) and suggest laminar melt flow.

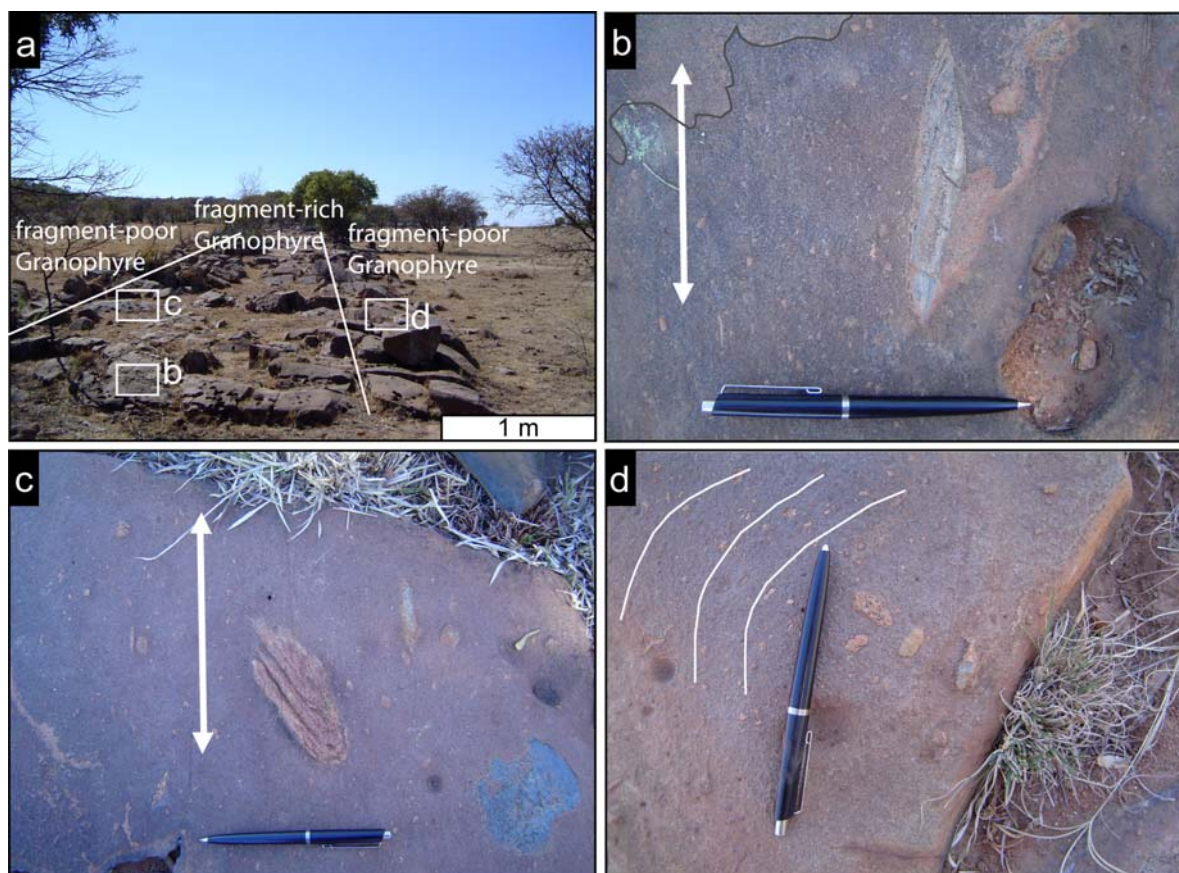


Figure 5.2: Outcrop images of Vredefort Granophyre dike in granitoid host rock. (a) Photo showing the zoning of the dike and locations of photos b – d. (b) and (c) Photos showing the fragment-rich zone containing elongate, up to 10 cm long, mostly angular fragments aligned parallel to dike margins. The planar shape fabric of fragments points to laminar flow during melt emplacement. Note evidence for melt mingling at top left in (b). (d) Photo showing convolute melt flow pattern in the fragment-poor marginal zone of Granophyre dike indicated by variable orientation of long axes of wall rock fragments.

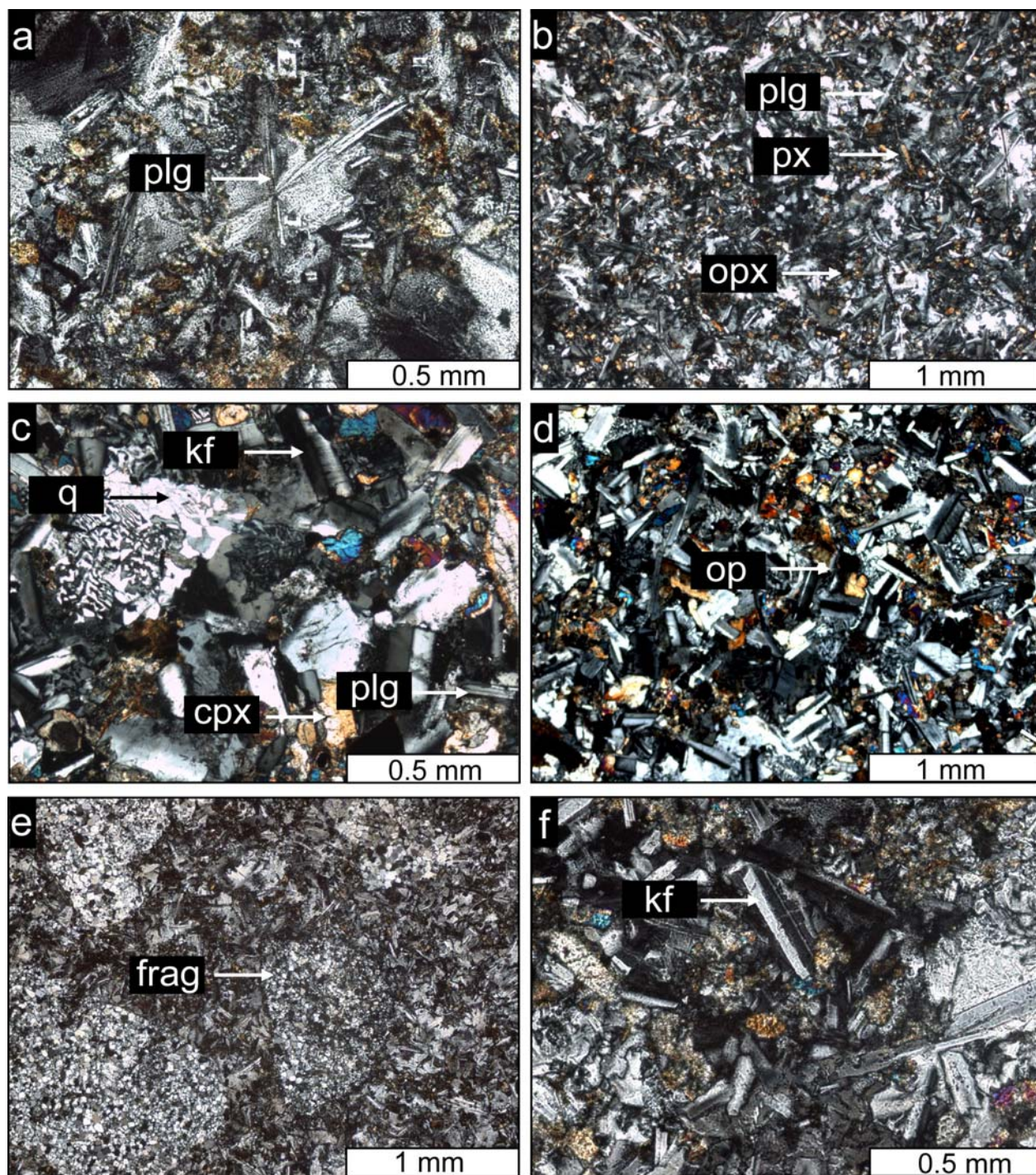


Figure 5.3: Thin section micrographs showing Granophyre matrices of selected samples. All micrographs are taken under crossed polarized light. (a-b) Spherulitic feldspar and pyroxene matrix from fragment-rich zone at site 188. (c-d) Granular feldspar and pyroxene matrix from fragment-poor zone at site 188. Note feldspar myrmekite in upper left corner of (c). (e) Spherulitic granophyre matrix in a zone with mm-wide rounded felsic fragments which comprise most quartz. (f) Granular feldspar and pyroxene matrix from fragment-poor zone at site 355. Note, plg = plagioclase, px = pyroxene, op = opaque mineral, opx = orthopyroxene, q = quartz, kf= kalifeldspar, plg = plagioclase.

Vredefort Granophyre dikes are characterized by a fine grained matrix of pyroxene, plagioclase, orthoclase, quartz, biotite and opaque minerals (Fig. 5.3a, b) as well as fragments of immediate wall rock types in the central dike portions (Fig. 5.3e). Matrices containing feldspar and pyroxene spherulites dominate fragment-rich zones (Fig. 5.3a, b, e). By contrast, granular textures are found in fragment-poor zones, the matrix of which consists of more plagioclase, hypersthene and clinopyroxene than the spherulitic matrices (Fig. 5.3c, d, f). The higher content of calcium in fragment-poor zones (Table 5-1 and Figure 5.4) may indicate the presence of clinopyroxene in the granular matrix. In this matrix, minerals are idiomorphic and larger than those in spherulitic matrices. Fragments in the Granophyre dikes of the granitoid core are compositionally similar to the granitoid wall rock (Fig. 5.2), whereas dikes at the core-collar boundary contain mostly quartzite, granitoid and epidiorite fragments.

5.2. XRF Analyses of Vredefort Granophyre

In order to characterize the compositional zonation in, and differences between, Granophyre dikes, fragment-rich and fragment-poor portions were analysed in two dikes from the core-collar boundary (Fig. 5.4). Nine Granophyre dike samples, i.e., 8 samples of dike 7 from site 188 and 1 sample of dike 8 from site 355 (Fig. 5.1b), were analysed for whole-rock chemical composition to investigate the compositional variation between dike margins and dike centres as well as the possible influence of a mafic Ventersdorp component on dike compositions (Table 5-1). In addition, published major and trace element contents for all nine Granophyre dikes and target rocks were compiled and compared to our data in order to determine the possible chemical heterogeneity between dikes from the core and the core-collar boundary as well as the possible influence of wall rock assimilation (Table 5-1) (Wilshire 1971; Bischoff 1972; McIver et al., 1981; Tankard et al., 1982; Reimold et al., 1990; Reimold 1991; Koeberl et al., 1996; Theriault et al., 1997).

In general, chemical trends of Vredefort Granophyre in terms of SiO_2 , Fe_2O_3 , Na_2O and some trace elements (e.g., Cr, Rb) are not apparent, whereby SiO_2 contents is 66-68 wt.%, Fe_2O_3 is 5-9 wt.% and CaO is about 4 wt.%. Granophyre dikes from the core-collar boundary are enriched in MgO, Fe_2O_3 and CaO but depleted in TiO_2 , K_2O and Sr, compared to the dikes from the core

(Table 5-1, Fig. 5.4b). Dikes from both areas show similar values in MnO, Al₂O₃ and Ba (Fig. 5.4; Table 5-1). Overall, Granophyre dikes from the core-collar boundary are more mafic than those from the core of the Dome. Fragment-poor zones, i.e., dike margins, are more mafic than fragment-rich zones, i.e., dike centres (Fig. 5.4a), and granitoid wall rock (Table 5-1). In particular, fragment-poor zones are enriched in CaO, MgO, Fe₂O₃, Al₂O₃, TiO₂, Cr and V, but depleted in SiO₂, K₂O, Rb, Sr, Zr and Ba with respect to all other Granophyre variants, including fragment-rich zones (Fig. 5.4a, b). For example, in the samples 188A1, 188A2, 188B1, 188B2 the MgO content is between 3.3 and 3.5 wt.%, that of SiO₂ between 66 and 68 wt.% and that of Cr between 388 and 406 ppm in the fragment-rich zones. In fragment-poor zones MgO ranges from 3.7 to 3.9 wt.%, SiO₂ from 61 to 62 wt.% and the Cr content is approximately 500 ppm. Dikes from the core-collar boundary, notably from within epidiorite wall rock (samples VAT 113 and VAT 156 in Table 5-1 and samples 2a in Figure 5.4) are enriched in Ni but depleted in Co, Cu and Zn with respect to fragment-poor Granophyre dikes (Table 5-1).

Granophyre dike compositions are intermediate between those of wall rock types, notably basaltic lava of the Ventersdorp Supergroup and granitoid wall rock (Fig. 5.5). This requires a significant involvement of a mafic component in the formation of the dikes, particularly in those that are located away from epidiorite and shale of the core-collar boundary. The fact that Granophyre dikes at this boundary are more mafic than those in the core of the Dome (Fig. 5.4a) can be attributed to assimilation of epidiorite wall rock (samples VAT 113, VAT 156 in Table 5-1) in fragment-rich zones (Fig. 5.4). In the most cases, however, the inner part of the Granophyre dikes is more mafic than the marginal part which suggests that the chemical differences can not only be explained by wall rock assimilation. Therefore, compositional differences between dikes from the core and those from the core-collar boundary as well as between fragment-poor and fragment-rich zones may indicate multiple pulses of melt emplacement into dikes.

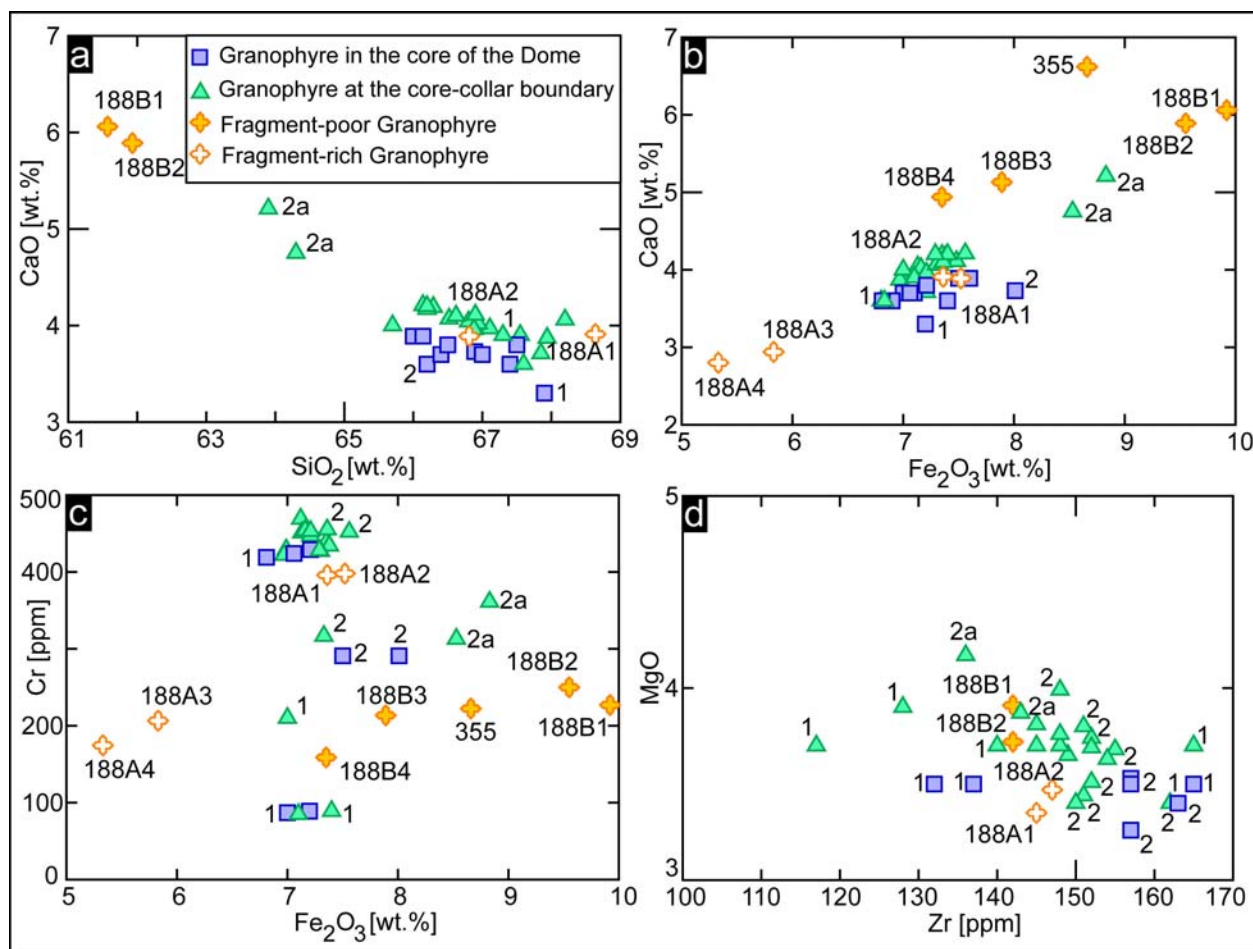


Figure 5.4: Diagrams showing selected major and trace element contents of Granophyre matrices with regard to the location in the core of the Vredefort Dome and fragment population obtained by XRF analyses. Published XRF data are from Reimold et al., 1990 – 1 and Theriault et al., 1997 – 2; - 2a (contact to epidiorite wall rock; sample numbers VAT 113 and VAT 156 in Table 5-1). (a) Diagram showing the distribution of CaO versus SiO₂. (b) Diagram showing the distribution of CaO versus Fe₂O₃. (c) Diagram showing the distribution of Cr versus Fe₂O₃. (d) Diagram showing the distribution of Zr versus MgO. Fragment-poor zones of Granophyre dikes show higher values of CaO, MgO, Fe₂O₃, most Cr and lower values of SiO₂ and Zr in contrast to fragment-rich zones. Chemical composition varies also within a given dike.

Table 5-1: XRF data of Granophyre matrices and wall rock types. Also shown are analyses of wall rock types from Bisschoff (1972, 1973); Wilshire (1971); McIver et al. (1981); Tankard et al. (1982); Reimold (1991) and Koeberl et al. (1996), as well as of Granophyre by Therriault et al. (1997) and Reimold et al. (1990).

Lithology	Granitoid	Granitoid	Granitoid	Granitoid	Granitoid	Granitoid	Granitoid	Quartzite/Conglomerate	Quartzite/Conglomerate	Quartzite
Sample number	669A3	592B	200C2	652B1	453A2	KuduA3	518A2	6A4	6A3	621A3
Major elements in [%]										
SiO ₂	72.10	70.35	73.25	74.54	73.12	72.99	67.13	96.92	82.11	91.55
TiO ₂	0.32	0.49	0.02	0.16	0.24	0.16	0.51	0.03	0.30	0.08
Al ₂ O ₃	13.89	15.28	15.55	14.08	14.47	13.97	14.46	1.06	9.87	4.96
Fe ₂ O ₃	2.33	2.83	0.30	1.38	1.40	1.49	5.77	0.38	1.32	1.34
MnO	0.02	0.05	0.01	0.02	0.03	0.02	0.07	0.00	0.02	0.00
MgO	0.34	0.46	0.01	0.10	0.24	0.28	1.18	0.05	0.59	0.01
CaO	1.16	1.62	1.13	0.82	1.07	1.35	2.21	0.04	0	0.00
Na ₂ O	2.52	5.31	5.02	4.88	5.25	8.23	5.03	0.02	0.30	0.03
K ₂ O	5.69	3.81	5.15	4.12	3.28	0.80	1.95	0.28	2.33	1.21
P ₂ O ₅	0.09	0.15	0.01	0.07	0.08	0.02	0.24	0.01	0.01	0.02
Lol.	0.75	0.60	0.39	0.46	0.96	0.99	1.88	1.72	1.75	1.11
Total	99.21	100.95	100.83	100.63	100.14	100.30	100.43	100.51	98.60	100.30
Trace elements in [ppm]										
Rb	155	156	101	161	113	23	61	7	8	40
Sr	280	438	390	224	240	664	627	9	11	28
Y	12	28	5	10	15	4	29	5	8	6
Zr	314	307	100	145	184	185	306	35	36	47
Nb	6	19	<3	6	6	<3	9	<3	<3	<3
Co	<6	<6	<6	<6	<6	7	10	<6	<6	<6
Ni	11	9	10	10	9	11	42	13	14	18
Cu	13	23	<6	5	<6	24	47	9	20	13
Zn	38	72	6	36	35	23	90	<6	<6	6
TiO ₂ [%]	0.30	0.49	0.01	0.16	0.24	0.16	0.54	0.02	0.30	0.09
V	25	30	<12	15	18	<12	47	<12	<12	21
Cr	144	115	138	239	104	186	1626	309	274	342
Ba	1492	991	1189	618	616	675	1205	88	92	330

Table 5-1 continued.

Quartzite	Quartzite	Quartzite	Quartzite	Alkali Granite	Epidiorit	Mafic Rock	Mafic Rock	Mafic Rock	Mafic Rock	Mafic Rock	Mafic Rock
64A1	64A1	64A3	102A2	4A2	564A2	LZ5	LZ18	LZ34	LE2	LE8	LE21
89.96	89.96	94.81	95.85	70.01	51.18	56.83	53.80	51.4	49.76	57.07	54.04
0.18	0.18	0.12	0.19	0.25	0.30	0.72	0.76	1.11	0.41	0.75	1.01
4.21	4.21	2.40	1.98	14.89	14.65	14.49	13.23	14.58	9.98	15.43	14.69
1.80	1.80	0.55	2.78	2.65	7.55	10.35	11.09	10.22	11.48	12.57	12.22
0.05	0.05	0.01	0.01	0.07	0.12	0.1	0.2	0.10	0.2	0.2	0.2
0.79	0.79	0.00	0.01	0.20	9.28	5.54	7.41	3.88	14.3	8.34	4.14
0.35	0.35	0.08	0.00	0.69	13.41	4.73	8.22	7.45	6.72	6	6.05
0	0	0.02	0.02	7.82	1.37	4.4	2.4	4.70	1.1	2.2	2.8
0.98	0.98	0.64	0.50	2.94	0.08	0.5	1.5	0.90	0.1	0.1	2
0.06	0.06	0.01	0.01	0.06	0.02	0.1	0.1	0.20	0.1	0.1	0.1
0.71	0.71	0.39	0.02	0.61	1.08	2.52	1.88	5.80	4.53	3.84	3.3
99.09	99.09	99.03	101.37	100.19	99.04	100.3	100.5	100.3	98.62	98.92	100.5
31	31	20	17	56	7	14.37	58.64	33.21	4.2	5.11	66.55
32	32	15	14	225	99	74.64	381.9	335	73.94	163.2	200.7
19	19	7	15	12	13	17.9	16.1	20.6	10.9	15.7	19
661	661	70	568	297	38	98.01	90.29	138.2	50.53	77.64	117.2
5	5	<3	4	18	3	1.63	1.27	5.02	2.4	1.48	3.7
24	24	<6	6	6	40	47.90	46.8	40.3	59.7	51.3	43.8
104	104	12	36	7	217	142.1	217.3	140.1	385.6	223.9	96.17
84	84	11	29	6	63	66.8	72.3	61.3	31.2		21.4
53	53	<6	7	55	58						
0.18	0.18	0.14	0.22	0.22	0.28	0.72	0.76	1.11	0.41	0.75	1.01
0.20	0.20	24	30	12	137	187.3	194.3	169.4	172.3	265.2	224.1
19	19	559	2282	137	985	155.6	474.4	66.34	1788	583.4	25.22
1069	1069	200	137	772	61						

Table 5-1 continued.

Mafic Rock	Mafic Rock	Mafic Rock	Mafic Rock	Mafic Rock	Mafic Rock	Mafic Rock	Mafic Rock	Mafic Rock	Mafic Rock
LE38	LE37	E1	E2	E3	C1	C2	A	H309	H1105
50.09	49.79	51.07	53.92	53.26	51.95	48.02	47.49	52.39	50.31
1.09	1.01	1.09	0.99	0.96	1.25	1.11	0.87	0.75	0.67
14.51	13.85	14.76	14.32	13.94	14.63	13.28	5.41	13.29	11.19
20.03	9.71	13.54	12.71	11.89	12.12	10.87	13.16	12.09	12.12
0.3	0.3	0.2	0.2	0.2	0.1	0.1	0.2	0.2	0.2
7.65	3.48	5.13	5.51	4.69	4.56	4.82	21.1	6.02	10
0.77	9.21	8.09	5.84	7.63	7.57	5.26	5.81	7.29	7.92
0	0	2.4	3.9	3.7	2.9	3.2	0.1	3.8	4.6
0.4	3.2	1.5	0.8	0.8	1.6	0.9	0	0.9	0.9
0.1	0.1	0.1	0.1	0.1	0.2	0.2	0.1	0.1	0.1
5.39	9.71	0.89	2.13	1.71	1.76	11.79	5.6	2.16	2.75
100.3	100.4	98.79	100.4	98.84	98.7	99.46	99.79	98.98	100.7
15.31	178.2	125	31	37	51	33	2	25	46
6.05	59.86	326	461	401	414	562	95	140	200
18.7	18.4	20.9	21.8	20.2	22.5	24.3	14.3	19	15.4
108.5	105.6	117.2	112.3	109.3	147.6	148	89.6	90.2	78.2
6.46	3.7	3.9	3.8	3.9	5.6	4.9	8.6	2.8	1.8
75.1	34.1	56	50	49	40	49	87	46	67
141.7	121.9	149	138	136	136	158	1207	160	340
7.64	82.4	104	61	84	112	57	99	69	56
		106	134	92	96	120	107	78	90
1.09	1.01	1.09	0.99	0.96	1.25	1.11	0.87	0.75	0.67
248.8	218.4	231	226	206	190	155	124	178	198
68.02	53.09	85	44	41	140	168	1540	246	1076
		457	350	354	890	431	63	203	323

Table 5-1 continued.

Mafic Rock	Mafic Rock	Mafic Rock	Alkali Granite	Epidiorite	Mafic Rock	Mafic Rock	Mafic Rock	Mafic Rock
LL9	L7-37	Bisschoff, (1972)	Bisschoff, (1973)	Wilshire, (1971)	McIver et al., (1981)	McIver et al., (1981)	Tankard et al., (1982)	Reimold, (1991)
53.69	54.33	54.80	73.57	52.80	43.56	49.02	54.92	50.70
0.61	1.08	1.60	0.15	0.43	1.00	1.04	1.22	1.80
15.13	13.74	15.70	13.58	14.50	8.56	8.44	14.72	13.50
11.57	11.17	8.50	8.40	8.30	1.27	1.06	12.70	14.30
0.2	0.1	0.16	0.05	0.15	0.21	0.18	0.19	0.20
6.25	6.27	2.70	0.13	8.50	17.58	14.42	4.93	6.00
4.07	8.07	5.80	0.49	12.10	8.50	7.91	6.88	9.30
2.1	3.1	5.70	5.85	1.70	0.04	0.83	3.51	2.20
2.8	0.9	1.50	3.98	0.14	0.21	0.18	0.68	1.00
0.1	0.1					0.21	0.27	0.30
3	1.79							
99.57	100.7	98.00	99.57	98.60	99.28	99.72	100.02	101.10
84.27	20.66					1	12	69
169.4	595.8				33	90	311	
15.1	19.3				16	15	22	
95.42	130.9				84	88	174	
1.07	4.19				5	4	4	
42.2	46.2							46
107.3	223.5				1241	804		124
29.4	117				98	88		
					103	56		
0.61	1.08							
177.3	181.2				200	196		
244.5	418				1982	1867		338
					67	129		270

Table 5-1 continued.

Norite	Shale	Granophyre	Granophyre	Granophyre	Granophyre	Granophyre	Granophyre	Granophyre	Granophyre
		7	7	7	7	7	7	7	7
Reimold, (1991)	Koeberl et al., (1996)	188A1	188A2	188A3	188A4	188B1	188B2	188B3	188B4
51.80	30.26	68.64	66.81			61.57	61.93		
0.40	0.11	0.51	0.52	0.42	0.40	0.67	0.66	0.58	0.49
15.70	2.49	12.45	12.48			13.30	13.51		
8.60	57.49	7.36	7.52	5.83	5.33	9.92	9.55	7.89	7.35
0.10	4.45	0.14	0.14	0.08	0.08	0.16	0.15	0.10	0.09
9.30	0.72	3.35	3.47			3.91	3.72		
12.70	0.27	3.91	3.89	2.94	2.80	6.06	5.89	5.13	4.94
1.40	0.01	2.76	2.62			3.34	3.44		
0.10	0.05	1.99	2.02	2.04	1.79	1.81	1.68	1.88	2.14
0.10	0.10	0.11	0.10			0.13	0.12		
1.10	3.57	0.01	0.02			0.02	0.01		
101.30	99.51	101.21	99.59			100.89	100.66		
3	6	66	69	65.31	57.24	59	60	67.05	64.45
	38	232	234	253.7	236.72	219	222	260.63	248.92
	9.6	18	18	29.18	26.96	21	22	30.13	28.86
	24	145	147	165.3	146.91	142	142	158.94	160.19
	2.1	6	6	22.37	17.84	7	7	25.25	19.67
43	15.70	25	29			28	31		
247	55.00	106	120	74.15	79.36	90	81	64.88	116.10
		48	45	50.22	45.21	58	55	76.37	94.09
	20	61	63	56.85	55.43	80	80	69.03	67.39
	0.11	0.51	0.52	0.42	0.40	0.67	0.66	0.58	0.49
	0	86	85			116	119		
138	142	396	398	222.33	174.57	227	250	213.43	158.85
111	240	516	513	59.17	251.34	388	406	204.05	139.99

Table 5-1 continued.

Granophyre	Granophyre	Granophyre	Granophyre	Granophyre	Granophyre	Granophyre
8	2	2	4	5	7	8
355	VAT 8a (Therriault et al., 1997)	VAT 8b (Therriault et al., 1997)	VAT 69 (Therriault et al., 1997)	AU 14A (Therriault et al., 1997)	VAT 113 (Therriault et al., 1997)	VAT 141 (Therriault et al., 1997)
	66.00	66.14	66.89	66.29	63.9	68.2
0.33	0.59	0.60	0.56	0.53	0.59	0.47
	12.82	12.81	12.60	12.67	12.86	12.6
8.66	7.50	7.60	8.01	7.35	8.83	7.33
0.27	0.13	0.12	0.13	0.17	0.14	0.15
	3.26	3.31	3.53	3.68	3.87	3.81
6.62	3.89	3.89	3.73	4.19	5.21	4.06
	2.28	1.85	2.22	2.82	2.76	2.75
1.38	2.32	2.34	2.11	2.15	1.9	2.23
	0.11	0.10	0.11	0.11	0.13	0.11
	0.02	0.02	0.21	0.04	0.32	0
	98.92	98.78	99.90	100	100.51	101.71
51.53	79		79	74	67	76
184.45	243		243	240	228	228
22.27	16		16	16	19	15
126.97	157		157	155	143	145
21.25	8		7	7	7	8
	21		23	23	22	21
138.60	87		92.80	96	114.4	103.9
77.39	43		40	46	45	34
91.90	53		62	59	62	54
0.33	0.59		0.56	0.53	0.59	0.47
	97		103.70	99	116	99.3
222.33	291		291	438	360.9	316.7
59.17	475		519	477	432	426

Table 5-1 continued.

Granophyre	Granophyre	Granophyre	Granophyre	Granophyre	Granophyre	Granophyre	Granophyre
8	8	8	8	8	8	8	8
AU 1A (Therriault et al., 1997)	AU 1B (Therriault et al., 1997)	AU 4 (Therriault et al., 1997)	AU 5 (Therriault et al., 1997)	AU 6 (Therriault et al., 1997)	VAT 6A (Therriault et al., 1997)	AU 7 (Therriault et al., 1997)	AU 10A (Therriault et al., 1997)
67.11	66.8	66.2	66.94	67.55	66.88	67.94	66.52
0.46	0.48	0.49	0.48	0.5	0.51	0.51	0.49
12.76	12.77	12.74	12.55	12.48	12.53	12.43	12.77
7.12	7.13	7.38	7.16	6.99	7.21	6.97	7.3
0.16	0.12	0.16	0.13	0.14	0.14	0.13	0.14
3.65	3.74	3.8	3.7	3.51	3.63	3.44	3.69
3.97	4.04	4.17	4.02	3.9	3.96	3.87	4.07
2.58	2.66	2.68	2.61	2.56	2.57	2.46	2.7
2.14	2.17	2.28	2.23	2.19	2.15	2.15	2.23
0.09	0.09	0.1	0.09	0.11	0.11	0.1	0.1
0.04	0	0	0.09	0.04	0.21	0	0
100.08	100	100	100	99.97	99.9	99.97	100.01
77	77	83	80	75	77	72	80
226	231	224	220	229	229	234	230
17	17	18	16	18	17	18	18
149	152	151	148	152	154	151	152
7	8	8	6	8	7	6	8
20	19	22	21	20	21	22	21
102	99	97	96	93	95	92	103
46	45	41	42	46	41	44	42
57	57	58	59	57	58	56	59
0.46	0.48	0.49	0.48	0.5	0.51	0.51	0.49
92	92	93	95	98	90	92	97
469	451	434	454	429	447	422	427
449	446	456	438	483	474	474	450

Table 5-1 continued.

Granophyre	Granophyre	Granophyre	Granophyre	Granophyre	Granophyre	Granophyre	Granophyre
9	9	9	9	9	1	1	1
VAT 143 (Therriault et al., 1997)	VAT 156 (Therriault et al., 1997)	AU 11 (Therriault et al., 1997)	AU 13 (Therriault et al., 1997)	AU 13A (Therriault et al., 1997)	BG 3 (Reimold et al., 1990)	VT 2004 (Reimold et al., 1990)	BG CB (Reimold et al., 1990)
66.9	64.3	67.85	66.14	66.62	67	66.2	67.9
0.44	0.5	0.52	0.49	0.47	0.5	0.2	0.5
12.7	12.48	12.48	12.57	12.67	13	12.5	12.6
7.48	8.53	7.21	7.56	7.36	7	7.4	7.2
0.14	0.16	0.14	0.15	0.14	0.14	0.25	0.13
3.7	4.17	3.4	3.99	3.76	3.5	3.1	3.2
4.11	4.75	3.71	4.21	4.1	3.7	3.6	3.3
2.98	2.69	2.54	2.58	2.53	2.7	3.4	2.5
2.23	1.98	2.07	2.18	2.27	2.4	2.65	2.4
0.1	0.12	0.1	0.09	0.09	0.1	0.3	0.13
0.63	0.08	0	0.05	0	0.05	0.2	0.09
101.43	99.76	100.02	100.01	100.01	100.09	99.8	99.95
77	71	68	81	85	78		
220	223	240	220	221			
15	18	17	19	16			
145	136	162	148	148	137		
8	6	6	8	6			
22	30	3	22	21	25		
92	92.6	93	101	99	93		
36	43	44	43	43			
59	64	58	58	57			
0.44	0.5	0.52	0.49	0.47	0.5		
	115	92	94	91			
	312.8	453	452	455	87		
420	429	474	436	430	497		

Table 5-1 continued.

Granophyre	Granophyre	Granophyre	Granophyre	Granophyre	Granophyre	Granophyre	Granophyre
1	1	1	3	7	8	8	8
BG 7 (Reimold et al., 1990)	BG 8 (Reimold et al., 1990)	BG 9 (Reimold et al., 1990)	BG 4 (Reimold et al., 1990)	BG 208 (Reimold et al., 1990)	BG 10 (Reimold et al., 1990)	BG 92 (Reimold et al., 1990)	BG 168 (Reimold et al., 1990)
66.4	66.5	67.4	67.5	65.7	67.6	67.3	66.2
0.55	0.57	0.52	0.5	0.5	0.49	0.5	0.5
12.8	12.7	12.6	12.7	12.5	12.6	12.4	12.8
7.1	7.2	6.9	7.2	7	6.8	7.1	7.4
0.13	0.14	0.13	0.14	0.14	0.13	0.14	0.15
3.5	3.3	3.4	3.5	3.7	3.4	3.9	3.7
3.7	3.8	3.6	3.8	4	3.6	3.9	4.2
3.3	3.3	3.1	2.5	2.9	3	2.6	2.6
2.3	2.3	2.3	2.1	2.2	2.3	2.2	2.3
0.11	0.13	0.1	0.1	0.1	0.1	0.1	0.1
0.12	0.04	0	0	1.3	0	0	0.1
100.01	99.98	100.05	100.04	99.9	100.02	100.14	100.05
			65	78		73	84
			132	165		128	117
			27	23		25	25
			100	111		105	134
			89	210		85	89
			512	451		438	470

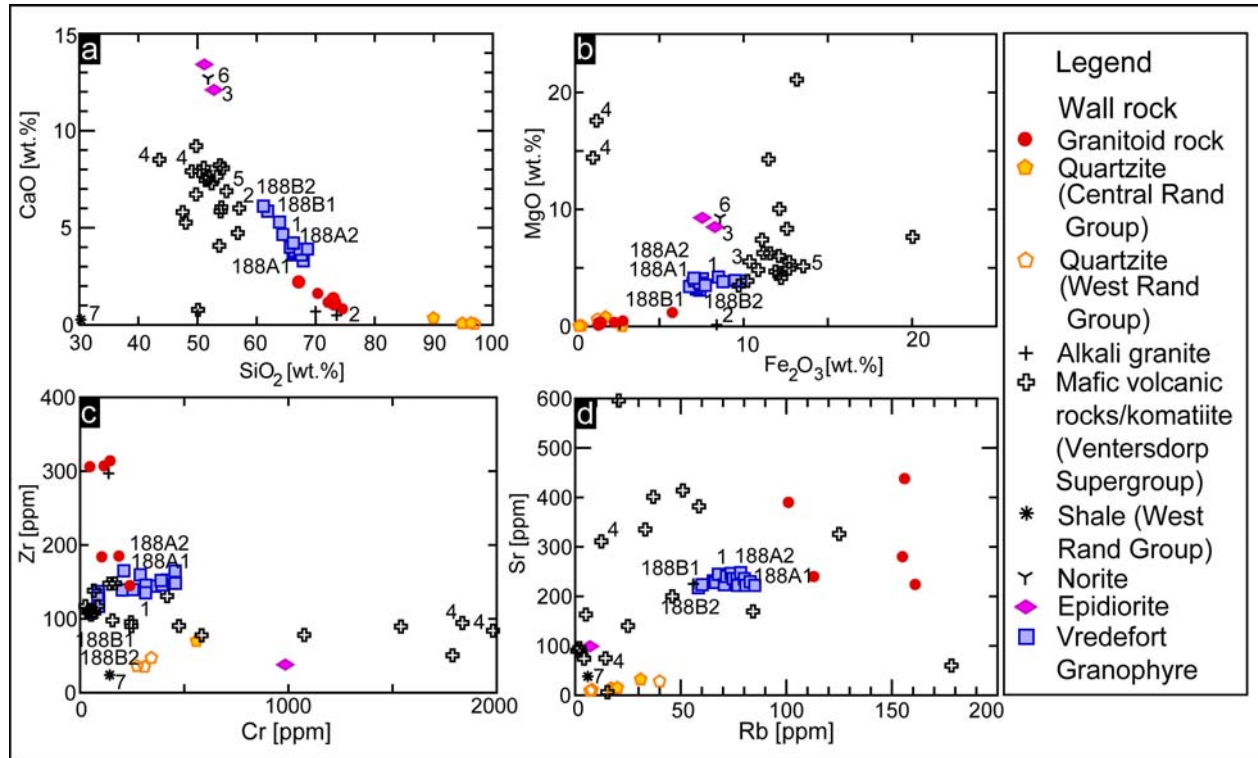


Figure 5.5: Diagrams showing selected major and trace element contents of Granophyre matrices and the target rocks obtained by XRF analyses and calculated mixing of the main component. Published XRF Granophyre data are from Therriault et al. (1997) – 1. Target rock data are from Bisschoff, (1972), Bisschoff, (1973) – 2, Wilshire, (1971) – 3, McIver et al. (1981) – 4, Tankard et al. (1982) – 5, Reimold, (1991) – 6 and Koeberl et al. (1996) – 7. (a) Diagram showing the distribution of CaO versus SiO₂. (b) Diagram showing the distribution of MgO versus Fe₂O₃. (c) Diagram showing the distribution of Zr versus Cr. (d) Diagram showing the distribution of Sr versus Rb. Granophyre composition is intermediate between that of all wall rock types, notably basalt of the Ventersdorp Supergroup and granitoid wall rock. This requires a significant involvement of a mafic component in the formation of Granophyre dikes, particularly in those that are located away from epidiorite and shale of the core-collar boundary.

6. Discussion

Compositional, petrographic and textural variability of Granophyre dikes are critical for understanding the mode and timing of dike formation with respect to stages of impact crater formation at Vredefort. The apparent compositional similarity of, and absence of mafic fragments in, the dikes was previously interpreted in terms of injection of impact melt without a melt component from Ventersdorp lava into crater floor fractures during crater formation (Dietz, 1961; French et al., 1989; French and Nielsen, 1990; Reimold et al., 1990; Koeberl et al., 1996;

Reimold and Gibson, 2006). However, mixing calculations by Therriault et al. (1997) suggest a significant mafic component in the Granophyre dikes.

Our petrographic and XRF analyses show that Granophyre dikes are heterogeneous with regard to texture and chemical composition, respectively. Regardless of dike positions, dike margins are fragment-poor, characterized by a granular matrix and are more mafic than dike centres, which are fragment-rich and have a spherulitic matrix. This is at variance with the notion that textural and mineralogical variation is observed only between dikes in the core and those at the core-collar boundary (Therriault et al. 1996). The compositional variation between dikes from these areas was attributed either to variable wall rock assimilation (Reimold and Reid, 1989; Therriault et al., 1997) or to the emplacement depth of the dikes (Therriault et al., 1996). If compositional zoning of the Vredefort Granophyre dikes were due to assimilation of wall rock, marginal zones of the Granophyre dikes should be more enriched in wall rock material than the inner part of these dikes. Based on our study, wall rock fragments in the marginal zones are rare.

If wall rock assimilation was important, MgO and SiO₂ contents in fragment-poor zones (3.8 wt.% and 62 wt.%, respectively) should be intermediate between that of fragment-rich zones (3.4 wt.% MgO and 67 wt.% SiO₂) and immediate wall rock (0.3 wt.% MgO and 72 wt.% SiO₂). Evidently, this is not the case (Table 5-1). Moreover, the low concentration of Zr and Si but higher concentration in Mg, Cr, Fe in fragment-poor zones indicates that these zones are enriched in a mafic component, compared to the fragment-rich zones. In addition, the higher content of Zr in the inner part of the Granophyre dikes shows that chemical fractionation within individual dikes can be excluded. During this process, fractionation of newly formed zircon should reduce Zr concentration in the inner part, but the opposite is observed (Table 5-1). The sum of these observations indicates that *in situ* assimilation of local wall rock material is unlikely to have caused major chemical differentiation of the Granophyre dikes. However, intrusion of two compositionally distinct melt phases can account for the observed chemical characteristics of the dikes.

Petrographical and chemical heterogeneity of Vredefort Granophyre may be due to assimilation of host rock at the base of the superheated impact melt sheet and differentiation of the sheet. Thereby, the chemical composition of the Granophyre dikes would depend on composition and volume of assimilated host rock type as well as on the heterogeneous distribution of target rock

types in contact with the base of the melt sheet. The composition of assimilated host rock may also change as a function of temperature. If compositional heterogeneity of dikes is caused by target rock assimilation during the evolution of the superheated basal impact melt sheet, dikes in the core of the dome must differ in chemical composition to those at the core-collar boundary, due to variable target rocks in contact with the melt sheet. Such difference in composition between dikes is evident (Table 5-1, Figure 5.4a). In particular, the high contents of MgO, CaO and Cr and the low content in Zr point to an enhanced influence of mafic target rock in dikes at the core-collar boundary. Thus, the compositional shift from dikes in the core to those at the core-collar boundary may well be due to assimilation of heterogeneous target rock types at the base of the impact melt sheet.

The compositional, textural, and petrographic characteristics of Granophyre dikes are remarkably similar to those of the so-called Offset Dikes of the Sudbury Igneous Complex (Grant and Bite, 1984), Canada. Riller et al. (2005) and Hecht et al. (2008) proposed a two-stage scenario for the formation of these dikes that may apply also for the origin of Granophyre dikes at Verdefort. In this scenario, the compositional shift from fragment-rich melt in the dike centres toward fragment-poor melt at dike margins is due to variable degrees of assimilation of different target rock types at the base of the initially superheated impact melt sheet. More specifically, initial melt derived from the impact melt sheet was contaminated with variable target rock lithologies, including mafic Ventersdorp strata, causing the melt emplaced first to be mafic and fragment-poor. As the first melt pulse was hotter than the following pulse more fragments were assimilated in the first pulse. During cooling of the impact melt sheet, its capacity to assimilate target rock, notably mafic ones, ceased, thus producing a more fragment-rich melt phase. Thus, mafic host rock fragments may have been entrained in the melt without being assimilated completely during later melt intrusion. Indeed, mafic fragments are present sporadically in the fragment-rich Granophyre (private communication with Uwe Reimold), which agrees with this scenario. Moreover, the presence of well-rounded and elliptical fragment shapes in the fragment-rich phase can be explained by such incomplete assimilation and thermal corrosion of fragment margins. Due to the lower liquidus temperature of felsic rocks, these rocks may have been assimilated at lower temperatures, thus generating more felsic and fragment-rich melt compared to initially emplaced melt.

Interestingly, the Granophyre dikes and pseudotachylite bodies at Vredefort display the same geometric pattern as the Offset Dikes at Sudbury, pointing to similar strain fields during emplacement of these melt bodies. Based on petrological evidence, the emplacement of Offset Dikes occurred up to ten thousand years after impact (Riller et al., 2005; Hecht et al., 2008) and is in agreement with the hypothesis of isostatically-driven crater floor fracturing for these dikes (Wichmann and Schultz, 1993). Such mechanism of dike formation is also conceivable for the Granophyre dikes at Vredefort. Notably, granophyre dikes at Vredefort are unstrained and cut across upturned supracrustal strata. Thus, formation of Granophyre dikes postdates the formation of pseudotachylite bodies (Bisschoff, 1988; 1996) and occurred after crater formation. By contrast, the formation of pseudotachylite dikes at Vredefort and Sudbury has been attributed to intrusion of impact melt into extension fractures during collapse of the central uplift (Lieber et al., 2009; Riller et al., 2010). Thus, Granophyre dikes at Vredefort, Offset Dikes at Sudbury and pseudotachylite bodies in both impact structures are essentially derived from the same melt pool, i.e., the impact melt sheet, and formed by the same mechanism, i.e., drainage of impact melt into extensional fractures of the crater floor. Differences in geometrical, textural, chemical and fragment characteristics between the individual melt bodies can be explained by operation of this mechanism at different times after impact.

7. Conclusions

Granophyre dikes of the Vredefort Dome are characterised by (1) compositional differences between dikes from the core and those from the core-collar boundary of the Dome, (2) marked compositional and textural differences within individual dikes, and (3) fragment-rich, felsic central dike portions and fragment-poor, mafic dike margins. Collectively, this suggests that melt was derived from compositionally different melt sources and emplaced in at least two pulses. Granophyre dikes formed by injection of melt from the overlying impact melt sheet into target rock fractures after cratering. Geochemical evidence suggests that *in situ* assimilation of local wall rock material is unlikely to have caused major chemical differentiation of the Vredefort dike. The chemical heterogeneity between fragment-rich and fragment-poor dike zones can be explained by variable assimilation of a mafic component during cooling of the impact melt sheet.

In addition, gravitational differentiation may have lead to accumulation of more mafic melt at the base of the melt sheet from which fragment-poor dike zones formed. This explains the mafic character of melt emplaced first in dikes and the more felsic and fragment-rich nature of melts during the second emplacement pulse, when the impact melt was less hot, thus, unable to digest large quantities of (mafic) wall rock fragments as well as enriched in felsic material caused by differentiation. Formation of Granophyre dikes was possibly driven by late-stage isostatic readjustment of crust underlying the impact structure. Differences in geometrical, textural, chemical and fragment characteristics between the Granophyre dikes and pseudotachylite bodies can be explained by impact melt drainage operating at different times after impact.

Acknowledgements

This work was funded by the German Science Foundation (grants Ri 916/8-1 and Re 528/6-2). K. Born provided technical support. L. Hecht helped with the interpretation of geochemical data.

CHAPTER 6: SUMMARY, SYNTHESIS AND OUTLOOK

6.1. Summary

6.1.1. Summary of structural data of pseudotachylites

1. Mapping of pre-impact metamorphic mineral shape fabrics in the crystalline core of the Dome shows that a sub-vertical, NW-SE striking fabric orientation prevails in the core centre and a circumferential fabric strike is found near the core-collar boundary. The high spatial coverage of the data revealed that fabric strike is symmetric about a NW-SE striking vertical mirror plane passing through the Dome centre.
2. Large pseudotachylite bodies are found chiefly in the outer core zone and sporadically in the collar rocks. By contrast, the inner core hosts pseudotachylite zones with rather low brecciation intensity, whereby the majority of stations are effectively devoid of pseudotachylite occurrences. A marked decrease in brecciation intensity and occurrence of pseudotachylite exposure toward the Dome centre occurs at a radial distance between 9 and 15 km from the core-collar boundary. In the outer core zone, maximal concentration of pseudotachylite zones occurs at radially inward distances of about 1 to 4 km and 7 to 9 km from the core-collar boundary. The arrangement of pseudotachylite zones shows a high centro-symmetric pattern in the Vredefort Dome.
3. Measurement of the horizontal component vector of the maximum dilation direction in the outer core of the Vredefort Dome indicates either radial or concentric stretching of material, regardless of pseudotachylite body orientation. Dilation magnitudes are maximal in the outer core zone close to the core-collar boundary, whereas the inner core is dominated by small dilation magnitudes and concentric stretching of material. The horizontal component vectors of dilation display a remarkably centro-symmetric pattern with respect to the Vredefort Dome.

4. Fragments in large pseudotachylite bodies are almost exclusively derived from the immediate host rock, generally display jigsaw geometry, vary greatly in size and are angular to well-rounded. Generally, fragments are more angular and elliptical near zone margins and more rounded and circular in the interior of pseudotachylite zones. The traces of pre-impact mineral fabrics on outcrop surfaces suggest that the fragments underwent limited but progressive rotation towards the centre of the pseudotachylite bodies.
5. The symmetry of pre-impact fabric and geometry of pseudotachylite zones are consistent with vertical stretching and uplift of the inner core and outward rotation and dilation in the outer core zone as is predicted for rocks at the current erosion level by numerical modelling of the impact event.

Comprehensive structural analysis of pre-impact mineral fabrics and properties of fragment-rich pseudotachylite in the Vredefort Dome suggests that melt is allochthonous and was emplaced at an advanced stage of cratering into tensional fracture zones within the crater floor. Tensional fracture zones opened in an overall dilational strain field towards the end of cratering, likely during collapse of the central uplift, and formed low pressure zones, into which melt was drawn. Melt may have been drained from the overlying impact melt sheet or from sites within the crater floor and transported into fragment-rich dilation zones. Our field-based analysis failed to identify the presence of bona fide shear faults that could potentially have generated in situ frictional melts and fragments. Furthermore, target rock fragmentation and melt generation that resulted in fragment-rich pseudotachylite bodies are processes separated in space and time during cratering.

6.1.2. Summary of geochemical data of pseudotachylites

1. XRF analyses of the contents of pseudotachylitic veins and dikes and their respective wall rocks from the Vredefort Dome indicate compositional differences between pseudotachylite matrix and immediate wall rock. Major elements of pseudotachylite matrices generally plot closer to those of the average Vredefort Granophyre composition than do major elements of their wall rocks. In fact, there are conspicuous trends in the

compositional deviation of pseudotachylite matrices from their respective wall rocks towards a granitoid composition.

2. SEM and electron microprobe analyses show the occurrence of two different Domains A and B which are characterized by high element peaks of Si, Al, Mg, Na and low element peaks of K, Ca, Ti and Fe obtained by EDX analyses, whereby Ca, Mg and Fe are more abundant in Domain B than in Domain A. In terms of abundance of wall rock fragments and mineralogical composition, the matrix in the Salvamento sample (large pseudotachylite body) is akin to that in Domain A from the vein at SunWa. Moreover, the matrix at Salvamento shows the same element distribution as Domain A in the vein from SunWa. This suggests that compositions of both matrices were influenced by assimilation of wall rock. In particular, assimilation seems to be more effective in large-volume pseudotachylite bodies, such as at Salvamento, that are devoid of any compositional zoning but rich in wall rock fragments. Domain B matrices, by contrast, are devoid of felsic wall rock fragments and thus, are mafic in character and, constitute likely less contaminated matrix material. These observations can be explained by the magnitude of assimilation being controlled by the surface area of (felsic) wall rock fragments and cooling rate of the pseudotachylitic melt.
3. SEM and Electron microprobe analyses indicate that transport of pseudotachylite melt in veins occurred over distances of at least centimetres to metres. As evident from the SunWa and Kudu locations, direction of melt transport was from larger pseudotachylite bodies toward smaller ones and into apophyses. Thereby, the ribbon indicates local entrainment of wall rock material into the pseudotachylite matrix of the apophysis, whereby transport of material occurred from the host vein into the apophysis. Electron microprobe analysis of Kudu shows the mafic character of the pseudotachylite matrix increases from sites A to D. This can be explained by input of a mafic wall rock component from sites B and C. The fact that the matrix at Kudu is significantly more mafic than its granitoid wall rock and pseudotachylite matrices elsewhere may be due to progressive incorporation of mafic material on the dm- or larger scale as the vein transects

other portions of amphibolite wall rock. Electron microprobe analysis points to melt transport from larger pseudotachylite bodies into smaller ones.

4. The initial estimated temperature of pseudotachylitic melt must have been at least between about 1200°C and 1700°C. Therefore, sulphide and silicate mineralogy may aid in estimating the temperature of this melt. Pyrrhotite and chalcopyrite are commonly found in the matrix of pseudotachylite veins. If formed from pyrite, which is present in wall rocks but not in the pseudotachylite matrix, the presence of pyrrhotite in the matrix points to temperatures of the pseudotachylite melt above 1200°C (Kullerud, 1967; Magloughlin, 2005). Furthermore, the margin of zircon in wall rock bordering on pseudotachylite is corroded. At ambient pressures, zircon decomposes to oxides at a temperature of about 1690°C (Finch and Hanchar, 2003). Generation of such hot melts is difficult to reconcile with mechanisms that are known from endogenous melt-forming processes, i.e., frictional heating and decompression, and calls for a mechanism that is capable of instantaneously producing large volumes of superheated silicate melt.

The geochemical data, in conjunction with structural information and the considerations delineated above suggest that hypothesis for an origin of pseudotachylitic melt adhering to *in situ* melting processes by, e.g., frictional shearing, decompression or shock loading below the crater floor, are implausible for the cases of large pseudotachylite occurrences. Geochemical characteristics of pseudotachylitic melt and the sheer volumes of this melt observed at Vredefort and Sudbury are suggestive of injection of superheated melt from the overlying impact melt sheet into target rock during cratering.

6.1.3. Summary of geochemical data of Vredefort Granophyre

1. On detailed consideration, our thin section and XRF analyses show heterogeneity with regards to chemical compositions and texture of matrices in Granophyre dikes e.g. more mafic, marginal, fragment-poor area with granular matrix and more felsic inner fragment-rich area, showing spherulitic matrix. Granophyre areas show different melt flow pattern, convolute pattern at the margins and laminar melt flow in the inner zones.
2. The geochemical data indicate a significantly chemical adjustment of wall rock and Granophyre matrix by assimilation. However, the mafic composition of fragment-poor area matrix in contrast to immediate wall rock which is located at the contact to the felsic wall rock and more felsic fragment-rich area matrix may not be due to assimilation. Consequently, assimilation is important in most cases, but it is difficult to explain in terms of the formation of more mafic fragment-poor zones.

Collectively, this suggests that melt was derived from compositionally different melt sources and emplaced in multiple, i.e., at least two, pulses. Granophyre dikes formed by injection of melt from the overlying impact melt sheet into target rock fractures after cratering. The chemical heterogeneity between fragment-rich and fragment-poor dike zones can be explained by variable assimilation of a mafic component, i.e., Ventersdorp basalt, at the base of impact melt sheet, when the melt sheet was hottest. This explains the mafic character of melt emplaced first in dikes and the more felsic and fragment-rich nature of melts during the second emplacement pulse, when the impact melt was less hot and thus unable to digest large quantities of (mafic) wall rock fragments. Formation of Granophyre dikes was possibly driven by late-stage isostatic readjustment of crust underlying the impact structure.

6.2. Synthesis

Comprehensive structural analysis of pre-impact mineral fabrics and properties of fragment-rich pseudotachylites in the Vredefort Dome suggests that the melt is allochthonous and was emplaced at an advanced stage of cratering into tensional fracture zones within the crater floor. The geochemical data, in conjunction with structural data suggest that the hypothesis for an origin of pseudotachylitic melt is adhering to *in situ* melting processes by, e.g., frictional shearing, decompression or shock loading below the crater floor, are implausible for the cases of large pseudotachylite occurrences. This synthesis is based on all results (see summary) of this thesis and is displayed in Fig. 6.1 and Fig. 6.2.

Fig. 6.1 represents a model of pseudotachylite formation during the cratering process. Thereby, four stages are evident which affected the pseudotachylite formation (French, 1998). Stage 1 represents the excavation phase and the beginning of central uplift of the target rocks shortly after impact. Thereby, shock-induced pseudotachylites were generated in the target rocks during the contact/compression stage (e.g. Martini 1991). However, it seems that not all small fractures consist of melt documented by small reddish and greyish veins in Chapter 4 with or without melt (Fig. 6.1). Stage 2 begins with the collapse of the central uplift and shows the centripetal and upward motion of rock during gravitational collapse of the transient cavity followed by gravitational outward spreading of uplifted rock. Thereby, tensional fracture zones opened in an overall dilational strain field and formed low pressure zones (Fig. 6.1), into which melt was drawn by pressure gradients. This is documented by SEM and Electron microprobe analyses which indicate that transport of pseudotachylite melt in veins occurred over distances of at least centimetres to metres. As evident from the SunWa and Kudu locations, direction of melt transport was from larger pseudotachylite bodies toward smaller ones and into apophyses. In addition, the arrangement of pseudotachylite zones shows a highly centro-symmetric pattern as well as a decrease of brecciation intensity directed to the centre of the Vredefort Dome which are consistent with vertical stretching and uplift of the inner core as well as outward rotation and dilation in the outer core zone as is predicted for rocks at the current erosion level by numerical modelling of the impact event. However, small shock-induced veins served as weakness zone in which impact melt could invade in still-molten shock networks (Fig. 6.1).

Stages 3 and 4 comprise the early and the later modification stage, whereby in stage 3 small pseudotachylite veins were displaced by fractures caused by gravitational downward movement of the collar rock (Fig. 6.1) as documented by Jahn and Riller, (2009). Such fractures may be formed by sliding of the target rocks (Fig. 6.1). The later modification stage is characterized by small reddish fractures and slight displacements within large pseudotachylite bodies. These characteristics are only possible upon colling and solidification of large pseudotachylite bodies (Fig. 6.1). The formation of these fractures may be caused by the same mechanism which formed fractures in which impact melt was intruded in order to form the Vredefort Granophyre dikes. Structural, petrographical and XRF analyses point to Vredefort Granophyre dike formation by crater floor fracturing, possibly driven by late-stage isostatic readjustment of crust underlying the impact structure like in Sudbury for the offset dike formation (Hecht et al., 2008). Correlation of melt temperature estimates of Offset Dikes with modelled cooling rates of the impact melt sheet at Sudbury suggests that Offset Dikes were emplaced up to ten thousand years after impact (Hecht et al., 2008). And, this could be the process and the timing which are responsible for the formation of the fractures and small displacements within large pseudotachylite bodies concluding in stage 4.

This model summarized that the input of impact melt in large pseudotachylite bodies is a viable process and that e.g. shock-induced pseudotachylites or weakness zones may form during the contact/compression stage into which impact melt intruded. However, the generation of some observed fractures during impact cratering is unclear.

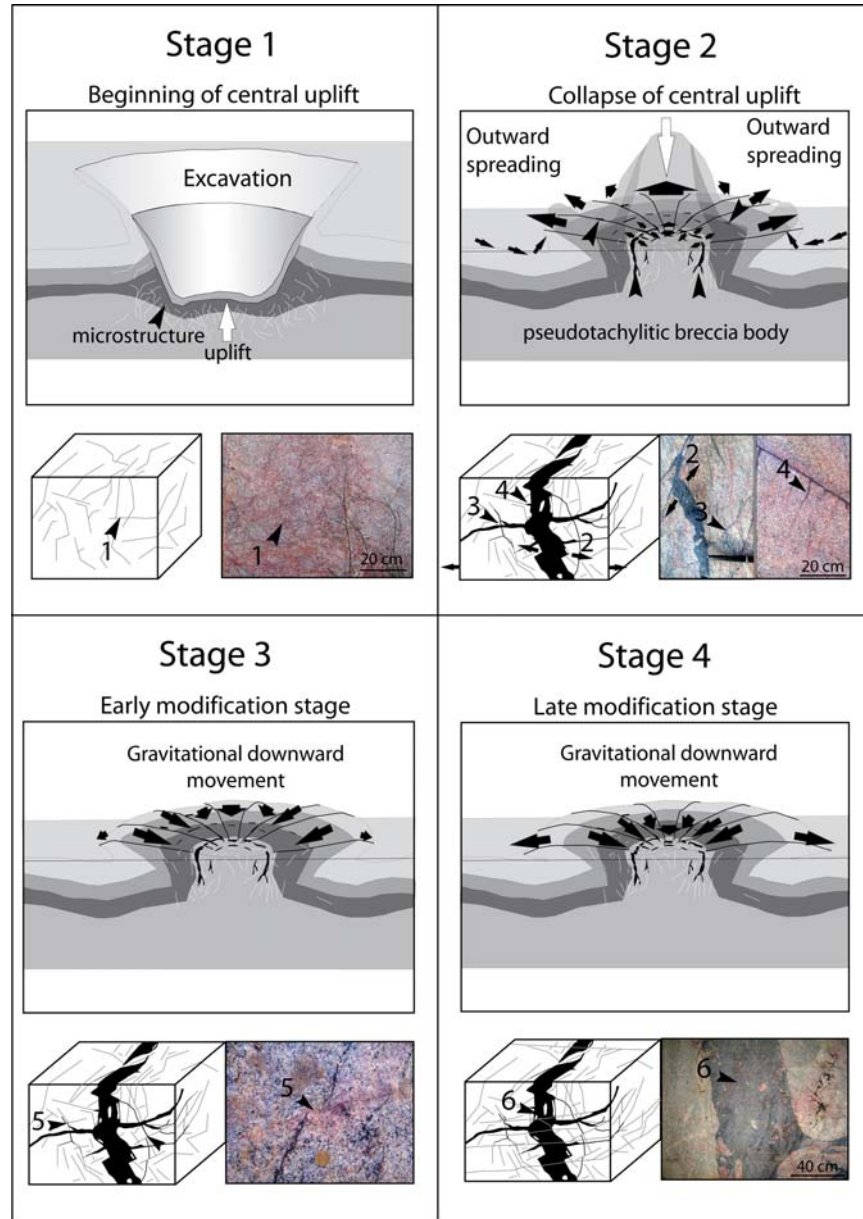


Figure 6.1: Model of the pseudotachylite formation in the cratering processes. Stage 1 represents phase 1 with the excavation and the beginning of central uplift of the target rocks short after the impact. Thereby, shock-induced microfractures figured as small reddish and greyish veins (1) are formed in the ground in the contact/compression stage. Stage 2 begins with the collapse of the central uplift and shows the centripetal and upward motion of rock during gravitational collapse of the transient cavity followed by gravitational outward spreading of uplifted rock. Thereby, tensional fracture zones opened in an overall dilational strain field and formed low pressure zones (2) and apophysis (3), into which melt was drawn. Melt may have been drained from the overlying impact melt sheet into low pressure sites including apophyses. However, small shock-induced veins served as weakness zone into which impact melt could have been emplaced in still-molten shock networks (4). Stages 3 and 4 comprise the early and the later modification stage, whereby in stage 3 pseudotachylite veins were displaced by gravitational downward movement of the target rock indicated by younger reddish veins (5). In the later modification stage large cooled pseudotachylite bodies were displaced or contain small reddish veins (6).

Fig. 6.2 represents a model of injection of impact melt from overlying melt sheet into low pressure sites and shows the variable magnitudes of assimilation. The initial estimated temperature of pseudotachylitic melt between about 1200°C and 1700°C shows that it is possible to find impact melt in this depth. SEM and electron microprobe analyses have shown that small veins have different compositional domains, but large pseudotachylite bodies have one domain with similar chemical composition like the wall rock. These observations can be explained by the magnitude of assimilation being controlled by the surface area of (felsic) wall rock fragments, cooling rate of the pseudotachylitic melt and depth of intrusion. This means that large pseudotachylite bodies cooled slower than small veins and consequently, large volume of melt assimilated more and longer wall rock fragments up to adaption their chemical compositions. Based on the pre-impact configuration of fragments in the pseudotachylite zones and the overall paucity of exotic fragments this thesis shows that the vast majority of fragments in the largest zones were not transported over distances larger than tens of metres. This suggests that brittle deformation caused by localization of bending strains accounts for *in situ* brecciation of target rock. Thus, fragmentation of target rock and melt generation to form pseudotachylitic breccia bodies are processes that are separated in time and space during cratering. The compositional change of the large pseudotachylite bodies is caused by the assimilation of the wall rock or the heterogeneity of the impact melt. However, it is possible that different compositional pseudotachylite zones e.g. pseudotachylite zones in quartzite and in granitoid wall rock are connected to each other and this could be responsible for the change of the chemical composition of pseudotachylites. However, this link of different pseudotachylite zones to each other remains to be ascertained. In summary, this model shows that the large volume of pseudotachylite bodies may explained by intruded impact melt, whereby the fragmentation of the target rock is *in situ*.

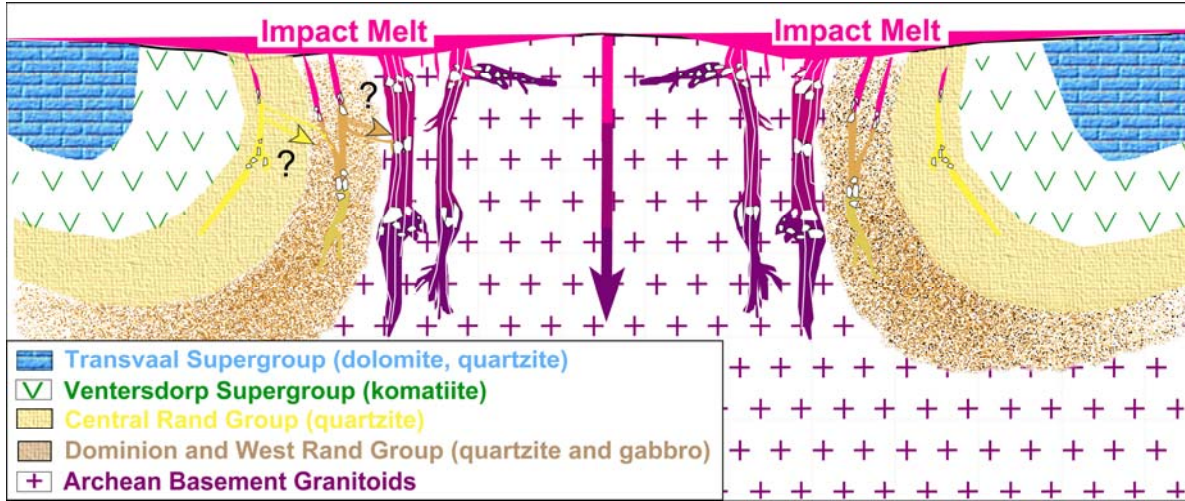


Figure 6.2: Model of injection of impact melt from the overlying melt sheet into low pressure sites in the Vredefort dome. Large pink to purple arrow indicates the variable magnitudes of assimilation. Note, fragmentation of target rock and melt generation to form pseudotachylitic breccia bodies are processes that are separated in time and space during cratering. Brittle deformation caused by localization of bending strains accounts for in situ brecciation of target rock and generation of low pressure sites. The link of different pseudotachylite zones to each other is unclear (yellow to brown arrow).

6.3. Outlook

1. Meteorite impacts, in particular large ones producing impact structures of several hundreds of kilometres in diameter, belong to the most fundamental geological processes in our planetary system. Much of our knowledge on the physics underlying impact processes comes from the comparison of the morphometry of natural impact structures with those resulting from numerical modelling using hydrocodes (e.g. Collins and Wünnemann, 2005; Ivanov 2005). For large impact structures in particular, such models predict a transient deformation mechanism, known as acoustic fluidization (Melosh, 1979), which affects target rocks for a few minutes after impact (e.g. Melosh and Ivanov, 1999). Within this short time span, high-frequency pressure fluctuation apparently cause target rocks to loose cohesion by pervasive fragmentation and, as a consequence, to behave mechanically like a fluid. Such transient deformation mechanism may well account for the generation and collapse of central uplift. Our field study of the geometry and distribution of pseudotachylite zones support such models for a better understanding of acoustic fluidization. According to my studies, pseudotachylite zones enclose large

rock blocks and consequently, these blocks are isolated. Thus, melt-filled fractures in the central uplift may be caused by acoustic fluidization and would be the first field evidence of this transient deformation mechanism. Therefore, it is necessary to investigate whether single rock blocks exist and whether the dimension of these blocks depends on the location in the central uplift.

2. Moreover, this study aims to a better understanding of transport, emplacement and chemical transformation of the impact melt after its formation due to a meteorite impact. In detail the processes of the formation of central uplift structures in large, complex impact craters and the formation of large pseudotachylite bodies as product of impact melt with assimilated immediate wall rock types are currently one of the least understood processes of impact cratering. The Vredefort and Sudbury impact structures are known for their prominent pseudotachylite bodies (e.g. Dressler, 1984, Reimold and Gibson, 2005). The geometry of these bodies ranges from mm- to cm-wide veins, dm- to m-scale dike-like bodies to tens of metres wide, irregular but overall planar zones. The presence of shock-metamorphic minerals in some very thin breccias (Martini 1978, 1991) indicates that these bodies formed as result of shock heating, whereby shear heating by friction may well have contributed to localized melting (Reimold and Gibson, 2005). However, neither in situ shock-induced nor frictional melting can explain the local occurrence of voluminous pseudotachylitic breccia bodies at Sudbury and Vredefort. This study resulted in a hypothesis advocating an allochthonous origin of the melt that was emplaced into tensional fracture systems in the crater floor at an advanced stage of cratering. Thereby, pseudotachylitic melt may have been drained from pools within nearby target rocks or from the overlying impact melt sheet. The tensional fracture system as well as the horizontal component vector of the maximum dilation direction, distribution, geometry and brecciation intensity of pseudotachylite bodies have shown centro-symmetric patterns what correspond geometrically to the variation in total strain predicted by numerical modelling. It is useful to investigate tensional fractures, dilation and geometries of pseudotachylite bodies of other central uplift structures e.g. Slate Island (Ontario) in order to confirm the hypothesis of the intruded impact melt. In addition, it is important to examine in more detail the geochemistry of wall rock-pseudotachylite matrix pairs on

different scales to find out possible other mechanisms of pseudotachylite formation. In addition, one should continue to further test the hypothesis of the involvement of impact melt in the pseudotachylite melt formation. Thereby, it would be important to include the origin of suevite deposits in impact structures in order to infer the timing and the genetic link of both melt types. If chemical compositions of suevite and pseudotachylite are from the same source (impact melt sheet), then their compositions should plot on a straight line but may well be modified chemically due to assimilated wall rock and differentiation. This may provide additional evidence that large pseudotachylitic melt bodies, besides suevite, form from impact melt.

3. Based on diverse results of the mixing calculation studies aided by diverse mixing programs (e.g. Stormer and Nicholls, 1978; Stöckelmann and Reimold, 1989; Reimold et al., 1990; Therriault et al., 1997) and different clast populations within the matrix, the Granophyre mixture can be produced by various melt proportions. There is still a large uncertainty whether granophyric melt comprises a significant component of Ventersdorp basalt, which is not validated by the actual clast population (Reimold et al., 1990; Reimold and Gibson, 2006). Reimold et al., (1990) did not model Ventersdorp basalt, because this lithology had not been observed in the Vredefort Granophyre, but Therriault et al. (1997) obtained a best-fit mixture of the Granophyre matrix with a Ventersdorp basalt component. In this regard, it is important to analyze the chemical composition of additional Vredefort Granophyre samples across the dikes and conduct a new mixing calculation with a mixing program. In addition, one should examine the fragment orientation within these dikes. Both are helpful in order to compare whether the formation of the Vredefort Granophyre resembles the formation of the Offset Dikes at Sudbury. In this study, only a single dike was analyzed. However, more chemical analyses of Granophyre dikes are needed to compare them geochemically to the Offset Dikes at Sudbury. Correlation of melt temperature estimates of Offset Dikes with modelled cooling rates of the impact melt sheet at Sudbury suggests that Offset Dikes were emplaced up to ten thousand years after impact (Hecht et al., 2008). This remains to be ascertained for the Vredefort Granophyre dikes.

REFERENCES

- Al Barazi S., Riller U. and Hecht, L., (2009). Geochemistry of pseudotachylites in target rocks of the Sudbury Impact Structure, Ontario, Canada. 72nd Annual Meteoritical Society Meeting, Nancy, France. Meteoritics & Planetary Science 44. #27 (abstr.).
- Armstrong, R.A., Compston, W., Retief, E.A., Williams, L.S., Welke, H.J., (1991). Zircon ion microprobe studies bearing on the age and evolution of the Witwatersrand basin. Precambrian Research 53, 243-266.
- Bickle, M.J. and Eriksson, K.A., (1982). Evolution and subsidence of early Precambrian sedimentary basins. Philosophical Transactions of the Royal Society of London Series A, 305, pp. 225-247.
- Bisschoff A.A., (1962). The pseudotachylite of the Vredefort Dome. Geological Society of South Africa Transaction 65, 207-226.
- Bisschoff A.A., (1972). The dioritic rocks of the Vredefort Dome. Geological Society of South Africa Transaction 75, 31-46.
- Bisschoff A.A., (1973). The petrology of some mafic and peralkaline intrusions in the Vredefort Dome. Geological Society of South Africa Transaction 76, 27-52.
- Bisschoff, A.A., (1982). Thermal metamorphism in the Vredefort Dome. Transactions of the Geological Society of South Africa 85, pp. 43-57.
- Bisschoff, A.A., (1988). The history and origin of the Vredefort Dome. South African Journal of Science 84, 413-417.

- Bisschoff, A.A., (1996). Note on the relative ages of the pseudotachylite and the basic granophyre in the Vredefort Dome. *South African Journal of Geology* 99, 89-92.
- Boon, J.D. and Albritton, J., (1936). Meteorite craters and their possible relationship to 'cryptovolcanic structures'. *Field Lab.* 5, 53-64.
- Brock, B.B., and Pretorius, D.A., (1964). Rand basin sedimentation and tectonics. In: Haughton, S.H. (Ed.), *The Geology of Some Ore Deposits in Southern Africa*. Geol. Soc. S. Afr., Johannesburg, pp. 549-599.
- Carter, N.L., (1968). Dynamic deformation in quartz. In: French, B.M., Short, N.M. (Eds.), *Shock Metamorphism of Natural Materials*. Mono Book Corp., Baltimore, pp. 453-474.
- Clarke, D.B., Henry, A.S. and White M.A., (1998). Exploding xenoliths and the absence of 'elephants' graveyards' in granite batholiths. *J. Struct. Geol.* 20, 1325-1343.
- Collins, G.S., and Wünnemann, K., (2005). How big was Chesapeake Bay impact? Insight from numerical modelling. *Geology* 33, 925-928.
- Collins, G.S., Melosh, H.J. and Ivanov, B.A., (2004). Modeling damage and deformation in impact simulations. *Meteoritics and Planetary Science* 39, 217-231.
- Coney L., (2002). The genesis of pseudotachylitic breccia in the Archaean rocks of the Vredefort Dome, South Africa. B.Sc. Honours Thesis, School of Geosciences, University of the Witwatersrand, Johannesburg.
- Coward, M.P., Spencer, R.M. and Spencer, C.E., (1995). Development of the Witwatersrand Basin, South Africa. In: Coward, M.P., Ries, A.C. (Eds.), *Early Precambrian Processes*. Geol. Soc. London, Spec. Publ. 95, pp. 243-269.

- Dence M.R., Grieve R.A.F. and Robertson P.B., (1977). Terrestrial impact structures: Principal characteristics and energy consideration. In *Impact and explosion cratering*: New York (eds. D.J. Roddy, R.O. Pepin and R.B. Merrill). Pergamon Press, pp. 247-275.
- De Ronde, C.E.J., and De Wit, M.J., (1994). Tectonic history of the Barberton greenstone belt, South Africa: 490 million years of Archean crustal evolution. *Tectonics* 13, pp. 983-1005.
- De Wit, M.J., (1998). On Archean granites, greenstones, cratons and tectonic: does the evidence demand a verdict? *Precambrian Research* 91, pp. 181-226.
- De Wit, M.J., Roering, R., Hart, R.J., Armstrong, R.A., De Ronde, C.E.J., Green, R.W.E., Tredoux, M., Peberdy, E. and Hart, R.A., (1992). Formation of an Archean continent. *Nature*, 357, 553 – 562.
- Dietz R.S., (1961). Vredefort ring structure: Meteorite impact scar? *J. Geol.*, 69, pp. 499-516.
- Du Toit, A.L., (1954). *Geology of South Africa*. Oliver and Boyd, Edinburgh and London 611pp.
- Dietz, R.S., (1947). Meteorite impact suggested by the orientation of shatter cones at the Kentland, Indiana, disturbance. *Science* 105 (2715), 42-43.
- Dressler B.O., (1984). The effects of the Sudbury event and the intrusion of the Sudbury igneous complex on the footwall rocks of the Sudbury structure. In *The geology and ore deposits of the Sudbury structure* (eds. E.G. Pye, A.J. Naldrett and P. E. Giblin). Special Volume 1. Toronto: Ontario Geological Survey, pp. 97-136.
- Dressler B.O. and Sharpton V.L., (1997). Breccia formation at a complex impact crater: Slate Islands, Lake Superior, Ontario, Canada. *Tectonophysics* 275, 285-311.

- Dressler, B.O., Reimold, W.U., (2004). Order or chaos? Origin and mode of emplacement of breccias in floors of large impact structures. *Earth Science Reviews* 67, 1-54.
- Dressler B.O., Reimold W.U., Sharpton V.L. and Gibson R.L., (2001). Pseudotachylites in central parts of impact craters – orientation and timing of emplacement. *Lunar and Planetary Science Conference XXXII. #1023 (abstr.)*.
- Erikson, P.G., Catuneanu, O., Els, B.G., Bumby, A.J., Van Rooy, J.L. and Popa, M., (2005). Kaapvaal Craton: Changing first- and second-order controls on sea level from 3.0 Ga to 2.0 Ga. *Sedimentary Geology* 176, 121-148.
- Fettes D., and Desmons J., (2007). *Metamorphic Rocks: A Classification and Glossary of Terms, Recommendations of the International Union of Geological Sciences Subcommittee on the Systematics of Metamorphic Rocks*: Cambridge University Press, Cambridge, UK, 244 p.
- Finch R.J. and Hanchar J.M., (2003). Structure and chemistry of zircon and zircon-group minerals. In *Zircon, Hanchar J. M. and Hoskin W. O. Reviews in Mineralogy and Geochemistry* 53. Washington, D.C.: Mineralogical Society of America, 1-25.
- Fiske, P.S., Nellis, W.J., Lipp, M., Lorenzana, H., Kikuchi, M. and Syono, Y., (1995). Pseudotachylites generated in shock experiments: Implications for impact cratering products and processes. *Science* 270, 281-283.
- Fletcher, P. and Reimold, W.U., (1989). Some notes and speculations on the pseudotachylites in the Witwatersrand basin and the Vredefort dome. *South African Journal of Geology* 92, pp. 223-234.

- French, B.M., (1998). *Traces of Catastrophe. A Handbook of Shock-metamorphic Effects in Terrestrial Meteorite Impact Structures*. Lunar and Planetary Institute Contribution No. 954, Lunar and Planet. Institute, Houston, 120pp.
- French, B.M. and Nielsen, R.L., (1990). Vredefort Bronzite Granophyre: chemical evidence for origin as a meteorite impact melt. *Tectonophysics* 171, 119-138.
- French, B.M., Orth, C.J. and Quintana, L.R., (1989). Iridium in the Vredefort bronzite granophyre: impact melting and limits on a possible extraterrestrial component. In: *Proceedings of the 19th Lunar Planetary Science Conference*. Cambridge University Press, Cambridge, UK, 733-744.
- Gibson, H.M. and Spray, J.G., (1998). Shock-induced melting and vaporization of shatter cone surfaces: Evidence from Sudbury impact structure. *Meteorit. Planet. Sci.* 33, pp. 329-336.
- Gibson, R.L., (2002). Impact-induced melting in Archean granulites in the Vredefort Dome, South Africa. In: *Anatexis of melt-pelitic granulites*. *Journal of Metamorphic Geology* 20, 57-70.
- Gibson R.L. and Wallmach T., (1995). Low pressure-high temperature metamorphism in the Vredefort Dome, South Africa: anticlockwise pressure-temperature path followed by rapid decompression. *Geological Journal* 30, 319-331.
- Gibson, R.L. and Reimold, W.U., (2001). The Vredefort Impact Structure, South Africa. Council for Geoscience South Africa, Memoir 92, pp. 111.
- Gibson, R.L. and Reimold, W.U., (2005). Shock pressure distribution in the Vredefort impact structure, South Africa. In: *Large Meteorite impacts*, edited by Kenkmann, T., Hörz, F. and Deutsch, A.. Geological Society of America Special Paper 384: 329-349.

- Gibson, R.L., Reimold, W.U. and Stevens, G., (1998). Thermal-metamorphic signature of an impact event in the Vredefort Dome, South Africa. *Geology* 26, 767-790.
- Gibson, R.L., Reimold, W.U., Phillips, D. and Layer, P.W., (2000). $^{40}\text{Ar}/^{39}\text{Ar}$ constraints on the age of metamorphism in the Witwatersrand Supergroup, Vredefort Dome (South Africa). *South African Journal of Geology* 103, pp. 175-190.
- Gibson, R.L., Reimold, W.U., Ashley, A.J. and Koeberl, C., (2002). Metamorphism on the Moon: A terrestrial analogue in the Vredefort Dome, South Africa. *Geology* 30, 375-478.
- Giesler, G.R., Weaver, R.P. and Mader, C.L., (2004). Two- and three-dimensional asteroid impact simulation. *Computing in Science & Engineering*, 46-55.
- Grant R.W. and Bite A., (1984). The Sudbury Quartz Diorite Offset Dikes. In: *The Geology and Ore Deposits of the Sudbury Structure*, edited by Pye E.G., Naldrett A.J., Giblin P.E. Special Publication 1. Toronto: Ontario Geological Survey, 275-300.
- Grieve, R.A.F. and Cintala, M.J., (1981). A method for estimating the initial impact conditions of terrestrial cratering events, exemplified by its application to Brent crater, Ontario. *Proc. Lunar Planet. Sci.* 12B, pp. 1607-1621.
- Grieve, R.A.F. and Therriault, A., (2000). Vredefort, Sudbury, Chicxulub: Three of a kind? *Annual Review of Earth and Planetary Sciences* 28, 305-338.
- Grieve, R.A.F., Reimold, W.U., Morgan, J., Riller, U. and Pilkington, M., (2008). Observations and interpretations at Vredefort, Sudbury and Chicxulub: Towards an empirical model of terrestrial impact basin formation. *Meteoritics and Planetary Sciences* 43, 855-882.

- Hall A.L. and Molengraaff G.A.F., (1925). The Vredefort Mountain Land in the Southern Transvaal and the Northern Orange Free State, Vol. 24. Verhandelingen, Koninklijke Akademie van Wetenschappen, Amsterdam. pp. 183.
- Hamilton, W., (1970). Bushveld complex – product of impact? In : Vissler, D.J.L. and von Gruenewaldt, G. (Eds.), Symposium on the Bushveld Igneous Complex and Other Layered Intrusion, Geol. Soc. S. Afr., Spec. Publ. 1, 367-379.
- Hargraves, R.B., (1961). Shatter cones in the rocks of the Vredefort Ring. Trans. Geol. Soc. S. Afr. 64, 147-161.
- Hart, R.J., Welke, H.J. and Nicolaysen, L.O., (1981). Geochronology of the deep profile through the Archaean Basement of Vredefort, with implication for early crustal evolution. Journal of Geophysical Research 86, pp. 10663-10680.
- Hart R.J., Andreoli, M.A.H., De Wit, M.J. and Tredoux, M., (1987). Geotraverse of the Vredefort structure: Implications for a mid-crustal discontinuity in the Kaapvaal Craton. Ext. Abstr. Int. Workshop Cryptoexplosions and Catastrophes in the geol. Rec., Parys, BPI Geophysics, Univ. Witwatersrand, Sect. H4, 7 pp.
- Hart, R.J., Andreoli, M.A.G., Tredoux, M. and De Wit, M.J., (1990a). Geochemistry across an exposed section of Archaean crust at Vredefort, South Africa: With implications for mid-crustal discontinuities. Chemical Geology 82, pp. 21-50.
- Hart, R.J., Andreoli, M.A.G., Smith, C.B., Otter, M.L., and Durrheim, R., (1990b). Ultramafic rocks in the centre of the Vredefort Structure: possible exposure of the upper mantle. Chemical Geology 82, pp. 233-248.

- Hecht, L., Wittek, A., Riller, U., Mohr, T., Schmitt, R.T. and Grieve, R.A.F., (2008). Differentiation and emplacement of the Worthington Offset Dike of the Sudbury Impact Structure, Ontario. *Meteoritics and Planetary Sciences* 43, 1659-1679.
- Heider, N. and Kenkmann, T., (2003). Numerical simulation of temperature effects at fissures due to shock loading. *Meteoritics and Planetary Science* 38, Nr. 10, pp. 1451-1460.
- Henkel, H. and Reimold, W.U., (1998). Integrated geophysical modelling of a giant, complex impact structure: anatomy of the Vredefort Structure, South Africa. *Tectonophysics* 287, 1-20.
- Heubeck, C. and Lowe, D.R., (1994). Depositional and tectonic setting of the Archaean Moodies Group, Barberton Greenstone Belt, South Africa. *Precambrian Research* 68, pp. 257-290.
- Ivanov, B. A., (2005). Numerical Modeling of the Largest Terrestrial Meteorite Craters. *Solar System Research*, Vol. 39, No. 5, 2005, pp. 381-409.
- Ivanov B.A. and Deutsch A., (1999). Sudbury impact event: cratering mechanics and thermal history. In *Large Meteorite Impacts and Planetary Evolution II*, (eds. B.O. Dressler and V.L. Sharpton). Geological Society of America Special Paper 339, pp. 389-398.
- Jahn, A., and Riller, U., (2009). A 3D model of first-order structural elements of the Vredefort Dome, South Africa – Importance for understanding central uplift formation of large impact structures. *Tectonophysics* 478, pp. 221-229.
- Jones, P.J., Price, G.D., Price, N.J., DeCarli, P.S. and Clegg, R.A., (2002). Impact induced melting and the development of large igneous provinces. *Earth and Planetary Science Letters* 202, 551-561.

- Kamo, S.L., Reimold W.U., Krogh T. E. and Colliston W.P., (1996). A 2.023 Ga age for the Vredefort impact event and a first report of shock metamorphosed zircons in pseudotachylite breccia and Granophyre. *Earth and Planetary Science Letters* 144, 369-388.
- Kenkmann, T., Hornemann, U. and Stöffler, D., (2000). Experimental generation of shock-induced pseudotachylites. *Meteoritics & Planetary Science* 35, 1275-1290.
- Kenkmann, T., Jahn, A., Scherler, D. and Ivanov, B.A., (2005). Structure and formation of a central uplift: A case study at the Upheaval Dome impact structure, Utah. In: Kenkmann, T., Hörz, F., and Deutsch, A. (eds.), *Large Meteorite Impacts III*. Geological Society of America Special Paper 384, 85-115.
- Kieffer, S.W. and Simonds, C.H., (1980). The role of volatiles and lithology in the impact cratering process. *Rev. Geophys. Space Phys.*, 18, pp. 143-181.
- Killick, A.M., (1994). The geochemistry of pseudotachylite and its host rocks from the West Rand Goldfield, Witwatersrand Basin, South Africa: implications for pseudotachylite genesis. *Lithos* 32, 193-205.
- Killick, A. M. and Reimold, W. U., (1990). Review of the pseudotachylites in and around the Vredefort Dome, South Africa. *South African Journal of Geology* 9, 350-365.
- Killick A.M., Thwaites A.M., Germs G.J.B. and Schoch A.E., (1988). Pseudotachylite associated with a bedding parallel fault zone between the Witwatersrand and Ventersdorp Supergroups, South Africa. *Geologische Rundschau* 77, 329-344.
- Koeberl, C., Reimold, W.U. and Shirley, S.B., (1996). Re-Os isotope study of the Vredefort Granophyre: clues to the origin of the Vredefort Structure, South Africa. *Geology* 24, 913-916.

- Kullerud, G., (1967) Sulfide studies. In *Researches in Geochemistry* (eds. P.H. Abelson). John Wiley and Sons, New York. pp. 286-321.
- Lafrance, B., Legault, D. and Ames, D.E., (2008). The formation of the Sudbury breccia in the North Range of the Sudbury impact structure. *Precambrian Research* 165, 107–119.
- Lambert, P., (1981). Geological constraints on the formation of complex craters. In *Multi-ring basins* (eds. Schultz P.H. and Merrill R.B.) Houston: Lunar and Planetary Science Institute. pp. 59-78.
- Lana, C., Gibson, R.L., Kisters, A.F.M. and Reimold, W.U., (2003a). Archean crustal structure of the Kaapvaal craton, South Africa - evidence from the Vredefort dome. *Earth Planet. Sci. Lett.* 206, 133-144.
- Lana, C., Gibson, R.L. and Reimold, W.U., (2003b). Impact tectonics in the core of the Vredefort dome, South Africa: Implications for central uplift formation in very large impact structures. *Meteoritics & Planetary Science* 38, Nr. 7, 1093-1107.
- Lana, C., Reimold, W.U., Gibson, R.L., Koeberl, C. and Siegesmund, S., (2004). Nature of the Archaean mid-crust in the core of the Vredefort Dome, Central Kaapvaal Craton, South Africa. *Geochim. Cosmochim. Acta.* 68, 623-642.
- Langenhorst F., Poirier J.P., Deutsch A. and Hornemann U., (2002). Experimental approach to generate shock veins in single crystal olivine by shear heating. *Meteoritics and Planetary Science* 37, 1541-1553.
- Leroux, H., Reimold, W.U. and Doukhan, J.-C., (1994). A T.E.M. investigation of shock metamorphism in quartz from the Vredefort dome, South Africa. *Tectonophys.* 230, 223-239.

- Lieger, D., (2005). Impaktgenetische Bedeutung von Pseudotachylitgängen der 1.85 Ga alten Sudbury-Impaktstruktur, Kanada. Unpublished Diploma Thesis: Free University of Berlin, Germany. 99 pp.
- Lieger D., Riller U. and Gibson R.L., (2009). Generation of fragment-rich pseudotachylite bodies during central uplift formation in the Vredefort impact structure, South Africa. *Earth and Planetary Science Letters* 279, 53-64.
- Lowe, D.R., (1994). Accretionary history of the Archean Barberton Greenstone Belt (3.55-3.22 Ga), *South African Journal of Geology* 22, pp. 1099-1102.
- Lowe, D.R., (1999). Geological evolution of the Barberton greenstone belt and vicinity, in *Geologic evolution of the Barberton greenstone belt, South Africa* (D.R. Lowe and G.R. Byerly, editors). Geological Society of America Special Paper 329, pp. 287-312.
- Machado, R., Lana, C., Stevens, G., Filho, C.R.S., Reimold, W.U. and McDonald, I., (2009). Generation, mobilization and crystallisation of impact-induced alkali-rich melts in granitic target rocks: Evidence from the Araguinha impact structure, central Brazil. *Geochimica et Cosmochimica Acta* 73, pp. 7183-7201.
- Maddock R.H., (1986). Partial melting of lithic porphyroblasts in fault-generated pseudotachylites.- *N. Jb. Miner. Abh.* 155, 1-14.
- Magloughlin J.F., (2005). Immiscible sulfide droplets in pseudotachylite: Evidence for high temperature (>1200° C) melts. *Tectonophysics* 402, 81-91.
- Martini J.E.J., (1978). Coesite and stishovite in the Vredefort Dome, South Africa. *Nature* 277, 495-496.

- Martini, J.E.J., (1991). The nature, distribution and genesis of coesite and stishovite associated with pseudotachylite of the Vredefort Dome, South Africa. *Earth and Planetary Science Letters* 103, 285-300.
- McCarthy, T.S., Stanistreet, I.G. and Robb, L.J., (1990). Geological studies related to the origin of the Witwatersrand Basin and its mineralization – an introduction and a strategy for research and exploration. *South African Journal of Geology* 93, pp. 1-4.
- McIver J.R., Cawthorn R.G. and Wyatt B.A., (1981). The Ventersdorp Supergroup – the youngest komatiitic sequence in South Africa. In *Komatiites* (eds. E.G. Nisbet and N.T. Arndt). Allen and Unwin, London.
- Melosh, H.J., (1979). Acoustic fluidization: A new geological process? *Journal of Geophysical Research* 84, 7513-7520.
- Melosh, H.J., (1989). *Impact Cratering – A Geologic Process*. Oxford University Press, New York. 245 pp.
- Melosh, H.J., (2000). Can impacts induce volcanic eruptions? In: *Catastrophic Events and Mass Extinctions: Impacts and Beyond*, Lunar and Planetary Institute, Houston, TX, Contrib. 1053, 141-142.
- Melosh H.J., (2005). The mechanics of pseudotachylite formation in impact events. In *Impact tectonics* (eds. C. Koeberl and H. Henkel). Springer. pp. 55-80.
- Melosh H.J. and Ivanov, B.A., (1999). Impact crater collapse. *Annual Review of Earth and Planetary Sciences* 27, 385-415.

- Minnitt, R.C.A., Reimold, W.U. and Colliston, W. P., (1994). The geology of the Greenlands Greenstone Complex and selected granitoid terranes in the south-eastern quadrant of the Vredefort dome. Economic Geology Research Unit, Information Circular 28. Johannesburg: University of Witwatersrand. 35 p.
- Mohr-Westheide T., Reimold W.U., Riller U. and Gibson, R, (2009). Pseudotachylitic breccia and microfracture networks in Archean gneiss of the central uplift of the Vredefort Impact Structure, South Africa. South African Journal of Geology 112, 1-22.
- Mohr-Westheide and Reimold W.U., (2010). Microchemical investigation of small-scale pseudotachylitic breccias from the Archean gneiss of the Vredefort dome, South Africa. GSA Special Paper 465, 619-643.
- Molengraaff, G.A.F., (1903). Remarks on the Vredefort Mountain Land. Transactions of the Geological Society of South Africa 6, pp. 20-26.
- Moser, D.E., (1997). Dating the shock wave and thermal imprint of the giant Vredefort impact, South Africa. Geology 25, 7-10.
- Moser, D.E., Flowers, R.M. and Hart, R.J., (2001). Birth of the Kaapvaal tectosphere 3.08 billion years ago. Science 291, pp. 465-468.
- Nicolaysen L.O., (1987). The Vredefort structure. Working Pap. international Workshop Cryptoexplosions Catastrophes geol. Rec., Parys, Orange Free State, 28 pp.
- Negi, J.G., Agrawal, P.K., Pandey, O.P. and Singh, A.P., (1993). A possible K-T boundary bolide impact site offshore Bombay and triggering of rapid Deccan volcanism. Phys. Earth Planet. Int. 76, 189-197.

- Nel, L.T., (1927). The Geology of the Country Around Vredefort. Spec. Publ. 6, Geol. Surv. S. Afr., Pretoria. Government Printer, Pretoria, 134 pp.
- Nelson, D.R., Trendall, A.F., de Lace, B., Grobler, N.J. and Fletcher, I.R., (1992). A study of geochemical and isotopic systems of late Archean flood basalts from the Pilbara Craton. *Precambrian Research* 54, pp. 29-56.
- Nicolaysen, L.O. and Ferguson, J., (1990). Cryptoexplosion structures, shock deformation and siderophile concentration related to explosive venting of fluids associated with alkaline ultramafic magmas. *Tectonophys.* 171, 303-335.
- Petford, N., Cruden, A.R., McCaffrey, K.J.W. and Vigneresse, J.L., (2000). Granite magma formation, transport and emplacement in the Earth's crust. *Nature* 408, 669-673.
- Phillips, N.G. and Law, J.D.M., (1994). Metamorphism of the Witwatersrand gold field: A review. *Ore Geology Reviews* 9, pp. 1-31.
- Pierazzo, E. and Melosh, H.J., (1999). Hydrocode modeling of Chicxulub as an oblique impact event. *Earth and Planetary Science Letters* 165, 163-176.
- Pohl, J., Stöffler, D., Gall, H. and Ernst, K., (1977). The Ries impact crater, in Roddy, D.J., Pepin, R.O., and Merrill, R.B., eds., *Impact and explosion cratering*: New York, Pergamon Press, 343-404.
- Pollard, D.D. and Segall, P., (1987). Theoretical displacements and stress near fractures in rocks, with applications of faults, joints, veins, dikes, and solution surfaces. In: Atkinson, B.K., ed., *Fracture mechanics of rocks*: London, England, Academic Press, 277-349.

- Poujol, M. and Robb, L.J., (1999). New U-Pb zircon ages on gneisses and pegmatite from south of the Murchison greenstone belt, South Africa. *South African Journal of Geology*, 102(2); 93-7.
- Poujol, M, Robb, L.J., Anhaeusser, C.R. and Bronwyn, G., (2003). Geochronological constraints on the evolution of the Kaapvaal craton, South Africa. *Precambrian Research*.
- Prevec, S.A. and Cawthorn, R.G., (2002). Thermal evolution and interaction between impact melt sheet and footwall: A genetic model for the contact sublayer of the Sudbury Igneous Complex, Canada. *Journal of Geophysical Research-Solid Earth* 107(B8), 217, doi:10.1029/2001JB000525.
- Ramberg, H., (1967). *Gravity, Deformation and the Earth's Crust*. Academic Press, London, 214pp.
- Reimold, W.U., (1991). Geochemistry of pseudotachylites from the Vredefort Structure, South Africa. *Neues Jahrbuch Mineralogie Abhandlungen* 161, 151-184.
- Reimold, W.U., (1995). Pseudotachylite in impact structures-Generation by friction melting and shock brecciation? A review and discussion. *Earth Science Reviews* 39, 247-265.
- Reimold W.U. and Ried A.M., (1989). Petrographic observations on granitic clasts in Granophyre of the Vredefort structure. *Bienn. Symp., Mineral. Assoc. South Africa, Pretoria*, pp. 16-21.
- Reimold, W.U. and Colliston, W.P., (1994). Pseudotachylites of the Vredefort Dome and the surrounding Witwatersrand Basin, South Africa. *Geological Society of America, Special Paper* 293, 177-196.

- Reimold, W.U. and Gibson, R.L., (2005a). Meteorite Impact! The danger from space and south africa's mega-impact the Vredefort Structure. Second Edition Council for Geoscience, Pretoria, Republic of South Africa, 1-319.
- Reimold, W.U. and Gibson, R.L., (2005). "Pseudotachylites" in large impact Structures. In: Koeberl, C., and Henkel, H. (eds.), Impact tectonics, Springer, 2-53.
- Reimold W.U. and Gibson R. L., (2006). The melt rocks of the Vredefort impact structure – Vredefort Granophyre and pseudotachylitic breccias: Implications for impact cratering and the evolution of the Witwatersrand Basin. *Chemie der Erde* 66, 1–35.
- Reimold, W.U., Andreoli, M. and Hart, R.J., (1985a). Pseudotachylite from the Vredefort Dome. *Lunar Planetary Science XVI*, 691-692. The Lunar and Planetary Institute, Houston.
- Reimold, W.U., Andreoli, M. and Hart, R.J., (1985b). A geochemical study on pseudotachylite and parent rocks from the Vredefort Structure. *Meteoritics* 20. 740-742.
- Reimold W.U., Horsch M. and Durrheim R.J., (1990). The bronzite granophyre from the Vredefort structure – a detailed analytical study and reflections on the origin of one of Vredefort's enigmas. In *Proceedings of the 20th Lunar Planet. Sci. Conf.*, Lunar and Planet. Inst., Houston. pp. 433-450.
- Reimold W.U., Horton J.W., Jr. and Schmitt, R.T., (2008). Debate about impact nomenclature – Recent problematics: Conference on Large Meteorite Impacts and Planetary Evolution IV, Vredefort Dome, South Africa, LPI Contribution 1423, Abstract 3033, 2 p.
- Riller, U., (2005). Structural characteristics of the Sudbury Impact Structure, Canada: impact-induced and orogenic deformation – a review. *Meteoritics and Planetary Science* 40, 1723-1740.

- Riller U., Lieger D., Gibson R.L., Grieve R.A.F. and Stöffler D., (2010). Origin of large-volume pseudotachylite in terrestrial impact structures. *Geology* 38, 619-622.
- Robb, L.J., Davis, D.W. and Kamo, S.L., (1991). Chronological framework for the Witwatersrand Basin and environs: towards a time-constrained depositional model. *South African Journal of Geology* 94, pp. 86-95.
- Rousell, D.H., Fedorowich, J.S. and Dressler, B.O., (2003). Sudbury Breccia (Canada): a product of the 1850 Ma Sudbury Event and host to footwall Cu-Ni-PGE deposits. *Earth-Science Reviews* 60, 147-174.
- Schmitz, M.D. and Bowring, S.A., (2003). Ultrahigh-temperature metamorphism in the lower crust during Neoproterozoic Ventersdorp rifting and magmatism, Kaapvaal Craton, southern Africa. *Geological Society of America Bulletin* 115, pp. 533-548.
- Schwarzman E.C., Meyer C.E. and Wilshire H.G., (1983). Pseudotachylite from the Vredefort Ring, South Africa, and the origin of some lunar breccias. *Geological Society of Africa Bulletin* 94, 926-935.
- Scott, R.G. and Benn, K., (2002). Emplacement of Sulfide Deposits in the Copper Cliff Offsets Dike during Collapse of the Sudbury Crater Rim: Evidence from Magnetic Fabric Studies. *Economic Geology* Volume 97, pp. 1447-1458.
- Seyfert, C.K. and Sirkin, L.A., (1979). *Earth History and Plate Tectonics*, Harper and Row, New York, 96 pp.
- Shand, S.J., (1916). The pseudotachylite of Parijs (Orange Free State), and its relation to "trap-shotten gneiss" and flinty-crush rock." *Geological Society of London Quarterly Journal* 72, 198-21.

- Slawson, W.F., (1976). Vredefort core: a cross-section of the upper crust? *Geochimica et Cosmochimica Acta* 40, pp. 117-121.
- Speers, E.C., (1957). The age relation and origin of common Sudbury Breccia. *Journal of Geology* 65, 497– 514.
- Spray, J.G., (1987). Artificial generation of pseudotachylite using friction welding apparatus: simulation of melting on a fault plane. *Journal of Structural Geology* 9, 49-60.
- Spray, J.G., (1992). A physical basic for the frictional melting of some rock-forming minerals. *Tectonophysics* 204, 205-221.
- Spray, J.G., (1995). Pseudotachylite controversy: fact or friction? *Geology* 23, 1119-1122.
- Spray, J.G., (1997). Superfaults. *Geology* 25, 579-582.
- Spray, J.G., (1998). Localized shock- and friction-induced melting in response to hypervelocity impact. In *Meteorites: Flux with time and impact effects*, edited by Grady, M. M., Hutchison R., McCall, G. J. H., and Rothery, D. A., Special Publication 140. London: Geological Society of London. 171-180.
- Spray, J.G., (2000). The role of fracture-fault systems in impact crater formation. *Eos, Transactions, American Geophysical Union (Supplement)*. 2000 Fall Meeting, pp. A162.
- Spray J.G. and Thomson L.M., (1995). Friction melt distribution in a multi-ring impact basin. *Nature* 373, 130-132.
- Spray, J. G., Butler, H. R. and Thompson, L. M., (2004). Tectonic influences on the morphometry of the Sudbury impact structure: Implications for terrestrial cratering and modeling. *Meteoritics & Planetary Science* 39, 287-301.

- Stepho, D., (1979). A geological and geophysical study of the central portion of the Vredefort Dome structure. Ph.D. Thesis (unpublished), University of the Witwatersrand, Johannesburg, 378pp.
- Stepho, D., (1990). The geology and gravity field in the central core of the Vredefort structure. *Tectonophysics* 171, pp. 75-103.
- Stöckelmann D. and Reimold W.U., (1989). The HMX mixing calculation program. *J. math. Geol.*, 21, pp 853-860.
- Stöffler, D., (1977). Research drilling Nördlingen 1973: Polymict breccias, crater basement, and cratering model of the Ries impact structure. *Geologica Bavarica* 75, 443-458.
- Stöffler, D., Knoll, H.D. and Maerz, U., (1979). Terrestrial and lunar impact breccias and the classification of lunar highland rocks: Lunar Science Conference, 10th, Proceedings, Volume 1: New York, Pergamon Press, 639-675.
- Stöffler, D. and Grieve, R.A.F., (2007). Impactites. Chapter 2.11 in Fettes, D., and Desmons, J. (eds.) *Metamorphic Rocks: A Classification and Glossary of Terms, Recommendations of the International Union of Geological Sciences*, Cambridge University Press, Cambridge, UK: 82-92, 111-125, and 126-242.
- Stormer J.C. and Nicholls J., (1978). XLFRAC: a program for the interactive testing of magmatic differentiation models. *Comput. Geosci.*, 4 143-159.
- Tankard A.J., Jackson M.P.A., Eriksson K.A., Hobday D.K., Hunter D.T. and Minter W.E.L., (1982). *Crustal Evolution of South Africa (3.8 Billion Years of Earth History)*. Springer, Berlin-Heidelberg. pp. 523.

- Therriault A.M., Reimold W.U. and Reid A.M., (1996). Field relations and petrography of the Vredefort Granophyre. *South African Journal of Geology* 99, 1-21.
- Therriault A.M., Reimold W.U. and Reid A.M., (1997). Geochemistry and impact origin of the Vredefort Granophyre. *South African Journal of Geology* 100, 115-122.
- Tipler, P.A., (1994). *Physik*. Spektrum Akademischer Verlag Heidelberg-Berlin-Oxford.
- Tredoux, M., Hart, R.J., Carlson, R.W. and Shirey, S.B., (1999). Ultramafic rocks at the center of the Vredefort Structure: Further evidence for the crust-on-edge model. *Geology* 27, pp. 923-926.
- Turtle, E.P., Pierazzo, E., Collins, G.S., Osinski, G.R., Melosh, H.J., Morgan, J.V. and Reimold, W.U., (2005). Impact structures: What does crater diameter mean? In Kenkmann, T., and Deutsch, A. (eds.), *Large Meteorite Impact III*. Geological Society of America Special Paper 384, 1-24.
- Walraven, F. and Martini, J., (1995). Zircon Pb-evaporation age determinations of the Oak Tree Formation, Chuniespoort Group, Transvaal Sequence: Implications for Transvaal-Griqualand West basin correlation. *South African Journal of Geology* 98, pp. 58-67.
- Wieland, F., Gibson, R.L. and Reimold, W.U., (2005). Structural analysis of the collar of the Vredefort Dome, South Africa – significance for impact-related deformation and central uplift formation. *Meteoritics and Planetary Science* 40, 1537-1554.
- Willemse J., (1937). On the old granite of the Vredefort region and some of its associated rocks. *Transactions Geological Society South Africa* 40, 195-206.
- Wilshire H.G., (1971). Pseudotachylite from the Vredefort Ring, South Africa. *Journal of Geology* 79, 195-206.

- Wünnemann, K. and Ivanov, B.A., (2003). Numerical modelling of the impact crater depth-diameter dependence in an acoustically fluidized target. *Planetary and Space Sciences* 51, 831-845.
- Wünnemann, K., Morgan, J.V. and Jödicke, H., (2005). Is Ries crater typical for its size? An analysis based upon old and new geophysical data and numerical modelling. In: Kenkmann, T., Hörz, F., and Deutsch, A. (eds.), *Large Meteorite Impacts III*. Geological Society of America Special Paper 384, 67-83.

APPENDIX I:
ORIGIN OF LARGE-VOLUME PSEUDOTACHYLITE IN TERRESTRIAL IMPACT
STRUCTURES

Ulrich Riller¹, Daniel Lieger², Roger L. Gibson³, Richard A.F. Grieve⁴, and Dieter Stöffler²

¹School of Geography and Earth Sciences & Origins Institute, McMaster University, 1280 Main Street West, Hamilton, Ontario, L8S 4K1, Canada

²Museum für Naturkunde, Humboldt-Universität zu Berlin, Invalidenstraße 43, 10115 Berlin, Germany

³Impact Cratering Research Group, School of Geosciences, University of the Witwatersrand, Private Bag 3, P.O. Wits 2050, Johannesburg, South Africa

⁴Earth Sciences Sector, Natural Resources Canada, Ottawa, Ontario, Canada, K1A 0E4

Published in *Geology* v. 38; no. 7; p. 619-622.

<http://dx.doi.org/10.1130/G30806.1>

Abstract

Large-volume pseudotachylite bodies in impact structures are dike-like and consist of angular and rounded wall-rock fragments enveloped by a microcrystalline and sporadically glassy matrix that crystallized from a melt. Knowledge of the formation of pseudotachylite bodies is important for understanding mechanics of complex crater formation. Most current hypotheses of pseudotachylite formation inherently assume that fragmentation and melt generation occur during a single process. Based on the structure of pseudotachylite bodies at Sudbury and Vredefort we show that these processes differ in time and space. We demonstrate that the cm- to km-scale bodies are effectively fragment- and melt-filled tension fractures that formed by differential rotation of target rock during cratering. Highly variable pseudotachylite characteristics can be accounted for by a single process, i.e., drainage of initially superheated impact melt into tension fractures of the crater floor.

1. Introduction

Models of pseudotachylite formation generally assume that fragmentation and melt generation are either caused by: (1) the interaction of the shock wave with the target rock (Gibson et al., 2002; Gibson and Reimold, 2005), (2) decompression of target rock (Martini, 1991; Reimold and Gibson, 2006) or (3) frictional sliding on faults (Thompson and Spray, 1994; Spray et al., 2004; Melosh, 2005). Thereby, pseudotachylitic melt is generally believed to have formed from its immediate wall rock (Martini, 1991; Gibson et al., 2002; Gibson and Reimold, 2005; Reimold and Gibson, 2006). This is, however, at variance with geochemical studies suggesting that the composition of the pseudotachylite matrix cannot be accounted for by melting of the immediate wall rock or its fragments alone (Speers, 1957; Dressler, 1984; Rousell et al., 2003). An allochthonous component of pseudotachylite melt is required. Structural data from the Sudbury impact structure, Canada, and the Vredefort Dome, South Africa, indicate the presence of such melt component and contribute greatly in elucidating the mechanics of cratering.

2. Geological Background

The central portion of the 1.85 Ga Sudbury impact structure (Krogh et al., 1984) consists of the Sudbury Basin (Fig. A.1A). The Basin is made up of the Sudbury Igneous Complex (SIC), the relic of an impact melt sheet (Grieve et al., 1991), clast-melt breccias of the overlying Onaping Formation and post-impact sedimentary rocks (Stöffler et al., 1994). Collectively, these units were folded and faulted during post-impact orogenic deformation (Riller, 2005). This accounts for the elliptical shape of the Basin in map view and has led to superb exposure of the impact structure's stratigraphy (Fig. A.1A). The SIC imparted an up to 1.2 km wide thermal aureole that includes grain-scale partial melt phenomena on its underlying Archean and Paleoproterozoic target rocks (Dressler, 1984; Riller et al., 1996; Rosenberg and Riller, 2000). Fragment-rich pseudotachylite, known as "Sudbury Breccia", in target rocks are pervasive in a ca. 15 km wide zone around the SIC (Rousell et al., 2003; Dressler, 1984). Due to post-impact deformation of the SIC, this zone exposes tilted target rocks that were uplifted during cratering.

With an estimated diameter of up to 250 km, the 2.02 Ga Vredefort impact structure (Kamo et al., 1996) is the oldest and largest impact structure currently known on Earth (Grieve and Therriault, 2000). The impact structure (Fig. A.1B) has been eroded to a depth of ~8–11 km (Gibson et al., 1998) and, thus, offers an unprecedented view of the target rock structure below a large, complex impact structure. The central portion of the impact structure, the so-called Vredefort Dome, is the eroded relic of rocks that were uplifted during cratering. The Vredefort Dome consists of a core, ca. 40 km in diameter, of Archean crystalline basement rocks and a 25 km wide ‘collar’ of subvertical to overturned supracrustal strata. Pseudotachylite bodies in the Vredefort Dome range from mm-wide veins to tens of meters wide dikes (Dressler and Reimold, 2004).

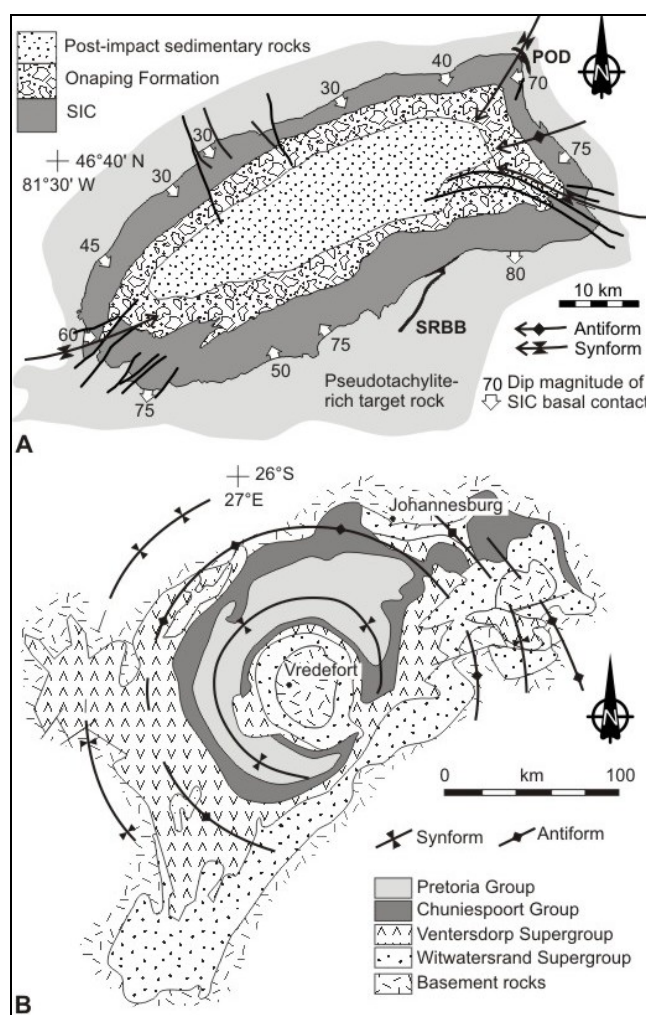


Figure A.1: Simplified geological maps of (A) the Sudbury Basin and (B) the Vredefort impact structure. SRBB and POD in (A) denote South Range Breccia Belt and Podolsky Dike, respectively.

3. Field Characteristics

At Sudbury, fragment-rich pseudotachylite bodies differ locally from each other in terms of shape, size and content of fragments, as well as texture of the matrix (Müller-Mohr, 1992; Dressler 1984; Rousell et al., 2003). The fragments are generally derived from the immediate wall rock. Within a distance of ~500 m from the SIC, mafic fragments within pseudotachylite have well-defined margins and are sub-circular in section (Fig. A.2A). By contrast, felsic fragments in the same pseudotachylite bodies display highly irregular shapes, cusped margins, strong ductile deformation and partial melting. Moreover, felsic fragments are highly stretched and mingled into the pseudotachylite matrix, collectively displaying convoluted patterns reminiscent of turbulent viscous flow. Partial melting of felsic fragments, as well as their entrainment in, and mingling with, the pseudotachylite matrix is at a maximum close to the SIC (Fig. A.2B). Beyond a distance of ~500 m from the SIC, such flow patterns are not apparent and fragments, as well as pseudotachylite dike margins, are sharp (Fig. A.2C) attesting to fracturing only, regardless of target rock lithology.

Pseudotachylite bodies at Vredefort resemble the ones at Sudbury that are more distal from the SIC. Fragments display jigsaw geometry (Fig. A.2D) and the traces of opposite margins of a given pseudotachylite dike or vein display close to perfect geometrical fit (Fig. A.2D, E, F). This indicates that hardly any material was removed from fragment and dike margins during and after fragmentation and that the bodies formed effectively in response to mode I extensional fracturing (Pollard and Segall, 1987). Pseudotachylite veins commonly display en-echelon geometry (Fig. A.2E), which underscores their formation as extension fractures. The geometry of vein margins indicates further that veins opened either transverse or oblique to their margins. Thus, the veins formed from hybrid faults, i.e., faults characterized by simultaneous wall-orthogonal and wall-parallel displacement, with the magnitude of the latter being generally less than a few centimeters. Hybrid faulting and the preservation of primary asperities of fracture margins exclude in situ generation of pseudotachylitic melt by frictional sliding on margins.

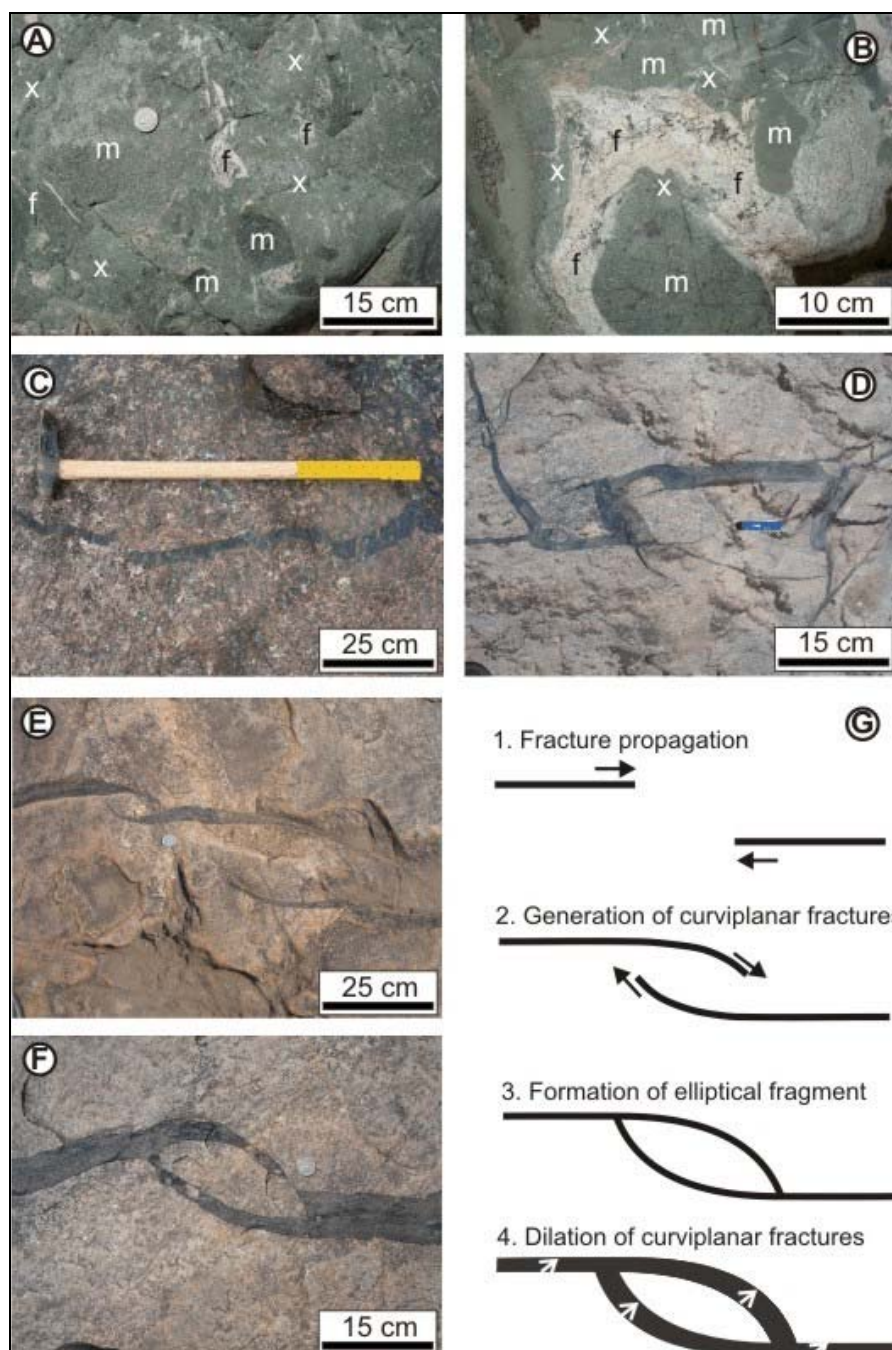


Figure A.2: A: Pseudotachylite body from Sudbury containing globular mafic fragments (m) and cusped felsic fragments (f) indicating a significant contrast in mechanical competency between both fragment types within matrix (x). B: Highly stretched and partially melted felsic fragment (f) entrained in convoluted matrix (x) containing globular mafic fragments (m) close to the SIC (Sudbury). C: Pseudotachylite dike in granitoid rock located ca. 3 km west of the SIC (Sudbury) shows geometric fit of its margins (Sudbury). D: Jigsaw geometry of pseudotachylite dikes and fragments in granitoid rock (Vredefort). E: En-echelon geometry of overstepping pseudotachylite veins (Vredefort). F: Elliptical host rock fragment enveloped by overstepping pseudotachylite vein (Vredefort). G: Schematic diagram displaying stages of elliptical fragment formation by overstepping en-echelon fractures propagating toward each other.

4. Mechanisms of fragmentation

Fragments in pseudotachylite bodies are generally elliptical and fragment diameters commonly exceed the width of their pseudotachylite host vein (Fig. A.2F). These properties can be explained by bridging between overstepping en-echelon fractures (Fig. A.2G). During this process, rotation of principal stresses at fracture tips causes the tips to propagate toward the neighboring fracture (Pollard and Segall, 1987). Propagation of curvi-planar fractures results in coalescence of fracture pairs and isolation of elliptical host rock fragments upon opening of the fractures and associated melt infiltration (Fig. A.2G). A full spectrum of stages of fracture tip propagation is preserved at Vredefort (Fig. A.2E, F) and Sudbury. The formation of pseudotachylite bodies replete with host rock fragments can, thus, be explained by propagation, coalescence and opening of multiple extension fractures followed by infiltration of melt. This process accounts for the well-known presence of parautochthonous fragments in pseudotachylite dikes at both impact structures.

A second mechanism of in situ fragmentation is evident in the enhanced spatial density of irregular fractures at acute tips of elongate fragments and separation of highly angular fragments from pseudotachylite body margins (Lieger et al., 2009). Such fracturing is typical of thermal corrosion that results from stresses induced by the temperature difference between melt and wall rock or fragments and is well known from endogenic intrusion breccias (Clarke et al., 1998). In summary, (1) pervasive extensional fracturing of target rock, (2) jigsaw geometry of fragments and vein margins, (3) en-echelon vein geometry, (4) evidence for incipient fragmentation and thermal corrosion of fragments, and (5) apparent lack of shear faults require a significant allochthonous component of pseudotachylitic melt.

New geochemical data from Vredefort (Fig. A.3) and Sudbury (Al Barazi et al., 2009) indicates an allochthonous pseudotachylitic melt component. For example, the variation of Fe_2O_3 with SiO_2 indicates that the compositions of pseudotachylite matrices and their immediate wall rocks are dissimilar, regardless of wall rock type (Fig. A.3). Sporadic compositional similarity of matrix and target rock can be explained by assimilation of the latter. Collectively, structural and geochemical data point to fragmentation and pseudotachylitic melt generation as processes that differ in time and space.

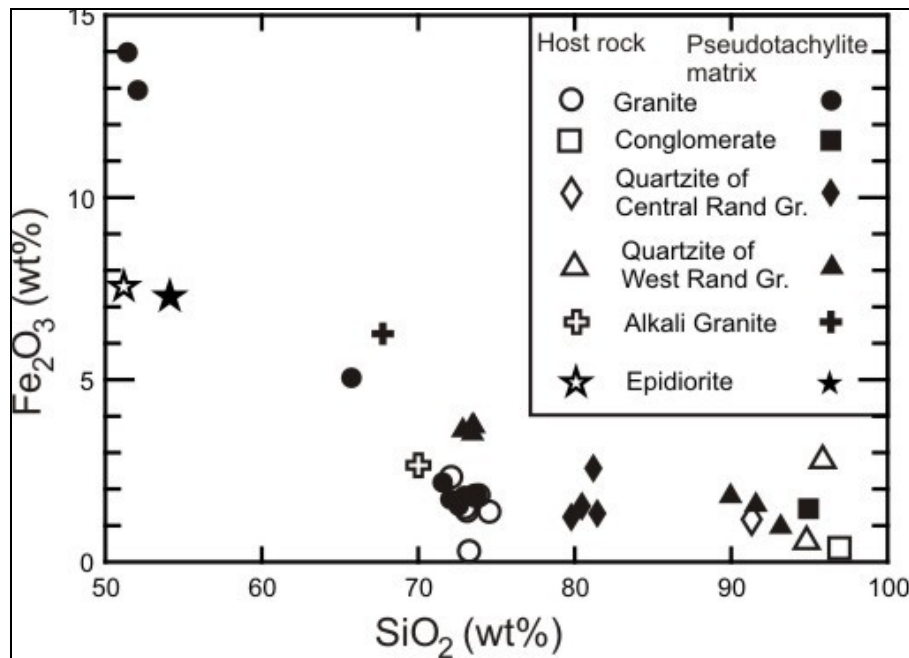


Figure A.3: Diagram depicting the variation in Fe_2O_3 with SiO_2 for pairs of pseudotachylite matrix and immediate host rock samples from the Vredefort impact structure. Note overall dissimilar composition of matrix and host rock, regardless of target rock type.

5. Formation of pseudotachylite bodies during cratering

Based on the pre-impact fit of opposite pseudotachylite vein and dike margins (Fig. A.2C - F), the horizontal component vectors of maximum dilation was determined at a total of 531 stations in the Vredefort Dome (Lieger et al., 2009). The component vectors indicate radial and concentric stretching of target rock (Fig. A.4A), regardless of pseudotachylite body orientation (Fig. A.4B). This centro-symmetric pattern of dilation vectors and orientation of pseudotachylite bodies agrees with directions of maximum principal stretching during the collapse of the central uplift at Vredefort predicted from numerical modeling (Ivanov, 2005).

Interestingly, there is a systematic spatial relationship between dilation magnitude and differential target rock rotation, i.e., rotation per unit length, during cratering at Vredefort. Within a radial distance of ~13 km from the Dome center, target rock rotation is minimal at the exposed crustal level, as rocks were mostly vertically translated and stretched (Fig. A.4E). Beyond this distance, rotation increases significantly, evident by overturned strata of supracrustal cover rocks

and the orientation of the basement-cover interface. The two zones of minimal and maximal target rock rotation correspond respectively to zones of minimal and maximal widths of pseudotachylite dikes, notably of concentric dikes (Fig. A.4C, D). This correlation may indicate that differential target rock rotation was accomplished by tensile fracturing, likely late in the cratering process.

Opening of tensile fracture zones and concomitant in situ fragmentation must have created low-pressure zones into which any nearby melt was transported. This process can explain the presence of pseudotachylite matrix in minute tensile and geometrically irregular fracture systems commonly found in the vicinity of larger ones and points to efficient melt transport into small fracture zones via larger ones (Rousell et al., 2003; Lieger et al., 2009).

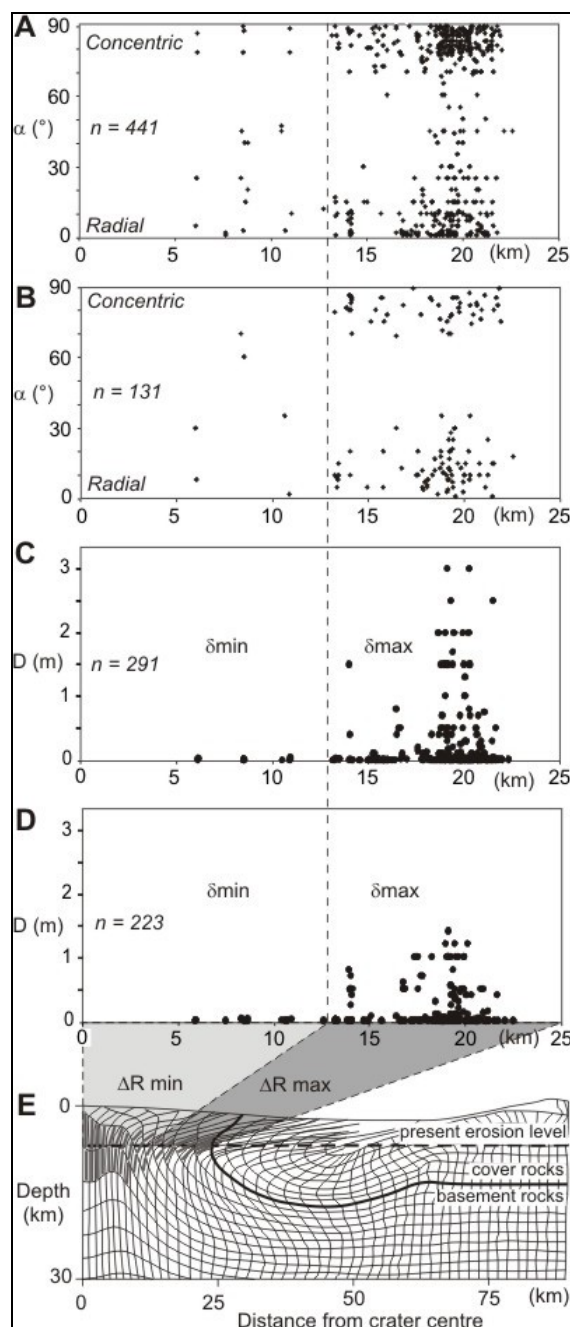


Figure A.4: Geometry of pseudotachylite dikes and impact-induced target rock distortion at Vredefort. A: Diagram showing angular departures from radial directions (α) of pseudotachylite dikes with distance to the crater center. B: Diagram showing angular departures from radial directions (α) of maximal dilation directions of pseudotachylite dikes with distance to the crater center. C: Diagram showing the width of concentric pseudotachylite dikes (D) with respect to distance from the crater center. D: Diagram showing the width of radial pseudotachylite dikes (D) with respect to distance from the crater center. Zones of low and high dilation in (C) and (D) are delineated by δ_{min} and δ_{max} , respectively. E: Radial profile of the Vredefort Dome depicting the variation in impact-induced target rock distortion after Ivanov (2005). Bold lines near present erosion level indicate directions of total stretching. Note uniform vertical stretching and limited differential target rock rotation (ΔR_{min}) in the inner part and subhorizontal stretching and significant differential rotation (ΔR_{max}) in the outer part of the Dome.

6. Emplacement of pseudotachylitic melt

The only melt pool known currently that is sufficiently voluminous and, thus, capable of filling up to hundreds of meter wide tensile fractures in target rock, is the coherent impact melt sheet. In fact, the most prominent fragment-rich pseudotachylite dikes at Sudbury, e.g., the South Range Breccia Belt (Spray et al., 2004) and Podolsky dike, are physically connected to the SIC (Fig. A.1A). We, therefore, consider most of the pseudotachylitic matrix to have crystallized from initially superheated, low-viscosity melt that was driven by pressure gradients and gravity during cratering from the impact melt sheet downward into tensile fractures. This is consistent with the modeled variation in temperature (Ivanov, 2005) and geochemical evidence for allochthonous melt (Speers, 1957; Dressler 1984; Rousell et al., 2003; Al Barazi et al., 2009) in target rock.

Close to the impact melt sheet, drained melt in tensile fractures is expected to be hottest and, thus, most effective in resorbing mafic and partially melting felsic target rock fragments. The presence of schlieric felsic target rock fragments as well as convoluted flow patterns in the matrix close to the SIC attest to turbulent intrusion of initially superheated melt. It is important to note that turbulent flow is evident only within pseudotachylite bodies close to the SIC. The wall rocks, however, do not show such viscous flow, despite their high-temperature overprint by the SIC (Dressler, 1984; Riller et al., 1996; Rosenberg and Riller, 2000). This excludes conductive heat transport as the cause for turbulent flow in the pseudotachylite matrix and indicates that heat in pseudotachylite bodies was advective, i.e., transported by allochthonous melt.

Contact of injected melt with colder fragments and fracture walls would have increasingly cooled the melt with increasing distance from the impact melt sheet. Thus, the more distal the melt-filled fractures are with respect to the melt sheet, the less the shapes of fragments and fracture margins are thermally corroded by the drained impact melt. Therefore, brittle fragmentation is evident best at Vredefort, where exposed pseudotachylite is located at a distance of at least 8 km from the (eroded) impact melt sheet. Moreover, cooling of melt is expected to be faster away from the heat source, i.e., the impact melt sheet. This agrees with the presence of a microcrystalline matrix texture in the pseudotachylite dikes near, and aphanitic to sporadically glassy texture remote from, the SIC at Sudbury (Dressler, 1984; Rousell et al., 2003). Thus, matrix texture as well as

fragment and dike margin shapes provide a vector for the direction of melt transport into target rock, which points away from the impact melt sheet.

7. Conclusions

Previous hypotheses for the formation of fragment-rich pseudotachylite in large terrestrial impact structures underestimated the significance of the strain field during cratering and, despite geochemical evidence, failed to consider an allochthonous melt component. Our structural observations from Sudbury and Vredefort point to emplacement of large volumes of pseudotachylitic melt into tensional fracture zones during central uplift formation. The only currently known melt pool from which to drain sufficiently large melt volumes to fill up to hundreds of meter wide tension fractures is melt from the initially superheated impact melt sheet. Drainage of this melt into tension fractures accounts for well-known characteristics of large-volume pseudotachylite bodies in both impact structures, notably: (1) variation in matrix texture and fragment shapes, (2) geometrical properties of pseudotachylite bodies and (3) dissimilar composition of pseudotachylite matrix and its immediate host rock. Pervasive target rock fracturing accomplished likely quasi-continuous rock flow during cratering, an important physical prerequisite for the formation of impact structures with flat crater floors (Melosh, 1989).

Acknowledgements

This study was funded by the German Science Foundation (grants Ri 916/5 and Ri 916/8) and the National Research Foundation of South Africa (GUN 2074407). Reviews by H.J. Melosh, B. Ivanov, an anonymous person and the Editor, P. Cowie, improved the quality of the manuscript.

References

- Al Barazi, S., Riller, U., Hecht, L. (2009). Geochemistry of pseudotachylites in target rocks of the Sudbury impact structure, Ontario, Canada [abs.]: *Meteoritics & Planetary Science*, v. 44, p. A27-A27.
- Clarke, D.B., Henry, A.S., and White, M.A., (1998). Exploding xenoliths and the absence of “elephants’ graveyards” in granite batholiths: *Journal of Structural Geology*, v. 20, p. 1325–1343, doi: 10.1016/S0191-8141(98)00082-0.
- Dressler, B.O., (1984). The effects of the Sudbury event and the intrusion of the Sudbury igneous complex on the footwall rocks of the Sudbury structure, in Pye, E.G., Naldrett, A.J., and Giblin, P.E., eds., *The geology and ore deposits of the Sudbury structure: Ontario Geological Survey Special Volume 1.*, Toronto, p. 97–136.
- Dressler, B.O., and Reimold, W.U., (2004). Order or chaos? Origin and mode of emplacement of breccias in floors of large impact structures: *Earth-Science Reviews*, v. 67, p. 1–54, doi: 10.1016/j.earscirev.2004.01.007.
- Gibson, R.L., Reimold, W.U., Ashley, A.J., and Koeberl, C., (2002). Metamorphism on the Moon: A terrestrial analogue in the Vredefort Dome, South Africa: *Geology*, v. 30, p. 475–478, doi: 10.1130/0091-7613(2002)030<0475:MOTMAT>2.0.CO;2.
- Gibson, R.L., and Reimold, W.U., (2005). Shock pressure distribution in the Vredefort impact structure, South Africa, in Kenkmann, T., Hörz, F., and Deutsch, A., eds., *Large Meteorite Impacts and Planetary Evolution III: Boulder, Colorado, Geological Society of America Special Paper 384*, p. 329–349.

- Gibson, R.L., Reimold, W.U., and Stevens, G., (1998). Thermal-metamorphic signature of an impact event in the Vredefort dome, South Africa: *Geology*, v. 26, p. 787–790, doi: 10.1130/0091-7613(1998)026<0787:TMSOAI>2.3.CO;2.
- Grieve, R.A.F., Stöffler, D., and Deutsch, A., (1991). The Sudbury Structure - Controversial or Misunderstood: *Journal of Geophysical Research. Planets*, v. 96, p. 22753–22764, doi: 10.1029/91JE02513.
- Grieve, R.A.F., and Theriault, A., (2000). Vredefort, Sudbury, Chicxulub: Three of a kind?: *Annual Review of Earth and Planetary Sciences*, v. 28, p. 305–338, doi: 10.1146/annurev.earth.28.1.305.
- Ivanov, B.A., (2005). Numerical Modeling of the Largest Terrestrial Meteorite Craters: *Solar System Research*, v. 39, p. 381–409, doi: 10.1007/s11208-005-0051-0.
- Kamo, S.L., Reimold, W.U., Krogh, T.E., and Colliston, W.P., (1996). A 2.023 Ga age for the Vredefort impact event and a first report of shock metamorphosed zircons in pseudotachylite breccia and Granophyre: *Earth and Planetary Science Letters*, v. 144, p. 369–388, doi: 10.1016/S0012-821X(96)00180-X.
- Krogh, T.E., Davis, D.W., and Corfu, F., (1984). Precise U-Pb zircon and baddeleyite ages for the Sudbury Area, in Pye, E.G., Naldrett, A.J., and Giblin, P.E., eds., *The geology and ore deposits of the Sudbury structure: Ontario Geological Survey Special Volume 1.*, Toronto, p. 431–446.
- Lieger, D., Riller, U., and Gibson, R.L., (2009). Generation of fragment-rich pseudotachylite bodies during central uplift formation in the Vredefort Impact Structure, South Africa: *Earth and Planetary Science Letters*, v. 279, p. 53–64, doi: 10.1016/j.epsl.2008.12.031.

- Martini, J.E.J., (1991). The nature, distribution and genesis of coesite and stishovite associated with pseudotachylite of the Vredefort Dome, South Africa: *Earth and Planetary Science Letters*, v. 103, p. 285–300, doi: 10.1016/0012-821X(91)90167-G.
- Melosh, H.J., (1989). *Impact Cratering – A Geologic Process*: Oxford University Press, New York. 245 p.
- Melosh, H.J., (2005). The mechanics of pseudotachylite formation in impact events, in Koeberl, C., and Henkel, H., eds., *Impact tectonics*: Springer, p. 55–80.
- Müller-Mohr, V., (1992). Breccias in the basement of a deeply eroded impact structure, Sudbury, Canada: *Tectonophysics*, v. 216, p. 219–226, doi: 10.1016/0040-1951(92)90168-6.
- Pollard, D.D., and Segall, P., (1987). Theoretical displacements and stress near fractures in rocks, with applications of faults, joints, veins, dikes, and solution surfaces, in Atkinson, B.K., ed., *Fracture mechanics of rocks*: London, England, Academic Press, p. 277–349.
- Reimold, W.U., and Gibson, R.L., (2006). The melt rocks of the Vredefort impact structure – Vredefort Granophyre and pseudotachylitic breccias: Implications for impact cratering and the evolution of the Witwatersrand Basin: *Chemie der Erde*, v. 66, p. 1–35, doi: 10.1016/j.chemer.2005.07.003.
- Riller, U., (2005). Structural characteristics of the Sudbury Impact Structure, Canada: impact-induced and orogenic deformation – a review: *Meteoritics & Planetary Science*, v. 40, p. 1723–1740.
- Riller, U., Cruden, A.R., and Schwerdtner, W.M., (1996). Magnetic fabric, microstructure and high temperature metamorphic overprint of the Murray granite pluton, central Ontario: *Journal of Structural Geology*, v. 18, p. 1005–1016, doi: 10.1016/0191-8141(96)00028-4.

- Rosenberg, C., and Riller, U., (2000). Partial-melt topology in statically and dynamically recrystallized granite: *Geology*, v. 28, p. 7–10, doi: 10.1130/0091-7613(2000)28<7:PTISAD>2.0.CO;2.
- Rousell, D.H., Fedorowich, J.S., and Dressler, B.O., (2003). Sudbury Breccia (Canada): a product of the 1850 Ma Sudbury Event and host to footwall Cu-Ni-PGE deposits: *Earth-Science Reviews*, v. 60, p. 147–174, doi: 10.1016/S0012-8252(02)00091-0.
- Speers, E.C., (1957). The age relation and origin of common Sudbury Breccia: *The Journal of Geology*, v. 65, p. 497–514, doi: 10.1086/626451.
- Spray, J.G., Butler, H.R., and Thompson, L.M., (2004). Tectonic influences on the morphometry of the Sudbury impact structure: Implications for terrestrial cratering and modelling: *Meteoritics & Planetary Science*, v. 39, p. 287–301.
- Stöffler, D., Deutsch, A., Avermann, M., Bischoff, L., Brockmeyer, P., Buhl, D., Lakomy, R., and Müller-Mohr, V., (1994). The formation of the Sudbury structure, Canada: Towards a unified impact model, in Dressler B.O., Grieve, R.A.F., and Sharpton, V.L., eds., *Large Meteorite Impacts and Planetary Evolution*: Boulder, Colorado, Geological Society of America Special Paper 293, p. 303–318.
- Thompson, L.M., and Spray, J.G., (1994). Pseudotachylytic rock distribution and genesis within the Sudbury Impact Structure, in Dressler B.O., Grieve, R.A.F., and Sharpton, V.L., eds., *Large Meteorite Impacts and Planetary Evolution*: Boulder, Colorado, Geological Society of America Special Paper 293, p. 275–287.

APPENDIX II: FIELD DATA

Waypoint	GPS E-Wert	GPS S-Wert	Lithology	S1	So	Breccia intensity	Dilation vector	Maximum Dilation in [cm]
1a	537867	7027910	Metasediment			1		
1b	538029	7027282	Amphibolite			1		
1c	535591	7026815	Metasediment			1		
1d	539951	7025738	Gneiss (OGG)			5		
1e	538417	7024483	Gneiss (OGG)			5		
1f	533530	7029734	Metasediment			1		
1g	525010	7027088	Metasediment		150/20	2		
2a	535520	7026636	Metasediment		115/60	1		
3a	535507	7026574	Metasediment		120/72	3	70 - 250	30
4a	537250	7019711	Gneiss (OGG)			0		
5a	537119	7019309	Granophyr			0		
6a	531981	7024698	Quartzite		140/25	2	130-310	12
7a	531800	7024709	Quartzite			0		
8a	531720	7024603	Quartzite			0		
9a	535507	7026574	Metasediment			2	70-250	
14a	558705	6999947	Gneiss (OGG)	315/65		4	45-225	
15a	538561	7024323	Gneiss (OGG)	100/80		1		
15b	538401	7024448	Gneiss (OGG)			2	60-220	30
15c	538407	7024458	Gneiss (OGG)			2	32-212	9
15d	538396	7024451	Gneiss (OGG)			2	35-215	3.7
15e	538397	7024447	Gneiss (OGG)	205/55		2	25-205	5
15f	538414	7024485	Gneiss (OGG)			2	25-205	14.5
15g	538517	7024373	Gneiss (OGG)	110/80; 105/85		2		
16a	535174	7025385	Metasediment	080/75		0		
21a	530437	6999415	Gneiss (OGG)			3	159-339	
83	529868	7001755	Gneiss (OGG)			2		
24a	560065	7025246	Quartzite	230/60		1		
25a	563808	7030377	Metasediment		215/65	0		
26a	560457	7024010	Gneiss (OGG)	040/85		0		
26b	560905	7023570	Gneiss (OGG)	045/85		2	020-200	
27a	546839	7028499	Gneiss (OGG)	002/79; 005/78		2		
28a	548221	7025737	Gneiss (OGG)	008/84		3	092-272	
28b	548217	7025740	Gneiss (OGG)	095/76; 155/72		0		
28c	548235	7025699	Gneiss (OGG)	200/55		0		
28d	548198	7025722	Gneiss (OGG)	160/88, 340/88		2	090-270	
20	538417	7024483	Gneiss (OGG)	308/78		2	055-235	
21	541483	7026770	Gneiss (OGG)	275/75; 280/71		2	030-210, 045-225	
31a	553459	7026900	Gneiss (OGG)			1	359-179	
31b	553564	7026937	Gneiss (OGG)			2	330-150	
32a	553503	7026994	Gneiss (OGG)			3		

32b	553688	7026949	Gneiss (OGG)	190/65; 210/59; 235/76		5	155-335; 140- 320; 165-345	
33	552095	7028349	Gneiss (OGG)	340/47		0		
8	537020	7014740	Inlandgneiss (ILG)	208/82		2	130-310; 145- 325	9
9	537026	7014780	Inlandgneiss (ILG)			2		
10	537025	7014903	Inlandgneiss (ILG)	250/73		1	145-325	2
11	536901	7014872	Inlandgneiss (ILG)			3	150-330; 160- 340	10
12	536915	7014763	Inlandgneiss (ILG)			3		
13	536876	7014740	Inlandgneiss (ILG)			3	145-325	9
14	536862	7014864	Inlandgneiss (ILG)			1		
15	536870	7014826	Inlandgneiss (ILG)			2		
16	536840	7014789	Inlandgneiss (ILG)			0		
17	536595	7015578	Inlandgneiss (ILG)	015/80		4	25-205; 145-325	10
18a	536537	7015632	Gneiss (OGG)	170/89; 190/80		5		
18b	536502	7015657	Gneiss (OGG)	190/80; 204/71; 200/80		5		
19	536493	7015584	Charnokit (ILG)			4	040-220	4
20	536560	7015532	Charnokit (ILG)			5		
22	532636	7014814	Gneiss (OGG)	310/25		1		
23	532539	7014746	Gneiss (OGG)	260/78		0		
24	532696	7015057	Gneiss (OGG)	265/55		1		
25	532575	7015483	Gneiss (OGG)	255/75		3	001-181	30
26	532603	7015512	Gneiss (OGG)			5		
27	532621	7015567	Gneiss (OGG)			5		
28	532581	7015593	Gneiss (OGG)	275/69		5		
29	532584	7015626	Gneiss (OGG)			4		
30	532541	7015639	Gneiss (OGG)			4		
31	532536	7015613	Gneiss (OGG)			4	135-315; 165- 345	5
32	532551	7015528	Gneiss (OGG)			5	135-315	15
33	531392	7016023	Gneiss (OGG)	280/48		2	155-335	2
34	550621	7032795	Quartzite		220/65	1		
35	550730	7032583	Quartzite		215/75	0		
36	550857	7033128	Diabas			0		
37	550748	7032798	Quartzite		220/74	1		
38	550424	7032870	Quartzite		222/66	1		
39	550349	7032915	Quartzite		219/78	1		
40	550262	7032959	Quartzite		221/72	1		
41	549758	7033208	Quartzite		210/74	1		
42	535682	7021933	Gneiss (OGG)	250/70; 252/85		2	05-185	10
43	535648	7021871	Gneiss (OGG)	220/82		5		

44	535622	7021779	Gneiss (OGG)	215/80		2	160-340; 155-335	7
45	535606	7021749	Gneiss (OGG)	225/75		5		
46	535432	7021698	Gneiss (OGG)	193/58		2	170-350	5
47	535318	7021746	Gneiss (OGG)	230/75		1		
48	535277	7021780	Gneiss (OGG)			3		
49	535219	7021779	Gneiss (OGG)			2	179-359	
50	535178	7021739	Gneiss (OGG)			2	170-350	
51	535233	7021801	Gneiss (OGG)			4		
52	535227	7021708	Gneiss (OGG)			2	175-355	
53	535255	7021649	Gneiss (OGG)			2		
54	535678	7022384	Gneiss (OGG)	225/84; 224/84; 280/85		3	170-350	
55	538404	7024442	Gneiss (OGG)			2	40-220	
56	538408	7024440	Gneiss (OGG)			0		
57	538306	7024433	Gneiss (OGG)			0		
58	538389	7024458	Gneiss (OGG)			0		
59	538409	7024465	Gneiss (OGG)			0		
60	541428	7019926	Gneiss (OGG)	070/72		1		
61	541485	7019902	Gneiss (OGG)			2	45-225	
62	541532	7019942	Gneiss (OGG)	200/70; 210/85		1	65-245; 47-227; 50-230	
63	541588	7019968	Gneiss (OGG)			4		
64	541621	7019966	Gneiss (OGG)	005/65; 020/65; 005/68		3	50-230	45
65	541626	7019970	Diabas			0		
66	541638	7019925	Diabas			0		
67	541669	7019894	Gneiss (OGG)	007/75		3		
68	541754	7019926	Gneiss (OGG)	192/65; 192/62; 190/68		3	42-222	10
69	541841	7019993	Gneiss (OGG)	110/71; 100/72		4	060-240; 65-245	3
70	541880	7020024	Gneiss (OGG)	020/85; 020/76		2	50-230; 12-192	10
71	541919	7019990	Gneiss (OGG)	014/85		1		
72	541960	7019958	Gneiss (OGG)	205/85; 195/60; 195/68		3	55-235	15
73	542004	7019922	Gneiss (OGG)	265/65		3	80-260	7
74	541993	7019801	Gneiss (OGG)	260/60		0		
75	541930	7019813	Gneiss (OGG)	050/85		0		
76	541653	7019826	Gneiss (OGG)	040/85		1		
77	549449	7032420	Gneiss (OGG)	180/69		2	45-225	8
78	531270	7001661	Gneiss (OGG)	255/72		2		
79	531255	7001642	Gneiss (OGG)	260/70		2		
80	531172	7001659	Gneiss (OGG)	265/70; 260/65		2	120-200	
81	531123	7001676	Gneiss (OGG)	258/60		2		
82	539064	7002016	Gneiss (OGG)	250/75		2		

84	528775	7000132	Gneiss (OGG)	210/80; 230/80; 230/70		1		
85	528810	7000091	Gneiss (OGG)	230/70		2		
86	528820	699955	Gneiss (OGG)	235/75		3	70-250	38
87	536523	7025812	Gneiss (OGG)	332/70		1		
88	538722	7025739	Gneiss (OGG)	330/85		0		
89	538411	7024481	Gneiss (OGG)	320/80		1	33-213	4
90	538388	7024467	Gneiss (OGG)	305/80		1	20-200	1
91	538431	7024509	Gneiss (OGG)	305/60		2	45-225	8
92	539946	7025726	Gneiss (OGG)	310/65		0		
93	539898	7025678	Gneiss (OGG)	290/70		4		
94	539876	7025706	Gneiss (OGG)	300/65		4		
95	539856	7025728	Gneiss (OGG)	310/70		3	150-330	
96	539947	7025736	Gneiss (OGG)	150/70		4	150-330	15
97	540837	7029217	Quartzite		220/78	1		
98	539838	7030642	Quartzite		170/75	2		
99	535489	7026342	Quartzite		145/80; 135/78	2		
100	535521	7026354	Quartzite		125/75	2		
101	535745	7026173	Quartzite		145/75	2	50-230	
102	538096	7027453	Amphibolite	175/80		1		
103	538032	7027299	Granophyre			1		
104	537952	7027938	Cordierit- Andalusit- Metasediment		160/60	1		
105	537617	7028600	Quartzite		185/80	1		
106	535601	7026609	Quartzite		120/60	0		
107	550381	7032224	Quartzite		225/85	3	160-340	2
108	548586	7033236	Quartzite		190/80; 180/65	1		
109	548523	7033239	Quartzite		165/80	2		
110	548420	7033212	Quartzite		175/85	1		
111	531190	7001653	Gneiss (OGG)			1		
112	531203	7001648	Gneiss (OGG)			1		
113	531228	7001643	Gneiss (OGG)			1		
114	531244	7001644	Gneiss (OGG)			1		
115	531261	7001639	Gneiss (OGG)			1		
116	543059	7024638	Gneiss (OGG)	230/65		3	50-230	5
117	540776	7019539	Gneiss (OGG)	060/78; 065/80		3	005-185	
118	538438	7016664	Gneiss (OGG)	035/80; 015/75; 040/75		2		
119	538420	7016642	Gneiss (OGG)	038/65; 040/60		2	070-250;150- 330	10
120	538369	7016558	Gneiss (OGG)	355/80		2	175-355	
121	538348	7016480	Gneiss (OGG)	030/75		4	115-295	
122	558705	6999947	Gneiss (OGG)	315/65		0		
123	538561	7024323	Gneiss (OGG)	100/80		0		
124	535174	7025385	Gneiss (OGG)	080/75		1		

125	560065	7025246	Gneiss (OGG)	230/60		0		
126	560457	7024010	Gneiss (OGG)	071/72		0		
127	546839	7028499	Gneiss (OGG)	002/79		2	159-339	5
128	548221	7025737	Gneiss (OGG)	008/84		0		
129	541483	7026770	Gneiss (OGG)	275/75		0		
130	553459	7026900	Gneiss (OGG)	227/76		2	055-235	3
131	553564	7026937	Gneiss (OGG)			2	150-330	2
132	553503	7026994	Gneiss (OGG)	190/65		0		
133	553688	7026949	Gneiss (OGG)	210/59		3	155-335	7
134	542074	7020986	Gneiss (OGG)	069/66		2	035-215	
135	530437	6999415	Gneiss (OGG)			2	159-339	4
136	541772	7027753	Gneiss (OGG)	115/75		5		
137	541800	7027717	Gneiss (OGG)	110/75		5		
138	541752	7027873	Gneiss (OGG)	145/80		2		
139	541851	7028016	Gneiss (OGG)	070/89		5		
140	541972	7027819	Gneiss (OGG)	272/80		0		
141	541800	7027446	Gneiss (OGG)	272/70		3		
142	541850	7027376	Gneiss (OGG)	170/72		1		
143	542006	7027425	Gneiss (OGG)	250/85		5		
144	541970	7027402	Gneiss (OGG)			4	85-265	10 cm
145	541879	7027132	Gneiss (OGG)	280/80		1		
146	541798	7027043	Gneiss (OGG)	300/80		0		
147	541817	7027076	Gneiss (OGG)	100/80		0		
148	542933	7026379	Gneiss (OGG)	140/70		0		
149	539123	7032809	Quartzite		170/80	1		
150	525266	7026457	Quartzite		140/75	2		
151	540978	7028846	Quartzite		240/80	0		
152	541113	7028846	Quartzite		195/78	0		
153	541013	7028912	Quartzite		290/80	0		
154	540690	7029530	Quartzite		145/60	0		
155	548200	7031078	Quartzite		350/80	0		
156	548053	7031180	Quartzite		355/80	0		
157	547614	7030846	Quartzite		205/89	0		
158	547689	7030794	Quartzite		050/85	0		
159	547716	7030788	Quartzite		340/89	0		
160	547855	7030716	Quartzite		285/70	0		
161	546993	7029450	Gneiss (OGG)	318/85		2		
162	546633	7029773	Gneiss (OGG)	340/80		0		
163	546157	7030037	Gneiss (OGG)	350/80		0		
164	546085	7029991	Gneiss (OGG)	005/85		0		
165	546013	7029972	Gneiss (OGG)	010/85		0		
166	545906	7030052	Gneiss (OGG)	320/80		0		
167	545994	7029964	Gneiss (OGG)	002/85		0		
168	546058	7029878	Gneiss (OGG)	050/85		0		
169	546114	7029888	Gneiss (OGG)	015/80		1	30-210	5
170	546227	7029469	Gneiss (OGG)	345/80		1		
171	546368	7029199	Gneiss (OGG)	340/80		0		

172	546571	7029219	Gneiss (OGG)	340/85		0		
173	546701	7029305	Gneiss (OGG)	340/82		0		
174	545633	7027898	Gneiss (OGG)	335/78		0		
175	541238	7028113	Gneiss (OGG)	300/89		0		
176	541020	7028174	Gneiss (OGG)	270/85		0		
177	540604	7026653	Gneiss (OGG)	315/80		0		
178	540613	7026726	Gneiss (OGG)	310/80		0		
179	540643	7026969	Gneiss (OGG)	300/85		2		
180	540854	7027046	Gneiss (OGG)	260/80		4		
181	526965	7008046	Quartzite		085/45	0		
182	526692	7008293	Banded iron formation		055/70	0		
183	526617	7008343	Metapelite		070/60	0		
184	526483	7008353	Metapelite		095/60	0		
185	525760	7007189	Quartzite		050/50	0		
186	538265	7026552	Gneiss (OGG)	185/75		2		
187	538117	7026695	Gneiss (OGG)	025/70		0		
188	538203	7026930	Granophyre			0		
189	538405	7027057	Granophyre			0		
190	539132	7032814	Quartzite		200/85	0		
191	547737	7018387	Inlandgneiss (ILG)	222/85		0		
192	548696	7017889	Inlandgneiss (ILG)	090/80		0		
193	547114	7019691	Inlandgneiss (ILG)	290/85		0		
194	544164	7024338	Gneiss (OGG)	025/70		5	60-240	15
195	552024	7022804	Gneiss (OGG)	065/80		2	95-275	4
196	554504	7020889	Gneiss (OGG)	280/85		0		
197	554517	7021061	Gneiss (OGG)	245/80		2	150-330	2
198	554470	7021137	Gneiss (OGG)	305/70		0		
199	554391	7021263	Gneiss (OGG)	290/85		0		
200	554467	7021056	Gneiss (OGG)	305/89		3		
201	556083	7020709	Gneiss (OGG)	275/89		0		
202	555943	7020612	Gneiss (OGG)	120/89		0		
203	555887	7020650	Gneiss (OGG)	240/85		1		
204	555761	7020848	Gneiss (OGG)	110/85		2		
205	555968	7020776	Gneiss (OGG)	230/85		3		
206	556303	7020899	Gneiss (OGG)	080/89		0		
207	556172	7020983	Gneiss (OGG)	065/80		1	70-250	1
208	562336	7021878	Gneiss (OGG)	200/80		3	130-310	5
209	562395	7021870	Gneiss (OGG)	150/89		4		
210	562291	7021962	Gneiss (OGG)	045/85		0		
211	562392	7021813	Gneiss (OGG)	055/89		3		
212	562419	7021759	Gneiss (OGG)	070/89		4	50-230	5
213	562436	7021645	Gneiss (OGG)	060/85		1		
214	562402	7021561	Gneiss (OGG)	055/80		2		
215	562423	7021406	Gneiss (OGG)	070/85		0		
216	562331	7021054	Gneiss (OGG)	065/85		0		
217	562305	7020408	Gneiss (OGG)	065/80		0		

218	562312	7020266	Gneiss (OGG)	095/85		0		
219	562382	7019968	Gneiss (OGG)	107/89		0		
220	562320	7019710	Gneiss (OGG)	085/70		0		
221	562327	7019602	Gneiss (OGG)	070/80		0		
222	562287	7019591	Gneiss (OGG)	075/80		0		
223	562309	7019618	Gneiss (OGG)	075/85		2		
224	562177	7019844	Gneiss (OGG)	085/80		0		
225	562094	7019843	Gneiss (OGG)	090/80		0		
226	562102	7019959	Gneiss (OGG)	082/80		0		
227	561953	7020081	Gneiss (OGG)	070/89		0		
228	561874	7019931	Gneiss (OGG)	115/80		0		
229	561905	7019866	Gneiss (OGG)	095/80		1		
230	561936	7019724	Gneiss (OGG)	110/85		1	35-215	1
231	562006	7020183	Gneiss (OGG)	265/80		0		
232	562325	7020376	Gneiss (OGG)	120/80		0		
233	562215	7020747	Gneiss (OGG)	220/70		0		
234	562211	7020837	Gneiss (OGG)	230/60		0		
235	562693	7020976	Gneiss (OGG)	135/80		1		
236	562757	7019176	Gneiss (OGG)	120/80		1	20-200	2
237	563057	7018557	Gneiss (OGG)	100/80		1		
238	562899	7018845	Gneiss (OGG)	105/85		0		
239	563437	7018582	Gneiss (OGG)	115/89		0		
240	564037	7018603	Gneiss (OGG)	115/89		0		
241	560316	7025666	Quartzite			0		
242	560316	7025562	Gneiss (OGG)	060/80		0		
243	560312	7025457	Gneiss (OGG)	250/60		1	120-300	1
244	560010	7025295	Gneiss (OGG)	220/89		2	20-200	4
245	560064	7025044	Gneiss (OGG)	235/85		1		
246	560211	7025099	Gneiss (OGG)	240/65		1		
247	560371	7025087	Gneiss (OGG)	245/85		2		
248	560559	7025069	Gneiss (OGG)	055/85		0		
249	560701	7024675	Gneiss (OGG)	240/80		1		
250	560629	7024580	Gneiss (OGG)		220/80	2		
251	560505	7024398	Gneiss (OGG)	060/89		1		
252	560737	7024347	Gneiss (OGG)	245/85		1		
253	560831	7024748	Gneiss (OGG)	220/80		1		
254	560364	7025142	Gneiss (OGG)	235/89		0		
255	560390	7025330	Gneiss (OGG)	225/80		0		
256	560162	7025700	Quartzite		220/85	0		
257	556633	7026220	Gneiss (OGG)	350/80		4		
258	556574	7025978	Gneiss (OGG)	350/60		0		
259	556541	7025601	Gneiss (OGG)			4		
260	556652	7024993	Gneiss (OGG)	180/80		2	20-200	3
261	548597	7027048	Gneiss (OGG)	025/89		1		
262	548513	7027437	Gneiss (OGG)	230/80		1		
263	548247	7027211	Gneiss (OGG)	210/70		0		
264	548201	7027294	Gneiss (OGG)	200/89		3		

265	548485	7027323	Gneiss (OGG)	215/85		0		
266	550457	7030485	Gneiss (OGG)			0		
267	550238	7029760	Gneiss (OGG)	005/85		0		
268	550423	7029577	Gneiss (OGG)	005/80		0		
269	550360	7029486	Gneiss (OGG)	015/85		1		
270	549099	7028454	Gneiss (OGG)	355/80		0		
271	549031	7028556	Gneiss (OGG)	010/85		0		
272	549176	7028563	Gneiss (OGG)	355/65		0		
273	550424	7027097	Dolerite	0		1		
274	554842	7030288	Gneiss (OGG)	025/60		0		
275	546583	7020007	Inlandgneiss (ILG)	085/70		0		
276	546719	7020009	Inlandgneiss (ILG)	010/70		1		
277	546857	7019975	Inlandgneiss (ILG)	072/80		0		
278	545315	7017525	Inlandgneiss (ILG)	075/85		2		
279	545298	7017537	Dolerite	0		2		
280	545222	7017741	Inlandgneiss (ILG)	065/80		0		
281	544872	7017912	Inlandgneiss (ILG)	060/85		0		
282	545128	7017653	Inlandgneiss (ILG)	080/80		2	65-245	2
283	544400	7014017	Inlandgneiss (ILG)	075/89		1		
284	540120	7010331	Inlandgneiss (ILG)	060/80		3	110-290	15
285	540172	7010384	Inlandgneiss (ILG)	088/85		3		
286	540075	7010435	Inlandgneiss (ILG)	060/89		2		
287	537338	7009376	Gneiss (OGG)	175/85		3	100-280	5
288	537347	7009488	Gneiss (OGG)	185/85		5		
289	534485	6993350	Gneiss (OGG)	250/89		0		
290	534495	6993245	Gneiss (OGG)	195/85		3		
291	534576	6993624	Gneiss (OGG)	190/85		4	160-340	14
292	535183	6999273	Gneiss (OGG)	205/85		3	60-240	5
293	534978	7001170	Gneiss (OGG)	235/85		1		
294	534402	7002100	Gneiss (OGG)	080/85		0		
295	534214	7002450	Gneiss (OGG)	055/80		1		
296	533974	7002450	Gneiss (OGG)	240/80		2		
297	533953	7002424	Gneiss (OGG)	230/70		2	60-240	3
298	533206	7002780	Gneiss (OGG)	240/80		1		
299	533177	7002676	Gneiss (OGG)	270/80		0		
300	533117	7002456	Gneiss (OGG)	270/89		0		
301	532991	7002484	Gneiss (OGG)	230/89		1		
302	533019	7002736	Gneiss (OGG)	092/89		1	30-210	4
303	535650	7026619	Quartzite		115/75	2		
304	534555	7028492	Quartzite		100/65	2	165-345	4
305	533539	7029739	Alkaligranite	125/85		4		
306	533583	7029671	Alkaligranite	105/80		4		
307	533525	7029673	Alkaligranite	100/85		4	30-210	12
308	525256	7026525	Alkaligranite			4		
309	526746	7019616	Alkaligranite	210/80		1		
310	538277	7026554	Gneiss (OGG)	160/89		3	170-350	7
311	538026	7026713	Gneiss (OGG)	160/75		0		

312	537975	7027348	Gneiss (OGG)	165/70		0		
313	538014	7027097	Quartzite		190/80	0		
314	537897	7026950	Quartzite		195/80	0		
315	537346	7026793	Granophyre			0		
316	537451	7026696	Gneiss (OGG)	190/89		2		
317	537584	7026678	Gneiss (OGG)	225/89		3	90-270	14
318	537721	7026655	Gneiss (OGG)	215/80		2	10-190	
319	537826	7026579	Gneiss (OGG)	150/80		1		
320	537820	7026561	Gneiss (OGG)	140/89		4		
321	538635	7026867	Gneiss (OGG)	160/85		1	20-200	5
322	538627	7026932	Gneiss (OGG)	040/85		1	25-205	1
323	538627	7026867	Gneiss (OGG)	135/89		1	5-185	3
324	538987	7026949	Gneiss (OGG)	140/89		1		
325	539106	7026994	Gneiss (OGG)	060/80		5		
326	539053	7026999	Gneiss (OGG)	135/89		3		
327	539273	7021120	Gneiss (OGG)	005/85		0		
328	539079	7021141	Gneiss (OGG)	030/89		0		
329	538897	7020924	Gneiss (OGG)	020/80		0		
330	539160	7020854	Gneiss (OGG)	015/89		0		
331	539273	7020766	Gneiss (OGG)	030/85		2		
332	539435	7020659	Gneiss (OGG)	040/89		0		
333	539508	7020540	Gneiss (OGG)	030/89		1	40-220	1
334	539674	7020332	Gneiss (OGG)	015/85		1	25-205	2
335	539565	7020765	Gneiss (OGG)	050/85		2	90-270	4
336	539573	7020948	Gneiss (OGG)	030/85		3	80-260	6
337	539416	7021231	Gneiss (OGG)	330/80		0		
338	539561	7021506	Gneiss (OGG)	320/85		3	100-280	7
339	536801	7023188	Gneiss (OGG)	030/85		4	20-200	20
340	536621	7023131	Gneiss (OGG)	320/85		2		
341	536546	7023098	Gneiss (OGG)	315/85		4		
342	536397	7023159	Gneiss (OGG)	345/85		5		
343	536387	7023069	Gneiss (OGG)	310/85		5		
344	536039	7023769	Gneiss (OGG)	330/80		1		
345	536027	7023757	Gneiss (OGG)	335/80		4	35-315	7
346	536008	7022909	Gneiss (OGG)	030/85		1		
347	535951	7023007	Gneiss (OGG)	350/85		2		
348	536095	7023149	Gneiss (OGG)	050/85		5		
349	535953	7023107	Gneiss (OGG)	300/85		0		
350	535931	7023192	Gneiss (OGG)	315/85		5		
351	535942	7023215	Gneiss (OGG)	330/85		0		
352	535882	7023328	Gneiss (OGG)	330/85		0		
353	535337	7023208	Gneiss (OGG)	320/89		0		
354	535247	7023233	Gneiss (OGG)	135/80		1		
355	534913	7023352	Granophyre			0		
356	534910	7023244	Gneiss (OGG)	260/75		0		
357	534676	7023016	Gneiss (OGG)	295/80		0		
358	534714	7022951	Gneiss (OGG)	295/85		0		

359	535098	7022003	Gneiss (OGG)	272/89		0		
360	535203	7021840	Gneiss (OGG)	045/89		4		
361	535269	7021769	Gneiss (OGG)	040/89		5	90-270	
362	535310	7021759	Gneiss (OGG)	050/80		2		
363	535352	7021856	Gneiss (OGG)	350/89		4	150-330	7
364	535356	7022086	Gneiss (OGG)	275/85		1		
365	535415	7022082	Gneiss (OGG)	285/85		4		
366	535294	7022316	Gneiss (OGG)	275/89		1		
367	535569	7022330	Gneiss (OGG)	040/89		0		
368	535653	7022330	Gneiss (OGG)	290/85		3		
369	535684	7022410	Gneiss (OGG)	045/85		4		
370	535797	7022665	Gneiss (OGG)	030/89		0		
371	535830	7022806	Gneiss (OGG)	310/85		0		
372	535902	7022962	Gneiss (OGG)	345/89		2	20-200	4
373	535355	7019720	Gneiss (OGG)	055/80		0		
374	534971	7019746	Gneiss (OGG)	050/85		0		
375	534917	7019929	Gneiss (OGG)	050/85		4		
376	534819	7020045	Gneiss (OGG)	300/80		2	115-295	4
377	534611	7020446	Gneiss (OGG)	070/85		5	110-290	30
378	534673	7020632	Gneiss (OGG)	045/85		2		
379	534609	7020699	Gneiss (OGG)	305/85		4		
380	534521	7020776	Gneiss (OGG)	040/85		5		
381	534531	7020864	Gneiss (OGG)	290/89		5		
382	534724	7021038	Gneiss (OGG)	035/89		0		
383	534774	7021041	Gneiss (OGG)	040/85		4		
384	534637	7021252	Gneiss (OGG)	040/85		0		
385	534379	7021449	Dolerite			0		
386	534400	7021875	Gneiss (OGG)	270/89		1		
387	534174	7022273	Gneiss (OGG)	060/89		1		
388	534303	7022428	Gneiss (OGG)	290/89		2		
389	534290	7022449	Gneiss (OGG)	270/80		1		
390	534378	7022500	Gneiss (OGG)	300/80		2		
391	534398	7022508	Gneiss (OGG)	280/85		3	70-250	
392	534666	7022793	Gneiss (OGG)	300/85		1		
393	534742	7023139	Gneiss (OGG)	300/80		2	20-200	
394	534747	7023235	Gneiss (OGG)	255/75		2	25-205	4
395	534702	7023305	Gneiss (OGG)	300/80		0		
396	534735	7023494	Gneiss (OGG)	275/80		2	10-190	3
397	534607	7023279	Gneiss (OGG)	270/80		1		
398	534497	7023094	Gneiss (OGG)	275/80		1		
399	534430	7023107	Gneiss (OGG)	278/85		3		
400	534368	7023041	Gneiss (OGG)	300/85		2		
401	534101	7023328	Gneiss (OGG)	060/89		2		
402	534100	7023544	Gneiss (OGG)	060/85		0		
403	533985	7023246	Gneiss (OGG)	270/89		2		
404	533947	7023155	Gneiss (OGG)	235/85		1		
405	533950	7023056	Gneiss (OGG)	040/89		3	120-300	10

406	533891	7022985	Gneiss (OGG)	270/89		3	35-215	10
407	533799	7022924	Gneiss (OGG)	060/75		4		
408	533919	7022594	Gneiss (OGG)	270/85		0		
409	534134	7022517	Gneiss (OGG)	320/85		0		
410	533885	7022079	Gneiss (OGG)	045/89		0		
411	533758	7021991	Gneiss (OGG)	310/85		3		
412	533667	7021954	Gneiss (OGG)	305/89		2		
413	533671	7021869	Gneiss (OGG)	300/85		2		
414	533724	7021706	Gneiss (OGG)	282/85		0		
415	533661	7021538	Gneiss (OGG)	250/89		0		
416	533749	7020824	Gneiss (OGG)	062/85		0		
417	534010	7020763	Gneiss (OGG)	050/89		1		
418	534335	7020706	Gneiss (OGG)	260/85		4	40-220	15
419	534426	7020575	Gneiss (OGG)	270/85		1		
420	534494	7020431	Gneiss (OGG)	045/85		3		
421	534516	7020358	Gneiss (OGG)	065/85		2	110-290	
422	534740	7020007	Gneiss (OGG)	080/80		2		
423	534779	7019966	Gneiss (OGG)	085/85		5		
424	534809	7019905	Gneiss (OGG)	030/89		0		
425	533963	7020236	Gneiss (OGG)	270/85		0		
426	533947	7020693	Gneiss (OGG)	290/89		0		
427	534011	7020761	Gneiss (OGG)	055/80		2		
428	533542	7021454	Gneiss (OGG)	310/89		0		
429	533458	7021570	Gneiss (OGG)	095/80		4		
430	533522	7021676	Gneiss (OGG)	115/80		0		
431	533653	7021730	Gneiss (OGG)	100/80		2	80-260	
432	533614	7021773	Gneiss (OGG)	100/80		4		
433	533413	7021663	Gneiss (OGG)	295/80		0		
434	533405	7021701	Gneiss (OGG)	315/89		0		
435	533438	7022026	Gneiss (OGG)	100/75		2		
436	533496	7022082	Gneiss (OGG)	120/80		0		
437	533588	7022202	Gneiss (OGG)	120/85		0		
438	533607	7022257	Gneiss (OGG)	105/85		1	85-265	
439	533613	7022373	Gneiss (OGG)	120/89		2	95-285	
440	533809	7022483	Gneiss (OGG)	080/89		0		
441	533615	7022749	Gneiss (OGG)	100/89		3		
442	533626	7022884	Gneiss (OGG)	100/89		1		
443	533602	7022945	Gneiss (OGG)	090/85		0		
444	533388	7023053	Gneiss (OGG)	130/89		0		
445	533406	7021221	Gneiss (OGG)	095/85		1		
446	533712	7020060	Gneiss (OGG)	095/85		1		
447	555695	7031993	Quartzite		330/85	0		
448	555693	7031655	Quartzite		055/80	1		
449	556193	7026609	Gneiss (OGG)	035/89		0		
450	556097	7026440	Gneiss (OGG)	030/89		0		
451	555656	7025849	Gneiss (OGG)	035/89		1		
452	555647	7025788	Gneiss (OGG)	020/89		3	30-210	4

453	555679	7025761	Gneiss (OGG)	020/85		3		
454	555802	7025643	Gneiss (OGG)	005/85		0		
455	555869	7025374	Gneiss (OGG)	020/85		0		
456	556150	7025069	Gneiss (OGG)	030/89		4		
457	556193	7025503	Gneiss (OGG)	050/85		4	140-320	15
458	556326	7025589	Gneiss (OGG)	055/85		5	20-200	35
459	556449	7025725	Gneiss (OGG)	330/85		4		
460	556461	7025725	Gneiss (OGG)	025/85		0		
461	556540	7025031	Gneiss (OGG)	022/85		5		
462	556597	7024916	Gneiss (OGG)	020/85		5	120-300	8
463	556557	7024752	Gneiss (OGG)	030/89		5	125-305	10
464	556755	7024834	Gneiss (OGG)	325/85		5	10-190	
465	542831	7004497	Inlandgneiss (ILG)	100/89		2	65-245	20
466	543968	7004331	Inlandgneiss (ILG)	300/80		0		
467	544129	7004572	Inlandgneiss (ILG)	250/85		0		
468	543435	7003233	Inlandgneiss (ILG)	050/85		0		
469	543826	7002399	Inlandgneiss (ILG)	305/85		0		
470	540084	7005882	Inlandgneiss (ILG)	035/70		0		
471	539803	7005368	Inlandgneiss (ILG)	050/85		1	130-310	
472	539746	7005926	Inlandgneiss (ILG)	055/80		3		
473	539904	7005852	Inlandgneiss (ILG)	060/80		3	140-320	7
474	539866	7005978	Inlandgneiss (ILG)	290/80		0		
475	538357	7011299	Gneiss (OGG)	285/80		0		
476	548033	7008696	Inlandgneiss (ILG)	030/80		0		
477	548909	7008210	Inlandgneiss (ILG)	005/70		0		
478	546917	7009090	Inlandgneiss (ILG)	020/80		0		
479	530429	7018696	Gneiss (OGG)	310/89		0		
480	529665	7018780	Granophyre			0		
481	529891	7018623	Gneiss (OGG)	130/80		0		
482	530454	7018615	Gneiss (OGG)	345/80		4		
483	530576	7018666	Gneiss (OGG)	340/85		5		
484	530544	7020531	Gneiss (OGG)	200/80		0		
485	530241	7020844	Quartzite		310/88	0		
486	530535	7020596	Gneiss (OGG)	125/80		0		
487	529433	7017700	Gneiss (OGG)	290/89		3		
488	530542	7016605	Gneiss (OGG)	325/80		4		
489	531405	7016007	Gneiss (OGG)	270/80		2		
490	531681	7015459	Gneiss (OGG)	285/85		0		
491	531576	7015489	Gneiss (OGG)	290/85		1	120-300	2
492	531957	7015075	Gneiss (OGG)	265/85		0		
493	532243	7015538	Gneiss (OGG)	260/85		0		
494	532298	7015538	Gneiss (OGG)	270/85		3	20-200	7
495	532525	7015608	Gneiss (OGG)	290/85		4	140-320	10
496	532584	7015511	Gneiss (OGG)	275/85		5		
497	532642	7015429	Gneiss (OGG)	275/80		0		
498	532674	7015077	Gneiss (OGG)	275/80		0		
499	532668	7015072	Gneiss (OGG)	235/80		1		

500	532432	7015279	Gneiss (OGG)	265/80		0		
501	532070	7015721	Gneiss (OGG)	255/60		4	110-290	25
502	532098	7015891	Dolerite					
503	532098	7015891	Gneiss (OGG)	260/85		4		
504	531993	7015591	Gneiss (OGG)	260/80		2		
505	529238	7017756	Gneiss (OGG)	260/80		2		
506	530322	7015997	Gneiss (OGG)	350/85		0		
507	530463	7016593	Gneiss (OGG)	320/85		3		
508	542342	7023209	Gneiss (OGG)	120/60		5	110-290	
509	542124	7023375	Gneiss (OGG)	110/85		2		
510	543332	7024461	Gneiss (OGG)	080/89		2		
511	541726	7024183	Gneiss (OGG)	015/85		0		
512	541587	7024822	Dolerite			2		
513	541517	7024965	Gneiss (OGG)	305/89		5		
514	541549	7025021	Gneiss (OGG)	275/89		1	50-230	2
515	541558	7025040	Gneiss (OGG)	280/85		3		
516	541499	7025029	Gneiss (OGG)	310/85		0		
517	541283	7025082	Gneiss (OGG)	310/85		3	1-181	5
518	541214	7025073	Gneiss (OGG)	295/85		5	145-325	10
519	541198	7024938	Gneiss (OGG)	320/85		3	110-290	6
520	541172	7024853	Gneiss (OGG)	307/85		5		
521	538942	7024545	Gneiss (OGG)	285/85		2		
522	538681	7024535	Gneiss (OGG)	320/85		1	100-280	4
523	540063	7023091	Gneiss (OGG)	265/85		4		
524	539803	7023418	Gneiss (OGG)	005/85		0		
525	539792	7025730	Gneiss (OGG)	350/60		4		
526	531801	6998343	Gneiss (OGG)	230/80		3	65-245	6
527	532035	6998273	Gneiss (OGG)	220/85		3		
528	532143	6998348	Gneiss (OGG)	170/80		5	150-330	35
529	532374	6998431	Gneiss (OGG)	310/85		0		
530	532566	6998237	Gneiss (OGG)	255/80		2	70-250	5
531	532781	6998294	Gneiss (OGG)	280/80		3	80-260	5
532	532428	6998064	Gneiss (OGG)	250/85		0		
533	532309	697990	Gneiss (OGG)	260/85		0		
534	532420	6997826	Gneiss (OGG)	270/89		0		
535	532393	6997585	Gneiss (OGG)	245/80		1	160-340	2
536	532271	6997487	Gneiss (OGG)	075/80		2		
537	532380	6997228	Gneiss (OGG)	115/89		1		
538	532460	6997155	Gneiss (OGG)	270/80		2		
539	532519	6997152	Gneiss (OGG)	100/89		4		
540	532648	6997015	Gneiss (OGG)	240/89		2		
541	532788	6996790	Gneiss (OGG)	095/80		3		
542	532857	6996486	Gneiss (OGG)	265/85		0		
543	532889	6996063	Gneiss (OGG)	265/85		0		
544	533125	6995602	Gneiss (OGG)	275/89		0		
545	532965	6995392	Diorite			0		
546	532718	6994794	Gneiss (OGG)	140/85		3		

547	532299	6994087	Gneiss (OGG)	210/85		0		
548	532472	6994295	Gneiss (OGG)	050/85		2		
549	532268	6994714	Gneiss (OGG)	080/85		0		
550	532121	6995020	Gneiss (OGG)	110/85		0		
551	531961	6995093	Gneiss (OGG)	280/80		1		
552	531924	6995196	Gneiss (OGG)	300/85		5		
553	531498	6995077	Gneiss (OGG)	290/80		2		
554	530870	6995059	Gneiss (OGG)	085/80		3		
555	530725	6995272	Gneiss (OGG)	140/89		2		
556	531300	6995303	Gneiss (OGG)	120/85		4		
557	531515	6995503	Gneiss (OGG)	065/80		4		
558	531617	6995595	Gneiss (OGG)	110/80		5		
559	531845	6995902	Gneiss (OGG)	085/80		4	50-230	15
560	531848	6996132	Gneiss (OGG)	220/80		4	120-300	30
561	531799	6996224	Gneiss (OGG)	200/80		3	165-345	15
562	531779	6996314	Gneiss (OGG)	025/85		0		
563	531751	6996663	Gneiss (OGG)	275/85		3	5-185	5
564	531784	6996833	Granophyre			3		
565	531845	6997197	Diorite			2		
566	531930	6997599	Gneiss (OGG)	025/85		0		
567	531457	6998924	Gneiss (OGG)	165/85		1		
568	531287	6999085	Gneiss (OGG)	275/85		0		
569	530680	6999331	Gneiss (OGG)	075/80		0		
570	530459	6999399	Gneiss (OGG)	255/80		1		
571	530375	6999517	Gneiss (OGG)	245/85		1		
572	530257	6999623	Gneiss (OGG)	340/89		0		
573	530056	6999622	Gneiss (OGG)	235/80		1	45-225	3
574	529990	6999557	Gneiss (OGG)	260/80		3		
575	530264	6999206	Gneiss (OGG)	265/80		3		
576	529973	6998897	Gneiss (OGG)	275/89		0		
577	529783	6998964	Gneiss (OGG)	270/80		0		
578	529715	6999110	Gneiss (OGG)	285/85		0		
579	529679	6999128	Gneiss (OGG)	275/80		2		
580	529445	6999101	Granophyre			0		
581	529057	6999546	Gneiss (OGG)	235/80		0		
582	530592	6997841	Gneiss (OGG)	110/70		0		
583	530837	6997774	Gneiss (OGG)	190/70		0		
584	531082	6997965	Gneiss (OGG)	195/85		0		
585	531162	6998061	Diorite			3		
586	531294	6998226	Gneiss (OGG)	250/85		4		
587	531508	6998513	Gneiss (OGG)	240/89		0		
588	532664	6999089	Gneiss (OGG)	230/85		4		
589	529429	7009319	Gneiss (OGG)	235/85		0		
590	529344	7009373	Gneiss (OGG)	275/89		0		
591	529214	7009560	Gneiss (OGG)	275/85		1	140-320	2
592	529112	7009744	Gneiss (OGG)	278/80		5		
593	529136	7009887	Gneiss (OGG)	300/89		0		

594	529091	7009893	Gneiss (OGG)	270/85		3	140-320	7
595	529072	7010125	Gneiss (OGG)	260/80		3	30-210	3
596	528913	7010177	Diorite			2		
597	528773	7010348	Gneiss (OGG)	260/85		0		
598	528743	7010552	Gneiss (OGG)	290/80		2		
599	528826	7010805	Gneiss (OGG)	300/85		0		
600	528785	7010923	Gneiss (OGG)	240/80		0		
601	528787	7011073	Gneiss (OGG)	270/80		0		
602	528794	7011270	Gneiss (OGG)	265/80		1		
603	528997	7011313	Gneiss (OGG)	250/80		0		
604	529191	7011089	Gneiss (OGG)	275/80		0		
605	529325	7010970	Gneiss (OGG)	285/89		0		
606	529376	7010960	Gneiss (OGG)	100/85		4		
607	529464	7010960	Gneiss (OGG)	060/85		4		
608	529519	7010966	Gneiss (OGG)	272/85		2	30-210	14
609	529736	7011002	Gneiss (OGG)	278/80		4	140-320	20
610	529701	7010447	Gneiss (OGG)	275/80		3		
611	529492	7010042	Gneiss (OGG)	270/89		0		
612	529499	7009936	Gneiss (OGG)	255/80		2		
613	531822	7003497	Gneiss (OGG)	245/80		3	85-265	4
614	530526	7002346	Gneiss (OGG)	235/85		0		
615	530590	7002205	Gneiss (OGG)	255/80		1		
616	544605	7039197	Quartzite		200/80	1	105-285	2
617	544764	7039342	Quartzite		210/80	1		
618	544829	7039342	Quartzite		200/80	1		
619	544906	7039279	Quartzite		250/80	0		
620	544996	7039216	Quartzite		235/70	0		
621	545097	7039155	Quartzite		255/60	2		
622	545447	7039772	Quartzite		350/85	0		
623	545565	7039869	Quartzite		345/85	0		
624	545548	7039911	Quartzite		350/88	0		
625	545621	7040185	Quartzite		182/83	0		
626	545627	7040330	Quartzite		335/85	1		
627	545895	7040339	Quartzite		200/55	0		
628	546016	7040459	Quartzite		220/85	4		
629	546027	7040616	Quartzite		255/60	5		
630	546040	7040720	Quartzite		255/80	5		
631	546078	7040709	Quartzite		220/60	0		
632	546135	7040639	Quartzite		260/30	0		
633	546278	7040444	Quartzite			4		
634	546428	7040290	Quartzite		130/60	0		
635	546300	7040271	Quartzite		185/80	0		
636	546212	7040214	Quartzite		160/80	0		
637	546083	7040166	Quartzite		195/70	0		
638	546018	7040220	Quartzite		175/60	4		
639	545955	7040384	Quartzite		195/80	0		
640	532113	7003164	Gneiss (OGG)	235/80		4		

641	532073	7003042	Gneiss (OGG)	225/80		4		
642	532123	7003009	Gneiss (OGG)	220/80		5		
643	532211	7002991	Gneiss (OGG)	230/80		4	10-190	8
644	532235	7003111	Gneiss (OGG)	210/85		0		
645	532257	7003267	Gneiss (OGG)	260/80		1		
646	529664	7001625	Gneiss (OGG)	270/89		1	10-190	1
647	529588	7001769	Gneiss (OGG)	230/89		0		
648	529425	7001723	Gneiss (OGG)	080/80		0		
649	529344	7001683	Gneiss (OGG)	250/80		1		
650	529390	7001435	Gneiss (OGG)	250/80		2		
651	529215	7001450	Gneiss (OGG)	255/88		1		
652	529253	7001566	Gneiss (OGG)	235/80		1		
653	529264	7001859	Gneiss (OGG)	270/85		0		
654	529509	7001884	Gneiss (OGG)	085/85		2	25-205	2
655	529561	7001849	Gneiss (OGG)	240/85		3	15-195	6
656	529666	7001795	Gneiss (OGG)	270/85		5	45-225	17
657	529908	7001522	Gneiss (OGG)	270/85		3		
658	530024	7001602	Gneiss (OGG)	240/89		2		
659	530106	7001641	Gneiss (OGG)	255/80		2		
660	530099	7001521	Gneiss (OGG)	240/85		2		
661	530329	7001183	Gneiss (OGG)	260/85		1		
662	530192	7001194	Gneiss (OGG)	265/80		0		
663	529973	7001228	Gneiss (OGG)	255/60		0		
664	529816	7001383	Gneiss (OGG)	255/85		4		
665	529089	7000541	Gneiss (OGG)	225/65		0		
666	529260	7000370	Gneiss (OGG)	210/80		0		
667	529201	7000542	Gneiss (OGG)	235/80		0		
668	540481	7024894	Gneiss (OGG)	160/85		5		
669	540549	7024782	Gneiss (OGG)	280/70		5	65-245	42
670	533382	7029848	Alkaligranite	235/89		3		
671	533327	7029877	Alkaligranite	200/80		3	170-350	
672	533230	7029828	Alkaligranite	215/80		3		
673	533202	7029803	Alkaligranite	200/85		1		
674	533303	7029815	Alkaligranite	210/85		1		
675	533380	7029685	Alkaligranite	245/89		0		
676	533487	7029866	Alkaligranite	230/89		3		
677	531642	7014635	Gneiss (OGG)	240/85		0		
678	532557	7014169	Gneiss (OGG)	210/80		0		
679	532549	7014119	Gneiss (OGG)	220/89		4		
680	532543	7014712	Gneiss (OGG)	275/89		0		
681	529738	7016256	Gneiss (OGG)	230/85		0		
682	529756	7016073	Gneiss (OGG)	255/85		0		
683	529891	7015678	Gneiss (OGG)	240/85		0		
684	528206	7016158	Banded iron formation	235/82		0		
685	528233	7016244	Quartzite			0		
686	528546	7016428	Dolerite			0		

687	529368	7017480	Gneiss (OGG)	240/89		0		
688	530516	7018566	Gneiss (OGG)	330/80		4		
689	529275	7015460	Gneiss (OGG)	285/85		0		
690	529443	7015408	Gneiss (OGG)	280/85		0		
691	530444	7015075	Gneiss (OGG)	280/85		1		
692	530487	7014774	Gneiss (OGG)	290/85		0		
693	529992	7013440	Gneiss (OGG)	295/70		0		
694	529912	7013424	Gneiss (OGG)	300/85		5	150-330	10
695	529813	7013470	Gneiss (OGG)	255/85		5		
696	529695	7013484	Gneiss (OGG)	260/80		0		
697	529666	7013481	Gneiss (OGG)	285/80		3		
698	528561	7013369	Gneiss (OGG)	225/30		0		
699	528428	7013291	Gneiss (OGG)	120/80		0		
700	529357	7013556	Gneiss (OGG)	285/80		0		
701	529541	7013589	Gneiss (OGG)	310/85		4	170-350	4
702	529581	7013561	Gneiss (OGG)	305/80		5		
703	529591	7013569	Gneiss (OGG)	305/80		3		
704	529617	7013588	Gneiss (OGG)	300/80		5	10-190	20
705	529679	7013546	Gneiss (OGG)	285/89		4		
706	529763	7013518	Gneiss (OGG)	275/89		0		
707	530113	7013482	Gneiss (OGG)	235/89		0		
708	530158	7013600	Gneiss (OGG)	110/85		0		
709	537374	7028521	Quartzite	162/53		2		
710	533761	7029898	Alkaligranite	260/80		5		
711	563812	7030377	Quartzite	230/65		1		
712	525760	7007108	Quartzite		240/60	2		
713	526035	7006918	Quartzite		245/75	3		
714	539560	7035900	Quartzite		070/85	0		
715	539296	7033107	Quartzite		180/60	0		
716	539418	7031313	Quartzite		190/65	1		
717	539444	7031248	Quartzite		185/85	2		
718	539766	7030856	Quartzite		195/80	1		
719	539829	7030616	Quartzite		165/70	4		
720	549660	7032515	Quartzite		350/60	0		
721	549430	7032423	Quartzite		170/80	3	120-300	10
722	535492	7026346	Quartzite		125/80	2		
723	527979	7025802	Quartzite		135/70	0		
724	526939	7019625	Quartzite		170/45	0		
725	519700	7020863	Quartzite		130/60	0		
726	517917	7041750	Quartzite		265/70	0		
727	519948	7041127	Quartzite		010/55	0		
728	538603	7024353	Gneiss (OGG)	300/65		n.d.		
729	538583	7024350	Gneiss (OGG)	300/60		n.d.		
730	538554	7024355	Gneiss (OGG)	330/75		n.d.		
731	538646	7024348	Gneiss (OGG)	296/75		n.d.		
732	538541	7024346	Gneiss (OGG)	288/75		n.d.		
733	538483	7024382	Gneiss (OGG)	250/80		n.d.		

734	535520	7026636	Quartzite		110/60	n.d.		
735	543335	7023910	Gneiss (OGG)	060/70		n.d.		
736	543909	7024307	Gneiss (OGG)	040/40		n.d.		
737	543886	7024299	Gneiss (OGG)	050/85		n.d.		
738	543357	7023922	Gneiss (OGG)	066/70		n.d.		
739	543880	7024333	Gneiss (OGG)	015/80		n.d.		
740	543862	7024297	Gneiss (OGG)	036/76		n.d.		
741	544144	7024336	Gneiss (OGG)	055/85		n.d.		
742	544299	7024401	Gneiss (OGG)	060/75		n.d.		
743	544122	7024943	Gneiss (OGG)	025/85		n.d.		
744	544196	7024983	Gneiss (OGG)	035/85		n.d.		
745	544261	7024358	Gneiss (OGG)	060/85		n.d.		
746	538265	7024514	Gneiss (OGG)	310/75		n.d.		
747	538233	7024539	Gneiss (OGG)	320/65		n.d.		
748	538282	7024702	Gneiss (OGG)	280/80		n.d.		
749	538195	7024686	Gneiss (OGG)	305/85		n.d.		
750	538015	7024310	Gneiss (OGG)	346/85		n.d.		
751	538139	7024719	Gneiss (OGG)	005/85		n.d.		
752	538071	7024749	Gneiss (OGG)	346/86		n.d.		
753	539720	7021029	Gneiss (OGG)	056/85		n.d.		
754	539636	7021139	Gneiss (OGG)	340/80		n.d.		
755	539719	7021392	Gneiss (OGG)	345/82		n.d.		
756	542809	7022950	Gneiss (OGG)	105/70		n.d.		
757	542809	7022945	Gneiss (OGG)	100/75		n.d.		
758	542889	7023031	Gneiss (OGG)	124/72		n.d.		
759	542830	7022836	Gneiss (OGG)	122/80		n.d.		
760	542862	7022884	Gneiss (OGG)	089/70		n.d.		
761	542994	7022247	Gneiss (OGG)	080/65		n.d.		
762	542268	7021802	Gneiss (OGG)	089/60		n.d.		
763	542358	7022037	Gneiss (OGG)	083/75		n.d.		
764	545512	7025273	Gneiss (OGG)	180/70		n.d.		
765	545790	7025224	Gneiss (OGG)	130/70		n.d.		
766	546032	7025300	Gneiss (OGG)	035/57		n.d.		
767	546316	7025359	Gneiss (OGG)	062/75		n.d.		
768	548059	7025147	Gneiss (OGG)	160/87		n.d.		
769	548507	7028649	Gneiss (OGG)	005/60		n.d.		
770	548571	7025813	Gneiss (OGG)	195/55		n.d.		
771	545081	7025041	Gneiss (OGG)	350/60		n.d.		
772	542023	7020956	Inlandgneiss (ILG)	180/75		n.d.		
773	541427	7021132	Inlandgneiss (ILG)	010/85		n.d.		
774	541502	7021179	Inlandgneiss (ILG)	030/85		n.d.		
775	540883	7020947	Gneiss (OGG)	220/78		n.d.		
776	540490	7021027	Gneiss (OGG)	358/78		n.d.		
777	539552	7020954	Gneiss (OGG)	330/80		n.d.		
778	539270	7021113	Gneiss (OGG)	350/85		n.d.		
779	538486	7022232	Gneiss (OGG)	020/85		n.d.		
780	538254	7022770	Gneiss (OGG)	033/78		n.d.		

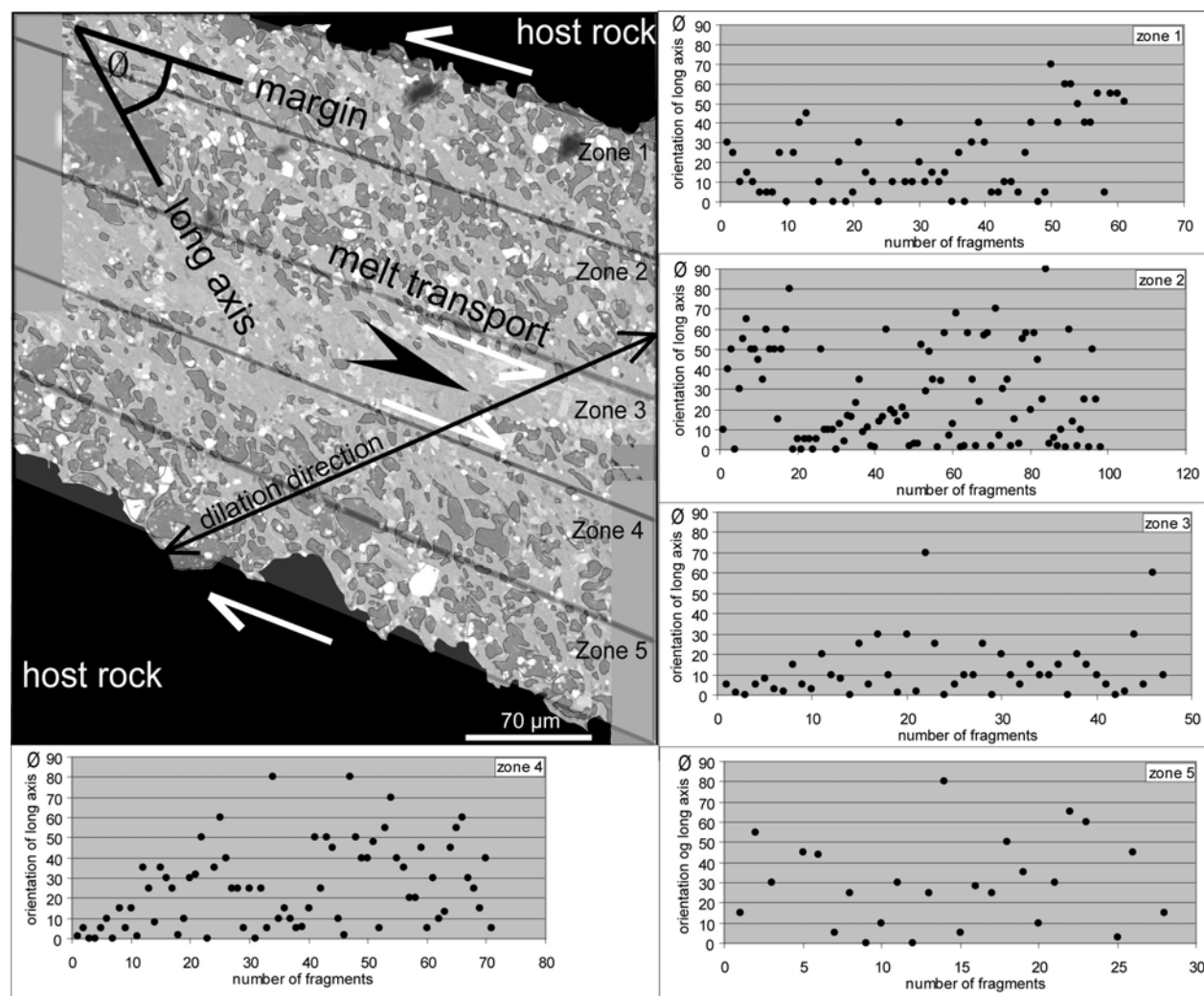
781	538285	7022842	Gneiss (OGG)	043/83		n.d.		
782	537032	7023284	Gneiss (OGG)	035/81		n.d.		
783	537266	7023986	Gneiss (OGG)	330/86		n.d.		
784	537217	7024012	Gneiss (OGG)	320/80		n.d.		
785	536801	7023446	Gneiss (OGG)	001/86		n.d.		
786	536688	7024124	Gneiss (OGG)	345/78		n.d.		
787	536726	7023890	Gneiss (OGG)	011/82		n.d.		
788	536326	7023870	Gneiss (OGG)	340/84		n.d.		
789	536060	7024534	Gneiss (OGG)	340/88		n.d.		
790	542599	7023606	Gneiss (OGG)	335/75		n.d.		
791	541951	7023468	Gneiss (OGG)	300/72		n.d.		
792	540049	7023100	Gneiss (OGG)	001/60		n.d.		
793	539781	7023284	Gneiss (OGG)	318/65		n.d.		
794	539781	7023426	Gneiss (OGG)	336/78		n.d.		
795	539436	7023397	Gneiss (OGG)	005/70		n.d.		
796	539788	7025721	Gneiss (OGG)	260/83		n.d.		
797	538730	7025725	Gneiss (OGG)	335/80		n.d.		
798	538442	7025796	Gneiss (OGG)	330/80		n.d.		
799	537918	7025704	Gneiss (OGG)	320/70		n.d.		
800	537734	7025206	Gneiss (OGG)	340/85		n.d.		
801	536453	7025681	Gneiss (OGG)	286/75		n.d.		
802	540969	7023008	Gneiss (OGG)	331/84		n.d.		
803	552095	7028349	Gneiss (OGG)	340/47		n.d.		
804	537612	7024219	Gneiss (OGG)	190/80		n.d.		
805	537875	7024232	Gneiss (OGG)	190/75		n.d.		
806	538713	7022821	Gneiss (OGG)	180/89		n.d.		
807	540086	7021373	Gneiss (OGG)	178/75		n.d.		
808	539552	7021678	Gneiss (OGG)	185/85		n.d.		
809	539133	7021945	Gneiss (OGG)	180/85		n.d.		
810	539018	7022288	Gneiss (OGG)	075/45		n.d.		
811	538942	7022631	Gneiss (OGG)	060/55		n.d.		
812	536960	7026329	Gneiss (OGG)	170/85		n.d.		
813	537570	7026634	Gneiss (OGG)	155/75		n.d.		
814	537531	7026062	Gneiss (OGG)	160/88		n.d.		
815	537913	7026252	Gneiss (OGG)	162/75		n.d.		
816	538256	7026481	Gneiss (OGG)	163/80		n.d.		
817	538332	7027053	Gneiss (OGG)	160/75		n.d.		
818	539209	7027244	Gneiss (OGG)	165/85		n.d.		
819	539361	7027396	Gneiss (OGG)	160/75		n.d.		
820	540467	7028006	Gneiss (OGG)	135/75		n.d.		
821	541534	7028330	Gneiss (OGG)	140/75		n.d.		
822	541763	7028597	Gneiss (OGG)	140/85		n.d.		
823	541954	7026843	Gneiss (OGG)	090/85		n.d.		
824	541420	7026538	Gneiss (OGG)	095/85		n.d.		
825	541153	7026081	Gneiss (OGG)	130/78		n.d.		
826	541039	7025814	Gneiss (OGG)	125/89		n.d.		
827	541001	7025509	Gneiss (OGG)	095/85		n.d.		

828	541382	7025433	Gneiss (OGG)	095/78		n.d.		
829	541153	7025166	Gneiss (OGG)	140/75		n.d.		
830	540848	7025013	Gneiss (OGG)	095/75		n.d.		
831	541077	7024823	Gneiss (OGG)	095/85		n.d.		
832	541916	7024823	Gneiss (OGG)	300/50		n.d.		
833	536121	7024899	Gneiss (OGG)	100/85		n.d.		
834	535778	7024518	Gneiss (OGG)	160/80		n.d.		
835	535663	7024060	Gneiss (OGG)	050/80		n.d.		
836	535625	7023908	Gneiss (OGG)	070/80		n.d.		
837	535587	7023527	Gneiss (OGG)	075/70		n.d.		
838	540810	7012280	Inlandgneiss (ILG)	230/75		n.d.		
839	539857	7012852	Inlandgneiss (ILG)	230/75		n.d.		
840	539285	7013538	Inlandgneiss (ILG)	225/85		n.d.		
841	539666	7013805	Inlandgneiss (ILG)	030/88		n.d.		
842	541153	7013577	Inlandgneiss (ILG)	230/75		n.d.		
843	541115	7013043	Inlandgneiss (ILG)	225/75		n.d.		
844	543212	7012128	Inlandgneiss (ILG)	040/85		n.d.		
845	543822	7012090	Inlandgneiss (ILG)	035/80		n.d.		
846	544470	7012052	Inlandgneiss (ILG)	035/75		n.d.		
847	545080	7012090	Inlandgneiss (ILG)	115/80		n.d.		
848	545004	7012662	Inlandgneiss (ILG)	115/75		n.d.		
849	545042	7013272	Inlandgneiss (ILG)	050/80		n.d.		
850	543326	7012776	Inlandgneiss (ILG)	150/86		n.d.		
851	544546	7012890	Inlandgneiss (ILG)	080/77		n.d.		
852	544813	7013996	Inlandgneiss (ILG)	040/75		n.d.		
853	544051	7013996	Inlandgneiss (ILG)	060/75		n.d.		
854	542221	7016550	Inlandgneiss (ILG)	350/80		n.d.		
855	542183	7016207	Inlandgneiss (ILG)	190/85		n.d.		
856	542907	7016093	Inlandgneiss (ILG)	170/75		n.d.		
857	543402	7016360	Inlandgneiss (ILG)	140/75		n.d.		
858	543212	7016703	Inlandgneiss (ILG)	280/77		n.d.		
859	543441	7016931	Inlandgneiss (ILG)	080/80		n.d.		
860	543479	7017274	Inlandgneiss (ILG)	075/82		n.d.		
861	543517	7017694	Inlandgneiss (ILG)	260/85		n.d.		
862	542221	7017046	Inlandgneiss (ILG)	035/75		n.d.		
863	542678	7017160	Inlandgneiss (ILG)	260/77		n.d.		
864	542983	7017541	Inlandgneiss (ILG)	255/80		n.d.		
865	542297	7017770	Inlandgneiss (ILG)	200/70		n.d.		
866	547520	7024975	Gneiss (OGG)	200/89		n.d.		
867	548130	7025128	Gneiss (OGG)	200/89		n.d.		
868	548358	7024861	Gneiss (OGG)	200/89		n.d.		
869	548702	7024404	Gneiss (OGG)	200/89		n.d.		
870	548054	7024747	Gneiss (OGG)	200/89		n.d.		
871	547977	7021201	Inlandgneiss (ILG)	270/75		n.d.		
872	548168	7020477	Inlandgneiss (ILG)	235/75		n.d.		
873	548816	7021468	Inlandgneiss (ILG)	265/85		n.d.		
874	549197	7021506	Inlandgneiss (ILG)	085/85		n.d.		

875	549159	7020591	Inlandgneiss (ILG)	250/80		n.d.		
876	548854	7017923	Inlandgneiss (ILG)	080/85		n.d.		
877	549273	7018380	Inlandgneiss (ILG)	070/85		n.d.		
878	549312	7017618	Inlandgneiss (ILG)	030/80		n.d.		
879	549769	7010134	Inlandgneiss (ILG)	270/80		n.d.		
880	549350	7019600	Inlandgneiss (ILG)	220/75		n.d.		
881	550379	7018609	Inlandgneiss (ILG)	230/75		n.d.		
882	551294	7018151	Inlandgneiss (ILG)	035/82		n.d.		
883	551828	7017579	Inlandgneiss (ILG)	040/85		n.d.		
884	551294	7018609	Inlandgneiss (ILG)	030/85		n.d.		
885	550760	7019181	Inlandgneiss (ILG)	035/75		n.d.		
886	535854	7013462	Gneiss (OGG)	040/88		n.d.		
887	535892	7013920	Gneiss (OGG)	035/85		n.d.		
888	536383	7013633	Gneiss (OGG)	040/88		n.d.		
889	535867	7014427	Gneiss (OGG)	015/80		n.d.		
890	536026	7014744	Gneiss (OGG)	020/75		n.d.		
891	536422	7014347	Gneiss (OGG)	025/75		n.d.		
892	537057	7013990	Gneiss (OGG)	040/75		n.d.		
893	536661	7013593	Gneiss (OGG)	035/76		n.d.		
894	537454	7013871	Inlandgneiss (ILG)	070/80		n.d.		
895	538645	7016040	Inlandgneiss (ILG)	250/89		n.d.		
896	538248	7015776	Inlandgneiss (ILG)	050/80		n.d.		
897	538050	7016094	Inlandgneiss (ILG)	060/80		n.d.		
898	537613	7016689	Gneiss (OGG)	080/77		n.d.		
899	537256	7017324	Gneiss (OGG)	030/80		n.d.		
900	538367	7016967	Inlandgneiss (ILG)	070/75		n.d.		
901	538724	7018395	Gneiss (OGG)	030/85		n.d.		
902	535351	7019745	Gneiss (OGG)	220/70		n.d.		
903	535986	7019546	Gneiss (OGG)	020/70		n.d.		
904	536661	7019229	Gneiss (OGG)	220/75		n.d.		
905	537573	7018832	Gneiss (OGG)	220/70		n.d.		
906	537970	7018634	Gneiss (OGG)	230/85		n.d.		
907	535589	7020062	Gneiss (OGG)	020/70		n.d.		
908	536065	7019864	Gneiss (OGG)	015/85		n.d.		
909	539081	7018673	Gneiss (OGG)	040/80		n.d.		
910	535589	7019269	Gneiss (OGG)	220/75		n.d.		
911	536383	7018991	Gneiss (OGG)	030/85		n.d.		
912	537335	7018594	Gneiss (OGG)	040/85		n.d.		
913	534517	7023396	Gneiss (OGG)	090/80		n.d.		
914	534240	7023317	Gneiss (OGG)	275/75		n.d.		
915	535510	7023158	Gneiss (OGG)	265/64		n.d.		
916	535708	7023158	Gneiss (OGG)	080/75		n.d.		
917	536026	7022920	Gneiss (OGG)	040/85		n.d.		
918	534994	7022840	Gneiss (OGG)	040/85		n.d.		
919	534478	7022880	Gneiss (OGG)	030/75		n.d.		
920	534557	7022563	Gneiss (OGG)	260/80		n.d.		
921	534835	7022602	Gneiss (OGG)	245/50		n.d.		

922	535271	7022642	Gneiss (OGG)	080/80		n.d.		
923	535629	7022523	Gneiss (OGG)	040/85		n.d.		
924	535986	7022245	Gneiss (OGG)	040/70		n.d.		
925	535113	7022364	Gneiss (OGG)	220/50		n.d.		
926	535073	7022086	Gneiss (OGG)	040/80		n.d.		
927	548408	7022761	Inlandgneiss (ILG)	040/89		n.d.		
928	540907	7020221	Inlandgneiss (ILG)	230/89		n.d.		
929	540748	7020023	Inlandgneiss (ILG)	220/89		n.d.		
930	540669	7019824	Inlandgneiss (ILG)	250/89		n.d.		
931	541344	7020023	Inlandgneiss (ILG)	230/80		n.d.		
932	541542	7020142	Inlandgneiss (ILG)	190/85		n.d.		
933	541820	7020062	Inlandgneiss (ILG)	190/70		n.d.		
934	542296	7020261	Inlandgneiss (ILG)	020/70		n.d.		
935	541463	7019745	Inlandgneiss (ILG)	040/75		n.d.		
936	541582	7019546	Inlandgneiss (ILG)	230/70		n.d.		
937	541820	7019745	Inlandgneiss (ILG)	190/80		n.d.		
938	542098	7019904	Inlandgneiss (ILG)	200/80		n.d.		
939	542376	7019784	Inlandgneiss (ILG)	200/70		n.d.		
940	542336	7020062	Inlandgneiss (ILG)	200/85		n.d.		

Appendix III



Fragment orientation and distribution in back-scattered electron image of the matrix of the apophysis SunWa (6) in point 5 will be illustrated in five zones (main vein on the left side). Five diagrams show the orientation of the clasts long axes of an about 500 clasts in five zones. The apophysis is 350 μm wide (divided in 5 zones a 70 μm). Larger clasts are located at the margin (zone 1 and 5) and smaller in the inner vein (zone 3). Progressive rotation of clasts with increasing distance to the vein margin has been observed. Values of orientation of long axis (θ) with respect to the vein margin are between 0 and 70° in zone 1 and 5. Large scattering of these values ($\theta=0-90^\circ$) has been observed in zone 2 and 4 with a concentration of these values between 0-20° and 50-60°. Fragments in zone 3 have preferred orientation of clasts between 0-30° with respect to the vein margin. The geometry of this smaller and more rounded clasts display a higher melt flow in the inner area as well as from larger into smaller ones.

Eidesstattliche Erklärung

Ich versichere an Eides Statt durch meine eigenhändige Unterschrift, dass ich die vorliegende Dissertation mit dem Titel:

“Structural and Geochemical Analyses of fragment-rich pseudotachylite bodies and the Vredefort Granophyre of the Vredefort Impact Structure, South Africa”

selbstständig und ohne fremde Hilfe angefertigt habe. Alle Stellen, die wörtlich oder dem Sinn nach auf Publikationen anderer Autoren beruhen, sind als solche kenntlich gemacht. Ich versichere außerdem, dass ich keine andere als die angegebene Literatur verwendet habe. Diese Versicherung bezieht sich auch auf alle in der Arbeit enthaltenen Abbildungen, Tabellen, bildlichen Darstellungen und dergleichen.

Die Arbeit wurde bisher keiner anderen Prüfungsbehörde vorgelegt und auch als Ganzes noch nicht veröffentlicht.

Berlin, den

Unterschrift

(Daniel Lieger)